International School for Advanced Studies

Doctoral Thesis

Aspects of holographic entanglement entropy: shape dependence and hyperscaling violating backgrounds

Author:
Piermarco Fonda

Supervisor:
Dr. Erik Tonni

Friday 18th September, 2015

Thesis submitted for the degree of
Doctor of Philosophy
in Physics

Contents

Chapter 1

Introduction

1.1 Overview

The Standard Model of Particle Physics has asserted as our best model for understanding particle physics with great experimental success. Consequently, the tools of Quantum Field Theory have proved to be incredibly useful in describing - in a phenomenologically accurate and verifiable way - the sub-nuclear phenomena. It became clear already in the '70s that a further effort was necessary to incorporate the theory of general relativity into a unique mathematical framework where gravity is quantized.

Among all attempts to unify the mathematical description of gravity with the other three fundamental forces, String Theory has played and still plays a predominant role in modern theoretical physics. At present day - and very presumably in the next future - it is still lacking any experimental evidence, and thus it has yet to be understood whether it can help us in understanding how quantum gravity is realized in Nature. Nonetheless the framework and the theoretical tools which have been developed in the long process of understanding String Theory have become a valuable subject of interest on its own. A great amount of progress has been made and nowadays the theoretical landscape is so varied and diversified that, although the original motivation is still to find a complete theory of quantum gravity, several branches have developed.

The mathematical strength and beauty of String Theory could be considered as a *per se* reason for pursuing research in this area, however the directions where the theory has developed are so broad and have touched almost all aspects of theoretical physics, ranging from abstract mathematics to the groundings of quantum field theories, from phenomenology of relativistic quark-gluon plasma to the study of high temperature superconductors.

In the last years, part of the field has seen some sort of paradigmatic shift where the ideas developed in String Theory have been used as tools to provide a better understanding of theories where other techniques have failed or are just too difficult to be used: this is true in the context of gauge/gravity duality, where the behaviour of a strongly coupled quantum field theory can be characterized - at least qualitatively - in terms of a theory of gravity.

The subject of this thesis falls in this framework: I have been dealing with holographic computations of entanglement entropy, which is a measure of entanglement for pure states in quantum systems and has been studied in the last decade in different areas of physics ranging from quantum information, condensed matter and quantum gravity.

1.2 Gauge/gravity duality

The AdS/CFT conjecture states that certain classes of conformal field theories in d dimensions admit a dual description in terms of a string theory living in a curved, higher-dimensional space-time. This means that every possible observable quantity (correlators, expectation values and more) of both theories match in a precise way, specified by a dictionary linking mathematical objects in the field theory to the gravitational string theory. In this sense, the dual field theory can be seen as a holographic description [1] of the gravity side, requiring one dimension less to describe the same phenomena.

In its original formulation [2, 3] the conjecture relates $\mathcal{N} = 4$ SYM theory with $SU(N)$ gauge group and type IIB string theory in an $AdS_5 \times S^5$ background with N units of F_5 flux on the S^5. The motivation for the duality comes from considering type IIB string theory in a $10-$dimensional Minkowski background with a stack of parallel $D3-$branes: then one can either look at the low-energy effective action of open strings attached to the branes or see the stack as a black-brane solution of type IIB supergravity in ten dimensions and consider the low energy fluctuations from the near-horizon region. In the former case [2] showed that the theory reduces to a super-Yang-Mills theory with special unitary gauge group of rank N, while in the latter the theory is again a string theory where now the background is not flat but $AdS_5 \times S^5$.

The correspondence is a weak/strong duality, because small couplings on one side correspond to large ones on the other. More precisely, in the large N limit of the gauge theory one has

$$\frac{\lambda}{4\pi N} = g_s \,, \tag{1.1}$$

where g_s and $\lambda = g_{YM}^2 N$ are respectively the string and the 't Hooft coupling constants, and g_{YM} is the Yang-Mills coupling. At fixed λ, it is clear that a large N expansion corresponds to a small string coupling. More precisely, if we take the *planar limit* of the gauge theory, i.e. we send $N \to \infty$ while keeping λ finite, equation (1.1) shows that the higher loops terms in a string amplitude can be discarded, since a stringy loop of genus χ is weighted by a factor $g_s^{-\chi}$.

Since the black-brane radius L (corresponding to the radius of both AdS_5 and of S^5) is directly related to the Ramond-Ramond flux, one can show that the following holds

$$\lambda = \left(\frac{L}{\ell_s}\right)^4 . \tag{1.2}$$

We see that in the planar limit of the gauge theory, or equivalently in the genus zero expansion of the string theory amplitude, a small λ corresponds to both a weakly coupled SYM theory and a highly curved background. Conversely, for $\lambda \to \infty$ the gauge theory becomes strongly coupled while in the string theory one needs to consider only strings fluctuations which have $\ell_s \ll L$, i.e. the strings can be considered as point-like objects as measured in terms of the AdS radius. Reducing strings to non-extended objects means that we need to take the zero-modes of type IIB String Theory, which are the ones of type IIB supergravity (on $AdS_5 \times S^5$). For large λ the string theory becomes an ordinary quantum field theory, and given that we are in the limit of small g_s, one can approximate quantum expectation values by classical correlators. Thus we have a correspondence between a classical (super-)gravitational theory and a strongly coupled (super-)conformal quantum field theory.

This crucial observation and the subsequent generalizations of the correspondence have led to the hope that this duality may indeed just be a particular case of a broader set of dualities, relating quantum field theories and classical gravitational theories. Such a consideration carries the name of gauge/gravity duality.

The general expectation is that given a quantum field theory admitting such a dual, the following relation holds

$$Z_{\text{grav}}[\Phi_{\text{bdy}}] = \left\langle e^{-\int d^d x \Phi_{\text{bdy}}(x) O(x)} \right\rangle_{QFT} , \tag{1.3}$$

i.e. the partition function of the gravitational theory, with field content Φ, such that on the conformal boundary $\Phi \to \Phi_{\text{bdy}}$, is exactly equal to the partition function of the field theory in presence of a source Φ_{bdy} for a certain single-trace operator O. The field Φ_{bdy} is said to be *dual* to the operator O.
At first order in the large N expansion of the QFT ($g_s \to 0$ in the language of supergravity theory), the duality relation can be approximated by

$$e^{-S^{o.s.}_{grav}[\Phi_{\text{bdy}}]} \simeq \left\langle e^{-\int d^d x \Phi_{\text{bdy}}(x) O(x)} \right\rangle_{QFT} , \tag{1.4}$$

where the left-hand side of the equation stands for the on-shell value of the gravitational action with the appropriate boundary conditions.

In the above discussion we intentionally specified that the duality is between a generic QFT and a gravitational theory, somehow extending the requirement that the theory must be conformal. Namely,

the gauge/gravity extends the AdS/CFT conjecture to theories which do not enjoy conformal symmetry, and as we will see later this has been precisely one of the subject of my research[1].

In fact the isometry group of AdS_{d+2} is $SO(d+1,2)$ which is also the conformal group in $d+1$ dimensions. For the dual field theory to be conformal, the requirement on the gravity side is that the space-time must be AdS. Conversely, if we want to study a QFT without conformal symmetry, the duality imposes to deal with geometries with less asymptotic isometries than Anti-de Sitter space-times.

Equation (1.4) not only gives a different way to look at strongly coupled field theories, but also shows how it is possible to compute QFT correlators using classical (super-)gravity actions. We should note however that for any asymptotically AdS space-time the conformal boundary is at infinite proper distance from any point in the bulk. As consequence of this fact, the evaluation of on-shell actions extending all the way down to the boundary gives a divergent quantity. From the gravity point of view, this is clearly an infrared divergence, originating from the behaviour of the fields at infinity. On the other hand, given that equation (1.3) has to hold, the QFT expectation value has to diverge as well, but now from this perspective the divergences have to arise because of ultra-violet effects. This aspect of the duality of divergences is called UV/IR connection [4][2].

From now on, in speaking of divergences we will always use the QFT language, so that UV will always refer to the infrared behaviour of the bulk space-time.

The systematic way to get rid of divergences in computing holographic correlators undergoes the name of *holographic renormalization* [5, 6]. The ideas behind this procedure have been extensively studied in the literature and a working description of the technique is beyond the scope of this thesis. In this procedure, the gravitational action is evaluated on-shell, arbitrarily close to the boundary, i.e. at arbitrarily small values of the UV regulator, and then a proper counter-term has to be added in order to eliminate every and each divergent term. The choice of the counter-term action reflects the scheme dependence of the dual QFT, and thus it has to be chosen with the maximal amount of space-time isometries and internal symmetries preserved. In AdS_{d+2} with d odd, the impossibility to choose a counter-term which preserves all the isometries (in particular the one associated to dilatations and special conformal transformations) reflects precisely the anomalous behaviour of the CFT Ward identities.

Already in the early days of the AdS/CFT correspondence it was understood that the duality goes beyond the possibility to compute local correlators using gravitational on-shell actions. This was somewhat to be expected, because in general a theory is not completely characterized by correlators of local operators. Indeed there are non-local quantities which carry non trivial information and are not accessible from computations of inherently local quantities as $n-$point functions. One of these quantities are Wilson loops, which in general are defined as

$$W(\mathcal{C}) = \mathrm{Tr}\left(P \exp \oint_{\mathcal{C}} A_\mu(s)\sigma^\mu ds\right) , \tag{1.5}$$

where P stands for path-ordered integration, A_μ is a gauge field, $\mathcal{C}$ is a generic a closed curve in Minkowski space and $\sigma^\mu = \sigma^\mu(s)$ is the vector tangent to the curve. The signature of $\mathcal{C}$ determines the nature of the loop (space-, time- or light-like). In [7] it was shown how the expectation value of a Wilson loop could be computed holographically by evaluating the on-shell value of a string world-sheet action, which in the classical limit of the gravity theory amounts to finding a surface $\gamma_{\mathcal{C}}$ homologous[3] to $\mathcal{C}$ whose area, computed in the curved background, is extremal. Then, the correspondence says that

$$\langle W(\mathcal{C})\rangle \simeq e^{-Area[\gamma_{\mathcal{C}}]} . \tag{1.6}$$

As we will see later, this relation is kind of anticipating the holographic prescription for computing entanglement entropy.

We should note that the asymptotic behaviour of bulk quantities is completely determined by the UV physics of the dual QFT and the regularization procedure depends only on the small-scale behaviour

[1] We should also mention that in general the gauge/gravity duality does not require the theories to be necessarily supersymmetric.

[2] This issue actually extends to other considerations and computations in the contest of AdS/CFT so that the UV/IR connection is intended as the fact that to any infrared divergence in the the bulk theory corresponds an ultraviolet one on the boundary. As we will see, this is also the case for the holographic entanglement entropy.

[3] Two (hyper-)surfaces are said to be homologous if they share the same boundary and are connected by a continuous set of deformations.

of the theory, and thus the physically interesting information about the IR of field theory quantities is holographically linked to the dynamics in the inside of the AdS space. For this reason, in dealing with holographic computations it is fundamental to find complete solutions which go deep into the bulk, so that some non-trivial IR information about the dual theory can be found.

1.3 Entanglement Entropy

Entanglement is one of the most striking features of quantum mechanics and has no classical analogue, and as such has no intuitive interpretation. It is natural to ask whether it exists a quantity which measures to some degree how much a system is entangled with its environment. Such a quantity would therefore tell also how much "non-classical" a system is, given that decoherence leads inevitably to disentanglement, and ordinary macroscopic systems at room temperature do not appear to be entangled. Among all possible measures, one is the *entanglement entropy*.

This concept, dating back to the early days of quantum mechanics and being extensively studied in the context of quantum information (see e.g. [8]) has a simple definition: consider a generic quantum system which is bipartite, i.e. its Hilbert space $\mathcal{H}$ is factorizable

$$\mathcal{H} = \mathcal{H}_A \otimes \mathcal{H}_{\bar{A}} \,, \tag{1.7}$$

where A and $\bar{A}$ are (bi-)partitions of the system. As in any quantum system, the density matrix ρ is an operator containing all information about the structure of $\mathcal{H}$, and due to the factorization (1.7), tracing over $\bar{A}$ is a well defined operation, which allows us to define the *reduced density matrix*

$$\rho_A \equiv \mathrm{Tr}_{\mathcal{H}_{\bar{A}}} \rho \,. \tag{1.8}$$

The Von Neumann entropy computed out of ρ_A is the entanglement entropy of A

$$S_A = -\mathrm{Tr}_{\mathcal{H}_A} \rho_A \log \rho_A \,. \tag{1.9}$$

This quantity has several interesting properties. First of all, it does what one expects: as we said at the beginning of this section, the purpose of S_A is measuring how entangled a system is. It can be shown (see e.g. [9–11]) that in the case of a quantum system consisting of an arbitrary number of qubits and partitioning the system by choosing a proper subset of those qubits (calling this partition A), S_A measures the number of entangled pairs between A and its complement. Otherwise stated [11], the quantity S_A is the logarithm of the minimal number of auxiliary states one would need to entangle with A in order to obtain ρ_A from a pure state[4].

The entropy of entanglement is always a non-negative quantity [8] and its value can be at most $\min\{\log d_A, \log d_{\bar{A}}\}$, where $d_A = \dim \mathcal{H}_A$ is the dimension of the partitioned Hilbert space. If the system is in a pure state $|\psi\rangle$, then $\rho = |\psi\rangle\langle\psi|$ and by Schmidt decomposition is easy to show

$$S_A = S_{\bar{A}} \,. \tag{1.10}$$

This is a remarkable property, because for spatial partitions[5] this hints that, for pure states, S_A can depend on the only thing A and $\bar{A}$ have in common: the boundary $\partial A = \partial \overline{A}$.

When the Hilbert space is partitioned in at least three regions, call them A, B and $C = \overline{A \cup B}$, one can define the *mutual information*

$$I_{A,B} = S_A + S_B - S_{A\cup B} \,. \tag{1.11}$$

For pure states, it can be shown that $I_{A,B} \geq 0$, with the equality holding if and only if $\rho_{A\cup B} = \rho_A \otimes \rho_B$, i.e. the two subsystems are completely disentangled.

The positivity of mutual information follows from a more general property of entanglement entropy, the so called *strong subadditivity* [8, 12]

$$S_A + S_B \geq S_{A\cup B} + S_{A\cap B} \,, \tag{1.12}$$

[4] In quantum information language, S_A counts the number of extra qubits necessary to *purify* ρ_A [10].

[5] By spatial partition we mean that A and $\bar{A}$ are partitioning the system in different spatial regions. In this case, S_A is often called *geometric entanglement entropy*.

which is one of the so called *entanglement inequalities*, which are true for any quantum system and can give non-trivial information about a specific theory, once the entanglement entropy is computed.

Another interesting inequality involving the mutual information is [13, 14]

$$I_{A,B} \geq \frac{1}{2}\left(\frac{< O_A O_B >_{\mathrm{c}}}{||O_A||\,||O_B||}\right)^2 , \tag{1.13}$$

where O_A and O_B are generic operators, $< \cdot >_{\mathrm{c}}$ stands for the connected Green's function and $||\cdot||$ stands for the operator norm. It shows how the knowledge of the mutual information allows to put bounds on any correlator in a quantum theory.

1.3.1 Entanglement Entropy in QFTs

Although S_A is a quantity introduced in quantum mechanics, in the last years there has been a growing interest in computing the entropy of entanglement in quantum field theories. In the pioneering work of [15–17] and later of [18] it was shown how to compute S_A in field theories.

The first step is understanding how to represent ρ in field theory. The density matrix for a generic QFT in $d+1$ dimensions can be written as an Euclidean path integral:

$$\rho\left(\phi_1(x_1), \phi_2(x_2)\right) = \frac{1}{Z}\int \mathcal{D}\varphi(t,x) \prod_x \delta\left(\varphi(0_+,x) - \phi_1(x_1)\right) \prod_x \delta\left(\varphi(0_-,x) - \phi_2(x_2)\right) e^{-S_E[\varphi]} , \tag{1.14}$$

where S_E is the Euclidean action, Z is a normalization constant which ensures $\mathrm{Tr}\rho = 1$ and the functional Dirac δ's fix the particular matrix element of the density matrix. Partial tracing over $\mathcal{H}_{\overline{A}}$ is straightforward and can be formally written as

$$\rho_A\left(\phi_1(x_1), \phi_2(x_2)\right) = \frac{1}{Z_A}\int \mathcal{D}\varphi(t,x) \prod_{x\in A} \delta\left(\varphi(0_+,x) - \phi_1(x_1)\right) \prod_{x\in A} \delta\left(\varphi(0_-,x) - \phi_2(x_2)\right) e^{-S_E[\varphi]} , \tag{1.15}$$

notice that the path integral integration variable $\mathcal{D}\varphi$ still involves integration over the whole space, while the δ's act only on points inside A.

Evaluating the trace of a logarithm of a field theory operator is not an easy task and the standard trick is to compute the trace of the $n-$th power of the reduced density matrix ρ_A, which is an operator defined on a replicated geometry of the original space-time.

One then can compute the so called Rényi entropies

$$S_A^{(n)} = \frac{\log \mathrm{Tr}_{\mathcal{H}_A}\rho_A^n}{1-n} , \tag{1.16}$$

which in the limit $n \to 1$ converges to $S_A^{(1)} = S_A$. Strictly speaking, (1.16) is defined only for integer n. One first has to analytically continue the Rényi entropies to non-integer values and take the limit $n \to 1$. The Rényi entropies contain more information about the system than just the entanglement entropy, since one could in principle reconstruct the whole spectrum of the reduced density matrix ρ_A.

Expression (1.14) is well defined in any dimension and for any QFT, however trying to compute the entanglement entropy out of it turns out to be a very hard task. Major simplifications happen for theories in two dimensions.

The remarkable result of [18] is that, if the theory enjoys conformal symmetry, the entanglement entropy of an interval takes the simple form

$$S_A = \frac{c}{3}\log\frac{\ell}{\varepsilon} , \tag{1.17}$$

where ε is a UV cut-off, ℓ is the interval width and c is the Virasoro central charge. This beautiful yet simple formula retains all the power of two-dimensional conformal symmetry, and has generated a field of active research. After that, many other results have been achieved in other two-dimensional theories and for different entangling regions (e.g. two disjoint intervals, where it can be shown that the entanglement entropy depends on the whole CFT data rather than just the central charge [19]).

Nonetheless, (1.17) is true for any theory admitting a UV fixed point (i.e. for any theory which in the small scale limit looks conformal). The central charge c can be promoted to an energy scale dependent quantity, called *c-function*, which takes the value of the Virasoro central charge at any conformal fixed point. This quantity has proven to be monotonically decreasing along flows from the UV to the IR, this fact being known as the *c-theorem* [20].

We should note however that a complete and systematic procedure for computing entanglement entropy in $d+1$ dimensions with $d \geq 2$ is still missing.

One feature of S_A computed on the ground state in a generic bosonic theory [21] is that it is expected to obey the so-called *area law*

$$S_A = \gamma \frac{\text{Area}(\partial A)}{\varepsilon^{d-1}} + \dots \,, \tag{1.18}$$

where γ is a dimensionless scheme-dependent quantity and the dots stand for less divergent terms. This can be proven to be true for any conformal theory. The other subleading divergences are also known (for *smooth* ∂A) although a general proof needs to rely on holographic considerations:

$$S_A = \gamma \frac{\text{Area}(\partial A)}{\varepsilon^{d-1}} + \frac{a_3}{\varepsilon^{d-3}} + \dots + \begin{cases} a_d & d \text{ even} \\ a_d \log \varepsilon & d \text{ odd} \end{cases} + \text{subleading terms}\,, \tag{1.19}$$

where the various coefficients a_i can sometimes be evaluated, depending on the theory under consideration, the shape of A and the dimension d.

For example, for a CFT_{2+1} the entanglement entropy has only one divergent term (which has to obey the area law), and takes the form

$$S_A = \frac{\text{Area}(\partial A)}{\varepsilon} - F_A\,, \tag{1.20}$$

where the finite quantity F_A does not depend on the choice of the UV cut-off. More generally, for theories which admit a UV fixed point, the equation (1.20) is still valid and F_A may provide, when A is a disk, the definition for an analogue of the *c-function* in three dimensions. The conjecture that the finite part of the entanglement entropy of a circular region decreases along RG flows is called *F-theorem* [22, 23].

Instead, for a CFT_{3+1} the entanglement entropy takes the form (see e.g. [24, 25])

$$S_A = \frac{\text{Area}(\partial A)}{4\pi\varepsilon^2} - c_A \log \varepsilon/\ell + \text{finite terms}\,, \tag{1.21}$$

where ℓ is a typical length characterizing the entangling region. The coefficient of the logarithm is proportional to the conformal anomaly of the CFT

$$c_A = a F_A^a + b F_A^b + c F_A^c\,, \tag{1.22}$$

where a,b and c are respectively the a-type, $b-$type and $c-$type anomalies. The coefficients $F_A^{a,b}$ depend on the geometry of A[6]:

$$F_A^a = \frac{\pi}{8} \int d^2x \left((\text{Tr}k)^2 - \text{Tr}k^2 \right)\,, \tag{1.23}$$

$$F_A^b = -\frac{\pi}{8} \int d^2x \left((\text{Tr}k)^2 - \frac{1}{2}\text{Tr}k^2 \right)\,, \tag{1.24}$$

where we assumed that the background of the CFT is flat and k_{ij} is the extrinsic curvature[7] of ∂A as embedded in $\mathbb{R}^3$ space[8]. We did not write an explicit expression for F_A^c because it depends on the background geometry, and in flat space it is equal to zero.

In four dimensions the $a-$type anomaly is the quantity which monotonically decreases along the RG flows [26] (this fact takes in this case the name of *a-theorem* and has been proved in [27, 28], where the proof however did not rely on entanglement entropy). When the entangling region is a sphere we have that $F_A^b = 0$, the entanglement entropy is eventually able to capture the right quantity to follow along the flow.

[6] We assume here that A has a smooth boundary, otherwise other divergences may appear, in particular $\log^2 \varepsilon$ terms.

[7] See equation (A.4) for the definition of the extrinsic curvature.

[8] Because of flatness of the background and because ∂A is embedded in a constant-time spatial slice, we have that the extrinsic curvature computed with the time-like normal to the surface vanishes, i.e. $k_{ij}^{(t)} = 0$.

It is conjectured that any dimensions admit a particular c-function, i.e. a quantity which decreases along the renormalization group flow from the UV to the IR. In even-dimensional theory this could be always given by the A-type anomaly coefficient, although a proof even just for CFT_{5+1} is still lacking.

The computation of (1.16) in higher dimensions has not yet been achieved in a generic QFT or even a CFT, although some results - with different techniques - have been obtained in free theories for disjoint entangling regions either [29–33], for some universal[9] coefficients of non-smooth boundaries [34, 35], some perturbative calculations around spherical regions [36–38], the divergence structure of four dimensional CFTs [24] and entanglement entropies for circular regions [39–41].

Another case of interest for the study of entanglement entropy is when the system is in a time dependent setting. When the quantum system is prepared in a state which is not an eigenstate of the Hamiltonian, S_A will evolve with time. In [42] it was studied the behaviour of entanglement entropy in a two-dimensional CFT following a *quench*: imagine to have the system to be in an eigenstate $|\psi_0\rangle$ of some Hamiltonian $H = H(\lambda_0)$, where λ is some coupling. At some given time $t = 0$ one suddenly changes λ_0 to λ and let the system evolve, with the new Hamiltonian still being invariant under conformal symmetry. The reduced density matrix (1.8) becomes time-dependent

$$\rho_A(t) = \mathrm{Tr}_{\mathcal{H}_{\bar{A}}} \left(e^{-iH(\lambda)t} \, |\psi_0\rangle \, \langle\psi_0| \, e^{iH(\lambda)t} \right) . \tag{1.25}$$

One then can proceed by evaluating the path-integral (1.15) and compute the Rényi entropies. It was found that $S_A(t)$ grows linearly with time for a time $t = \ell/s$, where ℓ is the interval width. This delay in the response can be explained by the fact that after the quench there are excited quasiparticles propagating at the speed of light which propagate inside the entangling region. Afterwards, saturation value is reached and the entanglement entropy becomes constant. Further studies on the time dependence of entanglement entropy in two-dimensional CFTs were done in [43–45].

1.4 Holographic Entanglement Entropy

In the seminal work [46, 47] Ryu and Takayanagi proposed a simple way to compute holographically the geometric entanglement entropy in a CFT with a gravitational dual:

$$S_A = \frac{\min_{\gamma_A} \mathrm{Area}[\gamma_A]}{4G_N^{(d+2)}} , \tag{1.26}$$

where γ_A is any codimension-two hypersurface embedded in AdS_{d+2}, homologous to A, i.e. it can be continuously deformed into A while keeping $\partial A = \partial\gamma_A$. $G_N^{(d+2)}$ is the bulk Newton constant for AdS_{d+2}.

This formula holds only for static backgrounds and for entangling regions embedded in constant-time slices of the bulk space-time which are asymptotically AdS.

Note that both sides of (1.26) are infinite, because the boundary of AdS is at infinite distance from any point in the bulk, and one has to regularize the area. This is achieved by cutting the bulk space-time at some hyperplane at finite but arbitrary large distance of order $1/\varepsilon$. This has the effect of reproducing the known expansion (1.19) and in particular the area law is correctly reproduced.

For AdS_3/CFT_2 the result (1.17) is readily recovered, because of the relation (L here is the AdS_3 radius) [48]

$$c = \frac{3}{2} \frac{L}{G_N^{(3)}} , \tag{1.27}$$

which can be proven by looking at the algebra of the generators of isometries in asymptotically AdS_3 spaces and after the identifications with the full, infinite-dimensional Virasoro algebra in two dimensions.

The minimal area prescription is something which was already present in the early days of AdS/CFT, namely the Maldacena prescription for computing the expectation values of Wilson loop operators. Equation (1.6) is of the same nature of (1.26). Note that the Ryu and Takayanagi prescription works with hypersurfaces at fixed codimension, while the Wilson loop expectation value is dual to a two-dimensional

[9] We call universal a quantity which does not depend on the choice of the UV cut-off.

surface. However, for loops with Euclidean signatures, computing Wilson loops and entanglement entropies in asymptotically AdS_4 space-times is, at least at leading order, one and the same thing. For this reason some results in holographic computations of entanglement entropy were already known in the context of holographic Wilson loops.

Since formula (1.26) holds for asymptotically AdS space-times, it should allow to compute entanglement entropy even in thermal theories. Indeed in [46] it was checked that in $d = 1$, i.e. for AdS_3/CFT_2, the prescription continues to hold even for black-hole solutions in the bulk, which in AdS_3 are known as BTZ black holes [49]. In this case, the length of a minimal geodesic connecting two points on the boundary takes precisely the same form as the expression for the entanglement entropy of an interval in a thermal CFT (after the identification (1.27)). This resembles the fact that in general the gravitational partition function of thermal AdS shows the same thermodynamical properties of the thermal CFT on the boundary [50].

Note that the minimal area prescription is assumed to hold even in gauge/gravity in its broad sense. In particular, and as we will see later, even for space-times which are not asymptotically AdS, like the *hvLif* geometries which we will review in Section 1.5.

One natural question to ask is whether (1.26) holds in dealing with time-dependence, either of the background or of the entangling region. This is a legitimate question, since in the case of Wilson loops the prescription is clear even in time-dependent backgrounds: one has to compute the on-shell string world-sheet action. In [51] Hubeny, Rangamani and Takayanagi answered to this question and what they found is probably the most natural answer, although with some caveat. Indeed, one would say that the obvious way to generalize the Ryu-Takayanagi proposal would be to extremize (rather than minimize) the area functional and compute the on-shell value of the area, picking the surface with the smallest area: this value would then provide the entanglement entropy in this time-dependent setting.

In particular, [51] gave motivations that computing the saddle points of the area functional is a well defined procedure only for space-times which, although time-dependent in the bulk, are still looking asymptotically like AdS, so that an asymptotic time-like killing vector exists on the boundary and there is a well-defined space-like foliation of the conformal boundary. In other words, one has to assume that the background metric of the CFT is not time dependent.

Another natural generalization is to consider gravity theories with higher derivative corrections to the standard Einstein-Hilbert action. These terms naturally arise when one considers string amplitudes involving higher modes (we recall that the zero modes of string theory are the ones which reproduce standard ten-dimensional supergravity action). In view of the fact that the prescription for computing the entanglement entropy holographically should exist at a stringy level, it is perfectly legitimate to try to generalize (1.26) when the bulk gravity action contains e.g. squared curvature terms. Although a final expression, valid at any order in $R_{\mu\nu\rho\sigma}$, is still under debate, proposals in this direction were given in [52, 53].

We should mention that the Ryu-Takayanagi prescription is not the only way to compute entanglement entropy in higher dimensions. Namely in [39, 40], for a spherical entangling region, it was shown that entanglement and Rényi entropies were calculable by means of the standard gauge/gravity dictionary: the reduced density matrix for the causal development of a sphere can be mapped to Rindler space-time and as such mapped to a thermal theory. Then, the entanglement entropy corresponds to the thermal entropy of a CFT in a hyperbolic background, which can be computed holographically as the partition function of a topological black hole.

As a closing remark to this section, let us note that Maldacena and Lewkowycz [54] were able to prove the conjecture of Ryu and Takayanagi by showing how to extend the replicated geometry on the boundary inside the bulk, with the bulk metric having a singularity sitting on a hypersurface. They showed that this hypersurface converges, as $n \to 1$, towards the minimal area surface. However, even the conjecture can be considered to be proven, the proof is not constructive, in the sense that does not make it easier to compute entanglement entropies in higher dimensions.

1.4.1 A closer look at minimal hypersurfaces in AdS space-times

In all the work presented in this thesis, every computation has been based on (1.26) and its generalizations. Before going into the details of my project, it is worth mentioning some simple and generic facts

about minimal surfaces in AdS space-times.

We have been working mainly with the Poincaré patch of anti-de Sitter, rather than its global cover. As long as we are interested in local quantities, it makes no difference which patch one uses, although the global behaviour (e.g. one cannot see the degeneracy of extremal surfaces ending on a given region in the Schwarzschild black hole background) may be quite different. For our purposes, the Poincaré patch always sufficed. In this case the metric reads

$$ds^2 = \frac{L^2}{z^2}\left(dz^2 - dt^2 + dx_i^2\right) , \tag{1.28}$$

where L is the curvature scale of AdS_{d+2}, the conformal boundary lies at $z = 0$ with $i = 1, \dots, d$ space-like flat dimensions.

Since (1.28) is the metric of AdS_{d+2}, a constant-time slice is the $(d+1)$-dimensional hyperbolic space $\mathbb{H}^{d+1}$ and the Ryu-Takayanagi prescription tells that γ_A is now a codimension-one surface embedded in $\mathbb{H}^{d+1}$. We show in Appendix A that any surface which extremizes the area has to satisfy the equation

$$H = 0 , \tag{1.29}$$

where $H \equiv \frac{1}{d}\mathrm{Tr}K$ is the hypersurface's mean curvature. This equation is a second order non-linear partial differential equation, and as such is very difficult to solve. There are cases where the symmetry of ∂A allows one to simplify considerably the equation and to find the explicit solution. When ∂A is either rotationally invariant (i.e. a sphere) or translation invariant (i.e. the half-plane or an infinite strip), (1.29) becomes an ordinary differential equation and can be solved analytically. Such cases were first studied in [47]. For more general surfaces with less symmetry one has to rely on numerical methods: in Chapter 2 we will extensively discuss a way to solve (1.29) for generic entangling regions.

Once the solution of (1.29) has been found, one needs to compute the area of the surface, namely the quantity

$$\mathcal{A} = \int_{\gamma_A} d^d\sigma \sqrt{\det h} , \tag{1.30}$$

where σ^i are coordinates parametrizing the surface and h is the induced metric on γ_A.

To understand the UV behaviour of S_A, we can solve the minimality equation and expand the solution near the boundary at $z = 0$, and compute the expansion of the determinant of the induced metric. The minimality requirement constrains the curvature of the surface near the boundary (see Fig. 1.1): we derived equation (A.34) in Appendix A.2 (but see also e.g. [55–57]), from which it can be shown that for $d \neq 2$

$$\mathcal{A} = \frac{1}{d-1}\frac{\mathrm{Area}\partial A}{\varepsilon^{d-1}} - \frac{1}{2(d-2)}\frac{\int_{\partial A} d^{d-1}\sigma\sqrt{\det\gamma}(\mathrm{Tr}k)^2}{\varepsilon^{d-3}} + \dots , \tag{1.31}$$

where the dots stand for subleading terms and γ and k are the first and the second fundamental forms of ∂A as embedded in $\mathbb{R}^d$. For $d = 3$ one should substitute the power-law divergence with a logarithm, but the dependence on ∂A of the coefficient remains the same. We proved that indeed the Ryu-Takayanagi prescription reproduces the area law (1.18) and the first subleading term is proportional to the integral of the square of the mean curvature of ∂A - except for AdS_4 where there is no subleading divergence.

While computing the divergent terms of the area is a somehow straightforward procedure, computing the finite terms (and thus getting information on the IR physics of the CFT) is extremely more difficult and necessarily requires to find the full solution of (1.29). Besides the already mentioned case of the sphere and infinite strip found in [47], there are few examples were explicit computations were carried out. In [58, 59] S_A was computed for angular regions in AdS_4 (an analytic generalization of the results to higher dimension is given in [60] and Appendix B.4). In [61] some perturbative results were obtained for nearly circular regions. In [62, 63], using tools developed in [55], some analytical solutions were found for a broad class of entangling regions in terms of generalized Riemann theta functions, although in their case the shape of ∂A could not be fixed a priori but was rather an outcome of a particular choice of some parameters in the solution.

1.4.2 Time-dependent holographic entanglement entropy

In [51], Hubeny, Rangamani and Takayanagi showed that, as long as one deals with asymptotically static AdS space-times, saddle points of the area functional may provide a natural generalization of

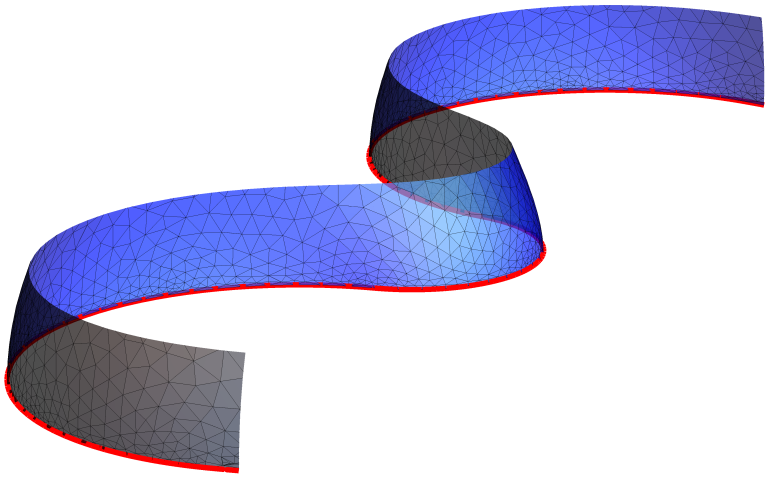

Figure 1.1: In asymptotically AdS_4 space-times, the boundary of minimal surfaces ending at $z = 0$ are *umbilic lines* (see A.2 for a definition): the two principal curvatures - i.e. the eigenvalues of the extrinsic curvature - coincide at the boundary. This means that locally at any point close to $z = 0$, the surface looks like a two-sphere, and in particular the direction of the bending along the z direction depends on the concavity of ∂A. In the figure it is shown a close-up of a portion of a surface with wavy entangling region.

the Ryu-Takayanagi prescription. Among all possible time-dependent backgrounds which asymptote to anti-de Sitter space, of particular interests are the ones described by an $AdS-$Vaidya type of metric [64, 65]. Such metric describes the formation of a black-hole after a collapse of a null shell of energy. This geometry is obtained explicitly by re-expressing the metric for an AdS black hole in Eddington-Finkelstein coordinates and promoting the emblackening factor to be time-dependent [66]:

$$ds^2 = \frac{1}{z^2}\left(-f(v,z)dv^2 - 2dvdz + dx_i^2\right) , \tag{1.32}$$

where $f(v,z) \to 1$ for $v \to -\infty$, so to recover the empty AdS geometry, while for $v \to +\infty$ tends to a static black hole solution with emblackening factor $f(z)$. If we imagine that the black hole is formed by the collapse of a shell of energy moving at the speed of light, we can set

$$f(v,z) = 1 - M(v)z^{d+1} , \tag{1.33}$$

with boundary conditions $\lim_{v\to-\infty} M(v) = 0$ and $\lim_{v\to+\infty} M(v) = M$, where M is the mass of the AdS-Schwarzschild black hole. The exact expression is left undetermined as a specific $M(v)$ corresponds to a specific choice for the profile of the shell, even though the null energy condition requires it to be monotonically increasing, $M'(v) \geq 0$. It should be remarked that (1.32) is not a solution of the vacuum Einstein equations, except at $v \to \pm\infty$, and thus it requires the support of matter fields to provide a non-zero $T_{\mu\nu}$.

The dual interpretation of (1.32) is that at early times we start with a CFT in its pure state at zero temperature which, as the time evolves, approaches a thermal theory with the temperature determined by the black-hole mass M,

$$T = \frac{d+1}{4\pi} M^{\frac{1}{d+1}} . \tag{1.34}$$

In this setup, studying the behaviour of geometric entanglement entropy as a function of time is something which can be straightforwardly done. Since on the CFT side the interpretation of the Vaidya background is an interpolation between a $T = 0$ and a thermal theory, the holographic study of quantities in the background (1.32) undergoes the name *holographic thermalization*. Computations of holographic entanglement entropy in the $AdS-$Vaidya background has been done in [66–71].

In Chapter 3 we considered geometries which are similar to (1.32), where the asymptotics of the space-time is changed in order to take into account dual theories which exhibit the presence of the strongly correlated analogue of a Fermi surfaces. The entanglement entropy computed for these systems has some specific properties which we are going to review in the next section.

1.5 Hyperscaling violation and holography

We are going to briefly touch in this introduction the role of holography as a tool in studying condensed matter systems, a branch of the gauge/gravity duality which is known as AdS/CMT. It is beyond the scope of this thesis to give a general review here (see e.g. [72–74]), and we will give just some basic information in order to let the reader understand what was done in Chapters 3 and 4.

In gauge/gravity there are two different approaches when searching for dual theories: *top-down* and *bottom-up*.

The first one tries to derive some effective gravitational theory from a particular string theory, as in the case of the original AdS/CFT correspondence. Each quantity in the low energy theory can be computed and linked to string quantities: in other words there is a UV-completion of the gravity side and, at least in principle, one is able to understand the origin of a given gravitational action in terms of more fundamental objects. The problem of top-down models is that they are difficult to deal with and more often than not are unnecessarily complicated when one tries to construct just effective gravitational theories able to capture the relevant features - may they be thermodynamical properties or linear responses - of some model QFT.

For this reason the more common approach in applications of holography is the bottom-up: ad-hoc geometries are constructed to test whether they are able to reproduce some desired behaviour of boundary quantities. In a bigger picture, any gravity theory should derive from some low-energy limit of a string theory, but the usefulness of the bottom-up approach is that it allows to check in first instance whether classical gravity can reproduce at all some known phenomena of some specific field theories.

In the latter years there has been some interest in understanding whether holography can describe strongly correlated fermions, and in particular non-Fermi liquids. One of the features of field theories with fermions is that they exhibit the so-called violation of the area law [75, 76]: the entanglement entropy computed for the ground state, regardless the dimension of the system, diverges logarithmically in the UV cut-off, and the leading term scales as

$$S_A \approx \ell^{d+1} \log \ell/\varepsilon + \dots \,, \tag{1.35}$$

for large enough entangling regions of size ℓ. This is expected to be true even in the case of strongly correlated fermions [77]: therefore, in a theory which can be described via the gauge/gravity duality, this behaviour of S_A should emerge from gravitational computations.

On the other hand, in the previous section we showed that indeed any asymptotically AdS space-time obeys the area law: if we want to change the leading divergent term for the area of a surface (assuming that the Ryu-Takayanagi prescription still holds) we need to change the asymptotic behaviour of the bulk space-time. This is what was suggested first in [78–80]. In those papers it was proposed that a suitable dual gravitational theory should asymptote to hyperscaling-violating Lifshitz space-times[10], for which the metric reads

$$ds^2 = \frac{1}{z^{2(1-\theta/d)}} \left(-z^{2(1-\zeta)} dt^2 + dz^2 + dx_i^2 \right) \,, \tag{1.36}$$

where θ, ζ are known as the hyperscaling-violation and Lifshitz exponent, respectively.

We will discuss extensively the implications of the so-called *hvLif* geometries for the entanglement entropy in Chapter 3.

[10] The name *hyperscaling*, according to [81], refers to any relation between universal exponents of critical theories which depends explicitly on the dimension of the theory; since in [78, 80] it was proved that the holographic entropy density of these holographic models scales as $s \approx T^{d-\theta}$, for $\theta \neq 0$ we have a *violation* of the hyperscaling relation between entropy density and temperature.

1.6 Outline

The structure of this thesis follows the various arguments I have been dealing with during the years of my PhD research. The common line has always been to give a better understanding of the shape dependence of minimal surfaces - and thus of entanglement entropy - in backgrounds which are either asymptotically *AdS* or *hvLif*.

- Chapter 2 reproduces [82]. We introduce for the first time in the context of holographic entanglement entropy the use of *Surface Evolver* [83], a software created for computing energies of surfaces in soft-matter applications. This software allows to compute numerically the area of a minimal surface ending on any compact ∂A. We show we are able to reproduce any known exact result in the literature, and furthermore show some new results on the holographic mutual information between two disjoint regions consisting of two circles, ellipses and other geometrical shapes.

- Chapter 3 reproduces [60], where the time-dependence of entanglement entropy is studied in *hvLif* space-times. We present extensive numerical computations of the renormalized area of of surfaces ending on spherical and strip-like entangling regions. We present as well some semi-analytical results concerning the initial, intermediate and final stage of the holographic entanglement entropy after a sharp quench.

- Chapter 4 reproduces [84]. We study the behaviour of entanglement entropy for non-smooth entangling regions in $hvLif$ space-times. As it was already known that in asymptotically AdS spaces the presence of cusp-like regions induced new logarithmic divergences from which new universal quantity can be extracted, we show when and for which values of the hyperscaling-violating exponent θ we have the appearance of new universal terms. We also check how these terms get modified by higher curvature corrections in the gravitational action for $\theta = 0$.

- In Chapter 5 we finally set the conclusion of the thesis and give an outlook on possible future developments.

- In the various Appendices, supplementary material is presented for each chapter.

Chapter 2

Computing HEE for arbitrary shapes in AdS_4

As we saw in the Introduction, for $d = 2$ the minimal surfaces to compute for the holographic entanglement entropy (1.26) are the same ones occurring in the gravitational counterpart of the correlators of spacelike Wilson loops. AdS_4 is the lowest dimensional space-time where the shape of the entangling region can be non-trivial. In this Chapter we will precisely present a method to compute numerically the holographic entanglement entropy for - in principle - any shape. As we already mentioned, analytic results have been found for the infinite strip and for the sphere when d is generic [46, 47]. Spherical domains play a particular role because their reduced density matrix can be related to a thermal one [39].

We recall that for $d = 2$, the $O(1)$ term in the expansion of S_A as $\varepsilon \to 0$ for circular domains provides the quantity F, which decreases along any renormalization group flow [22, 85, 86]. We should mention that some interesting results have been found about $\mathcal{A}_A$ for an entangling surface ∂A with somehow generic shapes [24, 57, 87–91], but a complete understanding is still lacking, and in no way there has been a direct way to compute the constant term of the area in AdS_4 for a completely generic entangling region.

When $A = A_1 \cup A_2$ is made by two disjoint spatial regions, an important quantity to study is the mutual information (1.12). The conneceted entanglement entropy $S_{A_1 \cup A_2}$ provides a measure for the entanglement between $A_1 \cup A_2$ and the remaining part of the spatial slice and does not quantify - as one would expect - the entanglement between A_1 and A_2, which is measured by other quantities, such as the logarithmic negativity [92–95]. In the combination (1.12), the area law divergent terms cancel and the subadditivity of the entanglement entropy guarantees that $I_{A_1,A_2} \geqslant 0$. For two dimensional conformal field theories, the mutual information depends on the full operator content of the model [19, 96–101]. When $d \geqslant 2$, the computation of (1.12) is more difficult because non local operators must be introduced along ∂A [29–31, 33, 41].

The holographic mutual information is (1.12) with S_A given by (1.26). The crucial term to evaluate is $S_{A_1 \cup A_2}$, which depends on the geometric features of the entangling surface $\partial A = \partial A_1 \cup \partial A_2$, including also the distance between A_1 and A_2 and their relative orientation, being ∂A made by two disjoint components. It is well known that, keeping the geometry of A_1 and A_2 fixed while their distance increases, the holographic mutual information has a kind of phase transition with discontinuous first derivative, such that $I_{A_1,A_2} = 0$ when the two regions are distant enough. This is due to the competition between two minima corresponding to a connected configuration and to a disconnected one. While the former is minimal at small distances, the latter is favoured for large distances, where the holographic mutual information therefore vanishes [102–104]. This phenomenon has been also studied much earlier in the context of the gravitational counterpart of the expectation values of circular spacelike Wilson loops [105–108]. The transition of the holographic mutual information is a peculiar prediction of (1.26) and it does not occur if the quantum corrections are taken into account [109]. A similar transition due to the competition of two local minima of the area functional occurs also for the holographic entanglement entropy of a single region at finite temperature [110–112].

Here we focus on $d = 2$ and we study the shape dependence of the holographic entanglement entropy and of the holographic mutual information (1.26) in AdS_4, which is dual to the zero temperature vacuum

state of the three dimensional conformal field theory on the boundary. This reduces to finding the minimal area surface $\tilde{\gamma}_A$ spanning a given boundary curve ∂A (the entangling curve) defined in some spatial slice of the boundary of AdS_4. The entangling curve ∂A could be made by many disconnected components. When ∂A consists of one or two circles, the problem is analytically tractable [7, 58, 59, 113, 114]. However, for an entangling curve having a generic shape (and possibly many components), finding analytic solutions becomes a formidable task. In order to make some progress, we tackle the problem numerically with the help of Surface Evolver [83], a widely used open source software for the modelling of liquid surfaces shaped by various forces and constraints. A section at constant time of AdS_4 gives the Euclidean hyperbolic space $\mathbb{H}_3$. Once the curve embedded in $\mathbb{H}_3$ is chosen, this software constructs a triangular mesh which approximates the surface spanning such curve which is a local minimum of the area functional, computing also the corresponding finite area. The number of vertices V, edges E and faces E of the mesh are related via the Euler formula, namely $V - E + F = \chi$, being $\chi = 2 - 2g - b$ the Euler characteristic of the surface, where g is its genus and b the number of its boundaries. In the following we will deal with surfaces of genus $g = 0$ with one or more boundaries.

The rest of the Chapter is organized as follows. In 2.1 we state the problem, introduce the basic notation and review some properties of the minimal surfaces occurring in our computations. In 2.2 we address the case of surfaces spanning simply connected curves. First we review two analytically tractable examples, the circle and the infinite strip; then we address the case of some elongated curves (i.e. ellipse, superellipse and the boundary of the two dimensional spherocylinder) and polygons. Star shaped and non convex domains are also briefly discussed. In 2.3 we consider ∂A made by two disjoint curves. The minimal surface spanning such disconnected curve can be either connected or disconnected, depending on the geometrical features of the boundary, including the distance between them and their relative orientation. The cases of surfaces spanning two disjoint circles, ellipses, superellipses and the boundaries of two dimensional spherocylinders are quantitatively investigated for a particular relative orientation. Further discussions and technical details are reported in the Appendix B.

2.1 Minimal surfaces in AdS_4

Finding the minimal area surface spanning a curve is a classic problem in geometry and physics. In $\mathbb{R}^3$ this is known as Plateau's problem. A physical realization of the problem is obtained by dipping a stiff wire frame of some given shape in soapy water and then removing it: as the energy of the film is proportional to the area of the water/air interface, the lowest energy configuration consists of a surface of minimal area. In this mundane setting, the requirement of minimal area results into a well known equation (1.29), i.e.

$$H = 0\,, \tag{2.1}$$

where $H = k^i_i/2$ is the mean-curvature given by the trace of the extrinsic curvature tensor defined in (A.3), such that the induced metric tensor h_{ij} is given in (A.21)

The metric of AdS_4 in Poincaré coordinates can be obtained from (1.28) by setting $d = 2$, reading

$$ds^2 = \frac{-dt^2 + dx^2 + dy^2 + dz^2}{z^2}\,, \tag{2.2}$$

where the AdS radius has been set to one for simplicity. The spatial slice $t = \text{const}$ provides the Euclidean hyperbolic space $\mathbb{H}_3$ and the region A is defined in the $z = 0$ plane. According to the prescription of [46, 47], to compute the holographic entanglement entropy, first we have to restrict ourselves to a $t = \text{const}$ slice and then we have to find, among all the surfaces γ_A spanning the curve ∂A, the one minimizing the area functional

$$\mathcal{A}[\gamma_A] = \int_{\gamma_A} d\mathcal{A} = \int_{U_A} \frac{\sqrt{\tilde{h}}\, du^1 du^2}{z^2}\,, \tag{2.3}$$

where U_A is a coordinate patch associated with the coordinates (u^1, u^2) and $\tilde{h} = \det(\tilde{h}_{ij})$ is the determinant of the induced metric of the surfaces seen as embedded in $\mathbb{R}^3$. We denote by $\tilde{\gamma}_A$ the area minimizing surface, so that $\mathcal{A}[\tilde{\gamma}_A] \equiv \mathcal{A}_A$ provides the holographic entanglement entropy through the Ryu-Takayanagi formula (1.26). Since all the surfaces γ_A reach the boundary of AdS_4, their area is divergent and therefore one needs to introduce a cut-off in the holographic direction to regularize it, namely $z \geqslant \varepsilon > 0$, where ε is an infinitesimal parameter. The holographic dictionary tells us that this cut-off corresponds to the

ultraviolet cut-off in the dual three dimensional conformal field theory. Considering $z \geqslant \varepsilon > 0$, the area $\mathcal{A}[\gamma_A]$ and therefore $\mathcal{A}_A$ as well become ε dependent quantities which diverge when $\varepsilon \to 0$. Important insights can be found by writing $\mathcal{A}_A$ as an expansion for $\varepsilon \to 0$. When ∂A is a smooth curve, this expansion reads

$$\mathcal{A}_A = \frac{P_A}{\varepsilon} - F_A + o(1)\,, \tag{2.4}$$

where $P_A = \text{length}(\partial A)$ is the perimeter of the entangling curve and $o(1)$ indicates vanishing terms when $\varepsilon \to 0$. When the entangling curve curve ∂A contains a finite number of vertices, also a logarithmic divergence occurs, namely

$$\mathcal{A}_A = \frac{P_A}{\varepsilon} - B_A \log(P_A/\varepsilon) - W_A + o(1)\,. \tag{2.5}$$

The functions F_A, B_A and W_A are defined through (2.4) and (2.5). They depend on the geometry of ∂A in a very non trivial way. We remark that the section of $\tilde{\gamma}_A$ at $z = \varepsilon$ provides a curve which does not coincide with ∂A because of the non trivial profile of $\tilde{\gamma}_A$ in the bulk.

As the area element in AdS_4 is factorized in the form $d\mathcal{A} = du^1 du^2 \sqrt{\tilde{h}}/z^2$, a surface in AdS_4 is equivalent to a surface in $\mathbb{R}^3$ endowed with a potential energy density of the form $1/z^2$. By using the standard machinery of surface geometry (see B.1), one can find an analog of (2.1) in the form

$$H + \frac{\hat{\boldsymbol{z}} \cdot \boldsymbol{N}}{z} = 0\,, \tag{2.6}$$

where $\hat{\boldsymbol{z}}$ is a unit vector in the z direction. The relation (2.6) implies that, in order for the mean curvature to be finite, the surface must be orthogonal to the (x, y) plane at $z = 0$: i.e. $\hat{\boldsymbol{z}} \cdot \boldsymbol{N} = 0$ at $z = 0$. As a consequence of the latter property, the boundary is also a geodesic of $\tilde{\gamma}_A$ (see B.1).

2.2 Simply connected regions

In this section we consider cases in which the region A is a simply connected domain. We first review the simple examples of the disk and of the infinite strip, which can be solved analytically [46, 47]. In 2.2.1 we numerically analyze the case in which A is an elongated region delimited by either an ellipse, a superellipse or the boundary of a two dimensional spherocylinder, while in 2.2.2 we address the case in which ∂A is a regular polygon. In 2.2.3, star shaped and non convex domains are briefly discussed.

If A is a disk of radius R, the minimal area surface $\tilde{\gamma}_A$ is a hemisphere, as it can be easily proved from a direct substitution in (2.6). Taking $\boldsymbol{N} = \boldsymbol{r}/|\boldsymbol{r}|$, with $\boldsymbol{r} = (x, y, z)$ and $|\boldsymbol{r}| = R$, one finds $\hat{\boldsymbol{z}} \cdot \boldsymbol{N} = z/R$, hence $H = -1/R$, which is the mean curvature of a sphere whose normal is outward directed. The area of the part of the hemisphere such that $\varepsilon \leqslant z \leqslant R$ is

$$\mathcal{A}_A = \frac{2\pi R}{\varepsilon} - 2\pi\,. \tag{2.7}$$

Comparing this expression with (2.4), one finds that $F_A = 2\pi$ in this case. It is worth remarking , as peculiar feature of the disk, that in (2.7) $o(1)$ terms do not occur.

A special case of (2.6) is obtained when the surface is fully described by a function $z = z(x, y)$ representing the height of the surface above the (x, y) plane at $z = 0$. In this case

$$\mathcal{A}[\gamma_A] = \int_{\gamma_A} \frac{1}{z^2} \sqrt{1 + z_{,x}^2 + z_{,y}^2}\, dxdy\,, \tag{2.8}$$

and (2.6) becomes the following second order non linear partial differential equation for z (see B.1 for some details on this derivation)

$$z_{,xx}(1 + z_{,y}^2) + z_{,yy}(1 + z_{,x}^2) - 2z_{,xy} z_{,x} z_{,y} + \frac{2}{z}(1 + z_{,x}^2 + z_{,y}^2) = 0\,, \tag{2.9}$$

with the boundary condition that $z = 0$ when $(x, y) \in \partial A$. The partial differential equation (2.9) is very difficult to solve analytically for a generic curve ∂A; but for some domains A it reduces to an ordinary differential equation. Apart from the simple hemispherical case previously discussed, this happens also

for an infinite strip $A = \{(x, y) \in \mathbb{R}^2, |y| \leqslant R_2\}$, whose width is $2R_2$. The corresponding minimal surface is invariant along the x axis and therefore it is fully characterized by the profile $z = z(y)$ for $|y| \leqslant R_2$. Taking $z_{,x} = 0$ in (2.9) yields

$$z_{,yy} + \frac{2}{z}(1 + z_{,y}^2) = 0\,. \tag{2.10}$$

Equivalently, the infinite strip case can be studied by considering the one dimensional problem obtained substituting $z = z(y)$ directly in (2.8) [46, 47, 115]. Since the resulting effective Lagrangian does not depend on y explicitly, one easily finds that $z^2\sqrt{1 + z_{,y}^2}$ is independent of y. Taking the derivative with respect to y of this conservation law, (2.10) is recovered, as expected. The constant value can be found by considering $y = 0$, where $z(0) \equiv z_*$ and $z_{,y}(0) = 0$. Notice that z_* is the maximal height attained by the curve along the z direction. Integrating the conservation law, one gets

$$y(z) = \frac{\sqrt{\pi}\,\Gamma(3/4)}{\Gamma(1/4)}\,z_* - \frac{z^3}{3z_*^2}\,{}_2F_1\left(\frac{1}{2}, \frac{3}{4}; \frac{7}{4}; \frac{z^4}{z_*^4}\right), \qquad z_* = \frac{\Gamma(1/4)}{\sqrt{\pi}\,\Gamma(3/4)}\,R_2\,, \tag{2.11}$$

where Γ is the Euler gamma and ${}_2F_1$ is the hypergeometric function. Thus, the minimal surface $\tilde{\gamma}_A$ consists of a tunnel of infinite length along the x direction, finite width R_2 along the y direction and whose shape in the (y, z) plane is described by (2.11). Considering a finite piece of this surface which extends for $R_1 \gg R_2$ in the x direction, whose projection on the (x, y) plane is delimited by the dashed lines in the bottom panel of Fig. 2.1, its area is given by [7, 46, 47, 116]

$$\mathcal{A}_A = \frac{4R_1}{\varepsilon} - \frac{R_1 s_\infty}{R_2} + o(1)\,, \qquad s_\infty \equiv \frac{8\pi^3}{\Gamma(1/4)^4}\,, \tag{2.12}$$

where $\varepsilon \leqslant z \leqslant z_*$. Comparing (2.4) with $P_A = 4R_1$ and (2.12), one concludes that $F_A = s_\infty R_1/R_2$.

In order to compare (2.12) with our numerical results, we find it useful to construct an auxiliary surface by closing this long tunnel segment with two planar "caps" placed at $x = \pm R_1$, whose profile is described in the (y, z) plane by (2.11), with a cut-off at $z = \varepsilon$. These regions are identical by construction and their area (see B.4.1) is given by $\mathcal{A}_{\text{cap}} = 2R_2/\varepsilon - \pi/2 + o(1)$. Thus, the total area of the auxiliary surface reads

$$\mathcal{A}_A + 2\mathcal{A}_{\text{cap}} = \frac{4(R_1 + R_2)}{\varepsilon} - \frac{R_1 s_\infty}{R_2} - \pi + o(1)\,, \tag{2.13}$$

where the coefficient of the leading divergence is the perimeter of the rectangle in the boundary (dashed curve in Fig. 2.1). It is worth remarking that this surface is not the minimal area surface anchored on the dashed rectangle in Fig. 2.1. Indeed, in this case an additional logarithmic divergence occurs (see 2.2.2).

Since in the following we will compute numerically $\mathcal{A}_A$ for various domains keeping ε fixed, let us introduce

$$\widetilde{F}_A \equiv -\left(\mathcal{A}_A - \frac{P_A}{\varepsilon}\right). \tag{2.14}$$

From (2.4) one easily observes that $\widetilde{F}_A = F_A + o(1)$ when $\varepsilon \to 0$. Notice that for the disk we have $\widetilde{F}_A = F_A$.

In Fig. 2.2 the values of $\widetilde{F}_A$ for the surfaces discussed above are represented together with other ones coming from different curves that will be introduced in 2.2.1: the black dot corresponds to the disk (see (2.7)), the dotted horizontal line is obtained from (2.12) for the infinite strip, while the dashed line is found from the area (2.13) of the auxiliary surface.

2.2.1 Superellipse and two dimensional spherocylinder

The first examples of entangling curves ∂A we consider for which analytic expressions of the corresponding minimal surfaces are not known are the superellipse and the boundary of the two dimensional spherocylinder, whose geometries depend on two parameters. The two dimensional spherocylinder nicely interpolates between the circle and the infinite strip.

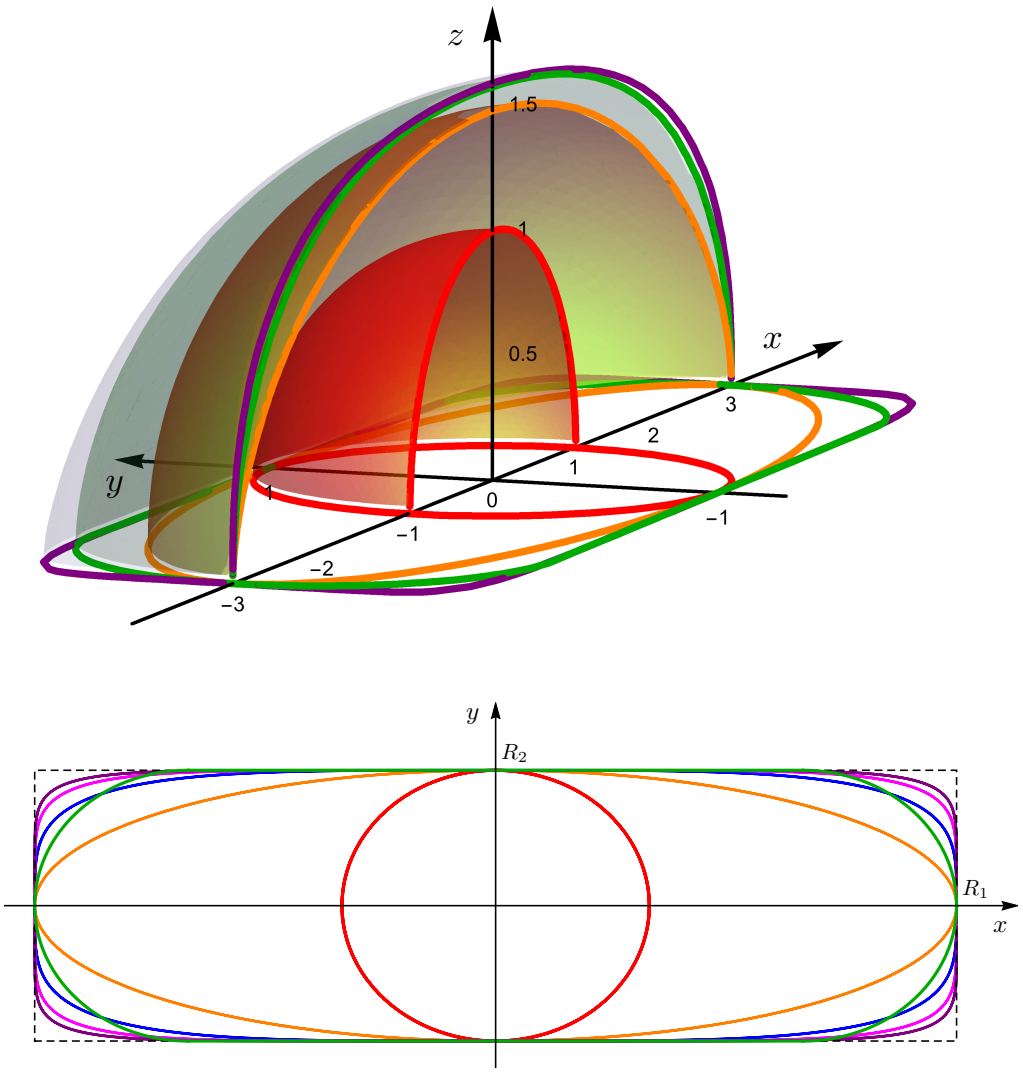

Figure 2.1: Top panel: Minimal surfaces constructed by using Surface Evolver where the entangling curve ∂A is a circle with radius $R = 1$ (red), an ellipse (orange), a superellipse (2.15) with $n = 8$ (purple) and the boundary of a spherocylinder (green) with $R_1 = 3R_2$. The cut-off is $\varepsilon = 0.03$ and only the $y \geqslant 0$ part of the minimal surfaces has been depicted to highlight the curves provided by the section $y = 0$. Bottom panel: In the (x, y) plane, we show the superellipses with $R_1 = 3R_2$ with $n = 2$ (orange), $n = 4$ (blue), $n = 6$ (magenta) and $n = 8$ (purple), the circle with radius R_1 (red curve) and the rectangle circumscribing the superellipses (dashed lines). The green curve is the boundary of the two dimensional spherocylinder with $R_2 = 3R_1$.

In Cartesian coordinates, a superellipse centered in the origin with axes parallel to the coordinate axes is described by the equation

$$\frac{|x|^n}{R_1^n} + \frac{|y|^n}{R_2^n} = 1\,, \qquad R_1 \geqslant R_2 > 0\,, \qquad n \geqslant 2\,, \tag{2.15}$$

where R_1, R_2 and n are real and positive parameters. The curve (2.15) is also known as Lamé curve and here we consider only integers $n \geqslant 2$ for simplicity. The special case $n = 2$ in (2.15) is the ellipse with semi-major and semi-minor axes given by R_1 and R_2 respectively. As the positive integer n increases, the superellipse approximates the rectangle with sides $2R_1$ and $2R_2$. When $R_1 = R_2$, the curves (2.15) for various n are known as *squircles* because they have intermediate properties between the ones of a circle ($n = 2$) and the ones of a square ($n \to \infty$). In the bottom panel of Fig. 2.1, we show some

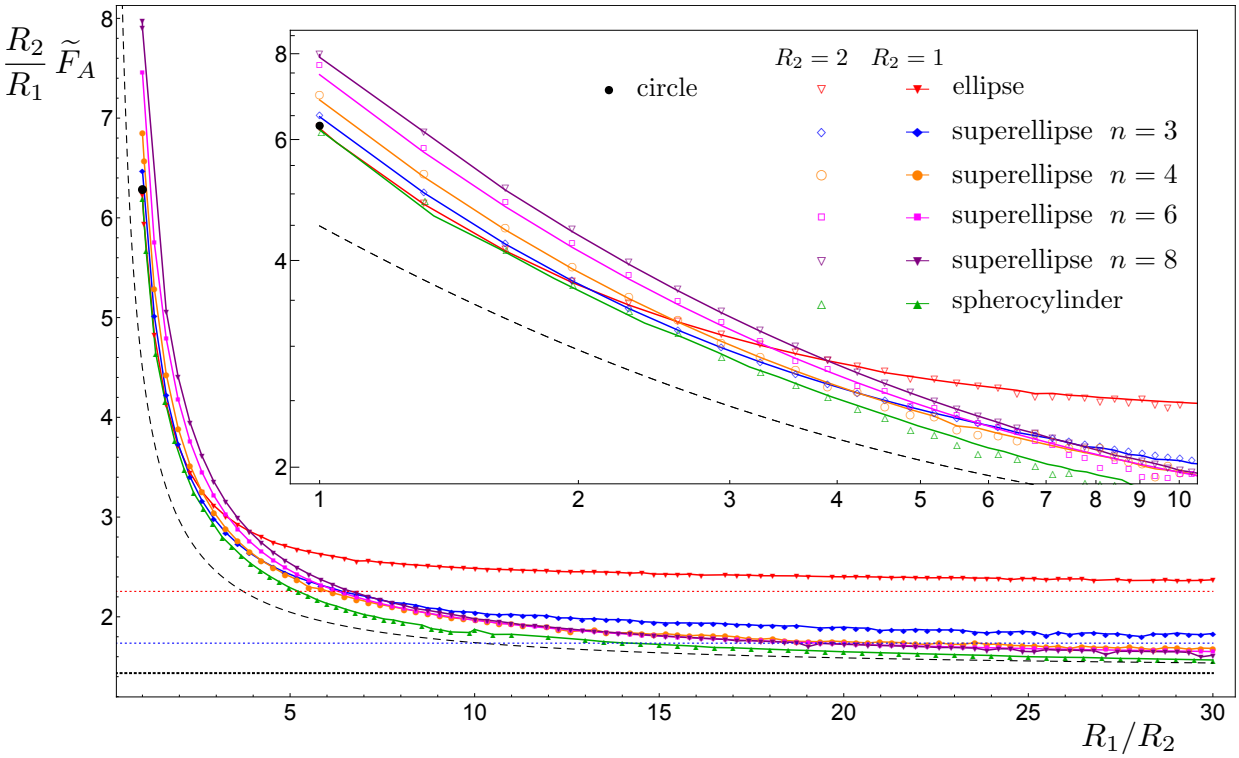

Figure 2.2: Numerical data for $\widetilde{F}_A$, defined in (2.14), corresponding to domains A which are two dimensional spherocylinders or delimited by superellipses. Here $\varepsilon = 0.03$. In the main plot $R_2 = 1$, while in the inset, which shows a zoom of the initial part of the main plot in logarithmic scale on both the axes, we have also reported data with $R_2 = 2$. The horizontal dotted black line corresponds to the infinite strip (2.12) and the dashed one to the auxiliary surface where the sections at $x = \pm R_1$ have been added (see (2.13)). The red and blue dotted horizontal lines come from the asymptotic result (B.17) evaluated for $n = 2$ and $n = 3$ respectively.

superellipses with $R_1 = 3R_2$, the circle with radius R_1 included in all the superellipses and the rectangle circumscribing them.

In order to study the interpolation between the circle and the infinite strip, a useful domain to consider is the two dimensional spherocylinder. The spherocylinder (also called capsule) is a three dimensional volume consisting of a cylinder with hemispherical ends. Here we are interested in its two dimensional version, which is a rectangle with semicircular caps. In particular, the two dimensional spherocylinder circumscribed by the rectangle with sides $2R_1$ and $2R_2$ is defined as the set $\mathcal{S} \equiv \lceil \cup \mathcal{C}_+ \cup \mathcal{C}_-$, where the rectangle $\lceil$ and the disks $\mathcal{C}_\pm$ are

$$\mathcal{D} \equiv \big\{(x,y)\,,\, |y| \leqslant R_2\,,\, |x| \leqslant R_1 - R_2\big\}\,, \qquad \mathcal{C}_\pm \equiv \big\{(x,y)\,,\, \big[x \pm (R_1 - R_2)\big]^2 + y^2 \leqslant R_2\big\}\,. \tag{2.16}$$

The perimeter of this domain is $P_A = 2\pi R_2 + 4(R_1 - R_2)$ and an explicit example of $\partial\mathcal{S}$ with $R_2 = 3R_1$ is given by the green curve in the bottom panel of Fig. 2.1. When $R_1 = R_2$, the curve $\partial\mathcal{S}$ becomes a circle, while for $R_1 \gg R_2$ it provides a kind of regularization of the infinite strip. Indeed, when $R_1 \to \infty$ at fixed R_2 the two dimensional spherocylinder $\mathcal{S}$ becomes the infinite strip with width $2R_2$. Let us remark that the curvature of $\partial\mathcal{S}$ is discontinuous while the curvature of the superellipse (2.15) is continuous. Moreover, the choice to regularize the infinite strip through the circles $\mathcal{C}_\pm$ in (2.16) is arbitrary; other domains can be chosen (e.g. regions bounded by superellipses) without introducing vertices in the entangling curve. A straightforward numerical analysis allows to observe that a superellipses with $n > 2$ intersects once the curve $\partial\mathcal{S}$ in the first quadrant outside the Cartesian axes.

In Fig. 2.2 we show the numerical data for $\widetilde{F}_A$, defined in (2.14), when A is given by the domains discussed above: disk, infinite strip, two dimensional spherocylinder and two dimensional regions delimited by superellipses. In particular, referring to the bottom panel of Fig. 2.1, we fixed R_2 and increased R_1. For the two dimensional spherocylinder, this provides an interpolation between the circle and the infinite

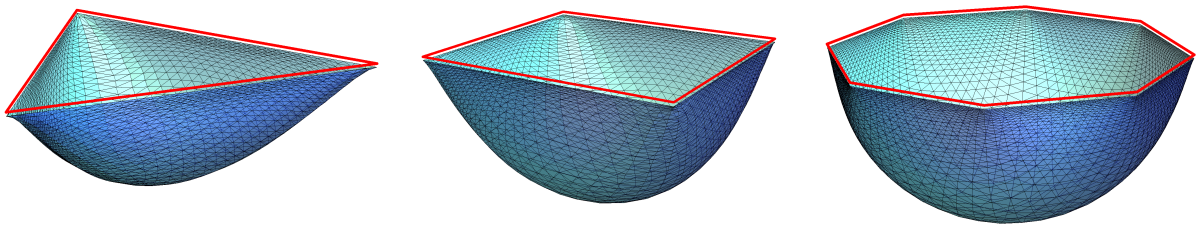

Figure 2.3: Minimal area surfaces constructed with Surface Evolver whose ∂A is a polygon with three (left), four (middle) and eight (right) sides. The red polygons ∂A lie in the plane at $z = 0$ and the z axis points downward but, according to our regularization, the triangulated surfaces are anchored to the same polygons at $z = \varepsilon$. The pair (V, F) giving the number of vertices V and the number of faces F for these surfaces is $(1585, 3072)$ (left), $(2113, 4096)$ (middle) and $(4225, 8192)$ (right). The number of edges can be found from the Euler formula with vanishing genus and one boundary.

strip. Surface Evolver has been employed to compute the area $\mathcal{A}_A$ and for the cut-off in the holographic direction we choose $\varepsilon = 0.03$. Below this value, the convergence of the local minimization algorithm employed by Surface Evolver becomes problematic, as well as for too large domains A, as discussed in B.2.

When $R_1 = R_2$, we observe that $\widetilde{F}_A$ for the squircles with different $n > 2$ increases with n. For large R_1/R_2, the limits of $\widetilde{F}_A/(R_1/R_2)$ for the domains we address are finite and positive. The values of these limits associated with the superellipses are ordered in the opposite way in n with respect to the starting point at $R_1 = R_2$ and therefore they cross each other as R_1/R_2 increases. We remark that the curve corresponding to the two dimensional spherocylinder stays below the ones associated with the superellipses for the whole range of R_1/R_2 that we considered. In Fig. 2.2 the horizontal black dotted line corresponds to the infinite strip (see (2.12)) while the dashed curve is obtained from the auxiliary surface described above (see (2.13)). The latter one is our best analytic approximation of the data corresponding to the two dimensional spherocylinder.

Focussing on the regime of large R_1/R_2, from Fig. 2.2 we observe that the asymptotic value of $\widetilde{F}_A/(R_1/R_2)$ for the two dimensional spherocylinder is very close to the one of the auxiliary surface obtained from (2.13) and therefore it is our best approximation of the result corresponding to the infinite strip. This is reasonable because the two dimensional spherocylinder is a way to regularize the infinite strip without introducing vertices in the entangling curve, as already remarked above. As for the minimal surfaces spanning a superellipse with a given $n \geqslant 2$, in B.3 an asymptotic lower bound is obtained (see (B.17)), generalizing the construction of [91]. In Fig. 2.2 this bound is shown explicitly for $n = 2$ and $n = 3$ (red and blue dotted horizontal lines respectively). Since this value is strictly larger than the corresponding one associated with the infinite strip (see (2.12)), we can conclude that $\widetilde{F}_A/(R_1/R_2)$ for the superellipse at fixed n does not converge to the value s_∞ associated with the infinite strip.

2.2.2 Polygons

In this section we consider the minimal area surfaces associated with simply connected regions A whose boundary is a convex polygon with N sides. These are prototypical examples of minimal surfaces spanning entangling curves with geometric singularities. For quantum field theory results about the entanglement entropy of domains delimited by such curves, see e.g. [34, 117, 118].

The main feature to observe about the area $\mathcal{A}_A$ of the minimal surface is the occurrence of a logarithmic divergence, besides the leading one associated with the area law, in its expansion as $\varepsilon \to 0$. We find it convenient to introduce

$$\widetilde{B}_A \equiv \frac{1}{\log(\varepsilon/P_A)} \left(\mathcal{A}_A - \frac{P_A}{\varepsilon} \right) . \tag{2.17}$$

Since (2.5) holds in this case, we have that $\widetilde{B}_A = B_A + o(1)$.

When ∂A is a convex polygon with N sides, denoting by $\alpha_i < \pi$ its internal angle at the i-th vertex,

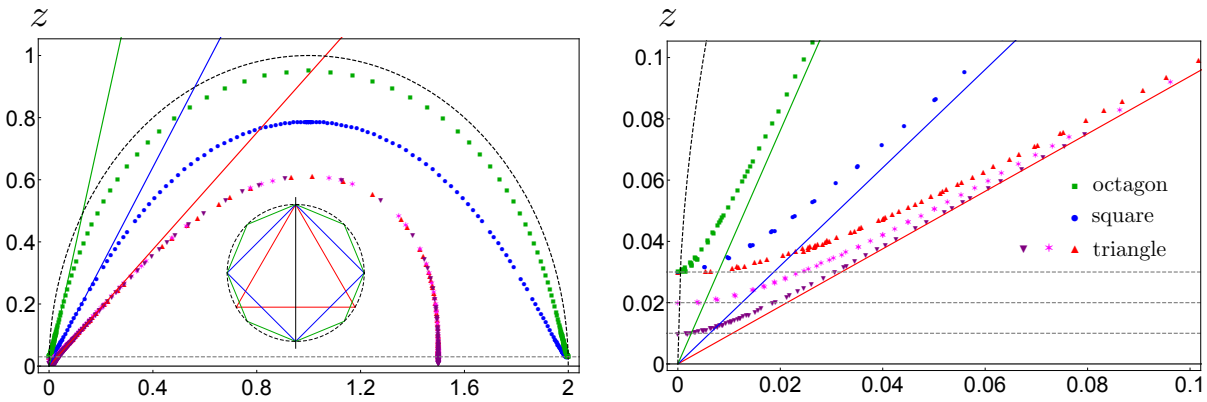

Figure 2.4: Left: Section of the minimal surfaces anchored to an equilateral triangle (red, magenta and purple points), a square (blue points) or an octagon (green points) inscribed in a circle, as indicated in the inset by the black line. The continuos lines are $z = \rho/f_0(\alpha_N)$, where $f_0(\alpha)$ is found from (2.21) with $N = 3$ (red), $N = 4$ (blue) or $N = 8$ (green). The dashed black curve is the hemisphere corresponding to the circle circumscribing the polygons at $z = 0$ (dashed in the inset), while the dashed grey horizontal line corresponds to the cut-off $\varepsilon = 0.03$. Right: A zoom of the left panel around the origin, placed in the common vertex of the polygons. For the triangle, three different values of $\varepsilon \in \{0.03, 0.02, 0.01\}$ has been considered to highlight how the agreement with the analytic result improves as $\varepsilon \to 0$.

for the coefficient of the logarithmic term in (2.5) we can write

$$B_A \equiv 2\sum_{i=1}^{N} b(\alpha_i)\,. \tag{2.18}$$

The function $b(\alpha)$ has been first found in [119], where the holographic duals of the correlators of Wilson loops with cusps have been studied, by considering the minimal surface near a cusp whose opening angle is α. Notice that (2.18) does not depend on the lengths of the edges but only on the convex angles of the polygon. Further interesting results have been obtained in the context of the holographic entanglement entropy [59, 120].

Introducing the polar coordinates (ρ, ϕ) in the $z = 0$ plane, one considers the domain $\{|\phi| \leqslant \alpha/2\,, \rho < L\}$, where $L \gg 1$. By employing scale invariance, one introduces the following ansatz [119]

$$z = \frac{\rho}{f(\phi)}\,, \tag{2.19}$$

in terms of a positive function $f(\phi)$, which is even in the domain $|\phi| \leqslant \alpha/2$ and $f \to +\infty$ for $|\phi| \to \alpha/2$. Plugging (2.19) into the area functional, the problem becomes one dimensional, similarly to the case of the infinite strip slightly discussed in 2.2. Since the resulting integrand does not depend explicitly on ϕ, the corresponding conservation law tells us that $(f^4 + f^2)/\sqrt{(f')^2 + f^4 + f^2}$ is independent of ϕ. Thus, the profile for $0 \leqslant \phi < \alpha/2$ (the part of the surface with $-\alpha/2 < \phi \leqslant 0$ is obtained by symmetry) is given by

$$\phi = \int_{f_0}^{f} \frac{1}{\zeta}\left[(\zeta^2+1)\left(\frac{\zeta^2(\zeta^2+1)}{f_0^2(f_0^2+1)} - 1\right)\right]^{-\frac{1}{2}} d\zeta\,, \tag{2.20}$$

being $f_0 \equiv f(0)$. When $f \to \infty$, we require that the l.h.s. of (2.20) becomes $\alpha/2$ and, by inverting the resulting relation, one finds $f_0 = f_0(\alpha)$. In this limit the integral in (2.20) can be evaluated analytically in terms of elliptic integrals Π and $\mathbb{K}$ (see B.5 for their definitions) as follows

$$\alpha(f_0) = 2\tilde{f}_0\sqrt{\frac{1-2\tilde{f}_0^2}{1-\tilde{f}_0^2}}\left[\Pi\big(1-\tilde{f}_0^2, \tilde{f}_0^2\big) - \mathbb{K}\big(\tilde{f}_0^2\big)\right], \qquad \tilde{f}_0^2 \equiv \frac{f_0^2}{1+2f_0^2} \in [0, 1/2]\,. \tag{2.21}$$

Notice that when $f_0 \to 0$ we have $\alpha \to \pi$, which means absence of the corner, while $\alpha \to 0$ for $f_0 \to \infty$.

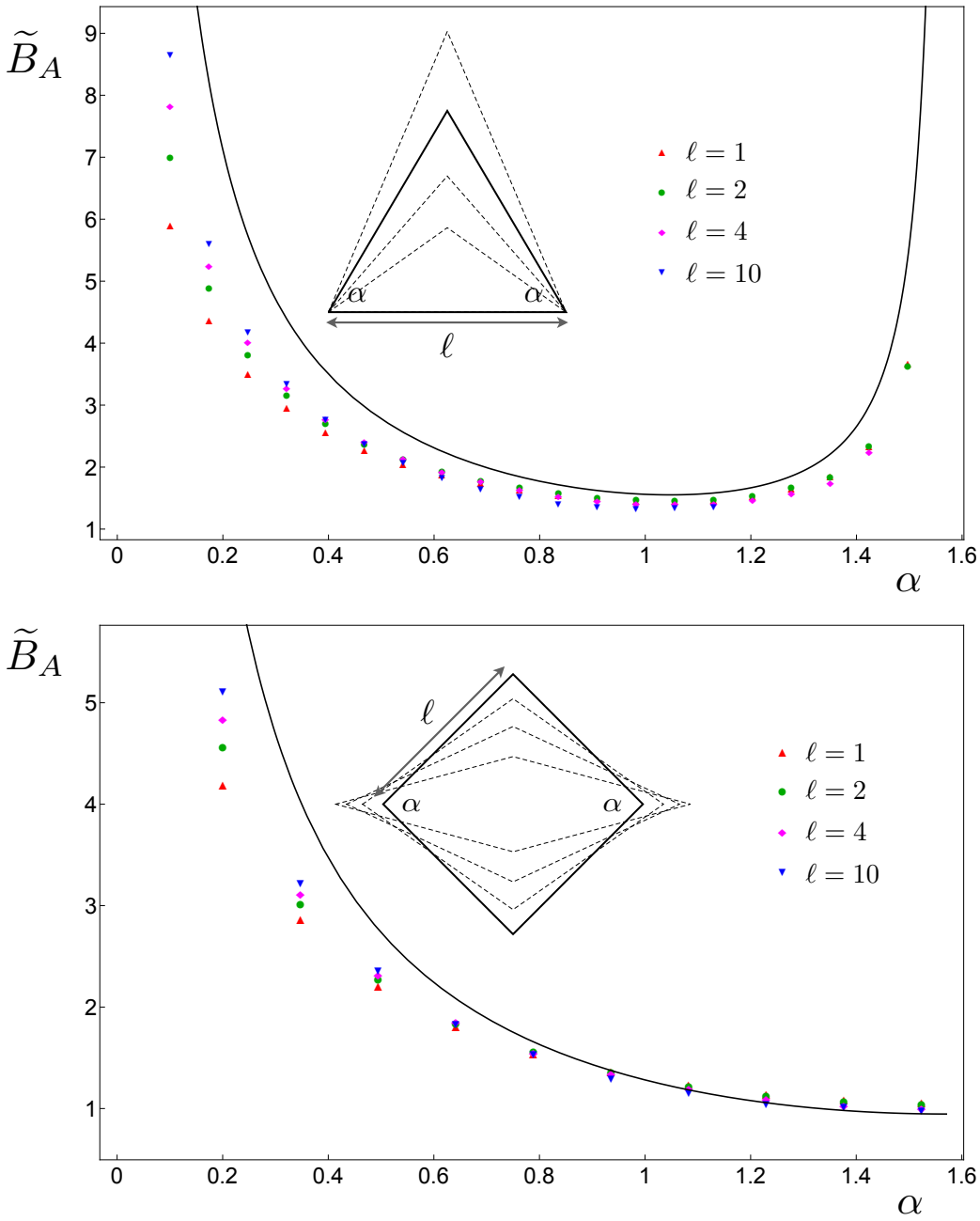

Figure 2.5: The quantity $\widetilde{B}_A$ in (2.17) with $\mathcal{A}_A$ evaluated with Surface Evolver when the entangling curve ∂A is either an isosceles triangle whose basis has length ℓ (top panel) or a rhombus whose side length is ℓ (bottom panel). Here $\varepsilon = 0.03$. The black continuous curves are obtained from (2.18) and (2.22).

As for the area of the minimal surface given by (2.19), one finds that

$$b(\alpha) \equiv \int_0^\infty \left(1 - \sqrt{\frac{\zeta^2 + f_0^2 + 1}{\zeta^2 + 2f_0^2 + 1}}\right) d\zeta \;=\; \frac{\mathbb{E}(\tilde{f}_0^2) - (1 - \tilde{f}_0^2)\mathbb{K}(\tilde{f}_0^2)}{\sqrt{1 - 2\tilde{f}_0^2}}\,, \tag{2.22}$$

where $f_0 = f_0(\alpha)$ can be found by inverting numerically (2.21). The function (2.22) has a pole when $\alpha \to 0$ (in particular, $b(\alpha) = \Gamma(\frac{3}{4})^4/(\pi\alpha) + \dots$) while $b(\pi) = 0$, which is expected because $\alpha = \pi$ means no cusp and the logarithmic divergence does not occur for smooth entangling curves.

An interesting family of curves to study is the one made by the convex regular polygons. They are equilateral, equiangular and all vertices lie on a circle. For instance, a rhombus does not belong to this

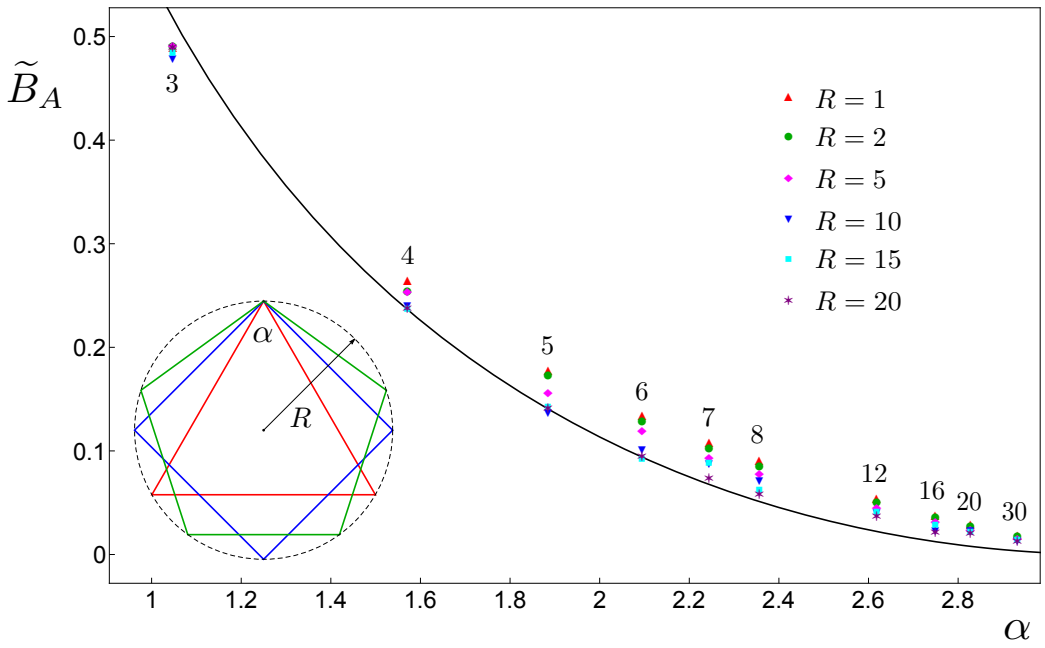

Figure 2.6: The quantity $\widetilde{B}_A$ in (2.17) corresponding to ∂A given by polygons with N equal sides circumscribed by a circle with radius R. The cut-off is $\varepsilon = 0.03$ and the values of N are indicated above the corresponding series of data points. The black curve is given by (2.18) and (2.22).

family. Denoting by R the radius of the circumscribed circle and by N the number of sides, the length of each side is $\ell = 2R\sin(\pi/N)$ and all the internal angles are $\alpha_N \equiv \frac{N-2}{N}\,\pi$. When $N \to \infty$ we have that $\alpha_N \to \pi$ and the polygon becomes a circle. Thus, the area of the minimal surface spanning these regular polygons is (2.5) with $P_A = N\ell$ and $B_A = 2Nb(\alpha_N)$.

It is interesting to compare the analytic results presented above with the corresponding numerical ones obtained with Surface Evolver. Some examples of minimal surfaces anchored on curves ∂A given by a polygon are given in Fig. 2.3, where the triangulations are explicitly shown. In Fig. 2.4 we take as ∂A an equilateral triangle, a square and an octagon which share a vertex and consider the section of the corresponding minimal surfaces through a vertical plane which bisects the angles associated with the common vertex, as shown in the inset of the left panel. Focussing on the part of the curves near the common vertex, we find that the numerical results are in good agreement with the analytic expression $z = \rho/f_0$, where $f_0 = f_0(\alpha_N)$ is obtained from (2.20). It would be interesting to find analytic results for the profiles shown in the left panel of Fig. 2.4.

By employing Surface Evolver, we can also consider entangling curves given by polygons which are not regular, as done in Fig. 2.5, where we have reported the data for $\widetilde{B}_A$ (defined in (2.17)) corresponding to the area of the minimal surfaces $\tilde{\gamma}_A$ when ∂A is either an isosceles triangle (top panel) or a rhombus with side ℓ (bottom panel). These examples allow us to consider also cusps with small opening angles. The size of the isosceles triangles has been changed by varying the angles α adjacent to the basis. Thus, the limiting regimes are the segment ($\alpha = 0$) and the semi infinite strip ($\alpha = \pi$). As for the rhombus, denoting by α the angle indicated in the inset, its limiting regimes are the segment ($\alpha = 0$) and the square ($\alpha = \pi$). The cut-off in the holographic direction has been fixed to $\varepsilon = 0.03$ (see the discussion in B.2). Increasing the size of the polygon improves the agreement with the curve given by (2.18) and (2.22), as expected, because ε/P_A gets closer to zero. Moreover, the agreement between the numerical data and the analytic curve gets worse as α becomes very small.

In Fig. 2.6 we report the data for $\widetilde{B}_A$ found with Surface Evolver for regular polygons with various number N of edges. The agreement with the curve given by (2.18) and (2.22) is quite good and it improves for larger domains.

It is worth emphasizing that, for entangling surfaces ∂A containing corners, the way we have employed to construct the minimal surfaces with Surface Evolver (i.e. by defining ∂A at $z = \varepsilon$) influences the term W_A in the expansion (2.5) for the area, as already remarked in [119].

It could be helpful to compute the length P_ε of the curve defined as the section at $z = \varepsilon$ of the

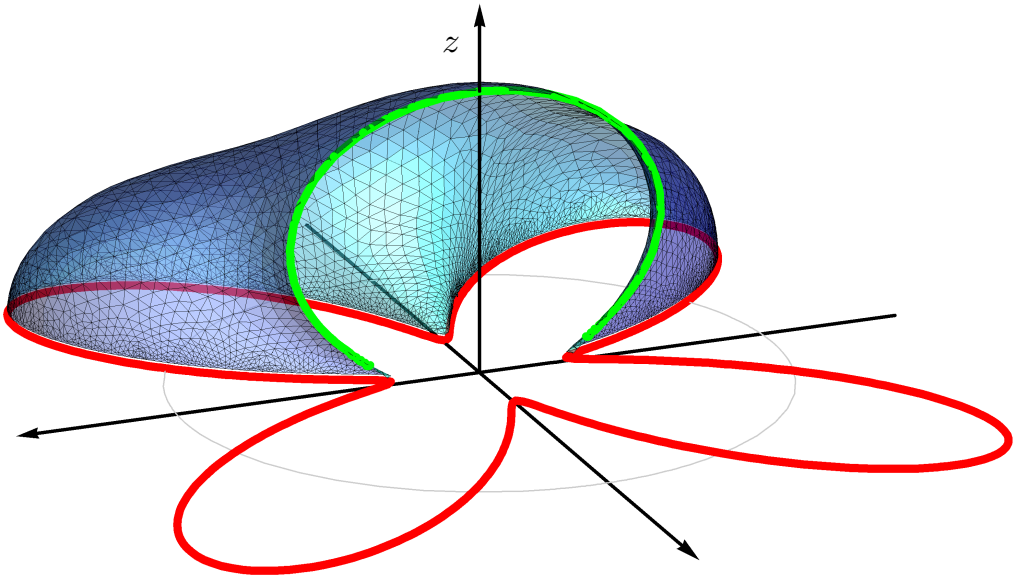

Figure 2.7: Minimal surface constructed with Surface Evolver corresponding to a star convex domain delimited by the red curve given by $r(\phi) = R_0 + a_0 \cos(k\phi)$ in polar coordinates in the $z = 0$ plane, with $R_0 = 1$, $a_0 = 0.7$ and $k = 4$. Here the cut-off is $\varepsilon = 0.03$ and $(V, F) = (6145, 11776)$. Only half of the minimal surface is shown in order to highlight the section given by the green curve.

minimal surface anchored on the long segments of a large wedge with opening angle α, which has been introduced above. From (2.19) we find that, in terms of polar coordinates whose center is the projection of the vertex at $z = \varepsilon$, this curve is given by $\rho = \varepsilon f(\phi)$. Being $L \gg 1$, we find that P_ε reads

$$P_\varepsilon = 2\int_0^{\alpha_\varepsilon/2} \sqrt{\rho^2 + (\partial_\phi \rho)^2}\, d\phi = 2\varepsilon \int_0^{\alpha_\varepsilon/2} \sqrt{f^2 + (\partial_\phi f)^2}\, d\phi = 2\varepsilon \int_{f_0}^{L/\varepsilon} \sqrt{1 + f^2(\partial_f \phi)^2}\, df = 2L - 2f_0\varepsilon + \ldots , \tag{2.23}$$

where $\alpha_\varepsilon \simeq \alpha$ is defined by the relation $L = \varepsilon f(\alpha_\varepsilon/2)$ and in the last step a change of variable has been performed. It is easy to observe that $\alpha_\varepsilon < \alpha$. Considering the integral in the intermediate step of (2.23), one notices that it diverges because of its upper limit of integration (see the text below (2.19)), while the lower limit of integration gives a finite result, providing a contribution $O(\varepsilon)$ to P_ε. The expression of $\partial_f \phi$ can be read from the integrand of (2.20), finding that $f^2(\partial_f \phi)^2 = O(1/f^6)$ when $f \to +\infty$. Since $L/\varepsilon \gg 1$, by expanding the integrand in (2.23) for large f, we obtain that this integral diverges like $L/\varepsilon - f_0 + \ldots$, where the finite term has been found numerically. As a cross check of the finite term, we observe that $f_0 = 0$ when $\alpha = \pi$ (see below (2.21)), as expected. Thus, we can conclude that $P_\varepsilon = 2L + O(\varepsilon)$, being $P_A = 2L$ the length of the boundary of the wedge at $z = 0$. Notice that, performing this computation for the minimal surface anchored on a circle of radius R, which is a hemisphere, one finds that $P_\varepsilon = 2\pi R + O(\varepsilon^2)$.

Let us remark that P_ε is not related to the regularization we adopt in our numerical analysis, as it can be realized from the right panel of Fig. 2.4. Indeed, in order to analytically the profiles given by the numerical data in the right panel of Fig. 2.4 the ansatz (2.19) cannot be employed and a partial differential equation must be solved.

2.2.3 Star shaped and non convex regions

The crucial assumption throughout the above discussions is that the minimal surface $\tilde{\gamma}_A$ can be fully described by $z = z(x, y)$, where $(x, y) \in A$. Nevertheless, there are many domains A for which this parameterization cannot be employed because there are pairs of different points belonging to the minimal surfaces $\tilde{\gamma}_A$ with the same projection $(x, y) \notin A$ in the $z = 0$ plane. In these cases, being the analytic approach quite difficult in general, one can employ our numerical method to find the minimal surfaces

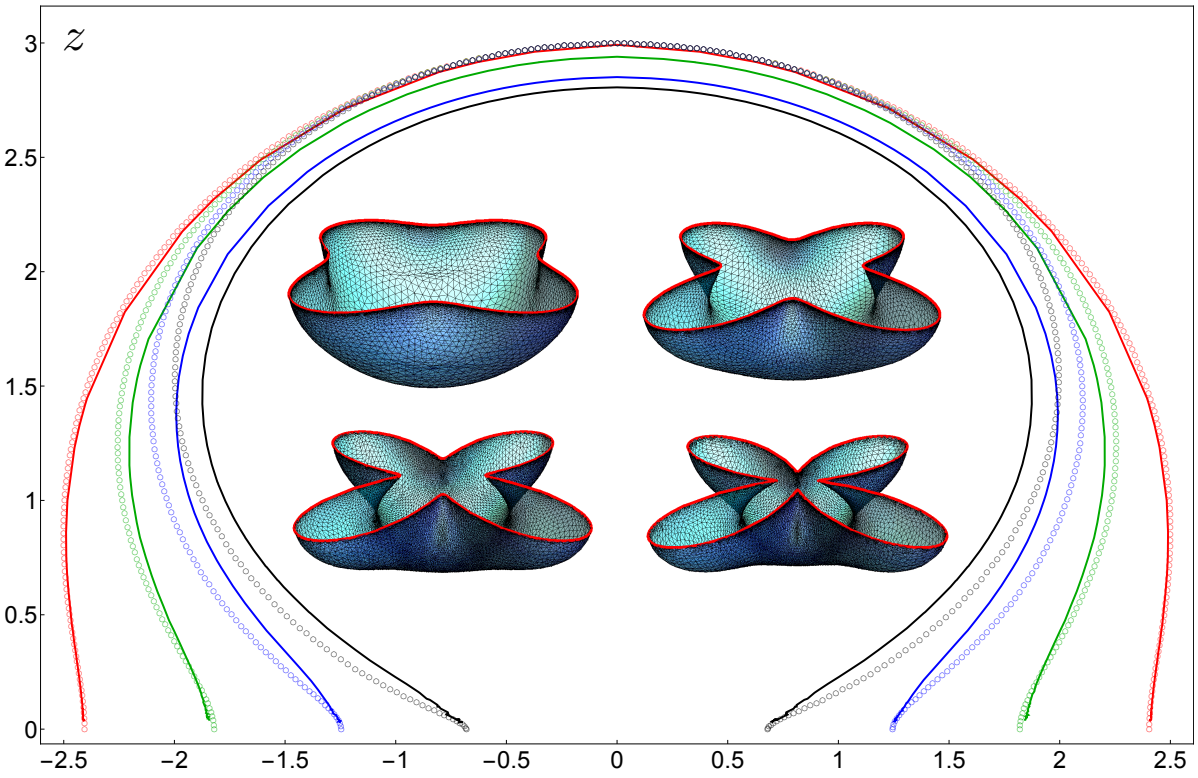

Figure 2.8: Minimal surfaces corresponding to entangling curves ∂A at $z = 0$ given by (2.27) with $R = 3$, $k = 4$, $\mu = 0$ and for different values of the parameter a, which delimit star shaped domains (red curves in the inset). In the inset, where the z direction points downward, we show the minimal surfaces constructed through Surface Evolver with $\varepsilon = 0.03$. In the main plot, the solid curves are their sections of the minimal surfaces of the inset at $\phi = \pi/4$ (like the green curve in Fig. 2.7), while the curves made by the empty small circles are obtained from the linearized solution of [61]. The colors in the main plot correspond to different values of $a \in \{0.2, 0.4, 0.6, 0.8\}$ (red, green, blue and black respectively), while in the inset a increases starting from the top left surface and going to the top right, bottom left and bottom right ones.

and to compute their area. The numerical data obtained with Surface Evolver would be an important benchmark for analytic results that could be found in the future.

An interesting class of two dimensional regions to consider is given by the star shaped domains. A region A at $z = 0$ belongs to this set of domains if a point $P_0 \in A$ exists such that the segment connecting any other point of the region to P_0 entirely belongs to A. As for the minimal surface anchored on a star shaped domain A, by introducing a spherical polar coordinates system (r, ϕ, θ) centered in P_0 (the angular ranges are $\phi \in [0, 2\pi)$ and $\theta \in [0, \pi/2]$), one can parameterize the entire minimal surface. Thus, we have $\rho = r \sin\theta$ and $z = r \cos\theta$, being (ρ, ϕ) the polar coordinates of the $z = 0$ plane. Some interesting analytic results about these domains have been already found. In particular, [61] considered minimal surfaces obtained as smooth perturbations around the hemisphere and in [87] the behaviour in the IR regime for gapped backgrounds [121] has been studied. Our numerical method allows a more complete analysis because, within our approximations, we can find (numerically) the area of the corresponding minimal surface without restrictions.

In Fig. 2.7 we show a star convex domain A delimited by the red curve at $z = 0$, which does not contain vertices, and the corresponding minimal surface $\tilde{\gamma}_A$ anchored on it. Notice that there are pairs of points belonging to $\tilde{\gamma}_A$ having the same projection $(x, y) \notin A$ on the $z = 0$ plane. It is worth recalling that in our regularization the numerical construction of the minimal surface with Surface Evolver has been done by defining the entangling curve ∂A at $z = \varepsilon$.

In order to give a further check of our numerical method, we find it useful to compare our numerical results against the analytic ones obtained in [61], where the equation of motion coming from (2.3) written

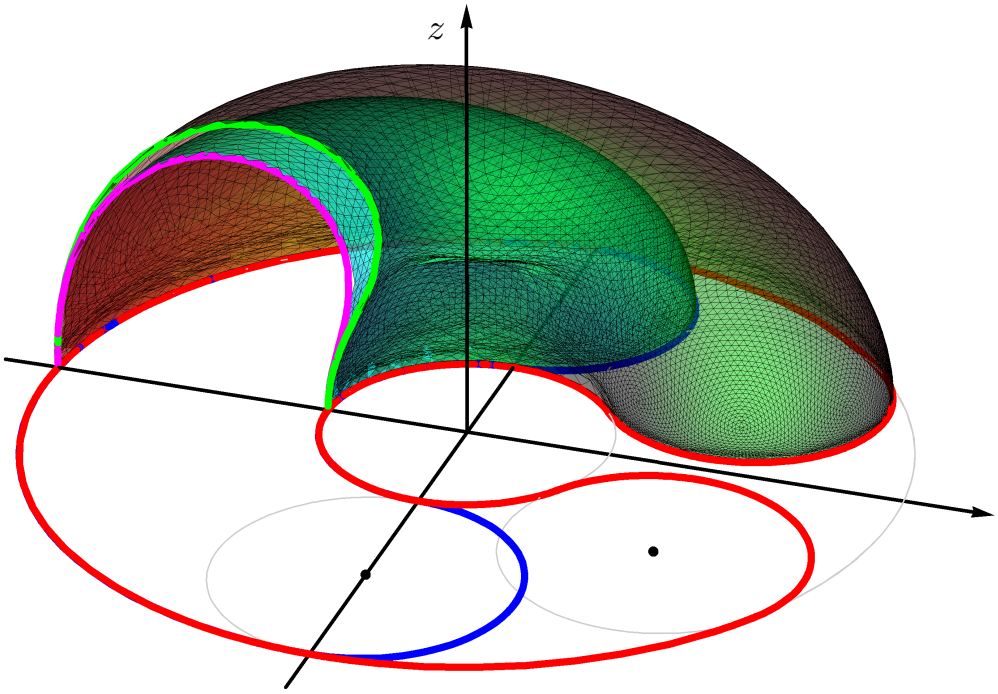

Figure 2.9: Minimal surfaces constructed with Surface Evolver corresponding to non convex domains at $z = 0$ delimited by the red and blue curves, which are made by arcs of circle centered either in the origin or in the points identified by the black dots. The green and magenta curves are sections of the minimal surfaces anchored on the red and the blue curves respectively.

in polar coordinates (r, ϕ, θ) has been linearized to second order around the hemisphere solution with radius R, finding

$$r(\theta, \phi) = R + a\, r_1(\theta, \phi) + a^2 r_2(\theta, \phi) + O(a^3)\,, \tag{2.24}$$

where the $r_1(\theta, \phi)$ and $r_2(\theta, \phi)$ are given by [61]

$$r_1(\theta, \phi) = [\tan(\theta/2)]^k (1 + k\cos\theta)\cos(k\phi)\,, \tag{2.25}$$

$$r_2(\theta, \phi) = \frac{[\tan(\theta/2)]^{2k}}{4R}\left\{(1 + k\cos\theta)^2 + \left[\mu\,(1 + 2k\cos\theta) + k^2\cos^2\theta\right]\cos(2k\phi)\right\}, \tag{2.26}$$

being $k \in \mathbb{N}$ and $\mu \in \mathbb{R}$ two parameters of the linearized solution. The minimal surface equation coming from (2.3) is satisfied by (2.24) at $O(a^2)$. Notice that $r_1(\theta = 0, \phi) = r_2(\theta = 0, \phi) = 0$, which means that the maximum value reached by the linearized solution along the z direction is R, like for the hemisphere. Neglecting the $O(a^3)$ terms in (2.24), one has a surface spanning the curve $r(\pi/2, \phi) \equiv R_2(\phi)$ at $z = 0$, which reads

$$R_2(\phi) \equiv R + a\cos(k\phi) + \frac{a^2}{4R}\left[1 + \mu\cos(2k\phi)\right]. \tag{2.27}$$

In Fig. 2.8 we construct the minimal surfaces providing the holographic entanglement entropy of some examples of star shaped regions A delimited by (2.27) where R and μ are kept fixed while a takes different values, taking the $\phi = \pi/4$ section of these surfaces (see also the green curve in Fig. 2.7). Compare the resulting curves (the solid ones in the main plot of Fig. 2.8) with the corresponding ones obtained from the second order linearized solution (2.24) (made by the empty circles), we observe that the agreement is very good for small values of a/R and it gets worse as a/R increases, as expected.

Our numerical method is interesting because it does not rely on any particular parameterization of the surface and this allows us to study the most generic non convex domain. In Fig. 2.9 we show two examples of non convex domains A which are not star shaped: one is delimited by the red curve and the other one by the blue curve. We could see these domains as two two dimensional spherocylinders

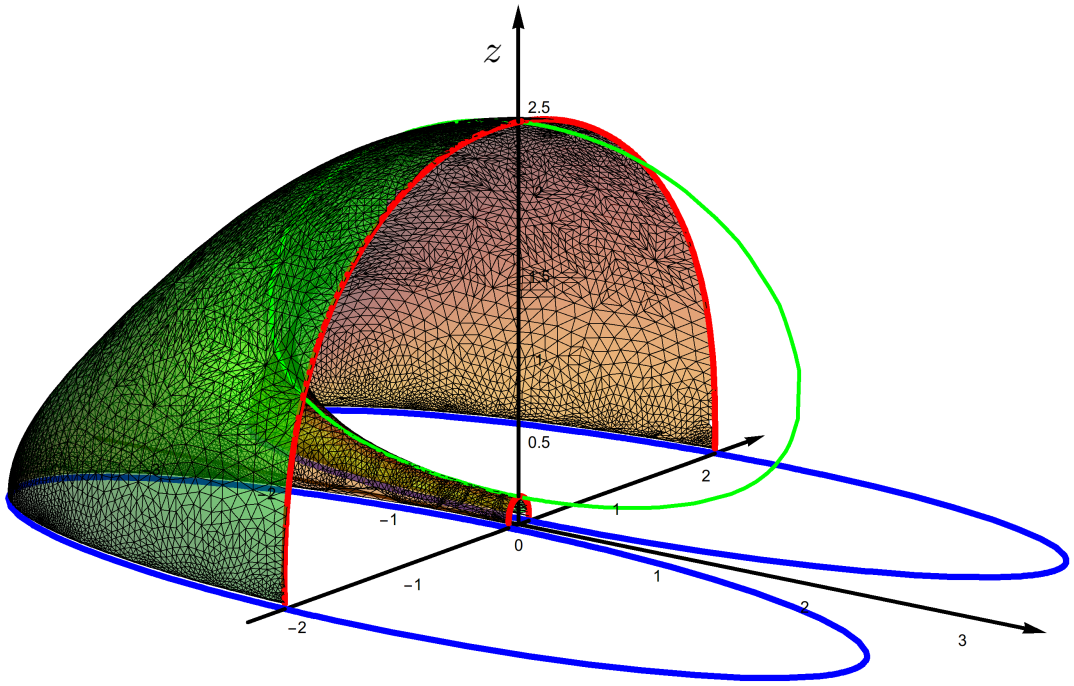

Figure 2.10: Minimal surface constructed with Surface Evolver for a domain $A = A_1 \cup A_2$ delimited by two disjoint and equal ellipses at $z = 0$ (blue curves). Here $\varepsilon = 0.03$ and the minimal surface is anchored on ∂A defined at $z = \varepsilon$, according to our regularization prescription. The minimal surface has $(V, F) = (18936, 37616)$ (the number of edges E can be found from the Euler formula with vanishing genus and two boundaries). Only half surface is shown in order to highlight the curves given by the two sections suggested by the symmetry of the surface.

which have been bended in a particular way. Constructing the minimal surfaces $\tilde{\gamma}_A$ anchored on their boundaries and considering their sections given by the green and magenta curves, one can clearly observe that some pair of points belonging to the minimal surfaces have the same projection $(x, y) \notin A$ on the $z = 0$ plane, as already remarked above. An analytic description of these surfaces is more difficult with respect to the minimal surfaces anchored on the boundary of star shaped domains because it would require more patches.

2.3 Two disjoint regions

In this section we discuss the main result of this Chapter, which is the numerical study of the holographic mutual information of disjoint equal domains delimited by some of the smooth curves introduced in 2.2.1. For two equal disjoint ellipses, an explicit example of the minimal surface whose area determines the corresponding holographic mutual information is shown in Fig. 2.10.

Let us consider two dimensional domains $A = A_1 \cup A_2$ made by two disjoint components A_1 and A_2, where each component is a simply connected domain delimited by a smooth curve. The boundary is $\partial A = \partial A_1 \cup \partial A_2$ and the shapes of ∂A_1 and ∂A_2 could be arbitrary, but we will focus on the geometries discussed in 2.2. Since the area law holds also for $S_{A_1 \cup A_2}$ and $P_A = P_{A_1} + P_{A_2}$, the leading divergence $O(1/\varepsilon)$ cancels in the combination (1.12), which is therefore finite when $\varepsilon \to 0$.

Considering the mutual information (1.12) with the entanglement entropy computed through the holographic formula (1.26), we find it convenient to introduce $\mathcal{I}_{A_1,A_2}$ as follows

$$I_{A_1,A_2} \equiv \frac{\mathcal{I}_{A_1,A_2}}{4G_N}\,, \tag{2.28}$$

where G_N is the four dimensional Newton constant. Since ∂A_1 and ∂A_2 are smooth curves, from (2.4)

and (2.14) we have

$$\mathcal{I}_{A_1,A_2} = \widetilde{F}_{A_1\cup A_2} - \widetilde{F}_{A_1} - \widetilde{F}_{A_2} = F_{A_1\cup A_2} - F_{A_1} - F_{A_2} + o(1)\,. \tag{2.29}$$

In the following we study $\mathcal{I}_{A_1,A_2}$ when ∂A is made either by two circles (2.3.1.2) or by two superellipses or by the boundaries of two two dimensional spherocylinders. Once A_1, A_2 and their relative orientation have been fixed, we can only move their relative distance. A generic feature of the holographic mutual information is that it diverges when A_1 and A_2 become tangent, while it vanishes when the distance between A_1 and A_2 is large enough.

2.3.1 Circular boundaries

In this section we consider domains A whose boundary ∂A is made by two disjoint circles. The corresponding disks can be either overlapping (in this case A is an annulus) [58, 59, 113] or disjoint [114].

2.3.1.1 Annular regions

Let us consider the annular region A bounded by two concentric circles with radii $R_{\rm in} < R_{\rm out}$. The complementary domain B is made by two disjoint regions and, since we are in the vacuum, $S_A = S_B$. The minimal surfaces associated with this case have been already studied in [58, 113] as the gravitational counterpart of the correlators of spatial Wilson loops and in [59] from the holographic entanglement entropy perspective.

In B.4.2 we discuss the construction of the analytic solution in d dimensions for completeness, but here we are interested in the $d = 2$ case. Because of the axial symmetry, it is convenient to introduce polar coordinates (ρ, ϕ) at $z = 0$. Then, the profile of the minimal surface is completely specified by a curve in the plane (ρ, z).

A configuration providing a local minimum of the area functional is made by the disjoint hemispheres anchored on the circles with radii $R_{\rm in}$ and $R_{\rm out}$. In the plane (ρ, z), they are described by two arcs centered in the origin with an opening angle of $\pi/2$ (see the dashed curve in Fig. B.4). Another surface anchored on ∂A that could give a local minimum of the area functional is the connected one having the same topology of a half torus. This solution is fully specified by its profile curve in the plane (ρ, z), which connects the points $(R_{\rm in}, 0)$ and $(R_{\rm out}, 0)$. Thus, we have two qualitatively different surfaces which are local minima of the area functional and we have to establish which is the global minimum in order to compute the holographic entanglement entropy. Changing the annulus A, a transition occurs between these two types of surfaces, as we explain below. This is the first case that we encounter of a competition between two saddle points of the area functional.

The existence of the connected solution depends on the ratio $\eta \equiv R_{\rm in}/R_{\rm out} < 1$. As discussed in B.4.2, a minimal value η_* can be found such that for $0 < \eta < \eta_*$ only the disconnected configuration of two hemispheres exists, while for $\eta_* < \eta < 1$, besides the disconnected configuration, there are two connected configurations which are local minima of the area functional (see Fig. B.4). In the latter case, one has to find which of these two connected surfaces has the lowest area and then compare it with the area of the two disconnected hemispheres. This comparison provides a critical value $\eta_c > \eta_*$ such that when $\eta \in (\eta_c, 1)$ the minimal surface is given by the connected configuration, while for $\eta \in (0, \eta_c)$ the minimal area configuration is the one made by the two disjoint hemispheres.

Let us give explicit formulas about these surfaces by specifying to $d = 2$ the results found in B.4.2 (in order to simplify the notation adopted in B.4.2, in the following we report some formulas from that appendix omitting the index d). The profile of the radial section of the connected minimal surface in the plane (ρ, z) is given by the following two branches

$$\begin{cases} \rho = R_{\rm in}\, e^{-f_{-,K}(z/\rho)}\,, \\ \rho = R_{\rm out}\, e^{-f_{+,K}(z/\rho)}\,, \end{cases} \tag{2.30}$$

where, by introducing $\tilde{z} \equiv z/\rho$, the functions $f_{\pm,K}(\tilde{z})$ are defined as follows (from (B.28))

$$f_{\pm,K}(\tilde{z}) \equiv \int_0^{\tilde{z}} \frac{\lambda}{1+\lambda^2}\left(1 \pm \frac{\lambda}{\sqrt{K\,(1+\lambda^2) - \lambda^4}}\right) d\lambda\,, \qquad 0 \leqslant \tilde{z} \leqslant \tilde{z}_m\,, \qquad \tilde{z}_m^2 = \frac{K + \sqrt{K(K+4)}}{2}\,. \tag{2.31}$$

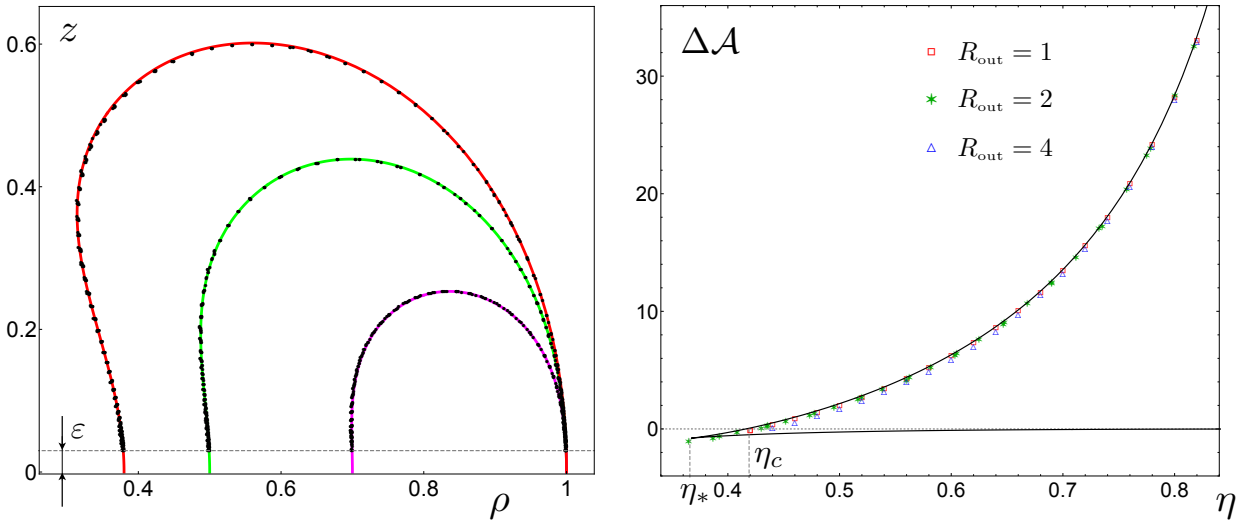

Figure 2.11: Left panel: Radial profiles of the connected surfaces anchored on the boundary of an annulus A which are local minima of the area functional. Comparison between the section of the surfaces constructed with Surface Evolver (black dots) and the analytic expressions reported in 2.3.1.1. While the external radius is kept fixed to $R_{\rm out} = 1$, for the internal one the values $R_{\rm in} = 0.38$ (red), 0.5 (green) and 0.7 (magenta) have been chosen. The cut-off is $\varepsilon = 0.03$ and, according to our regularization prescription, ∂A has been defined at $z = \varepsilon$ in the numerical construction. Right panel: The sign of $\Delta\mathcal{A}$ establishes the minimal area surface between the connected surface and the two disjoint hemispheres. The black curve is obtained from (2.39) by varying $K > 0$ and it is made by two branches joining at $\eta = \eta_*$, where the lower one corresponds to the connected solution which is not the minimal one between the two connected ones. The data points have been found with Surface Evolver for various annular domains. Notice that in the left panel $\eta < \eta_c$ only for the red curve.

The integral occurring in $f_{\pm,K}$ can be computed in terms of the incomplete elliptic integrals of the first and third kind (see B.5), finding

$$f_{\pm,K}(\tilde{z}) = \frac{1}{2}\log(1+\tilde{z}^2) \pm \kappa \sqrt{\frac{1-2\kappa^2}{\kappa^2-1}} \left[\mathbb{F}\big(\omega(\tilde{z})|\kappa^2\big) - \Pi\big(1-\kappa^2, \omega(\tilde{z})|\kappa^2\big)\right], \tag{2.32}$$

where we have introduced

$$\omega(\tilde{z}) \equiv \arcsin\left(\frac{\tilde{z}/\tilde{z}_m}{\sqrt{1+\kappa^2(\tilde{z}/\tilde{z}_m - 1)}}\right), \qquad \kappa \equiv \sqrt{\frac{1+\tilde{z}_m^2}{2+\tilde{z}_m^2}}\,. \tag{2.33}$$

The matching condition of the two branches (2.30) provides a relation between $\eta \geqslant \eta_*$ and the constant K, namely (from (B.30))

$$\log(\eta) = -\int_0^{\tilde{z}_m} \frac{2\,\lambda^2}{(1+\lambda^2)\sqrt{K(1+\lambda^2)-\lambda^4}}\, d\lambda = 2\kappa \sqrt{\frac{1-2\kappa^2}{\kappa^2-1}} \Big(\mathbb{K}\big(\kappa^2\big) - \Pi\big(1-\kappa^2, \kappa^2\big)\Big), \tag{2.34}$$

where $\mathbb{K}(m)$ and $\Pi(n,m)$ are the complete elliptic integrals of the first and third kind respectively.

The relation (2.34) tells us $\eta = \eta(K)$ and $\kappa \in [1/\sqrt{2}, 1]$. As discussed in B.4.2, where also related figures are given, plotting this function one gets a curve whose global minimum tells us that $\eta_* = 0.367$. From this curve it is straightforward to observe that, for any given $\eta \in (\eta_*, 1)$, there are two values of K fulfilling the matching condition (2.34). This means that, correspondingly, there are two connected surfaces anchored on the same pair of concentric circles on the boundary which are both local minima of the area functional. We have to compute their area in order to establish which one has to be compared with the configuration of disjoint hemispheres to find the global minimum.

Performing the following integral up to an additive constant (from (B.37) for $d = 2$)

$$\int \frac{d\tilde{z}}{\tilde{z}^2\sqrt{1+\tilde{z}^2-\tilde{z}^4/K}} = \frac{\sqrt{(\tilde{z}_m^2-\tilde{z}^2)(\tilde{z}_m^2+\tilde{z}^2\tilde{z}_m^2+\tilde{z}^2)}}{\tilde{z}\,\tilde{z}_m^3} + \frac{\mathbb{E}\big(\arcsin(\tilde{z}/\tilde{z}_m)|\kappa^2\big)+(\kappa^2-1)\mathbb{F}\big(\arcsin(\tilde{z}/\tilde{z}_m)|\kappa^2\big)}{\sqrt{2\kappa^2-1}}\,, \tag{2.35}$$

one obtains the area of the connected surface [113, 119]

$$\mathcal{A}_{\rm con} = 2\pi\left(\int_{\varepsilon/R_{\rm out}}^{\tilde{z}_m}\frac{d\tilde{z}}{\tilde{z}^2\sqrt{1+\tilde{z}^2-\tilde{z}^4/K}}+\int_{\varepsilon/R_{\rm in}}^{\tilde{z}_m}\frac{d\tilde{z}}{\tilde{z}^2\sqrt{1+\tilde{z}^2-\tilde{z}^4/K}}\right) \tag{2.36}$$

$$= \frac{2\pi(R_{\rm in}+R_{\rm out})}{\varepsilon} - \frac{4\pi}{\sqrt{2\kappa^2-1}}\Big(\mathbb{E}\big(\kappa^2\big)-(1-\kappa^2)\,\mathbb{K}\big(\kappa^2\big)\Big)+O(\varepsilon)\,. \tag{2.37}$$

Plotting the $O(1)$ term of this expression in terms of K, it is straightforward to realize that the minimal area surface between the two connected configurations corresponds to the smallest value of K.

As for the area of the configuration made by two disconnected hemispheres, from (B.40) one gets

$$\mathcal{A}_{\rm dis} = 2\pi\left(\int_{\varepsilon/R_{\rm in}}^{\infty}\frac{d\tilde{z}}{\tilde{z}^2\sqrt{1+\tilde{z}^2}}+\int_{\varepsilon/R_{\rm out}}^{\infty}\frac{d\tilde{z}}{\tilde{z}^2\sqrt{1+\tilde{z}^2}}\right) = \frac{2\pi(R_{\rm in}+R_{\rm out})}{\varepsilon}-4\pi+O(\varepsilon)\,. \tag{2.38}$$

We find it convenient to introduce $\Delta\mathcal{A} \equiv \mathcal{A}_{\rm dis}-\mathcal{A}_{\rm con}$, which is finite when $\varepsilon \to 0$. In particular, $\Delta\mathcal{A} \to 2\pi\Delta\mathcal{R}$ as $\varepsilon \to 0$, where $\Delta\mathcal{R}$ is (B.44) evaluated at $d = 2$. From (2.37) and (2.38), we have

$$\lim_{\varepsilon\to 0}\Delta\mathcal{A} = 4\pi\left(\frac{\mathbb{E}\big(\kappa^2\big)-(1-\kappa^2)\,\mathbb{K}\big(\kappa^2\big)}{\sqrt{2\kappa^2-1}}-1\right). \tag{2.39}$$

Considering as the connected surface the one with minimal area, the sign of $\Delta\mathcal{A}$ determines the minimal surface between the disconnected configuration and the connected one and therefore the global minimum of the area functional. The root η_c of $\Delta\mathcal{A}$ can be found numerically and one gets $\eta_c = 0.419$ [58, 107]. Thus, the connected configuration is minimal for $\eta \in (\eta_c, 1)$, while for $\eta \in (0, \eta_c)$ the minimal area configuration is the one made by the disjoint hemispheres.

By employing Surface Evolver, we can construct the surface anchored on the boundary of the annulus at $z = 0$ which is a local minimum, compute its area and compare it with the analytic results discussed above. This is another important benchmark of our numerical method.

In the left panel of Fig. 2.11 we consider the profile of the connected configuration in the plane (ρ, z). The black dots correspond to the radial section of the surface obtained with Surface Evolver, while the solid line is obtained from the analytic expressions discussed above. Let us recall that the triangulated surface is numerically constructed by requiring that it is anchored to the two concentric circles with radii $R_{\rm in} < R_{\rm out}$ at $z = \varepsilon$ and not at $z = 0$, as it should. Despite this regularization, the agreement between the analytic results and the numerical ones is very good for our choices of the parameters. It is worth remarking that, when $\eta \geqslant \eta_*$ and therefore two connected solutions exist for a given η, Surface Evolver finds the minimal area one between them. Nevertheless, it is not able to establish whether it is the global minimum. Indeed, for example, the red curve in the left panel of Fig. 2.11 has $\eta_* < \eta < 1$ and therefore the corresponding surface is minimal but it is not the global minimum. Instead, considering an annulus with $\eta < \eta_*$, even if one begins with a rough triangulation of a connected surface, Surface Evolver converges towards the configuration made by the two disconnected hemispheres.

In the right panel of Fig. 2.11 we compare the values of $\Delta\mathcal{A}$ obtained with Surface Evolver with the analytic curve from (2.39), finding a very good agreement. Numerical points having $\eta_* < \eta < \eta_c$ are also found, for the reason just explained.

2.3.1.2 Two disjoint disks

In this section we consider domains A made by two disjoint disks by employing the analytic results for the annulus reviewed in 2.3.1.1 and some isometries of $\mathbb{H}_3$. This method has been used in [122] for the case of a circle, while the case of two disjoint circles has been recently studied in [114]. The analytic results found in this way provide another important benchmark for the numerical data obtained with Surface Evolver.

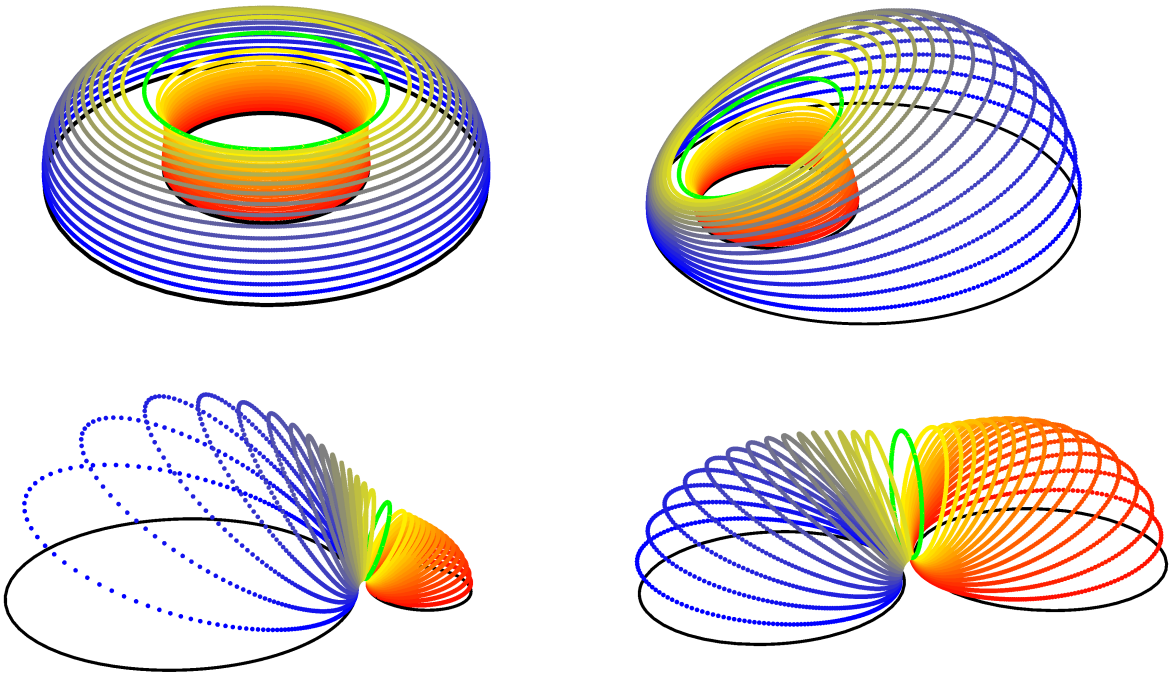

Figure 2.12: The connected surface anchored on the boundary of an annulus at $z = 0$ (top left panel), which is a local minimum of the area functional, can be mapped through (2.40) into one of the connected surfaces anchored on the configurations of circles at $z = 0$ shown in the remaining panels, depending on the value of the parameter of the transformation (2.40), as discussed in 2.3.1.2. The mapping preserves the color code. The green circle in the top left panel corresponds to the matching of the two branches given by (2.30) and (2.34) (see the point P_m in Fig. B.4) and it is mapped into the vertical circle in the bottom right panel.

Let us consider the following reparameterizations of $\mathbb{H}_3$, which correspond to the special conformal transformations on the boundary [122]

$$\tilde{x} = \frac{x + b_x(|\boldsymbol{v}|^2 + z^2)}{1 + 2\boldsymbol{b}\cdot\boldsymbol{v} + |\boldsymbol{b}|^2(|\boldsymbol{v}|^2 + z^2)}\,, \qquad \tilde{y} = \frac{y + b_y(|\boldsymbol{v}|^2 + z^2)}{1 + 2\boldsymbol{b}\cdot\boldsymbol{v} + |\boldsymbol{b}|^2(|\boldsymbol{v}|^2 + z^2)}\,, \qquad \tilde{z} = \frac{z}{1 + 2\boldsymbol{b}\cdot\boldsymbol{v} + |\boldsymbol{b}|^2(|\boldsymbol{v}|^2 + z^2)}\,, \tag{2.40}$$

being $\boldsymbol{b} \equiv (b_x, b_y)$ a vector in $\mathbb{R}^2$ and $\boldsymbol{v} \equiv (x, y)$.

When $z = 0$ in (2.40), the maps $(x, y) \to (\tilde{x}, \tilde{y})$ are the special conformal transformations of the Euclidean conformal group in two dimensions. These transformations in the $z = 0$ plane send a circle $\mathcal{C}$ with center $\boldsymbol{c} = (c_x, c_y)$ and radius R into another circle $\widetilde{\mathcal{C}}$ with center $\tilde{\boldsymbol{c}} = (\tilde{c}_x, \tilde{c}_y)$ and radius $\widetilde{R}$ which are given by

$$\tilde{c}_i = \frac{c_i + b_i(|\boldsymbol{c}|^2 - R^2)}{1 + 2\boldsymbol{b}\cdot\boldsymbol{c} + |\boldsymbol{b}|^2(|\boldsymbol{c}|^2 - R^2)} \qquad i \in \{x, y\}\,, \qquad \widetilde{R} = \frac{R}{\left|1 + 2\boldsymbol{b}\cdot\boldsymbol{c} + |\boldsymbol{b}|^2(|\boldsymbol{c}|^2 - R^2)\right|}\,. \tag{2.41}$$

Notice that the center $\tilde{\boldsymbol{c}}$ is not the image of the center $\boldsymbol{c}$ under (2.40) with $z = 0$. Moreover, when $\boldsymbol{c}$ is such that the denominator in (2.41) vanishes, the circle is mapped into a straight line [122].

Considering two concentric circles at $z = 0$ with radii $R_{\text{in}} < R_{\text{out}}$, their images are two different circles at $z = 0$ which do not intersect. In order to deal with simpler expressions for the mapping, let us place the center of the concentric circles in the origin, i.e. $\boldsymbol{c} = (0, 0)$. By introducing $\eta \equiv R_{\text{in}}/R_{\text{out}} < 1$ for the initial configuration of concentric circles centered in the origin and denoting by $\widetilde{R}_1 \equiv R_{\text{in}}/|1 - |\boldsymbol{b}|^2 R_{\text{in}}^2|$ and $\widetilde{R}_2 \equiv R_{\text{out}}/|1 - |\boldsymbol{b}|^2 R_{\text{out}}^2|$ the radii of the circles after the mapping, the distance between the two centers reads

$$d = \frac{(1 - \eta^2)\beta}{|(1 - \beta^2)(\beta^2 - \eta^2)|}\, R_{\text{in}} = \frac{(1 - \eta^2)\beta}{|\beta^2 - \eta^2|}\, \widetilde{R}_1\,, \tag{2.42}$$

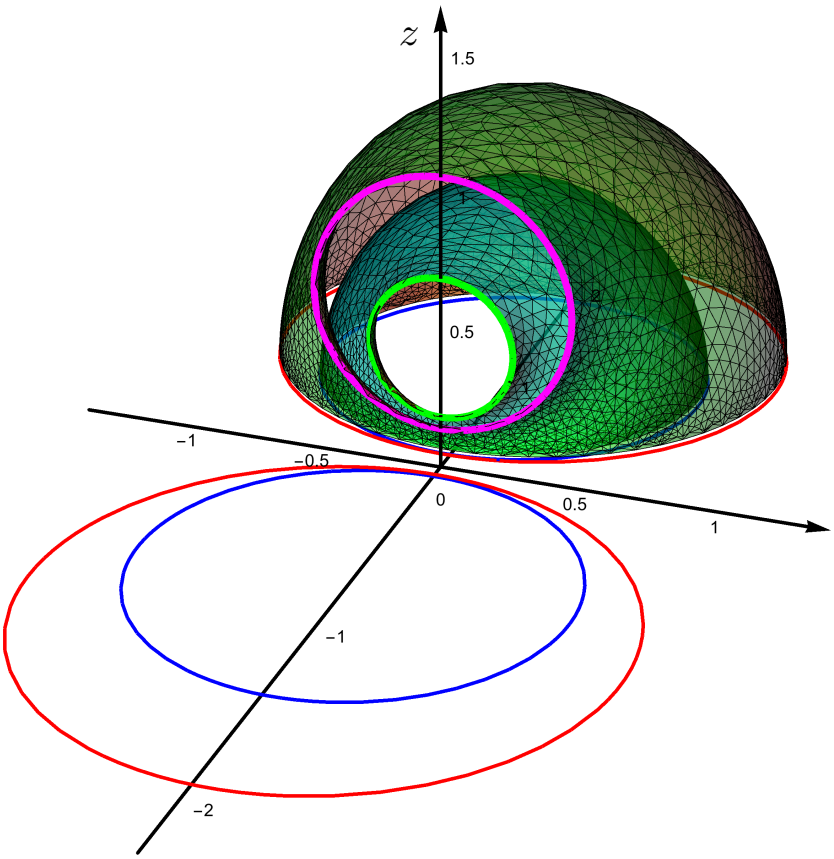

Figure 2.13: Two examples of minimal surfaces (constructed with Surface Evolver) corresponding to A made by two disjoint and equal disks (∂A is given by the red and blue circles). Only half of the surfaces is shown in order to highlight their section through a plane orthogonal to $z = 0$ and to the segment connecting the centers. This section provides a circle whose radius and center are given in (2.47). In this figure $\varepsilon = 0.03$, the red circles have radius $R = 1$ and the distance between their centers is $d = 2.16$, while for the blue ones $R = 0.75$ and $d = 1.68$.

where $\beta^2 \equiv |\boldsymbol{b}|^2 R_{\text{in}}^2$. Thus, η and β fix the value of the ratio $\tilde{\delta} \equiv d/\widetilde{R}_1$. The final disks are either disjoint or fully overlapping, depending on the sign of the expression within the absolute value in the denominator of (2.42). In particular, when $\beta^2 \in (\eta^2, 1)$ the two disks are disjoint, while when $\beta^2 \in (0, \eta^2) \cup (1, +\infty)$ they overlap. As for their ratio $\tilde{\eta} \equiv \widetilde{R}_1/\widetilde{R}_2$, we find

$$\tilde{\eta} = \begin{cases} \dfrac{\beta^2 - \eta^2}{\eta(\beta^2 - 1)} & \beta^2 \in (0, \eta^2) \cup (1, \infty) \qquad \text{overlapping disks}\,, \\ \dfrac{\beta^2 - \eta^2}{\eta(1 - \beta^2)} & \beta^2 \in (\eta^2, 1) \qquad \text{disjoint disks}\,. \end{cases} \tag{2.43}$$

Notice that $\tilde{\eta} \to 1/\eta > 1$ for $\beta^2 \to \infty$. Thus, given η and β, the equations (2.42) and (2.43) provide $\tilde{\delta}$ and $\tilde{\eta}$. By inverting them, one can write η and β in terms of $\tilde{\delta}$ and $\tilde{\eta}$. The system is made by two quadratic equations and some care is required to distinguish the various regimes.

When the disks after the mapping are disjoint, i.e. $\eta^2 < \beta^2 < 1$, an interesting special case to discuss is $\widetilde{R}_1 = \widetilde{R}_2$, namely when the disjoint disks have the same radius $\widetilde{R} = R_{\text{in}}/(1 - \eta) = R_{\text{out}}/(\eta^{-1} - 1)$, being $R_{\text{in}} < R_{\text{out}}$ the radii of the two concentric circles at $z = 0$ centered in the origin. Setting $\tilde{\eta} = 1$ in (2.43), one finds that it happens for $\beta^2 = \eta$, i.e. $|\boldsymbol{b}|^2 = 1/(R_{\text{in}} R_{\text{out}})$. The distance corresponding to this value of β can be found from (2.42) and it is given by $d/R_{\text{in}} = (1 + \eta)/\big[\sqrt{\eta}(1 - \eta)\big]$ or, equivalently, by $\tilde{\delta} = (1 + \eta)/\sqrt{\eta}$. By inverting this relation, one finds $\eta(\tilde{\delta}) = \big\{\tilde{\delta}^2 - 2 - \big[(\tilde{\delta}^2 - 2)^2 - 4\big]^{1/2}\big\}/2$, where the root $\eta(\tilde{\delta}) < 1$ has been selected and $\tilde{\delta} > 2$ must be imposed in order to avoid the intersection of the two

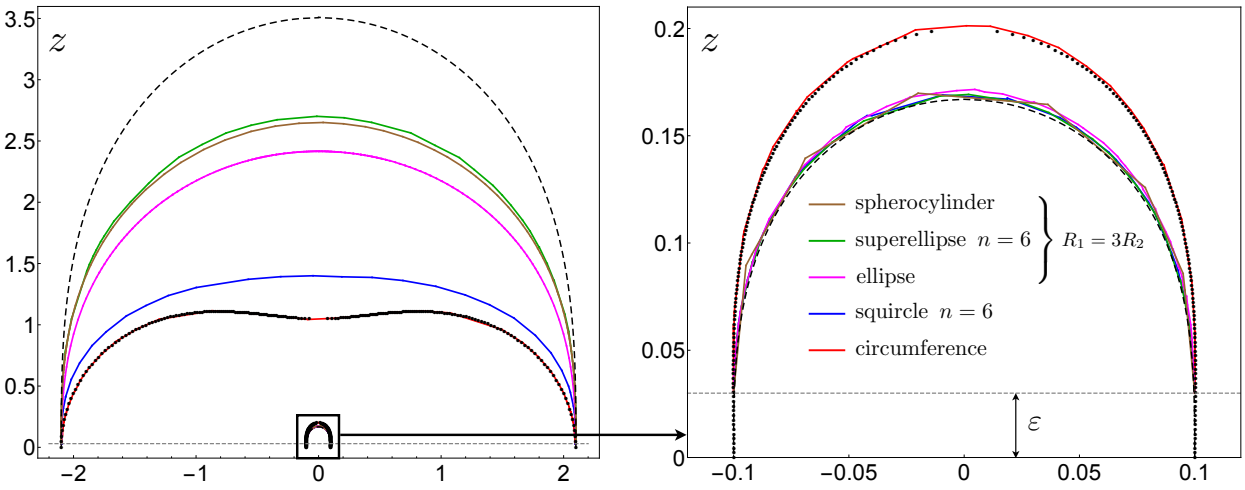

Figure 2.14: Left: Sections of minimal surfaces when A is made by two equal disjoint domains with smooth boundaries, like the red curves in Fig. 2.10. The coloured solid lines are the numerical results found with Surface Evolver for the shapes indicated in the common legend in the right panel. Here $R_2 = 1$ and $\varepsilon = 0.03$. The black dots (notice that they reach $z = 0$) correspond to the minimal surface for two disjoint circles and they have been found by mapping the connected minimal surface for the annulus through the transformations (2.40) (see 2.3.1.2 and Fig. 2.12). The dashed curve corresponds to two infinite strips. Right: Zoom of the part of the left panel enclosed by the black rectangle.

equal disks.

Once the vector $\boldsymbol{b} = (b_x, b_y) = |\boldsymbol{b}|(\cos\phi_b, \sin\phi_b)$ is chosen by fixing the initial and final configurations of circles at $z = 0$, the transformations (2.40) for the points in the bulk are fixed as well and they can be used to map the points belonging to the minimal surfaces spanning the initial configuration of circles. In particular, let us consider a circle given by $(R_\star \cos\phi, R_\star \sin\phi, z_\star)$ for $\phi \in [0, 2\pi)$, lying in a plane at $z = z_\star$ parallel to the boundary. This circle is mapped through (2.40) into another circle $\widehat{\mathcal{C}}$ whose radius is given by

$$\widehat{R} = \frac{R_\star}{\sqrt{1 + 2|\boldsymbol{b}|^2(z_\star^2 - R_\star^2) + |\boldsymbol{b}|^4(z_\star^2 + R_\star^2)^2}}\,, \tag{2.44}$$

and whose center $\hat{\boldsymbol{c}} \equiv (\hat{c}_x, \hat{c}_y, \hat{c}_z)$ has coordinates

$$\hat{c}_i = \frac{|\boldsymbol{b}|^2(R_\star^2 + z_\star^2)^2 + z_\star^2 - R_\star^2}{1 + 2|\boldsymbol{b}|^2(z_\star^2 - R_\star^2) + |\boldsymbol{b}|^4(z_\star^2 + R_\star^2)^2}\, b_i \qquad i \in \{x, y\}\,, \qquad \hat{c}_z = \frac{[1 + |\boldsymbol{b}|^2(R_\star^2 + z_\star^2)]\, z_\star}{1 + 2|\boldsymbol{b}|^2(z_\star^2 - R_\star^2) + |\boldsymbol{b}|^4(z_\star^2 + R_\star^2)^2}\,. \tag{2.45}$$

Setting $z_\star = 0$, $R_\star = R$ and $\widehat{R} = \widetilde{R}$ in (2.44) and (2.45), the expressions in (2.41) with $\boldsymbol{c} = (0, 0)$ are recovered. The circle $\widehat{\mathcal{C}}$ lies in a plane orthogonal to the following unit vector

$$\boldsymbol{v}_\perp = (-\cos\phi_b \sin\theta_\perp, -\sin\phi_b \sin\theta_\perp, \cos\theta_\perp)\,, \qquad \theta_\perp \equiv \arcsin(2z_\star|\boldsymbol{b}|\widehat{R}/R_\star)\,, \tag{2.46}$$

where $2z_\star|\boldsymbol{b}|\widehat{R}/R_\star < 1$, as can be easily observed from (2.44).

In the top left panel of Fig. 2.12 we consider as initial configuration the annulus at $z = 0$ for some given value of η and the corresponding connected minimal surface in the bulk anchored on its boundary, which has been discussed in 2.3.1.1. The transformation (2.40) with $\beta = \sqrt{\eta}$ maps this surface into the connected surface anchored on two equal and disjoint circles (bottom right panel in Fig. 2.12). It is interesting to follow the evolution of the former surface into the latter one as $\beta \in [0, \sqrt{\eta}]$ increases: in Fig. 2.12 we show two intermediate steps where the surfaces are qualitatively different and they correspond to different regimes of β separated by $\beta = \eta$. For $0 < \beta < \eta$ the disks at $z = 0$ are still overlapping but they are not concentric (top right panel of Fig. 2.12). Within this range of β, the radius of the largest disk, which is $R_{\rm out}/|1 - \beta^2/\eta^2|$, increases with β and it diverges when as $\beta \to \eta$. When $\eta < \beta \leqslant \sqrt{\eta}$, instead, the disks at $z = 0$ are disjoint and the images of the initial surface through (2.40) are shown in the bottom panels of Fig. 2.12, where the surface on the left has $\eta < \beta < \sqrt{\eta}$, while the one on the

right corresponds to the final stage of disjoint equal disks ($\beta = \sqrt{\eta}$). In Fig. 2.12 the mapping preserves the color code and we have highlighted the green circle because in the top left panel it corresponds to the circle at $z = z_m$ along which the two branches given by (2.30) match, as imposed by the condition (2.34). When $\beta = \sqrt{\eta}$, this matching circle is mapped into the vertical one shown in the bottom right panel, whose radius $\widetilde{R}_v$ and whose coordinate $z_v > \widetilde{R}_v$ of its center along the holographic direction are given respectively by

$$\widetilde{R}_v = \frac{1-\eta}{2\tilde{z}_m\sqrt{\eta}}\,\widetilde{R}\,, \qquad z_v = \frac{(1-\eta)\sqrt{1+\tilde{z}_m^2}}{2\tilde{z}_m\sqrt{\eta}}\,\widetilde{R}\,, \tag{2.47}$$

where $\widetilde{R}$ is the radius of the two equal disjoint disks written above and $\tilde{z}_m$ is a function of η (see (2.31) and (2.34)). In Fig. 2.13 we show two examples of minimal surfaces constructed with Surface Evolver which provide the holographic mutual information of two equal disjoint disks. Considering the section of these surfaces through a vertical plane which is orthogonal to the boundary and to the line passing through the centers of the disks, we find a good agreement with (2.47).

As for the finite part of the area, once η and β have been written in terms of $\tilde{\eta}$ and $\tilde{\delta}$ by inverting (2.42) and (2.43), the limit $\varepsilon \to 0$ of either $\Delta\mathcal{A}$ or $\mathcal{I}_{A_1,A_2}$ (depending on whether the final disks are either overlapping or disjoint respectively) is given by the r.h.s. of (2.39), where $\kappa = \kappa(\eta)$ is obtained through the numerical inversion of (2.34), being $\eta = \eta(\tilde{\delta}, \tilde{\eta})$ found above.

The special case of two equal disjoint disks corresponds to $\tilde{\eta} = 1$ and $\tilde{\delta} = (1+\eta)/\sqrt{\eta}$, and therefore the limit $\varepsilon \to 0$ of $\mathcal{I}_{A_1,A_2}$ depends only on the parameter $\tilde{\delta}$, as expected. The relation $\tilde{\delta} = (1+\eta)/\sqrt{\eta}$ can be used to find the critical distance d_c between the centers beyond which the holographic mutual information vanishes and also the distance $d_* > d_c$ beyond which the connected surface does not exist anymore. They correspond to η_c and η_* respectively and, in particular, one gets $\tilde{\delta}_c = 2.192$ and $\tilde{\delta}_* = 2.256$.

In order to check that the surfaces obtained through (2.40) are local minima of the area functional, one can compare the analytic results found as explained above against the corresponding surfaces constructed by Surface Evolver. In Fig. 2.14 we have performed this check for a section profile: the black dots come from the surface obtained as in the bottom right panel of Fig. 2.12 (notice that the black dots reach $z = 0$), while the red curve is the section of the corresponding surface constructed by Surface Evolver (see also the red curves in Fig. 2.10 for a similar construction with different A). In Fig. 2.15 we have performed another comparison between the analytic expressions and the numerical data of Surface Evolver by computing the holographic mutual information of a domain A made by two equal disjoint disks. The black triangles have been found by mapping the black curve for the annulus in the right panel of Fig. 2.11 (which is given by the r.h.s. of (2.39)) through $\eta = \eta(\tilde{\delta})$ found above. The agreement with the corresponding data obtained with Surface Evolver (red curve) is very good. Notice that, as already observed for the annulus in 2.3.1.1, also in this case Surface Evolver finds a surface which is a local minimum of the area functional, even if it is not the global minimum. Let us conclude by emphasizing that, while this numerical method is very efficient in finding surfaces which are local minima for the area functional when they exist, it is not suitable for studying the existence of a surface with a given topology.

2.3.2 Other shapes

In 2.3.1.2 we have considered the holographic mutual information of two disjoint circular domains, for which analytic results are available. When $A = A_1 \cup A_2$ is not made by two disjoint disks, analytic results for the corresponding holographic mutual information are not known and therefore a numerical approach could be very useful. Here we employ Surface Evolver to study $\mathcal{I}_{A_1,A_2}$ (defined in (2.28)) of disjoint regions delimited by some of the smooth curves introduced in 2.2.1.

The holographic mutual information of non circular domains depends on the geometries of their boundaries, on their distance and also on their relative orientation. Independently of the shapes of ∂A_1 and ∂A_2, once the domains and their relative orientation have been fixed, the holographic mutual information vanishes when the distance between A_1 and A_2 is large enough. The critical distance d_c beyond which $\mathcal{I}_{A_1,A_2} = 0$ depends on the configuration of the domains. This transition occurs because, for a generic distance d between the centers of A_1 and A_2, the global minimal area surface comes from a competition between a connected surface anchored on ∂A and a configuration made by two disconnected surfaces spanning ∂A_1 and ∂A_2, which are both local minima. Beyond the critical distance between the centers, the disconnected configuration becomes the global minimum and therefore $\mathcal{I}_{A_1,A_2}$ vanishes.

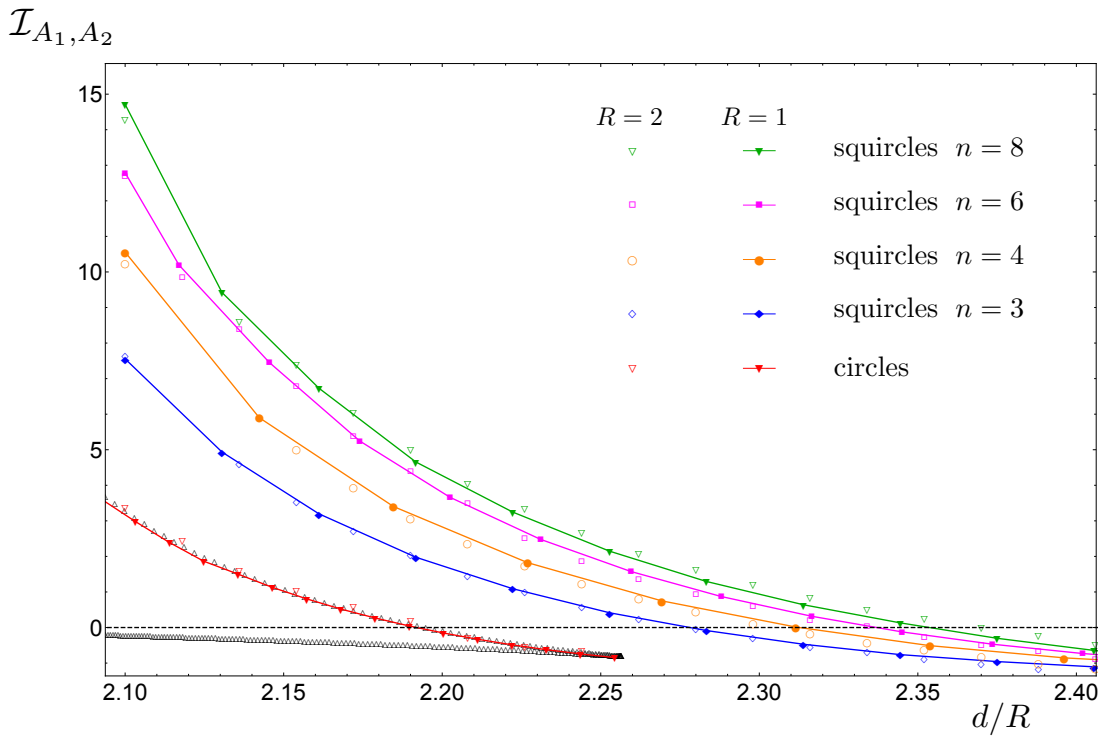

Figure 2.15: Holographic mutual information of two disjoint and equal domains delimited by squircles for various n. The coloured points are the numerical data obtained with Surface Evolver, while the black triangles correspond to the solid black curve of Fig. 2.11 (right panel) mapped through the transformation (2.43) with $\beta^2 = \eta$. The transition between the connected surface and the configuration of disconnected surfaces occurs at the zero of each curve. A point having $\mathcal{I}_{A_1,A_2} < 0$ corresponds to a connected surface which is a local minimum of the area functional but it is not the global minimum for the corresponding entangling curve.

In Fig. 2.10 we show an example of a connected surface constructed with Surface Evolver where ∂A is made by two equal and disjoint ellipses at $z = 0$. Let us recall that in our numerical analysis we have regularized the area by defining ∂A at $z = \varepsilon$, as discussed in B.2. In the figure, we have highlighted two sections of the surface suggested by the symmetry of this configuration of domains, which are given by the red curves and by the green one.

We have constructed minimal area connected surfaces also for configurations of equal disjoint domains with other shapes and in Fig. 2.14 we have reported the corresponding curves obtained from the section giving the red curves in Fig. 2.10. The red curves in Fig. 2.14 are associated with circular domains and they can be recovered analytically (black dots), as explained in 2.3.1.2. Instead, for the remaining curves analytic expressions are not available and therefore they provide a useful benchmark for analytic results that could be found in the future.

Besides the profiles for various sections, Surface Evolver computes also the area of the surfaces that it constructs. Considering a configuration of disjoint domains with given shapes and relative orientation, we can compute $\mathcal{I}_{A_1,A_2}$ while the distance d between their centers changes. In Fig. 2.15 we show the results of this analysis when ∂A_1 and ∂A_2 are squircles (i.e. (2.15) with $R_1 = R_2 \equiv R$). As for their relative orientation, drawing the squares that circumscribe ∂A_1 and ∂A_2, their edges are parallel. Since $\mathcal{I}_{A_1,A_2} \geqslant 0$, the critical distance d_c corresponds to the zero of the various curves and $\mathcal{I}_{A_1,A_2}$ vanishes for $d \geqslant d_c$. Thus, $\mathcal{I}_{A_1,A_2}$ is continuos with a discontinuous first derivative at $d = d_c$. The points found numerically which have $\mathcal{I}_{A_1,A_2} < 0$ correspond to connected surfaces that Surface Evolver constructs but they are not the global minimum for the area functional because the disconnected configuration is favoured for that distance.

Once the relative orientation has been chosen, a configuration of two equal and disjoint squircles is completely determined by two parameters: the distance d between the centers and the size R of the squircles. Instead, when A_1 and A_2 are two equal two dimensional spherocylinders or equal domains

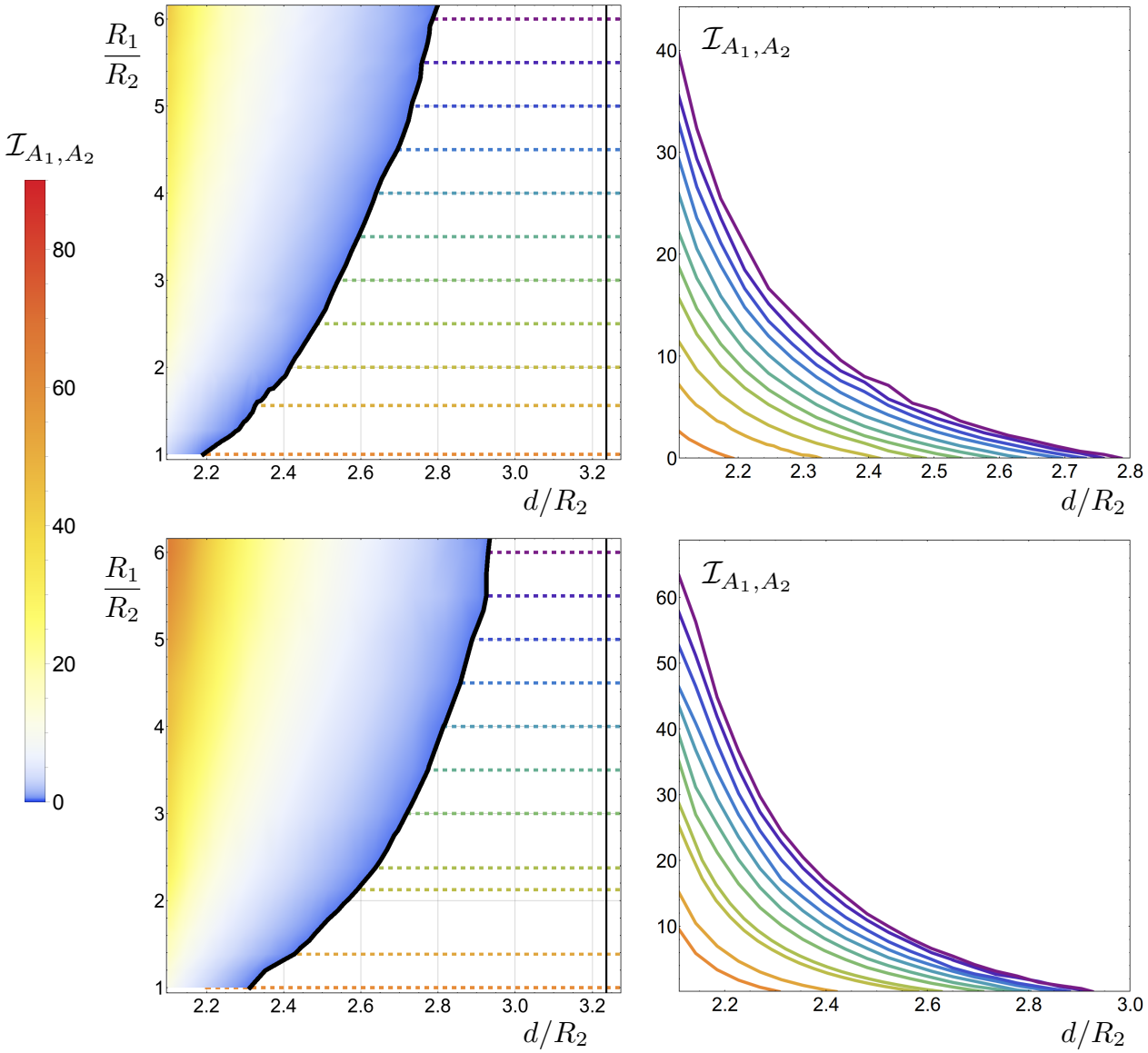

Figure 2.16: Holographic mutual information of two equal and disjoint domains delimited by ellipses (top panels) or superellipses with $n = 4$ (bottom panels), which are defined by R_1 and R_2 (see the bottom panel of Fig. 2.1 and (2.15)), while d is the distance between their centers. The relative orientation is like in Fig. 2.10. Left panels: Density plots for $\mathcal{I}_{A_1,A_2}$ whose zero provides the corresponding transition curve (solid black line) in the plane $(d/R_2, R_1/R_2)$. The straight vertical line indicates the transition when A is made by two equal and disjoint infinite strips whose width is $2R_2$ and the distance between their central lines is d. Right panels: $\mathcal{I}_{A_1,A_2}$ in terms of d/R_2 for various fixed values of R_1/R_2 indicated by the horizontal dashed lines in the corresponding left panel, with the same color code. The lower curves (orange) in the right panels correspond to the squircles ($R_1 = R_2$) with $n = 2$ (top) and $n = 4$ (bottom) and therefore they reproduce the red and orange curves in Fig. 2.15 respectively. The data reported here have been found with $R_2 = 1$ and some checks have been done also with $R_2 = 2$.

delimited by two disjoint superellipses and the relative orientation has been chosen, we have three parameters to play with: the distance d between the centers and the parameters R_1 and R_2 which specify the two equal domains (see the bottom panel of Fig. 2.1). In Fig. 2.16 we show $\mathcal{I}_{A_1,A_2}$ for two disjoint domains delimited by ellipses and superellipses with $n = 4$, whose relative orientation is like in Fig. 2.10. In the left panels, the black thick curve is the transition curve along which the holographic mutual information vanishes, while the continuos straight line identifies the transition value corresponding to

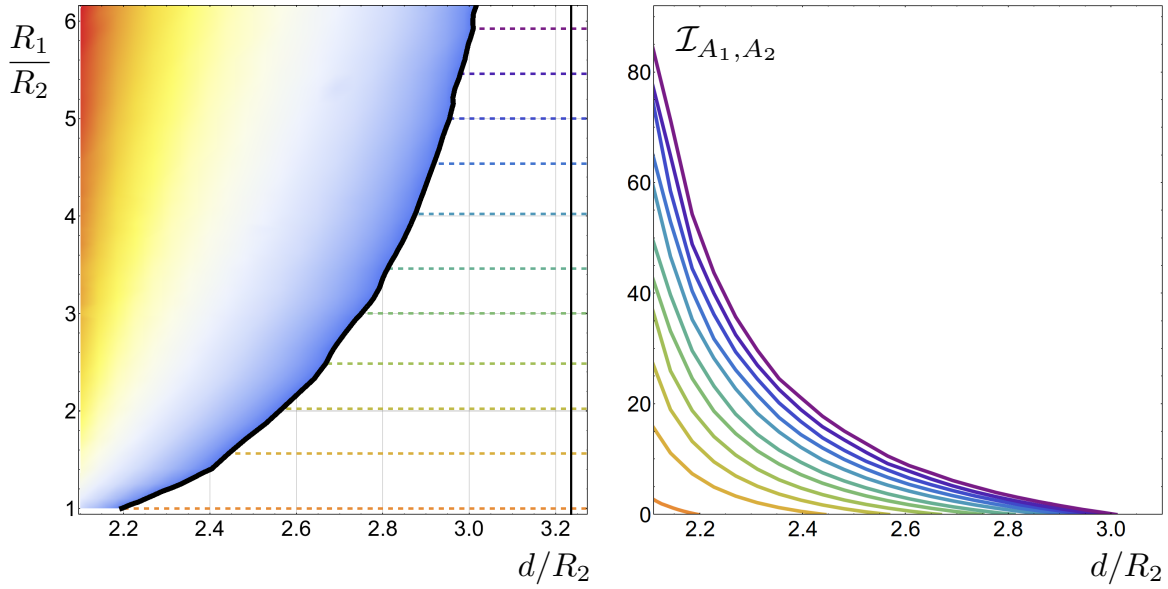

Figure 2.17: Holographic mutual information of two equal and disjoint two dimensional spherocylinders oriented like the two ellipses in Fig. 2.10. The parameters R_1 and R_2 specify the domains (see the bottom panel of Fig. 2.1 and (2.16)) and d is the distance between their centers. The same notation and color coding of Fig. 2.16 has been adopted.

two disjoint infinite strips [104]. Comparing the transition curve in the top left panel with the one in the bottom left panel, it is evident that the one associated with the superellipses having $n = 4$ is closer to the value corresponding to the infinite strips than the one associated with the ellipses. In Fig. 2.17 we study $\mathcal{I}_{A_1,A_2}$ for a domain A made by two equal and disjoint two dimensional spherocylinders. In this case the transition curve is closer to the line corresponding to the transition for two infinite strips with respect to the transition curves of Fig. 2.16. Nevertheless, from our data we cannot conclude that the transition curve for the two dimensional spherocylinders approaches the value corresponding to the infinite strips as $R_1/R_2 \to \infty$. It would be interesting to have further data and some analytic argument to understand whether some bounds prevent the transition curves to approach the value associated with the infinite strips for $R_1/R_2 \to \infty$. Let us remark that the lowest curves (orange) in the right panels of Figs. 2.16 and 2.17 correspond to disjoint squircles with $n = 2$ (i.e. circles) or $n = 4$ and therefore they reproduce the red and the orange curves of Fig. 2.15. Configurations of domains having smaller values of d than the ones shown in the plots provide unstable numerical results.

By employing Surface Evolver, we could also study the holographic mutual information of disjoint domains whose boundaries contain corners. In particular, one could take both A_1 and A_2 bounded by polygons, but also A_1 bounded by a smooth curve and A_2 by a polygon. In Fig. 2.18 we show the minimal area surfaces corresponding to ∂A made by two equal and disjoint squares having different relative orientation. As discussed in 2.2.2, when ∂A has vertices a further logarithmic divergence occurs after the area law term in the $\varepsilon \to 0$ expansion (see (2.5)). If the coefficient of the logarithmic divergence in (2.5) is additive, i.e. $B_{A_1 \cup A_2} = B_{A_1} + B_{A_2}$ for two disjoint regions, then the holographic mutual information is finite. An expression like (2.18) with the sum extended over the vertices of both the components of ∂A is additive, leading to a finite $\mathcal{I}_{A_1,A_2}$. Also for these cases we could find plots similar to Figs. 2.16 and 2.17 but the curves would not be suitable for a comparison with an analytic formula because of the regularization procedure that we have adopted. Indeed, in our numerical computations ∂A is defined at $z = \varepsilon$ and this regularization affects the $O(1)$ term in (2.5) [119], as already mentioned in the closing part of 2.2.2.

Summarizing, in this Chapter we have studied the area of the minimal surfaces in AdS_4 occurring in the computation of the holographic entanglement entropy and of the holographic mutual information,

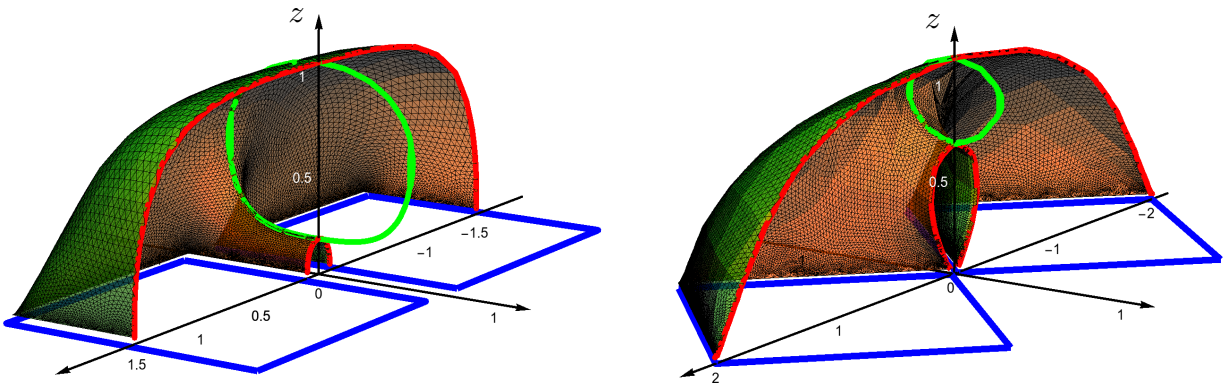

Figure 2.18: Minimal surfaces obtained with Surface Evolver for a domain $A = A_1 \cup A_2$ made by the interior of two disjoint and equal squares. All the squares have the same size but the relative orientation of A_1 and A_2 is different in the two panels.

focussing on their dependence on the shape of the entangling curve ∂A in the boundary of AdS_4.

Our approach is numerical and the main tool we have employed is the program Surface Evolver, which allows to construct triangulated surfaces approximating a surface anchored on a given curve ∂A which is a local minimum of the area functional. We have computed the holographic entanglement entropy and the holographic mutual information for entangling curves given by (or made by the union of) ellipses, superellipses or the boundaries of two dimensional spherocylinders, for which analytic expressions are not known. We have also obtained the transition curves for the holographic mutual information of disjoint domains delimited by some of these smooth curves (see Figs. 2.15, 2.16 and 2.17), providing a solid numerical benchmark for analytic expressions that could be found in future studies. We focused on these simple examples, but the method can be employed to address more complicated domains.

Besides the fact that the surfaces constructed by Surface Evolver are triangulated, a source of approximation in our numerical analysis is the way employed to define the curve spanning the minimal surface. Indeed, once the cut-off $\varepsilon > 0$ in the holographic direction has been introduced to regularize the area of the surfaces, the numerical data have been found by defining ∂A at $z = \varepsilon$. It would be interesting to understand better this regularization with respect to some other ones and also to decrease ε in a stable and automatically controlled way in order to get numerical data which provide better approximations of the analytic results.

Chapter 3

Time-dependent hvLif backgrounds

One of the interesting questions regarding quantum information is how fast quantum correlations can propagate in a physical system. In a groundbreaking study in 1972, Lieb and Robinson [123] derived an upper bound for the speed of propagation of correlations in an interacting lattice system and in recent years there has been growing interest in this and related questions in connection with a number of new advances. The study of ultracold atom systems has developed to the level where experiments on the time evolution of quantum correlations are possible (see e.g. [124]), new techniques have been developed for the theoretical study of time evolution of observables in perturbed quantum lattices (see e.g. [125]), analytical results have been obtained for the time evolution of observables after quenches in conformal field theory [42–44] and entanglement entropy has been given a geometric interpretation [46, 47, 51, 126] in the context of the holographic duality of strongly interacting conformal field theory [2].

In the context of holographic duality, different ways of introducing quenches in a conformal theory have been studied. One line of work focuses on constructing holographic duals for quenches in strongly coupled theories [127–131], in the spirit of similar work in weakly coupled quantum field theory involving a sudden change in the parameters of the Hamiltonian [42–44, 132–135]. In another approach, the focus has instead been on perturbing the state of the system by turning on homogeneous sources for a short period of time. By a slight abuse of terminology, this process has also been called a "quench", although perhaps a "homogenous explosion" would be a closer term to describe the sudden change in the state of the boundary theory. There are two good reasons to study this model. One of them is that there is an elegant and tractable gravitational dual description of such a process in terms of the gravitational collapse of a thin shell of null matter to a black hole, the AdS-Vaidya geometry. The other good reason is that the time evolution of quantum correlations manifested in the holographic entanglement entropy following such an explosion was found to behave in the same manner as in the 1+1 dimensional conformal field theory work [42–44] – in a relativistic case quantum correlations were found to propagate at the speed of light [66–70, 136–139]. The interesting lesson there is that even a strongly coupled conformal theory with no quasiparticle excitations may behave as if the correlations were carried by free-streaming particles. The model also allows for an easy extrapolation of the results to higher dimensional field theory at strong coupling. In generic dimensions, it turns out that the time evolution of holographic entanglement entropy has a more refined structure, characterized by different scaling regimes [140, 141]: (I) a pre-local equilibrium power law growth in time, (II) a post-local equilibration linear growth in time, (III) a saturation regime. For entanglement surfaces of more general shape, one can also identify late-time memory loss, meaning that near saturation the time-evolution becomes universal with no memory on the detailed shape of the surface.

Many condensed matter and ultracold atom systems feature more complicated critical behavior with anisotropic (Lifshitz) scaling [142], characterized by the dynamic critical exponent $\zeta > 1$, or hyperscaling violation characterized by a non-zero hyperscaling violation exponent θ [78, 80, 143]. Hyperscaling violation leads to an effective dimension $d_\theta = d - \theta$. It was found that for a critical value $d_\theta = 1$ the entanglement entropy exhibits a logarithmic violation from the usual area law [79], which is also generic for compressible states with hidden Fermi surfaces [75–77, 144].

By now there exist various holographic dual models for critical points involving Lifschitz scaling and hyperscaling violation [78–80, 143, 145–161]. In the light of the rich scaling structure in the time evolution of entanglement entropy, it is interesting to see how it carries over to systems with Lifshitz

scaling and hyperscaling violation. In [162] a Lifshitz scaling generalization of the AdS-Vaidya geometry was constructed, and it was found that time evolution of entanglement entropy still contains a linear regime, where entanglement behaves as if it was carried by free streaming particles at finite velocity. This is non-trivial, since in the non-relativistic case $\zeta > 1$ there is no obvious characteristic scale like the speed of light in relativistic theories. The authors of [140, 141], on the other hand, considered a relativistic system with hyperscaling violation, and found that their previous analysis easily carries over to that case, with the spatial dimension d replaced by the effective dimension d_θ. In this Chapter we extend the analysis to systems that exhibit both Lifshitz scaling and hyperscaling violation. We do this by first constructing the extension of the Lifshitz-AdS-Vaidya geometry to the hyperscaling violating case, and then analyzing the time evolution of the entanglement entropy for various boundary regions. We compute numerically the evolution of the holographic entanglement entropy for the strip and the sphere in backgrounds with non-trivial ζ and θ. We then extract some analytic behavior in the thin shell limit for the temporal regimes (I), (II) and (III), generalizing the results of [140, 141] to the case of $\zeta \neq 1$ and $\theta \neq 0$. In Appendix C.4, we also consider briefly quench geometries where the critical exponents themselves are allowed to vary. This can be motivated from a quasiparticle picture and one could, for instance, consider a system where the dispersion relation is suddenly altered from $\omega \sim k^2 + \cdots$ to $\omega \sim k + \cdots$ or vice versa, by rapidly adjusting the chemical potential. We take some steps in this direction by considering holographic geometries where the dynamical critical exponent and the hyperscaling violation parameter are allowed to vary with time and show that such solutions can be supported by matter satisfying the null energy condition, at least in some simple cases. We leave a more detailed study for future work.

This Chapter is organized as follows. Hyperscaling violating Lifshitz-AdS-Vaidya solutions are introduced in Section 3.1 and parameter regions allowed by the null energy condition determined. In Section 3.2 the holographic entanglement entropy for a strip and for a sphere is analyzed in static backgrounds and Vaidya-type backgrounds are considered in Section 3.3. In Section 3.4 scaling regions in the time evolution of the entanglement entropy are studied for differently shaped surfaces. The details of some of the computations are presented in appendices C along with a brief description of holographic quench geometries where the hyperscaling violation parameter and the dynamical critical exponent are allowed to vary with time.

3.1 Backgrounds with Lifshitz and hyperscaling exponents

The starting point of our analysis is the following gravitational action [162]

$$S = \frac{1}{16\pi G_N}\int\left(R - \frac{1}{2}(\partial\phi)^2 - V(\phi) - \frac{1}{4}\sum_{i=1}^{N_F} e^{\lambda_i\phi}F_i^2\right)\sqrt{-g}\,d^{d+2}x\,, \tag{3.1}$$

which describes the interaction between the metric $g_{\mu\nu}$, N_F gauge fields and a dilaton ϕ. The simplest $d+2$ dimensional time independent background including the Lifshitz scaling ζ and the hyperscaling violation exponent θ is given by equation (1.36) (see also [78, 80, 143])

$$ds^2 = z^{-2d_\theta/d}(-z^{2-2\zeta}dt^2 + dz^2 + dx_i^2)\,, \tag{3.2}$$

where $z > 0$ is the holographic direction and the cartesian coordinates x_i parameterize $\mathbb{R}^d$. Hereafter the metric (3.2) will be referred as hvLif. In (3.2) we have introduced the convenient combination

$$d_\theta \equiv d - \theta\,. \tag{3.3}$$

When $\theta = 0$ and $\zeta = 1$, (3.2) reduces to AdS_{d+2} in Poincaré coordinates.

In the following, we will consider geometries that are asymptotic to the hyperscaling violating Lifshitz (hvLif) space-time (3.2). In particular, static black hole solutions with Lifshitz scaling and hyperscaling violation have been studied in [78, 158, 159]. The black hole metric is

$$ds^2 = z^{-2d_\theta/d}\left(-z^{2-2\zeta}F(z)dt^2 + \frac{dz^2}{F(z)} + dx_i^2\right)\,, \tag{3.4}$$

where the emblackening factor $F(z)$, which contains the mass M of the black hole, is given by

$$F(z) = 1 - Mz^{d_\theta+\zeta}\,. \tag{3.5}$$

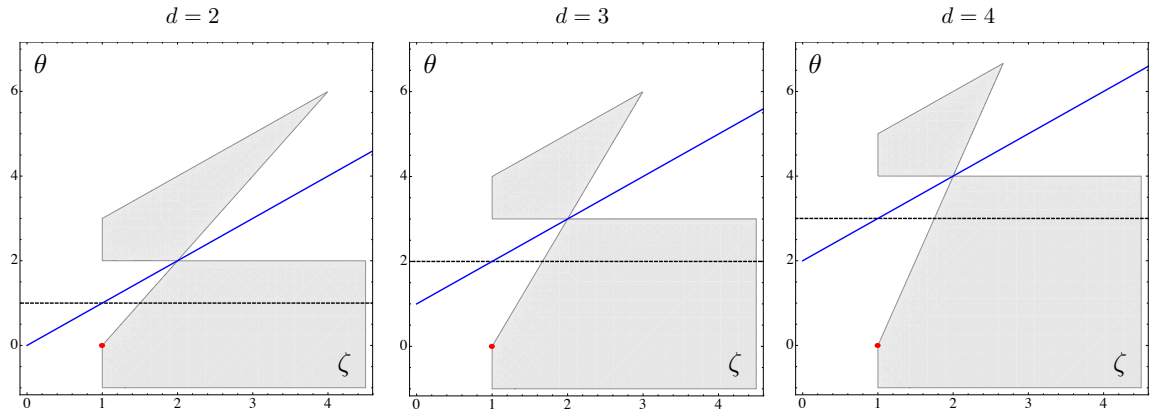

Figure 3.1: The grey area is the region of the (ζ, θ) plane defined by (3.7) and (3.8), obtained from the Null Energy Condition, and also (3.6). The panels show $d = 2, 3, 4$. The red dots denote AdS_{d+2} and the horizontal dashed lines indicate the critical value $\theta = d - 1$. The blue lines denote the upper bound defined by the condition (3.86).

The position z_h of the horizon is defined as $F(z_h) = 0$ and the standard near horizon analysis of (3.4) provides the temperature of the black hole $T = z_h^{1-\zeta}|F'(z_h)|/(4\pi)$. In order to have $F(z) \to 1$ when $z \to 0$, we need to require

$$d_\theta + \zeta \geqslant 0\,. \tag{3.6}$$

The Einstein equations are $G_{\mu\nu} + g_{\mu\nu}\Lambda = T_{\mu\nu}$, where $G_{\mu\nu}$ is the Einstein tensor and $T_{\mu\nu}$ the energy-momentum tensor of the matter fields, *i.e.* the dilaton and gauge fields in (3.1). The Null Energy Condition (NEC) prescribes that $T_{\mu\nu}N^\mu N^\nu \geqslant 0$ for any null vector N^μ. On shell, the NEC becomes $G_{\mu\nu}N^\mu N^\nu \geqslant 0$ and, through an astute choice of N^μ, one finds [78]

$$d_\theta(\zeta - 1 - \theta/d) \geqslant 0\,, \tag{3.7}$$

$$(\zeta - 1)(d_\theta + \zeta) \geqslant 0\,. \tag{3.8}$$

In the critical case $\theta = d - 1$, they reduce to $\zeta \geqslant 2 - 1/d$. In Fig. 3.1 we show the region identified by (3.7) and (3.8) in the (ζ, θ) plane.

In order to construct an infalling shell solution, it is convenient to write the static metric (3.4) in an Eddington-Finkelstein-like coordinate system, by introducing a new time coordinate v through the relation

$$dv = dt - \frac{dz}{z^{1-\zeta}F(z)}\,, \tag{3.9}$$

and rewriting (3.4) as

$$ds^2 = z^{-2d_\theta/d}(-z^{2(1-\zeta)}F(z)dv^2 - 2z^{1-\zeta}\,dv\,dz + dx_i^2)\,. \tag{3.10}$$

The dynamical background that we are going to consider is of Vaidya type [64, 65] and it is obtained by promoting the mass M in (3.10) to a time dependent function $M(v)$, namely

$$ds^2 = z^{-2d_\theta/d}(-z^{2(1-\zeta)}F(v,z)dv^2 - 2z^{1-\zeta}\,dv\,dz + dx_i^2)\,, \tag{3.11}$$

where

$$F(v,z) = 1 - M(v)z^{d_\theta+\zeta}\,. \tag{3.12}$$

The metric (3.11) with the emblackening factor (3.12) is a solution of the equation of motion $G_{\mu\nu} = T_{\mu\nu}$, where the energy-momentum tensor is given by the one of the static case with M replaced by $M(v)$, except for the component T_{vv}, which now contains the following additional term

$$\tilde{T}_{vv} = \frac{d_\theta}{2}\,z^{d_\theta}M'(v)\,. \tag{3.13}$$

Now consider the null vectors $N^\mu = (N^v, N^z, \boldsymbol{N}^{x_i})$ given by

$$N^\mu_{\rm I} = (0,1,\mathbf{0})\,, \qquad N^\mu_{\rm II} = \left(-\frac{2z^{\zeta-1}}{F(v,z)},1,\mathbf{0}\right)\,, \qquad N^\mu_{\rm III} = \left(\pm\frac{z^{\zeta-1}}{\sqrt{F(v,z)}},0,\boldsymbol{n}_1\right)\,, \tag{3.14}$$

where $\boldsymbol{n}_1$ is a $d-1$ dimensional vector with unit norm. The NEC for the vectors (3.14) leads to the following inequalities

$$d_\theta(\zeta-1-\theta/d) \;\geqslant\; 0\,, \tag{3.15}$$

$$d_\theta\left[(\zeta-1-\theta/d)F^2 - 2z^\zeta F_v\right] \;\geqslant\; 0\,, \tag{3.16}$$

$$2(\zeta-1)(d_\theta+\zeta)F^2 + [zF_{zz} - (d_\theta+3(\zeta-1))F_z]zF - z^\zeta d_\theta F_v \;\geqslant\; 0\,, \tag{3.17}$$

where the notation $F_z \equiv \partial_z F$, $F_v \equiv \partial_v F$ and $F_{zz} \equiv \partial_z^2 F$ has been adopted. When $F(v,z)=1$ identically, (3.16) and (3.17) simplify to (3.7) and (3.8) respectively. Plugging 3.12 into (3.16) and (3.17), we get

$$d_\theta\big[\,(\zeta-1-\theta/d)(1-M(v)z^{d_\theta+\zeta})^2 + 2z^{d_\theta+2\zeta}M'(v)\big] \;\geqslant\; 0\,, \tag{3.18}$$

$$2(\zeta-1)(d_\theta+\zeta)(1-M(v)z^{d_\theta+\zeta}) + z^{d_\theta+2\zeta}d_\theta M'(v) \;\geqslant\; 0\,. \tag{3.19}$$

In the special case of $\theta=0$ and $\zeta=1$ we recover the condition $M'(v)\geqslant 0$, as expected. Notice that the NEC for the AdS-Vaidya backgrounds modeling the formation of an asymptotically AdS charged black hole also leads to a non trivial constraint [163], similar to the ones in (3.18) and (3.19).
Here we will choose the following profile for $M(v)$

$$M(v) = \frac{M}{2}\big(1+\tanh(v/a)\big)\,, \tag{3.20}$$

which is always positive and increasing with v. It goes to 0 when $v\to-\infty$ and to M when $v\to+\infty$. The parameter $a>0$ encodes the rapidity of the transition between the two regimes of $M(v)\sim 0$ and $M(v)\sim M$. In the limit $a\to 0$ the mass function becomes a step function $M(v)=M\theta(v)$. This is the thin shell regime and it applies to many of the calculations presented below. We have checked numerically that the profiles (3.20) that we employ satisfy the inequalities (3.18) and (3.19) for all v and z.

3.2 Holographic entanglement entropy for static backgrounds

3.2.1 Strip

Let us briefly review the simple case when the region A in the boundary theory is a thin long strip, which has two sizes $\ell \ll \ell_\perp$ [46, 47, 78]. Denoting by x the direction along the short length and by y_i the remaining ones, the domain in the boundary is defined by $-\ell/2\leqslant x\leqslant \ell/2$ and $0\leqslant y_i\leqslant \ell_\perp$, for $i=1,\ldots,d-1$. Since $\ell\ll\ell_\perp$, we can assume translation invariance along the y_i directions and this implies that the minimal surface is completely specified by its profile $z=z(x)$, where $z(\pm\ell/2)=0$. We can also assume that $z(x)$ is even. Computing from (3.4) the induced metric on such a surface, the area functional reads

$$\mathcal{A}[z(x)] = 2\ell_\perp^{d-1}\int_0^{\ell/2}\frac{1}{z^{d_\theta}}\sqrt{1+\frac{z'^2}{F\,(z)}}\,dx\,. \tag{3.21}$$

Since the integrand does not depend on x explicitly, the corresponding integral of motion is constant giving a first order equation for the profile

$$z' = -\sqrt{F(z)\big[(z_*/z)^{2d_\theta}-1\big]}\,. \tag{3.22}$$

Here we have introduced $z(0)\equiv z_*$ and we have used that $z'(0)=0$ and $z'(x)<0$. Plugging (3.22) into (3.21), it is straightforward to find that the area of the extremal surface is

$$\mathcal{A} = 2\ell_\perp^{d-1}z_*^{d_\theta}\int_0^{\ell/2-\eta} z(x)^{-2d_\theta}dx = 2\ell_\perp^{d-1}\int_\epsilon^{z_*}\frac{z_*^{d_\theta}}{z^{d_\theta}\sqrt{F(z)\big[z_*^{2d_\theta}-z^{2d_\theta}\big]}}\,dz\,, \tag{3.23}$$

with $z(x)$ a solution of (3.22). A cutoff $z \geqslant \epsilon > 0$ has been introduced to render the integral (3.23) finite, and a corresponding one along the x direction

$$z(\ell/2 - \eta) = \epsilon \,. \tag{3.24}$$

The relation between z_* and ℓ reads

$$\frac{\ell}{2} = \int_0^{z_*} \frac{dz}{\sqrt{F(z)\big[(z_*/z)^{2d_\theta} - 1\big]}} \,. \tag{3.25}$$

The vacuum case of $F(z) = 1$ can be solved analytically. Indeed, one can then integrate (3.22), obtaining

$$x(z) = \frac{\ell}{2} - \frac{z_*}{1+d_\theta}\left(\frac{z}{z_*}\right)^{d_\theta+1} {}_2F_1\left(\frac{1}{2}, \frac{1}{2} + \frac{1}{2d_\theta}; \frac{3}{2} + \frac{1}{2d_\theta}; (z/z_*)^{2d_\theta}\right), \tag{3.26}$$

where ${}_2F_1$ is the hypergeometric function. Imposing $x(z_*) = 0$ in (3.26) one finds

$$\frac{\ell}{2} = \frac{\sqrt{\pi}\,\Gamma(\frac{1}{2} + \frac{1}{2d_\theta})}{\Gamma(\frac{1}{2d_\theta})}\, z_* \,. \tag{3.27}$$

The area (3.23) with $F(z) = 1$ is then [78]

$$\mathcal{A} = \begin{cases} \dfrac{2\ell_\perp^{d-1}}{d_\theta - 1}\left[\dfrac{1}{\epsilon^{d_\theta - 1}} - \dfrac{1}{\ell^{d_\theta - 1}}\left(\dfrac{\sqrt{\pi}\,\Gamma(\frac{1}{2} + \frac{1}{2d_\theta})}{\Gamma(\frac{1}{2d_\theta})}\right)^{d_\theta}\right] + O\left(\epsilon^{1+d_\theta}\right) & d_\theta \neq 1 \\ 2\ell_\perp^{d-1}\log(\ell/\epsilon) + O\left(\epsilon^2\right) & d_\theta = 1 \end{cases} \tag{3.28}$$

The critical value $d_\theta = 1$ is characterized by this divergence, which is logarithmic instead of power-like.

3.2.2 Sphere

If the perimeter between the two regions in the boundary theory is a $d-1$ dimensional sphere of radius R it is convenient to adopt spherical coordinates in the bulk (we denote by ρ the radial coordinate) for $\mathbb{R}^d$ in (3.2) and (3.4), namely $dx_i^2 = d\rho^2 + \rho^2 d\Omega_{d-1}^2$. In this case, the problem reduces to computing $z = z(\rho)$. The area functional reads

$$\mathcal{A}[z(\rho)] = \frac{2\pi^{d/2}}{\Gamma(d/2)} \int_0^R \frac{\rho^{d-1}}{z^{d_\theta}} \sqrt{1 + \frac{z'^2}{F(z)}}\, d\rho \,, \tag{3.29}$$

where the factor in front of the integral is the volume of the $d-1$ dimensional unit sphere. The key difference compared to the strip (see (3.21)) is that now the integrand of (3.29) depends explicitly on ρ and one has to solve a second order ODE to find the $z(\rho)$ profile,

$$z\big[\rho F_z - 2(d-1)z'\big]z'^2 - 2F\big[\rho\, z\, z'' + (d-1)z\, z' + d_\theta \rho\, z'^2\big] - 2d_\theta \rho F^2 = 0 \,, \tag{3.30}$$

subject to the boundary conditions $z(R) = 0$ and $z'(0) = 0$. For a trivial emblackening factor $F(z) = 1$ the equation of motion (3.30) simplifies to

$$\rho\, z\, z'' + \big[d_\theta \rho + (d-1)z\, z'\big]\big(1 + z'^2\big) = 0 \,. \tag{3.31}$$

In the absence of hyperscaling violation ($\theta = 0$) it is well known that $z(\rho) = \sqrt{R^2 - \rho^2}$ describes an extremal surface for any dimension d [46]. Since the extremal surface is computed for $t = $ const., the Lifshitz exponent ζ does not enter in the computation but equation (3.31) does involve the hyperscaling exponent through the effective dimension d_θ. The extremal surface cannot be found in closed form for general values of $d_\theta \neq 0$ but the leading behavior of the extremal surface area, including the UV divergent part, can be obtained from the small z asymptotics when $\rho = R$ is approached from below. We find it convenient to rewrite (3.31) in terms of a dimensionless variables $z = R\,\tilde{z}(x)$, $\rho = R(1-x)$,

$$(1-x)\tilde{z}\ddot{\tilde{z}} + \big[d_\theta(1-x) - (d-1)\tilde{z}\dot{\tilde{z}}\big]\big(1 + \dot{\tilde{z}}^2\big) = 0 \,, \tag{3.32}$$

where $\dot{\tilde{z}}$ denotes $d\tilde{z}/dx$.
In the appendix §C.1 we construct a sequence of parametric curves $\{x_i(s), \tilde{z}_i(s)\}$ for $i \in \mathbb{N}$ such that the asymptotic one $\{x_\infty(s), \tilde{z}_\infty(s)\}$ solves (3.32). These curves are obtained in order to reproduce the behavior of the solution near the boundary (i.e. small x) in a better way as the index i increases. Unfortunately, when i is increasing, their analytic expressions become difficult to integrate to get the corresponding area. Nevertheless, we can identify the following pattern. Given an integer $k_0 \geqslant 0$, which fixes the order in ϵ that we are going to consider, the procedure described in C.1 leads to the following expansion for the area (3.29)

$$\mathcal{A}[z(\rho)] \,=\, \frac{2\pi^{d/2}R^{d-1}}{\Gamma(d/2)\,\epsilon^{d_\theta-1}}\left\{\sum_{k=0}^{k_0}\omega_k(d,d_\theta)\left(\frac{\epsilon}{R}\right)^{2k}+O\big(\epsilon^{2(k_0+1)}\big)\right\}, \qquad d_\theta \neq \{1,3,5,\ldots,2k_0+1\}\,, \tag{3.33}$$

where

$$\omega_k(d,d_\theta) \equiv \frac{\gamma_{2k}(d,d_\theta)}{\prod_{j=0}^{k}\big[d_\theta-(2j+1)\big]^{\alpha_{k,j}}}\,, \qquad \alpha_{k,j}\in\mathbb{N}\setminus\{0\}\,. \tag{3.34}$$

The coefficients $\gamma_{2k}(d,d_\theta)$ should be found by explicit integration. For $k=0$, we get $\gamma_0(d,d_\theta)=1/(d_\theta-1)$. The peculiar feature of the values of d_θ excluded in (3.33) is the occurrence of a logarithmic divergence, namely, for $0\leqslant\tilde{k}\leqslant k_0$ we have

$$\mathcal{A}[z(\rho)] \,=\, \frac{2\pi^{d/2}R^{d-1}}{\Gamma(d/2)\,\epsilon^{2\tilde{k}}}\left\{\sum_{k=0}^{\tilde{k}-1}\omega_k(d,d_\theta)\left(\frac{\epsilon}{R}\right)^{2k}+\beta_{2\tilde{k}}(d,d_\theta)\left(\frac{\epsilon}{R}\right)^{2\tilde{k}}\log(\epsilon/R)+O\big(\epsilon^{2\tilde{k}}\big)\right\}, \quad d_\theta=2\tilde{k}+1\,. \tag{3.35}$$

In C.1.1 the result for $i=2$ is discussed and it gives (see C.1.1.1)

$$\mathcal{A}[z(\rho)] \,=\, \begin{cases} \dfrac{2\pi^{d/2}R^{d-1}}{\Gamma(d/2)\,\epsilon^{d_\theta-1}}\left[\dfrac{1}{d_\theta-1}-\dfrac{(d-1)^2(d_\theta-2)}{2(d_\theta-1)^2(d_\theta-3)}\,\dfrac{\epsilon^2}{R^2}+O(\epsilon^4)\right] & d_\theta\neq 1,3 \\ -\,\dfrac{2\pi^{d/2}R^{d-1}}{\Gamma(d/2)}\,\log(\epsilon/R)\left[1+\dfrac{(d-1)^2}{4}\,\dfrac{\epsilon^2}{R^2}\log(\epsilon/R)+\ldots\right] & d_\theta=1 \\ \dfrac{2\pi^{d/2}R^{d-1}}{\Gamma(d/2)\,\epsilon^2}\left[\dfrac{1}{2}-\dfrac{(d-1)(d-5)}{8}\,\dfrac{\epsilon^2}{R^2}\log(\epsilon/R)+o(\epsilon^2)\right] & d_\theta=3 \end{cases} \tag{3.36}$$

Notice that the first expression in (3.36) for $\theta=0$ provides the expansion at this order of the hemisphere [46].
Comparing the result (3.36) for the spherical region with the one in (3.28), which holds for a strip, it is straightforward to observe that, while for the sphere logarithmic divergences occur whenever d_θ is odd, for a strip this happens only when $d_\theta=1$. The logarithmic terms lead to an enhancement of the area for $d_\theta=1$, but only contribute at subleading order for higher odd integer d_θ.

3.3 Holographic entanglement entropy in Vaidya backgrounds

3.3.1 Strip

In this section we consider the strip introduced in 3.2.1 as the region in the boundary and compute holographically its entanglement entropy in the background given by the Vaidya metric (3.11), employing the prescription of [51]. The problem is more complicated than in the static case considered in 3.2.1 because the profile is now specified by two functions $z(x)$ and $v(x)$ which must satisfy $v(-\ell/2)=v(\ell/2)=t$ and $z(-\ell/2)=z(\ell/2)=0$, with t the time coordinate in the boundary. Since in our problem $v(x)$ and $z(x)$ are even, the area functional reads

$$\mathcal{A}[v(x),z(x)] = 2\ell_\perp^{d-1}\int_0^{\ell/2}\frac{\sqrt{\mathcal{B}}}{z^{d_\theta}}\,dx\,, \qquad \mathcal{B}\equiv 1-F(v,z)z^{2(1-\zeta)}v'^2-2z^{1-\zeta}z'v'\,, \tag{3.37}$$

and the boundary conditions for $v(x)$ and $z(x)$ are given by

$$z'(0)=v'(0)=0\,, \qquad v(\ell/2)=t\,, \qquad z(\ell/2)=0\,. \tag{3.38}$$

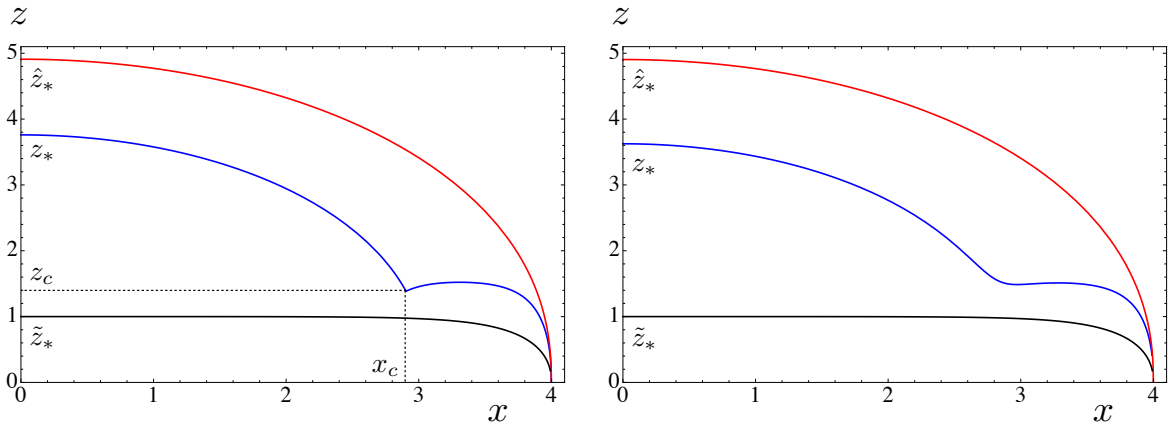

Figure 3.2: The profiles $z(x)$ of the extremal surfaces for a strip with $\ell = 8$ for different boundary times: $t = 0$ (hvLif regime, red curve), $t = 3.6$ (intermediate regime, when the shell is crossed, blue curve) and $t = 5$ (black hole regime, black curve). The final horizon is $z_h = 1$. These plots have $d = 2$, $\theta = 2/3$ and $\zeta = 1.5$. The left panel shows the situation in the thin shell limit ($a = 0.01$), while in the right panel $a = 0.5$.

Since the integrand in (3.37) does not depend explicitly on x, the corresponding integral of motion is constant, namely $z^{d_\theta}\sqrt{\mathcal{B}} = \text{const}$. By recalling that $z(0) \equiv z_*$, this constancy condition can be written as

$$\left(\frac{z_*}{z}\right)^{2d_\theta} = \mathcal{B}\,. \tag{3.39}$$

The equations of motion obtained extremizing the functional (3.37) are

$$\partial_x\big[z^{1-\zeta}(z^{1-\zeta}Fv' + z')\big] \;=\; z^{2(1-\zeta)}F_v v'^2/2\,, \tag{3.40}$$

$$\partial_x\big[z^{1-\zeta}v'\big] \;=\; d_\theta\mathcal{B}/z + z^{2(1-\zeta)}F_z v'^2/2 + (1-\zeta)z^{-\zeta}(z' + z^{1-\zeta}Fv')v'\,. \tag{3.41}$$

In Fig. 3.2 the typical profiles $z(x)$ obtained by solving these equations numerically are depicted. For $t \leqslant 0$ the extremal surface is entirely in the hvLif part of the geometry. As time evolves and the black hole is forming, part of the surface enters into the shell and for large times, when the black hole is formed, the extremal surface stabilizes to its thermal result. In the special case of $\theta = 0$ and $\zeta = 1$, (3.40) and (3.41) simplify to

$$F_v v'^2 = 2\big[Fv'' + (F_v v' + F_z z')v' + z''\big]\,, \tag{3.42}$$

$$2zv'' = zF_z v'^2 + 2d(1 - Fv'^2 - 2z'v')\,. \tag{3.43}$$

Once a solution of (3.40) and (3.41) satisfying the boundary conditions (3.38) has been found, the surface area is obtained by plugging the solution into (3.37). By employing (3.39), one finds that the area of the extremal surface reads

$$\mathcal{A} = 2\ell_\perp^{d-1}\int_0^{\ell/2}\frac{z_*^{d_\theta}}{z^{2d_\theta}}\,dx\,. \tag{3.44}$$

The integral is divergent and we want to consider its finite part. As in the static case, one introduces a cutoff ϵ along the holographic direction and a corresponding one η along the x direction, as defined in (3.24). One way to obtain a finite quantity is to subtract the leading divergence, which, for the strip, is the only one (see (3.28) for the static case),

$$d_\theta \neq 1 \qquad A^{(1)}_{\text{reg}} \equiv \int_0^{\ell/2-\eta}\frac{z_*^{d_\theta}}{z^{2d_\theta}}\,dx - \frac{1}{(d_\theta-1)\,\epsilon^{d_\theta-1}}\,, \tag{3.45}$$

$$d_\theta = 1 \qquad A^{(1)}_{\text{reg}} \equiv \int_0^{\ell/2-\eta}\frac{z_*^{d_\theta}}{z^{2d_\theta}}\,dx - \log(\ell/\epsilon)\,.$$

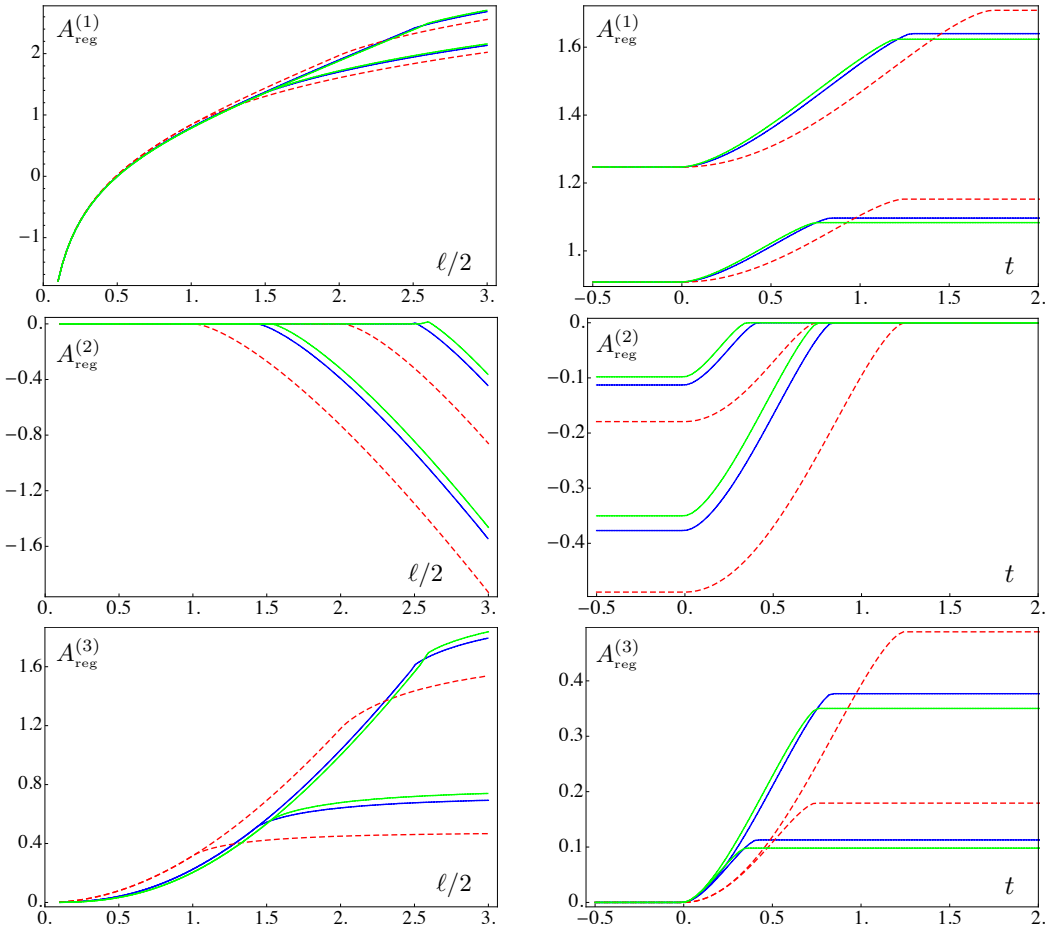

Figure 3.3: Strip and $a = 0.01$ (thin shell). Regularizations (3.45), (3.46) and (3.47) of the area for $d = 1$ (dashed red), $d = 2$ (blue) and $d = 3$ (green) with $\theta = d-1$ and $\zeta = 2-1/d$. Left panels: areas as functions of $\ell/2$ for fixed $t = 1.5$ (bottom curves) and $t = 2.5$ (upper curves). Right: area as functions of the boundary time t with fixed $\ell = 3$ and $\ell = 5$. The latter ones are characterized by larger variations.

Another way to get a finite result is by subtracting the area of the extremal surface at late time, after the black hole has formed

$$A^{(2)}_{\rm reg} \equiv \int_0^{\ell/2-\eta} \frac{z_*^{d_\theta}}{z^{2d_\theta}}\, dx - \int_0^{\ell/2-\tilde{\eta}} \frac{z_*^{d_\theta}}{\tilde{z}^{2d_\theta}}\, dx\,, \tag{3.46}$$

or by subtracting the area of the extremal surface at early time, when the background is hvLif, namely

$$A^{(3)}_{\rm reg} \equiv \int_0^{\ell/2-\eta} \frac{z_*^{d_\theta}}{z^{2d_\theta}}\, dx - \int_0^{\ell/2-\hat{\eta}} \frac{\hat{z}_*^{d_\theta}}{\hat{z}^{2d_\theta}}\, dx\,. \tag{3.47}$$

The quantities corresponding to the the black hole are tilded, while the ones associated to hvLif are hatted. In particular, $\tilde{z}(\ell/2-\tilde{\eta}) = \epsilon$ and $\hat{z}(\ell/2-\hat{\eta}) = \epsilon$. In Fig. 3.3 we compare the regularizations (3.45), (3.46) and (3.47) as functions of ℓ and of the boundary time t at the critical value $\theta = d-1$.

3.3.1.1 Thin shell regime

Let us consider the limit $a \to 0$ in (3.20), which leads to a step function

$$M(v) = M\theta(v)\,. \tag{3.48}$$

The holographic entanglement entropy in this background has been studied analytically for $\theta = 0$, $\zeta = 1$ and $d = 1$ in [67, 68]. For more general values of θ and ζ the thin shell regime is obtained by solving the

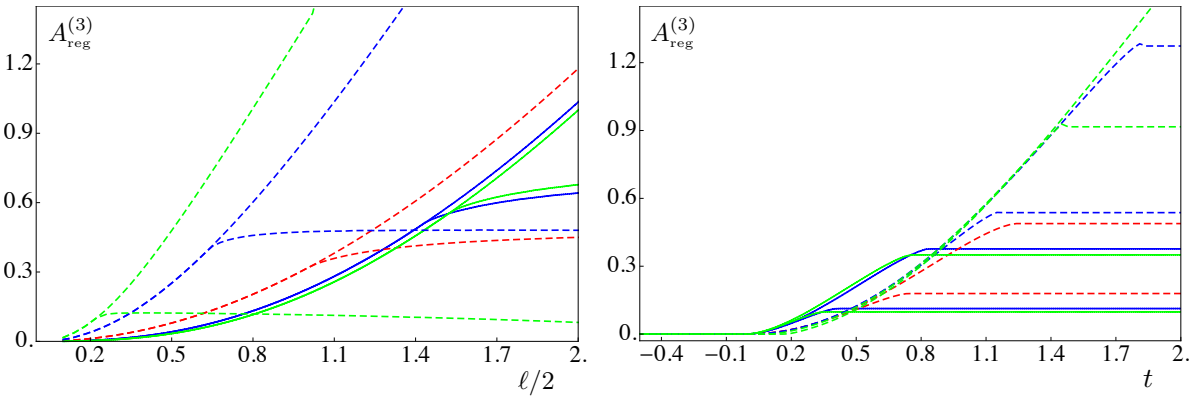

Figure 3.4: Regularized area (3.47) for the strip in the thin shell regime ($a = 0.01$) for the critical value $\theta = d - 1$ and $\zeta = 2 - 1/d$ (continuous curves) compared with the corresponding cases without hyperscaling $\theta = 0$ (dashed curves). We plot $d = 1$ (red), $d = 2$ (blue) and $d = 3$ (green). Left panel: plots at fixed $t = 1.5$ (bottom curves) and $t = 2.5$ (upper curves). Right panel: plots at fixed $\ell = 3, 5$ (larger strips have larger variations for $A^{(3)}_{\rm reg}$). Strips with smaller ℓ thermalize earlier.

differential equations (3.40) and (3.41) in the vacuum (hvLif) for $v < 0$ and in the background of a black hole of mass M for $v > 0$. The solutions are then matched across the shell. Thus, the metric is (3.11) with

$$F(v,z) = \begin{cases} 1 & v < 0 \quad \text{hvLif}\,, \\ F(z) & v > 0 \quad \text{black hole}\,, \end{cases} \tag{3.49}$$

where $F(z)$ is given by (3.5). Recall that the symmetry of the problem allows us to work with $0 \leqslant x \leqslant \ell/2$. From Fig. 3.2 and by comparing Fig. 3.3 with Fig. 3.5, one can appreciate the difference between the thin shell regime and the one where $M(v)$ is not a step function. Denoting by x_c the position where the two solutions match, we have

$$v(x_c) = 0\,, \qquad z(x_c) \equiv z_c\,. \tag{3.50}$$

Thus, when the extremal surface crosses the shell, the part having $0 \leqslant x < x_c$ is inside the shell (hvLif geometry) and the part with $x_c < x \leqslant \ell/2$ is outside the shell (black hole geometry).
The matching conditions can be obtained in a straightforward way by integrating the differential equations (3.40) and (3.41) in a small interval which properly includes x_c and then sending to zero the size of the interval. In this procedure, since both $v(x)$ and $z(x)$ are continuous functions with discontinuous derivatives, only a few terms contribute [164]. In particular, $F_v = -M z^{d_\theta+\zeta}\delta(v)$ is the only term on the r.h.s.'s of (3.40) and (3.41) that provides a non vanishing contribution. Thus, considering (3.41) first, we find the following matching condition

$$v'_+ = v'_- \equiv v'_c\,, \qquad \text{at} \quad x = x_c\,. \tag{3.51}$$

Then, integrating across the shell (3.40) and employing (3.51) (we have also used that $\delta(v) = \delta(x - x_c)/|v'_c|$, where $v'_c > 0$, as discussed below), we find (notice that the term containing v' on the l.h.s. provides a non vanishing contribution)

$$z'_+ - z'_- = \frac{z_c^{1-\zeta} v'_c}{2}\big(1 - F(z_c)\big)\,, \qquad \text{at} \quad x = x_c\,. \tag{3.52}$$

Since F_v vanishes for $v \neq 0$, the differential equation (3.40) tells us that

$$z^{1-\zeta}\left(v' z^{1-\zeta} F + z'\right) = \text{const} \equiv \begin{cases} E_- & 0 \leqslant x < x_c \quad \text{hvLif}\,, \\ E_+ & x_c < x \leqslant \ell/2 \quad \text{black hole}\,. \end{cases} \tag{3.53}$$

Let us consider the hvLif part ($v < 0$) first, where $F = 1$. Since $v'(0) = 0$ and $z'(0) = 0$, (3.53) tells us that $E_- = 0$. Thus, (3.53) implies that

$$v' = -\, z^{\zeta-1} z'\,, \qquad 0 \leqslant x < x_c\,. \tag{3.54}$$

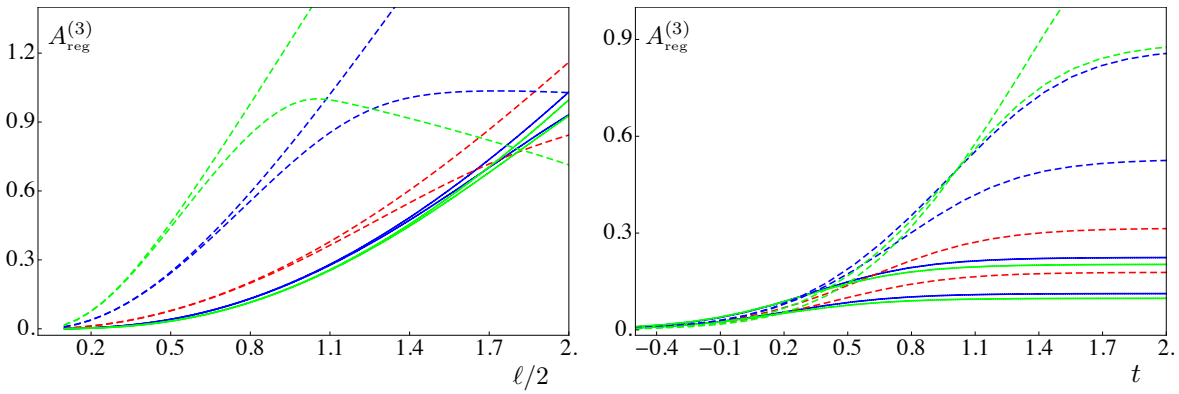

Figure 3.5: Regularized area (3.47) for the strip with $a = 0.5$. These plots should be compared with Fig. 3.4, because the parameters d, θ and ζ and the color code are the same.

Plugging this result into (3.39) with $F = 1$, it reduces to the square of (3.22) with $F = 1$, as expected. Taking the limit $x \to x_c^-$ of (3.54), one finds a relation between the constant value v_c' defined in (3.51) and z_-', i.e.

$$v_c' = -\, z_c^{\zeta-1} z_-' > 0\,, \tag{3.55}$$

where we have used that $z_-' < 0$. Integrating (3.54) from $x = 0$ to $x = x_c$, we obtain that

$$z_c^\zeta = z_*^\zeta + \zeta v_*\,. \tag{3.56}$$

Now we can consider the region outside the shell ($v > 0$), where the geometry is given by the black hole. From (3.53) with $F = F(z)$ given in (3.5) we have that

$$v' = \frac{1}{z^{1-\zeta} F(z)} \left(\frac{E_+}{z^{1-\zeta}} - z' \right), \qquad x_c < x \leqslant \ell/2\,. \tag{3.57}$$

Then, plugging this result into (3.39), one gets

$$z'^2 = F(z) \left[\left(\frac{z_*}{z} \right)^{2d_\theta} - 1 \right] + \frac{E_+^2}{z^{2(1-\zeta)}}\,, \qquad x_c < x \leqslant \ell/2\,. \tag{3.58}$$

We remark that (3.58) becomes (3.22) when $E_+ = 0$. The constant E_+ can be related to z_-' by taking the difference between the equations in (3.53) across the shell. By employing (3.51), the result reads

$$E_+ - E_- = z_c^{1-\zeta} \left[z_+' - z_-' + z_c^{1-\zeta} v_c' \big(F(z_c) - 1 \big) \right]. \tag{3.59}$$

Then, with $E_- = 0$, the matching conditions (3.52) and (3.55) lead to

$$E_+ = \frac{z_c^{1-\zeta}}{2} \big(1 - F(z_c) \big) z_-'\,, \tag{3.60}$$

where $E_+ < 0$ because of (3.54). Moreover, from (3.39), one finds that

$$\mathcal{B}_+ = \mathcal{B}_- = \left(\frac{z_*}{z_c} \right)^{2d_\theta}, \qquad \text{at} \quad x = x_c\,. \tag{3.61}$$

Finally, the size ℓ can be expressed in terms of the profile function $z(x)$ (we recall that $z' < 0$) by summing the contribution inside the shell (from (3.58) with $F(z) = 1$) and the one outside the shell (from (3.58))

$$\frac{\ell}{2} = \int_{z_c}^{z_*} z^{d_\theta} \big(z_*^{2d_\theta} - z^{2d_\theta} \big)^{-1/2} dz + \int_0^{z_c} \left\{ F(z) \left[\left(\frac{z_*}{z} \right)^{2d_\theta} - 1 \right] + \frac{E_+^2}{z^{2(1-\zeta)}} \right\}^{-1/2} dz\,. \tag{3.62}$$

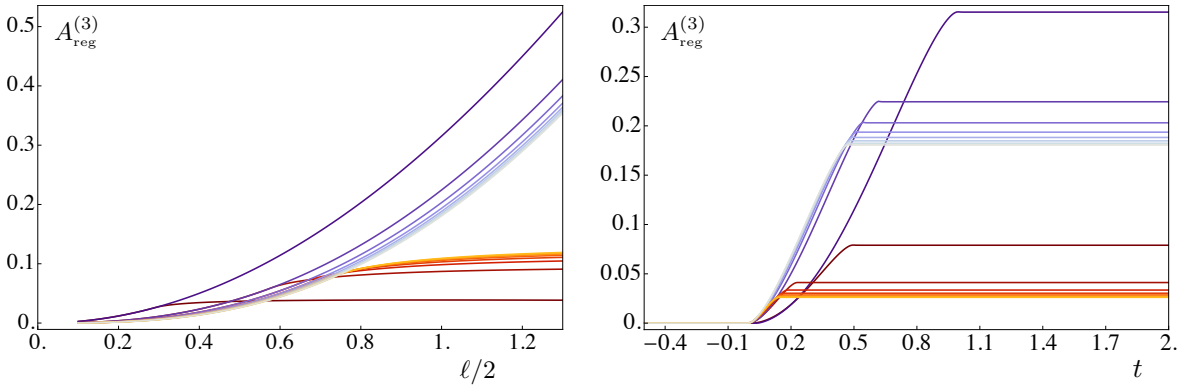

Figure 3.6: Regularized area (3.47) for the strip in the thin shell regime ($a = 0.01.$) with $\theta = d-1$ and $\zeta = 2-1/d$ for various dimensions $d = 1, 2, 3, \ldots, 8$. The darkest curve within each group has $d = 1$ and the brightest one has $d = 8$. Left panel: the red curves have $t = 0.15$ and the blue ones have $t = 0.7$. Right panel: the red curves have $\ell = 1$ and the blue ones have $\ell = 2$.

Notice that we cannot use (3.58) for the part outside the shell because $E_+ \neq 0$. Similarly, we can find the boundary time t by considering first (3.38) and (3.50), and then employing (3.57). We find

$$t = \int_0^t dv = \int_{x_c}^{\ell/2} v' dx = \int_0^{z_c} \frac{z^{\zeta-1}}{F(z)} \left[1 + E_+ z^{\zeta-1} \left\{ F(z) \left[\left(\frac{z_*}{z} \right)^{2d_\theta} - 1 \right] + \frac{E_+^2}{z^{2(1-\zeta)}} \right\}^{-1/2} \right] dz \,, \tag{3.63}$$

where in the last step (3.57) and (3.58) have been used (we recall that $z' < 0$).
The area of the extremal surface (3.44) is obtained by summing the contributions inside and outside the shell in a similar manner. The result is

$$\mathcal{A} = 2\ell_\perp^{d-1} z_*^{d_\theta} \left(\int_{z_c}^{z_*} z^{-d_\theta} \left(z_*^{2d_\theta} - z^{2d_\theta} \right)^{-1/2} dz + \int_\epsilon^{z_c} z^{-2d_\theta} \left\{ F(z) \left[\left(\frac{z_*}{z} \right)^{2d_\theta} - 1 \right] + \frac{E_+^2}{z^{2(1-\zeta)}} \right\}^{-1/2} dz \right) , \tag{3.64}$$

where the cutoff ϵ must be introduced to regularize the divergent integral, as already discussed. In Fig. 3.6 we show $A^{(3)}_{\rm reg}$ for various dimensions. It seems that a limiting curve is approached as d increases.

It is straightforward to generalize the above analysis to the case of n dimensional surfaces extended in the bulk which share the boundary with an n dimensional spatial surface in the boundary, i.e. surfaces with higher codimension than the extremal surface occurring for the holographic entanglement entropy. For a strip whose sides have length ℓ in one direction and $\ell_\perp$ in the remaining $n-1$ ones, the area functional to be extremized reads

$$\mathcal{A}[v(x), z(x)] = 2\ell_\perp^{n-1} \int_0^{\ell/2} \frac{\sqrt{\mathcal{B}}}{z^{n d_\theta/d}} \, dx \,, \tag{3.65}$$

where $\mathcal{B}$ has been defined in (3.37). This functional reduces to the one in (3.37) for the holographic entanglement entropy when $n = d$. The extrema of the functional (3.65) with $n = 2$ are employed to study the holographic counterpart of the spacelike Wilson loop, while the $n = 1$ case describes the holographic two point function.
The equations of motion of (3.65) are simply given by (3.40) and (3.41) where the d_θ in the r.h.s. of (3.41) is replaced by nd_θ/d, while $F(v, z)$ is kept equal to (3.12). Similarly, we can adapt all the formulas within 3.3.1 to the case $n \neq d$ by replacing d_θ by nd_θ/d whenever it does not occur through $F(v, z)$ or $F(z)$, which remain equal to (3.12) and (3.5) respectively.

3.3.2 Sphere

Let us consider a circle of radius R in the boundary of the asymptotically hvLif space-time. As discussed in 3.2.2 for the static case, it is more convenient to adopt spherical coordinates in the Vaidya metric

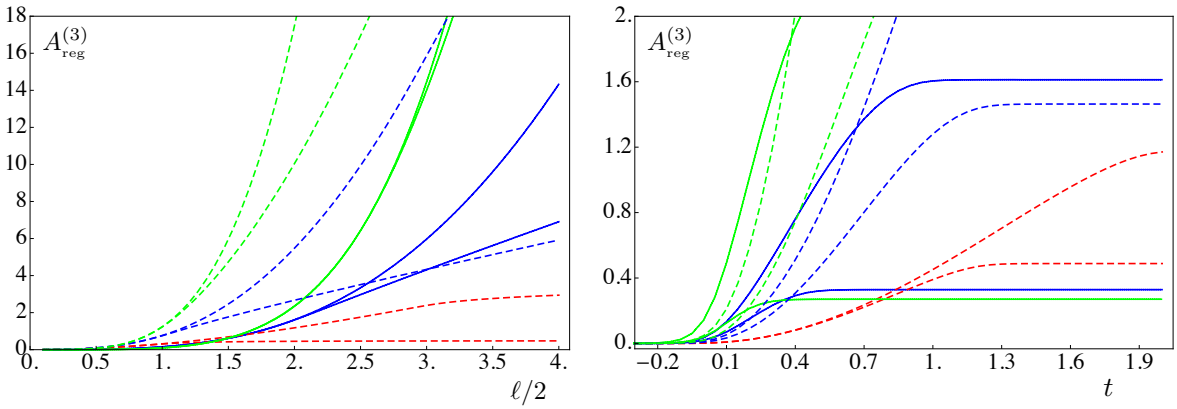

Figure 3.7: Holographic entanglement entropy for the sphere in the thin shell regime with $a = 0.01$ (see 3.3.2). The parameters d, θ and ζ are the same of Fig. 3.4 (same color coding). Left panel: fixed $t = 1.5$ (lower curve) and $t = 3$ (upper curve). Right panel: fixed $R = 2$ and $R = 4$ (larger spheres thermalize later).

(3.11) for $\mathbb{R}^d$. The area functional is given by

$$\mathcal{A}[v(\rho), z(\rho)] = \frac{2\pi^{d/2}}{\Gamma(d/2)} \int_0^R \frac{\rho^{d-1}}{z^{d_\theta}} \sqrt{\mathcal{B}}\, d\rho\,, \qquad \mathcal{B} \equiv 1 - F(v,z) z^{2(1-\zeta)} v'^2 - 2 z^{1-\zeta} z' v'\,, \tag{3.66}$$

where now the prime denotes the derivative w.r.t. ρ. An important difference compared to the strip, as already emphasized for the static case, is that the Lagrangian of (3.66) depends explicitly on ρ. This implies that we cannot find an integral of motion which allows to get a first order differential equation to describe the extremal surface. Thus, we have to deal with the equations of motion, which read

$$\frac{z^{d_\theta}\sqrt{\mathcal{B}}}{\rho^{d-1}}\, \partial_\rho \left[\frac{\rho^{d-1} z^{1-\zeta-d_\theta}}{\sqrt{\mathcal{B}}} \left(v' z^{1-\zeta} F + z' \right) \right] = \frac{z^{2(1-\zeta)}}{2} F_v v'^2\,, \tag{3.67}$$

$$\frac{z^{d_\theta}\sqrt{\mathcal{B}}}{\rho^{d-1}}\, \partial_\rho \left[\frac{\rho^{d-1} z^{2(1-\zeta)-d_\theta}}{\sqrt{\mathcal{B}}}\, v' \right] = \frac{d_\theta}{z}\, \mathcal{B} + \frac{z^{2(1-\zeta)}}{2} F_z v'^2 + \frac{1-\zeta}{z^\zeta} (z' + z^{1-\zeta} F v') v'\,. \tag{3.68}$$

These equations have to be supplemented by the following boundary conditions

$$v(R) = t\,, \qquad v'(0) = 0\,, \qquad \text{and} \qquad z(R) = 0\,, \qquad z'(0) = 0\,. \tag{3.69}$$

We are again mainly interested in the limiting case of a thin shell (3.48).

3.3.2.1 Thin shell regime

Considering the thin shell regime, defined by (3.48), we can adopt to the sphere some of the observations made in 3.3.1.1 for the strip. Again, there is a value ρ_c such that for $0 \leqslant \rho < \rho_c$ the extremal surface is inside the shell (hvLif geometry), while for $\rho_c < \rho \leqslant R$ it is outside the shell (black hole geometry).
The matching conditions can be found by integrating (3.67) and (3.68) across the shell, as was done in 3.3.1.1 for the strip. Introducing

$$\breve{v}' \equiv \frac{v'}{\sqrt{\mathcal{B}}}\,, \qquad \breve{z}' \equiv \frac{z'}{\sqrt{\mathcal{B}}}\,, \tag{3.70}$$

we can use (3.68), whose r.h.s. does not contain F_v, to obtain

$$\breve{v}'_+ = \breve{v}'_-\,, \qquad \text{at} \;\; \rho = \rho_c\,, \tag{3.71}$$

while from (3.67) and employing (3.71) as well, we get

$$\breve{z}'_+ - \breve{z}'_- = \frac{z_c^{1-\zeta}\, \breve{v}'_c}{2} \left(1 - F(z_c) \right), \qquad \text{at} \;\; x = x_c\,. \tag{3.72}$$

Considering (3.67), since $F_v = 0$ for $v \neq 0$, we have

$$\frac{\rho^{d-1} z^{1-\zeta-d_\theta}}{\sqrt{\mathcal{B}}} \left(v' z^{1-\zeta} F + z'\right) = \text{const} \equiv \begin{cases} E_- & 0 \leqslant \rho < \rho_c \quad \text{hvLif}\,, \\ E_+ & \rho_c < \rho \leqslant R \quad \text{black hole}\,, \end{cases} \tag{3.73}$$

where $E_- = 0$ because $v'(0) = 0$ and $z'(0) = 0$. By using (3.70), one can write

$$1/\mathcal{B}_+ = 1 + \check{v}'_+ z_c^{(1-\zeta)} \left[z_c^{(1-\zeta)} \check{v}'_+ F(z_c) + 2\check{z}'_+\right], \tag{3.74}$$

$$1/\mathcal{B}_- = 1 + \check{v}'_- z_c^{(1-\zeta)} (z_c^{(1-\zeta)} \check{v}'_- + 2\check{z}'_-)\,. \tag{3.75}$$

Taking the difference of these expressions and using (3.71) and (3.72), one finds

$$\mathcal{B}_+ = \mathcal{B}_-\,. \tag{3.76}$$

By using (3.71), (3.72) and (3.73), we get

$$E_+ = \frac{\rho_c^{d-1} z_c^{2(1-\zeta)-d_\theta}}{2\sqrt{\mathcal{B}_+}} (F(z_c) - 1) v'_c\,. \tag{3.77}$$

Then, from (3.73) in the black hole region, one obtains

$$v' = \frac{z^{\zeta-1}}{F(z)} \left(\frac{A E_+ \sqrt{1 + z'^2/F(z)}}{\sqrt{1 + A^2 E^2/F(z)}} - z' \right), \qquad A \equiv \frac{z^{d_\theta+\zeta-1}}{\rho^{d-1}}\,. \tag{3.78}$$

Plugging this expression into (3.68) leads to

$$\begin{aligned} 2d_\theta \rho F^2 + z\left[\rho F_z - 2(d-1)z'\right] z'^2 - 2F\left[\rho\, z\, z'' + (d-1) z\, z' + d_\theta \rho\, z'^2\right] \\ + E_+^2 A^2 \rho \left[z(F_z + 2z'') - 2(\zeta - 1)(F + z'^2)\right] = 0\,, \end{aligned} \tag{3.79}$$

which reduces to (3.30) when $E_+ = 0$, as expected. The boundary time t is obtained by integrating (3.78) outside the shell $\rho_c \leqslant \rho < R$ (see e.g. (3.63) for the strip)

$$t = \int_{\rho_c}^{R} \frac{z^{\zeta-1}}{F(z)} \left(\frac{A E_+ \sqrt{1 + z'^2/F(z)}}{\sqrt{1 + A^2 E_+^2/F(z)}} - z' \right) d\rho\,. \tag{3.80}$$

Notice that we cannot provide a similar expression for R, like we did for the strip in (3.62). Finally, the area of the extremal surface at time t is the sum of two contributions, one inside (finite) and one outside (infinite) the shell, and is given by

$$\mathcal{A} = \frac{2\pi^{d/2}}{\Gamma(d/2)} \left(\int_0^{\rho_c} \frac{\rho^{d-1} \sqrt{1 + z'^2}}{z^{d_\theta}}\, d\rho + \int_{\rho_c}^{R} d\rho \frac{\rho^{d-1} \sqrt{1 + z'^2/F(z)}}{z^{d_\theta} \sqrt{1 + A^2 E_+^2/F(z)}} \right). \tag{3.81}$$

Numerical results for the regularized extremal area $A^{(3)}_{\text{reg}}$ for a sphere (defined via an appropriate adaptation of (3.47)) in the thin shell regime are shown in Fig. 3.7.

3.4 Regimes in the growth of the holographic entanglement entropy

In this section we extend the analysis performed in [140, 141] to $\theta \neq 0$ and $\zeta \neq 1$. For $t < 0$ we have $A^{(3)}_{\text{reg}} = 0$ because the background is hvLif. When $t > 0$, it is possible to identify three regimes: an initial one, when the growth is characterized by a power law, an intermediate regime where the growth is linear and a final regime, when $A^{(3)}_{\text{reg}}(t)$ saturates to the thermal value. We report our results for the different regimes in the main text while the details of the computation are described in Appendix C.2.

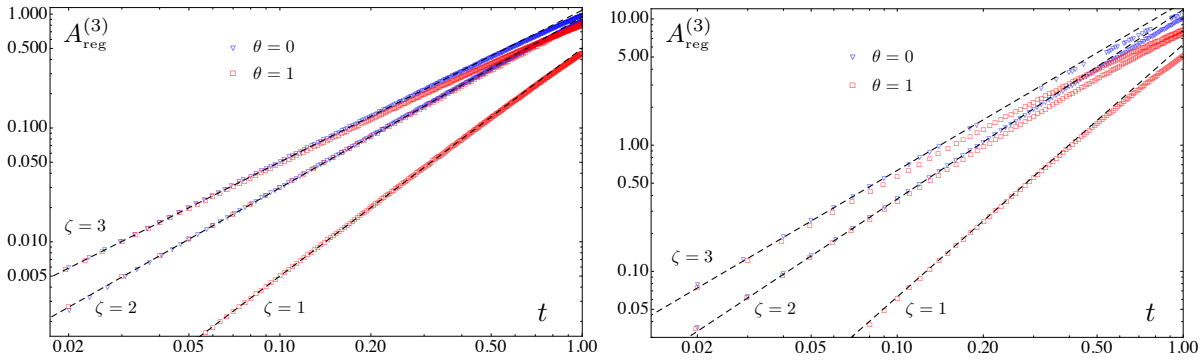

Figure 3.8: Initial growth of the holographic entanglement entropy for $d = 2$ (see 3.4.1). The points come from the numerical solution of (3.40)-(3.41) for the strip (left) and (3.67)-(3.68) for the sphere (right) in the thin shell regime. The black dashed lines are obtained through the formula (3.84), which is independent of θ and of the shape of the region in the boundary. Left panel: strip with $\ell = 4$. Right panel: sphere with $R = 4$.

3.4.1 Initial growth

The initial regime is characterized by times that are short compared to the horizon scale

$$0 < t \ll z_h \,. \tag{3.82}$$

In Appendix C.2.1, following [141], we expand $A^{(3)}_{\rm reg}$ around $t = 0$ and consider the first non trivial order for an n dimensional spatial region whose boundary Σ has a generic shape. Given the metric (3.11) with (3.49), the final result for this regime is (see (C.44))

$$\mathcal{A}^{(3)}_{\rm reg}(t) = \frac{M A_\Sigma (\zeta t)^{[d_\theta(1-n/d)+\zeta+1]/\zeta}}{2[d_\theta(1-n/d)+\zeta+1]} \,, \tag{3.83}$$

where A_Σ is the area of Σ. Notice that for the holographic entanglement entropy $n = d$, for the holographic counterpart of the Wilson loop $n = 2$ and for the holographic two point function $n = 1$. Explicitly, for the holographic entanglement entropy, (3.83) becomes

$$\mathcal{A}^{(3)}_{\rm reg}(t) = \frac{M A_\Sigma \, \zeta^{1+1/\zeta}}{2(\zeta+1)} \, t^{1+1/\zeta} \,, \tag{3.84}$$

which is independent of d and θ. This generalizes the result of [141] (see [112] for $d = 1$). In Fig. 3.8 we show some numerical checks of (3.84) both for the strip and for the sphere.

3.4.2 Linear growth

When z_* is large enough, the holographic entanglement entropy displays a linear growth in time. The computational details for the strip are explained in Appendix C.2.2. The result for (3.49) is that, in the regime given by

$$z_h \ll t \ll \ell \,, \tag{3.85}$$

and if the following condition is satisfied

$$d_\theta \geqslant 2 - \zeta \,, \tag{3.86}$$

we find a linear growth in time for the holographic entanglement entropy, namely

$$\mathcal{A}^{(3)}_{\rm reg}(t) \equiv 2\ell_\perp^{d-1} v_{\rm linear} \, t \,. \tag{3.87}$$

The method of [141] for the thin shell regime, extended to $\theta \neq 0$ and $\zeta \neq 1$, tells us that

$$\mathcal{A}^{(3)}_{\rm reg}(t) = 2\ell_\perp^{d-1} A^{(3)}_{\rm reg}(t) \,, \qquad A^{(3)}_{\rm reg}(t) = \frac{\sqrt{-F(z_m)}}{z_m^{d_\theta+\zeta-1}} \, t \equiv \frac{v_E}{z_h^{d_\theta+\zeta-1}} \, t \,, \tag{3.88}$$

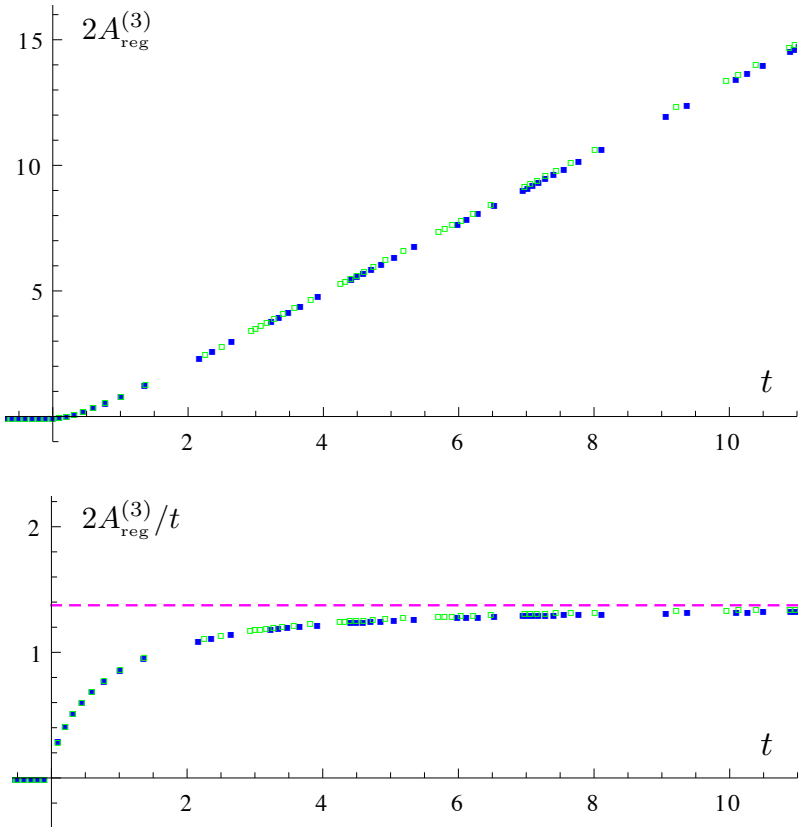

Figure 3.9: Typical example of linear growth for the holographic entanglement entropy in the thin shell regime. Here $d = 2$, $z_h = 1$, $\theta = 1$ and $\zeta = 2$ for two large strips: $\ell \sim 16$ (green squares) and $\ell \sim 20$ (blue squares). In the bottom panel, the dashed line is obtained through (3.88) and (3.89).

where, for $F(z)$ given by (3.5), v_E reads

$$v_E = \frac{(\eta-1)^{\frac{\eta-1}{2}}}{\eta^{\frac{\eta}{2}}}\,, \qquad \eta = \frac{2(d_\theta+\zeta-1)}{d_\theta+\zeta}\,. \tag{3.89}$$

It can be easily seen that $v_E = 1$ when $\eta = 1$ and $v_E \to 0$ as $\eta \to +\infty$ monotonically. Notice that the linear regime depends only on the combination $d_\theta + \zeta$. In Fig. 3.9, where the points are computed using the numerical solutions of (3.40) and (3.41), we see a typical linear behavior in time for two strips with large ℓ. The agreement between the slope of the numerical data and the value computed from (3.89) is quite good. In Fig. 3.10 we compare the slopes of the numerical curves with the values obtained from (3.89) for other values of θ and ζ. We consider the linear growth regime for more generic backgrounds in Appendix C.3 In order to get a better understanding of the origin of the ζ dependence in (3.88).

The functional form of the velocity in (3.89) suggests that $\eta < 1$ corresponds to qualitatively different behavior than the $\eta \geqslant 1$ and our calculations are not easily extended to cover this case. In particular, we are not able to determine whether there is linear growth in the holographic entanglement entropy for $\eta < 1$. We note that when combined with the null energy condition (as displayed in Fig. 3.1), this case corresponds to $d_\theta < 0$ which is problematic for several reasons. This includes finiteness of S_A in the UV, negative specific heat for black branes, and lack of a decoupling limit in string theory realizations of the hvLif metric [78]. Specifically, we run into problems when trying to extend our calculations to $\eta < 1$, both in implementing the methods of [140, 141] as described in C.2.2 and in setting up initial conditions for the numerical shooting method in C.2.4.

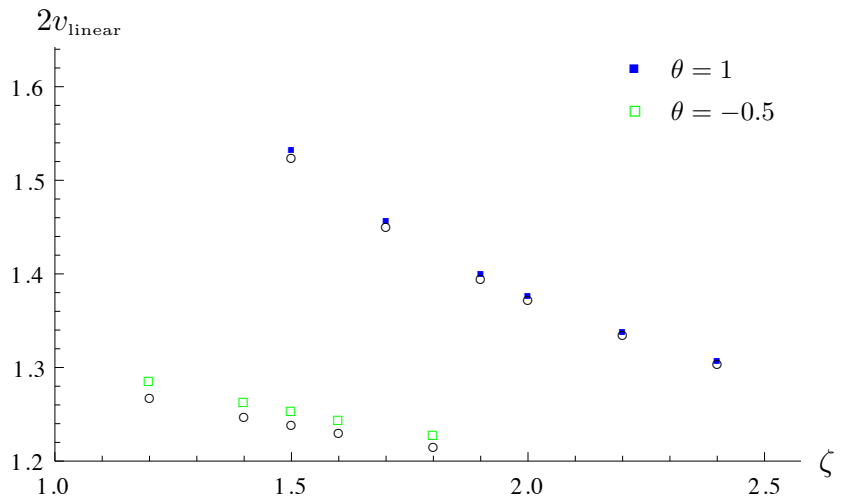

Figure 3.10: Linear regime for the strip: the colored squares are values of the slope (see (3.87)) found from the numerical data as in the bottom panel of Fig. 3.9. The black empty circles denote the corresponding results of v_E from (3.89). In this plot $z_h = 1$.

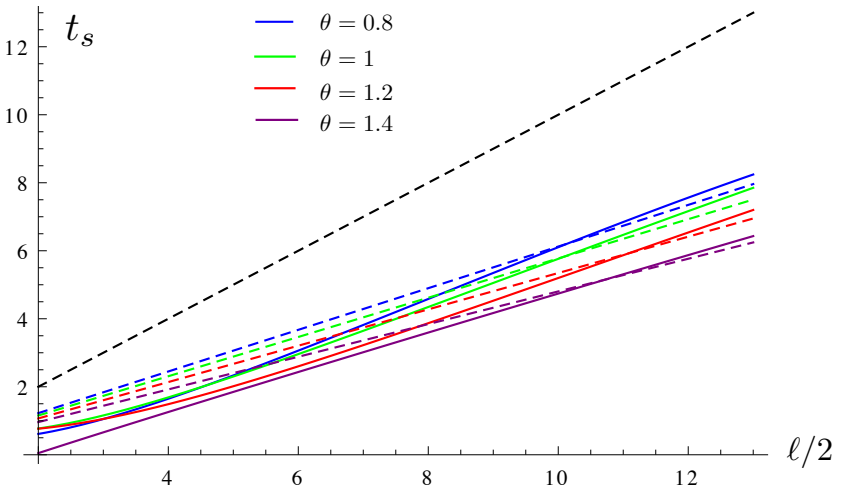

Figure 3.11: Saturation time as a function of the transverse length scale ℓ for geodesic correlators. The dashed black line is a reference line with slope equal to 1, while the colored ones are obtained through (3.92) with $n = 1$, $\zeta = 2$ and the corresponding values of θ indicated in the legend. The agreement improves for large ℓ.

3.4.3 Saturation

We define the saturation time t_s as the boundary time such that, for $t > t_s$, the extremal surface probes only the black hole part of the geometry. It is possible to estimate t_s as a function of z_* for sufficiently large regions with generic shapes. The relevant computations for this regime are explained in Appendix C.2.3. To leading order, t_s is given by

$$t_s = -\frac{z_h^{\zeta-1}}{F_h'} \log(z_h - z_*)\,, \tag{3.90}$$

where $F_h' \equiv -\partial_z F(z)|_{z=z_h}$. Since the relation between z_* and the characteristic length of the boundary region depends on its shape, we have to consider the strip and the sphere separately. For a strip, if

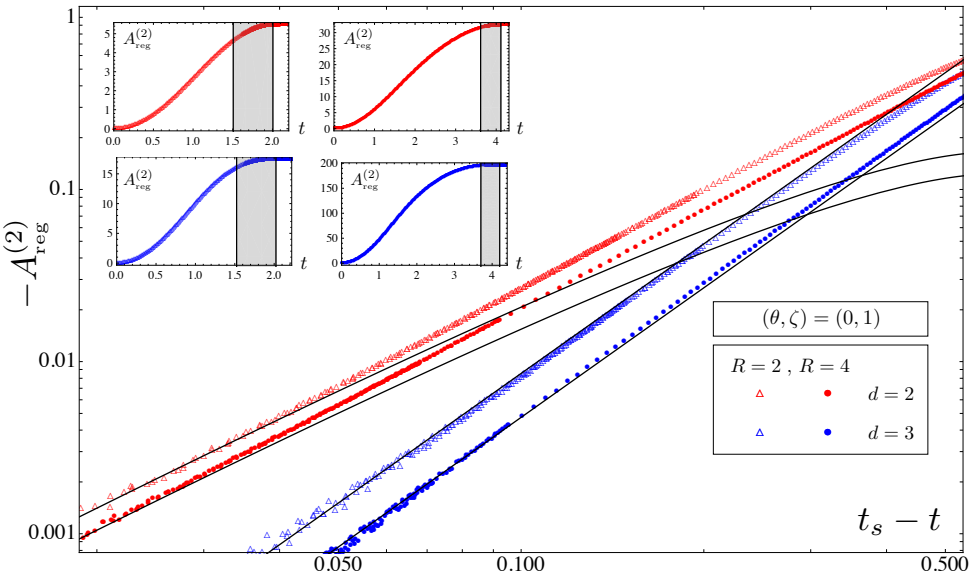

Figure 3.12: Saturation regime for the holographic entanglement entropy in the thin shell limit ($a = 10^{-4}$) for a spherical region of radius R in the boundary. In this plot $\theta = 0$ and $\zeta = 1$, which is the situation considered in [140, 141]. The continuos black curves are obtained through (3.95) with the corresponding values of d. The inset shows the entire sets of data describing the complete evolution of the four cases considered (the plots are shown in the same positions of the corresponding points in the legend). The gray regions have $\Delta t = 0.5$ and show the parts of the curves which have been reported in the main plot.

$\partial_t A_{\rm reg}(t)$ is continuous at $t = t_s$, we find the following linear relation

$$t_s = z_h^{\zeta-1} \sqrt{\frac{d_\theta}{2 z_h F_h'}}\, \ell + \dots \,, \tag{3.91}$$

where the dots denote subleading orders at large ℓ. Notice that (3.91) can be generalized to n dimensional spatial surfaces in the boundary according to the observation made in the end of 3.3.1.1, namely d_θ should be replaced by $n d_\theta / d$ while $F(z)$ kept equal to (3.5). This gives

$$t_s = z_h^{\zeta-1} \sqrt{\frac{n d_\theta}{2 d z_h F_h'}}\, \ell + \dots \,. \tag{3.92}$$

It can also be shown that, whenever $\partial_t \mathcal{A}_{\rm reg}(t)$ is continuous at saturation, we have

$$\mathcal{A}^{(2)}_{\rm reg}(t) \propto (t - t_s)^2 + o((t - t_s)^2) \,, \tag{3.93}$$

for a strip for any values of ζ and θ (see Appendix C.2.3.3).
The saturation time has also been evaluated numerically for the geodesic correlator, with the following procedure from [162]. The action for the geodesics has solutions with turning points either inside or outside the horizon. We first choose turning points z_* inside the horizon, generate the corresponding geodesic and find the coordinates of the endpoints at the boundary and the length of the geodesic. The results are regulated by subtracting the vacuum value. For sufficiently large ℓ, at early times the bulk geodesics will all have turning points inside the horizon, and also pass through the infalling shell extending into the part of the space-time with vacuum geometry. In this case the corresponding observable will not be thermal. At later times the turning point will be outside the horizon and the observable takes a thermal value. The conversion between these two types of behavior is sharp and defines the saturation time. Following [162], the saturation times can be calculated by fitting surfaces to the data of the above

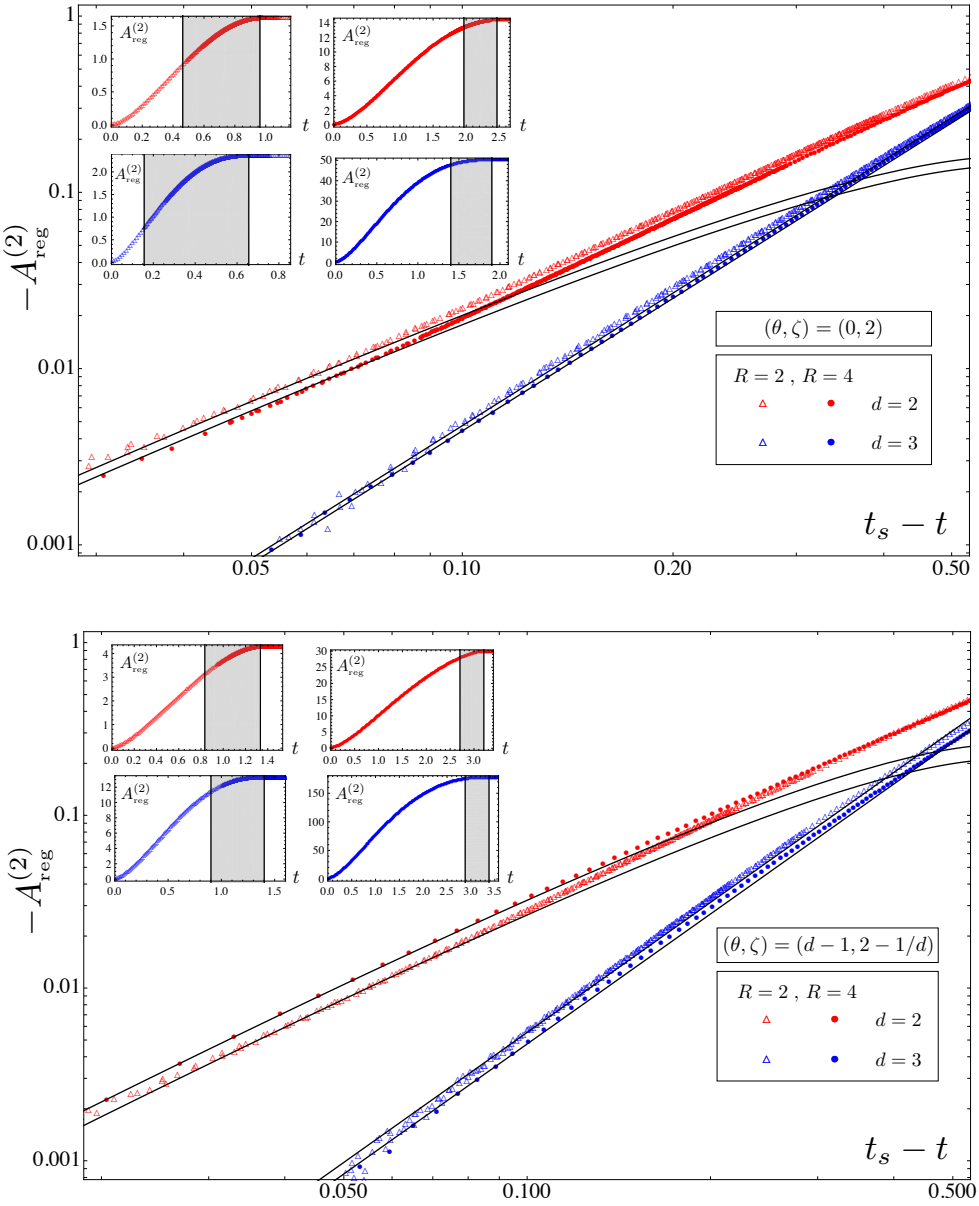

Figure 3.13: Saturation regime for the holographic entanglement entropy in the thin shell limit ($a = 10^{-4}$) for a spherical region of radius R in the boundary. Here $(\theta,\zeta) = (0,2)$ (top panel) and $(\theta,\zeta) = (d-1, 2-1/d)$ (bottom panel). The plots are constructed as in Fig. 3.12. The agreement with the continuos black curves from (3.95) indicates that the saturation regime is independent of (θ,ζ).

solution. The intersection of the surfaces then defines the curve for the saturation time as a function of the transverse length scale. In Fig. 3.11 the numerical results for the saturation time of the geodesics are compared with the corresponding results from (3.92). Notice that the agreement improves for large ℓ, as expected.

When the boundary region is a sphere and in the regime of large R, the transition to the saturated value is always smooth. In Appendix C.2.3.2, we show that

$$t_s = z_h^{\zeta-1}\sqrt{\frac{2d_\theta}{z_h F_h'}}\,R - z_h^{\zeta-1}\,\frac{(d-1)}{F^{(1)}(z_h)}\log R + \dots\ . \tag{3.94}$$

Moreover, by extending the analysis of [141] to backgrounds with non trivial ζ and θ, in C.2.3.4 we find that

$$\mathcal{A}^{(2)}_{\rm reg} \propto \begin{cases} -(t_s - t)^2 \log(t_s - t) & d = 2 \\ (t_s - t)^{1+d/2} & d > 2 \end{cases} \tag{3.95}$$

telling us that the saturation regime is independent of ζ and θ. In Figs. 3.12 and 3.13 we show the saturation regime for the holographic entanglement entropy in the thin shell limit ($a = 10^{-4}$) for the two cases of $R = 2$ and $R = 4$ with the dimensionality given by either $d = 2$ or $d = 3$. The agreement between the numerical data and the expression (3.95) is quite good.

Chapter 4

Singular Surfaces in hvLif

The central charge of a two-dimensional CFT is an important quantity. It is ubiquitous in many expressions such as the central extension of Virasoro algebra, the two point function of energy-momentum tensor, in the Weyl anomaly and is the coefficient of the logarithmically divergent term in the entanglement entropy (as we saw in (1.17)). The *number* - because it is dimensionless - c may be thought of as a measure of the number of degrees of freedom of the theory, and the c-theorem shows explicitly that along any renormalization group flow connecting two fixed points, the central charge decreases along the flow, indicating that IR fixed points are characterized by fewer degrees of freedom.

In higher dimensional conformal field theories the situation is completely different. First of all the conformal group in higher dimensions does not have a central extension and thus it is finite dimensional, namely being $SO(d+1,2)$. Moreover the parameter which appears in the two point function of the energy-momentum tensor is not generally related to the one multiplying the Euler density in the Weyl anomaly in even dimensional conformal field theories, nor is directly related to the cut-off independent terms of the entanglement entropy computed for a smooth entangling region.

Indeed if one computes entanglement entropy for a given smooth entangling region in a $d+1$-dimensional conformal field theory, one finds that the divergence structure is given by (1.19), which can be rewritten in a compact way as

$$S_E = \sum_{i=0}^{[\frac{d}{2}]-1} \frac{A_{2i}}{d-2i-1}\,\frac{1}{\varepsilon^{d-2i-1}} + \delta_{2[\frac{d}{2}]+1,d}\, A_{2[\frac{d}{2}]} \log\frac{H}{\varepsilon} + \text{finite terms}, \tag{4.1}$$

where ε is a UV cut-off, A_i's are some constant parameters (in particular A_0 is proportional to the area, see (1.18)) and $[x]$ denotes the integer part of x[1]. H is a typical scale in the model which could be the size of entangling region. For an even dimensional field theory (odd d in our notation) the coefficient of the logarithmic term, $A_{2[\frac{d}{2}]}$, is a universal constant in the sense that it is independent of the UV cut-off: in other words it is fixed by the intrinsic properties of the theory. Two-dimensional CFTs fall in this case since the central charge is indeed a universal quantity.

In general for an even dimensional conformal field theory it can be shown that the coefficient of the universal logarithmic term is given in terms of the Weyl anomaly (see for example [24, 39]). In particular, when the entangling region is a sphere the coefficient is exactly the same as the one multiplying the Euler density. For odd dimensional space-times (even d) one still has a universal constant term which might provide a generalization of the c-theorem for odd dimensional conformal field theories [34, 165].

Having said this, it is natural to pose the question whether one could find further logarithmic divergences in the expression of the entanglement entropy whose coefficients, being universal in the sense specified above, could reflect certain intrinsic properties of the theory under consideration. Moreover, if there is such a universal term, it would be interesting to understand if any relation between it and other charges of the theory is present. Indeed these questions, for some particular cases, have been addressed in the literature (see for example [59, 119, 120]). In particular, it was shown that there is also a logarithmic term in three dimensions for sets of entangling regions with non-smooth boundary. More precisely, for

[1] By integer part here and in the following we mean the *floor* function, i.e. the decimal digits are simply discarded.

an entangling region with a cusp in three dimensions one has [59, 119, 120]

$$S = S_1 \frac{L}{\epsilon} + a(\varphi) \log \epsilon + S_0 \tag{4.2}$$

where the cusp is specified by an angle defined such that $\varphi = \pi/2$ corresponds to a smooth line. Here L is the length of the boundary of the entangling region and S_1 is a constant which depends on the UV cut-off, while $a(\varphi)$ and S_0 are universal parameters.

More recently based on early results [59, 119, 120] it was shown that "the ratio $\frac{a(\varphi)}{C_T}$, where C_T is the central charge in the stress-energy tensor correlator, is an almost universal quantity" [166, 167](see also [168]). Indeed it was conjectured in those works that in a generic three-dimensional conformal field theory there is a universal ratio [166]

$$\frac{\sigma}{C_T} = \frac{\pi^2}{24}, \tag{4.3}$$

where σ is defined through the asymptotic behaviour of $a(\varphi)$, *i.e.* $a(\varphi \to \pi/2) \approx \sigma\ (\varphi - \pi/2)^2$.

The aim of the present Chapter is to extend the above consideration to higher dimensional field theories[2]. Nonetheless, we will consider cases where the dual field theory does not even have conformal symmetry. More precisely here we shall explore different logarithmic divergences for the entanglement entropy of strongly coupled field theories whose gravitational dual are provided by geometries with a hyperscaling violating factor[143, 145]. The corresponding geometry in $d+2$ dimensions is given by (see Appendix D.1)

$$ds^2 = r^{-2\frac{\theta}{d}} \left(-r^{2z} dt^2 + r^2 \sum_{i=1}^{d} dx_i^2 + \frac{dr^2}{r^2} \right), \tag{4.4}$$

where the constants z and θ are dynamical and hyperscaling violation exponents, respectively. This is the most general geometry which is spatially homogeneous and covariant under the following scale transformations

$$t \to \lambda^z t, \quad r \to \lambda^{-1} r, \quad x_i \to \lambda x_i, \quad ds_{d+2} \to \lambda^{\frac{\theta}{d}} ds_{d+2}. \tag{4.5}$$

Note that with a non-zero θ, the line element is not invariant under rescalings which in the context of AdS/CFT correspondence indicates violations of hyperscaling in the dual field theory. More precisely, while in $(d+1)$-dimensional theories without hyperscaling violating exponent the entropy scales as T^d with temperature, in the present case, where the metric has a non-zero θ, the entropy scales as $T^{(d-\theta)/z}$ [80, 143].

Holographic entanglement entropy [46, 47] for hyperscaling violating geometries has been studied in *e.g.* [78, 79, 169]. An interesting feature of metric (4.4) is that for the special value of the hyperscaling violating exponent $\theta = d-1$, the holographic entanglement entropy shows a logarithmic violation of the area law[79, 80], indicating that the background (4.4) could provide a gravitational dual for a theory with an $\mathcal{O}(N^2)$ Fermi surface, where N is the number of degrees of freedom.

We will study holographic entanglement entropy in the background (4.4) for an entangling region with the form of $c_n \times \mathbb{R}^{d-n-2}$ where c_n is an n-dimensional cone. We will see that holographic computations indicate the presence of new divergences which could include both log and $\log^2$ terms. Such terms could provide a new universal charge for the model. Unlike the Weyl anomaly, this charge can be defined in both even and odd dimensional theories. We also note that there is another quantity, defined in arbitrary dimensions, which is the coefficient entering in the expression of stress-energy tensor two-point function. Following the ideas in [166], we investigate whether there is a relation between these two charges. We further show that there is a relation between them that remains unchanged even when we add corrections due to the presence of (certain) higher curvature terms. Therefore it is reasonable to conjecture that the relation between these two charges is an intrinsic property of the underling theory. It is worth mentioning that although we will mainly consider a theory with hyperscaling violation, when it comes to the comparison of charges we will restrict ourselves to $\theta = 0$, though making a comment on generic θ.

The rest of the Chapter is organized as follows. In the next Section we will study entanglement entropy of an entangling region consisting of an n-dimensional cone. In Section 3 we will compare the

[2] Holographic entanglement entropy for certain singular surfaces in various dimensions has been studied in [120] where it was shown that some specific non-smooth entangling regions exhibit new divergences that include logarithmic ones (see Table1 there).

results with that of smooth entangling region where we will see that the corresponding entanglement entropy for the singular surfaces exhibit new divergent terms which include certain logarithmic terms. In Section 4, from the coefficient of logarithmic divergent terms, we will introduce a new charge for the theory which could be compared with other central charges in the model. The last section is devoted to conclusions.

4.1 Entanglement entropy for a higher dimensional cone

In this section we shall study holographic entanglement entropy on a singular region consisting of an n-dimensional cone c_n. To proceed it is convenient to use the following parametrization for the metric in $d+2$ dimensions

$$ds^2 = \frac{L^2}{r_F^{2\frac{\theta}{d}}} \frac{-r^{2(1-z)}dt^2 + dr^2 + d\rho^2 + \rho^2(d\varphi^2 + \sin^2\varphi\, d\Omega_n^2) + d\vec{x}^2_{d-n-2}}{r^{2(1-\frac{\theta}{d})}}. \tag{4.6}$$

Here L is the radius of curvature of the space-time and r_F is a dynamical scale. Indeed the above metric could provide a gravitational dual for a strongly coupled field theory with hyperscaling violation below the dynamical scale r_F[78].

The entangling region, which we choose to be $c_n \times \mathbb{R}^{d-n-2}$, i.e. an n-cone extended in $d-n-2$ transverse dimensions, may be parametrized in the following way

$$t = \text{fixed} \qquad 0 \leq \varphi \leq \Omega\,. \tag{4.7}$$

When $n=0$ the entangling region, which we call a crease, will be delimited by $-\Omega \leq \varphi \leq \Omega$.

Following [46, 47], in order to compute holographic entanglement entropy one needs to minimize the area of a codimension-two hypersurface in the bulk geometry (4.6) whose boundary coincides with the boundary of the entangling region. Given the symmetry of both the background metric and of the shape of the entangling region, we can safely assume that the corresponding codimension-two hypersurface can be described as a function $r(\rho,\varphi)$ and therefore the induced metric on the hypersurface is

$$ds^2_{\text{ind}} = \frac{L^2}{r_F^{2\frac{\theta}{d}}} \frac{(1+r'^2)d\rho^2 + (\rho^2+\dot{r}^2)d\varphi^2 + 2r'\dot{r}d\rho d\varphi + \rho^2\sin^2\varphi\, d\Omega_n^2 + d\vec{x}^2_{d-n-2}}{r^{2(1-\frac{\theta}{d})}}. \tag{4.8}$$

where $r' = \partial_\rho r$ and $\dot{r} = \partial_\varphi r$. By computing the volume element associated to this induced metric we are able to compute the area of the surface, and thus the holographic entanglement entropy, as follows

$$\mathcal{A} = \epsilon_n \frac{\Omega_n V_{d-2-n} L^d}{r_F^\theta} \int d\rho\, d\varphi\, \frac{\rho^n \sin^n\varphi}{r^{d-\theta}} \sqrt{\rho^2(1+r'^2)+\dot{r}^2}, \tag{4.9}$$

where V_{d-n-2} is the regularized volume of $\mathbb{R}^{d-n-2}$ space and Ω_n is the volume of the $n-$sphere, S^n. We introduced $\epsilon_n = 1+\delta_{n0}$ to make sure that for $n=0$ there is a factor of 2, as for $n=0$ the integral over φ still span from 0 to Ω.

Treating the above area functional as an action for a two-dimensional dynamical system, we just need to solve the equations of motion coming from the variation of the action to find the profile $r(\rho,\varphi)$. Note, however, that since the entangling region is invariant under rescaling of coordinates, dimensional analysis allows to further constrain the solution to take the form

$$r(\rho,\varphi) = \rho\, h(\varphi) \tag{4.10}$$

so that $h(\Omega)=0$ and, given radial symmetry of the background and of the entangling region, $h'(0)=0$. To find the area one should then compute the on-shell integral (4.9). However, given that the integral is UV-divergent, we have to restrict the integration over the portion of surface $r \geq \varepsilon$, and eventually perform the limit $\varepsilon \to 0$ only after a regularization. In this regard, the domain Σ_ε over which the integration has to be carried out becomes

$$\Sigma_\varepsilon = \left\{\rho \in [\varepsilon/h_0, H] \text{ and } \varphi \in [0, h^{-1}(\varepsilon/\rho)]\right\} \tag{4.11}$$

where $h_0 \equiv h(0)$ and $H \gg \varepsilon$ is an arbitrarily big cut-off for the length of the sides of the singular surfaces. Moreover from the positivity of r it follows $h^{-1}(\varepsilon\rho) < \Omega$.

To solve the equation of motion derived from the action (4.9) it is more convenient to consider φ as a function of h, *i.e.* $\varphi = \varphi(h)$. In this notation, setting $r = \rho h$, the area (4.9) reads

$$\mathcal{A} = \epsilon_n \frac{\Omega_n V_{d-n-2} L^d}{r_F^\theta} \int_{\varepsilon/h_0}^{H} \frac{d\rho}{\rho^{d_\theta - n - 1}} \int_{\varepsilon/\rho}^{h_0} dh \frac{\sin^n \varphi}{h^{d_\theta}} \sqrt{1 + (1+h^2)\,\varphi'^2}, \tag{4.12}$$

where $d_\theta \equiv d - \theta$. The equation of motion for $\varphi(h)$ is then

$$nh\left(\varphi'^2 + \frac{1}{1+h^2}\right)\cot\varphi + \varphi'\left[\left(\left(h^2+1\right)d_\theta - h^2\right)\varphi'^2 + d_\theta - \frac{2h^2}{(h^2+1)}\right] - h\varphi'' = 0, \tag{4.13}$$

For $n = 0$ this equation, and the expression for the area (4.9), simplify significantly, and become equivalent to the equation and area functional first studied *e.g.* in [59]. Indeed in this case the corresponding singular surface is a pure crease $k \times \mathbb{R}^{d-2}$.

Since (4.13) is invariant under $h \to -h$ we have that $\varphi(h)$ is an even function. Therefore, if we want to understand the behaviour of the solution near the boundary, we can Taylor expand $\varphi(h)$ as follows

$$\varphi(h) = \sum_{i=0}^{+\infty} \varphi_{2i}\, h^{2i}, \tag{4.14}$$

so that, by substituting it in (4.13), the solution can be found order by order by fixing the coefficients φ_{2i}. Indeed for the first three orders one finds

$$\begin{aligned}
&\Big(2(d_\theta - 1)\varphi_2 + n\cot\Omega\Big)h \\
&+\Big[8\varphi_2^3 d_\theta + n\cot\Omega\left(4\varphi_2^2 - \varphi_2\cot\Omega - 1\right) - \varphi_2(n+4) + 4\varphi_4(d_\theta - 3)\Big]h^3 \\
&+\Big[-n\left(4\varphi_2^3 - \varphi_2 + \varphi_4\right)\cot^2\Omega + \varphi_2^3(8d_\theta - 4n - 8) + 48 d_\theta \varphi_2^2 \varphi_4 + n\left(\varphi_2^2 + 16\varphi_2\varphi_4 + 1\right)\cot\Omega \\
&\quad + n\varphi_2^2\cot^3\Omega + (n+4)\varphi_2 - (n+8)\varphi_4 + 6(d_\theta - 5)\varphi_6\Big]h^5 + \cdots = 0.
\end{aligned} \tag{4.15}$$

It is clear from this expression that for $d_\theta = 2k+1$ with $k = 0, 1, \cdots$, the coefficient φ_{2k+2} cannot be fixed by this Taylor series. In fact when d_θ is an odd number one has to modify the expansion by allowing for a non-analytic logarithmic term, as in [120]. More precisely for generic d_θ one has

$$\varphi(h) = \sum_{i=0}^{[\frac{d_\theta}{2}]-1} \varphi_{2i}\, h^{2i} + \varphi_{2[\frac{d_\theta}{2}]} h^{2[\frac{d_\theta}{2}]}\left(c + \frac{1}{2}\delta_{2[\frac{d_\theta}{2}]+1, d_\theta}\log h^2\right) + \mathcal{O}(h^{2[\frac{d_\theta}{2}]+2}), \tag{4.16}$$

where we denote with $[y]$ the integer part of y. With this Taylor expansion the equation of motion can be solved up to order $\mathcal{O}(h^{2[\frac{d_\theta}{2}]})$ which is enough to fix all φ_{2i} for $i = 1, \cdots, [\frac{d_\theta}{2}]$. Note the constant c in the above expansion remains undetermined. The explicit expression for the coefficients φ_{2i} for the few first terms is presented in the Appendix D.2.

Since the solution is regular at the boundary, we can expand in the same manner the integrand of the area functional (4.12) around $h = 0$

$$\frac{\sin^n\varphi}{h^{d_\theta}}\sqrt{1 + (1+h^2)\varphi'^2} = \sum_{i=0}^{[\frac{d_\theta}{2}]-1} \frac{a_{2i}}{h^{d_\theta - 2i}} + \frac{a_{2[\frac{d_\theta}{2}]}}{h}\delta_{2[\frac{d_\theta}{2}]+1, d_\theta} + \text{finite terms}, \tag{4.17}$$

where the coefficients a_{2i} can be expressed in terms of φ_{2i}. The explicit expression of the coefficients a_{2i} for few first terms are presented in Appendix D.2.

To regularize the area functional one may add and subtract the singular terms to make the integration over h finite. Denoting the regular part of the integrand by $A_{\rm reg}$ the equation (4.12) reads

$$\mathcal{A}=\epsilon_n\frac{\Omega_n V_{d-n-2}L^d}{r_F^\theta}\int_{\varepsilon/h_0}^{H}\frac{d\rho}{\rho^{d_\theta-n-1}}\left[\int_0^{h_0}dh\;A_{\rm reg}+\int_{\varepsilon/\rho}^{h_0}dh\left(\sum_{i=0}^{[\frac{d_\theta}{2}]-1}\frac{a_{2i}}{h^{d_\theta-2i}}+\frac{a_{2[\frac{d_\theta}{2}]}}{h}\delta_{2[\frac{d_\theta}{2}]+1,d_\theta}\right)\right], \tag{4.18}$$

where

$$A_{\rm reg}=\frac{\sin^n\varphi}{h^{d_\theta}}\sqrt{1+(1+h^2)\varphi'^2}-\left(\sum_{i=0}^{[\frac{d_\theta}{2}]-1}\frac{a_{2i}}{h^{d_\theta-2i}}+\frac{a_{2[\frac{d_\theta}{2}]}}{h}\delta_{2[\frac{d_\theta}{2}]+1,d_\theta}\right). \tag{4.19}$$

It is then straightforward to perform the integration over h for the last term. Doing so, one arrives at

$$\mathcal{A}=\epsilon_n\frac{\Omega_n V_{d-n-2}L^d}{r_F^\theta}A_0\int_{\varepsilon/h_0}^{H}\frac{d\rho}{\rho^{d_\theta-n-1}}+\epsilon_n\frac{\Omega_n V_{d-n-2}L^d}{r_F^\theta}\int_{\varepsilon/h_0}^{H}d\rho A_1(\rho), \tag{4.20}$$

where

$$\begin{aligned}A_0 &= \sum_{i=0}^{[\frac{d_\theta}{2}]-1}\frac{-a_{2i}}{(d_\theta-2i-1)h_0^{d_\theta-2i-1}}+a_{2[\frac{d_\theta}{2}]}\delta_{2[\frac{d_\theta}{2}]+1,d_\theta}\log h_0+\int_0^{h_0}dh\;A_{\rm reg}\,,\\ A_1(\rho) &= \sum_{i=0}^{[\frac{d_\theta}{2}]-1}\frac{a_{2i}}{(d_\theta-2i-1)}\frac{\rho^{n-2i}}{\varepsilon^{d_\theta-2i-1}}+a_{2[\frac{d_\theta}{2}]}\delta_{2[\frac{d_\theta}{2}]+1,d_\theta}\frac{\log\frac{\rho}{\varepsilon}}{\rho^{d_\theta-n-1}}\,.\end{aligned} \tag{4.21}$$

In order to evaluate the last integral in the equation (4.20) special care is needed. Indeed if n is an odd number then one may get a logarithmically divergent term from integration over ρ when $i=[\frac{n}{2}]+1$, which may happen only if $[\frac{n}{2}]\leq[\frac{d_\theta}{2}]-2$, which can happen only for $d_\theta\geq 4$. Therefore it is useful to rewrite $A_1(\rho)$ as follows

$$A_1(\rho)=\sum_{i=0}^{[\frac{d_\theta}{2}]-1\,\prime}\frac{a_{2i}}{(d_\theta-2i-1)}\frac{\rho^{n-2i}}{\varepsilon^{d_\theta-2i-1}}+\delta_{2[\frac{n}{2}]+1,n}\frac{a_{2[\frac{n}{2}]+2}\;\varepsilon^{3-d_\theta+2[\frac{n}{2}]}}{(d_\theta-2[\frac{n}{2}]-3)\rho}+\delta_{2[\frac{d_\theta}{2}]+1,d_\theta}\frac{a_{2[\frac{d_\theta}{2}]}\log\frac{\rho}{\varepsilon}}{\rho^{d_\theta-n-1}}, \tag{4.22}$$

where the prime in the summation indicates that when n is an odd number the term at position $i=[\frac{n}{2}]+1$ should be excluded from the sum. With this notation and for $d_\theta-n\neq 2$ one finds

$$\begin{aligned}\int_{\varepsilon/h_0}^{H}d\rho\;A_1(\rho)=&\sum_{i=0}^{[\frac{d_\theta}{2}]-1\,\prime}\frac{a_{2i}}{(n-2i+1)(d_\theta-2i-1)}\left(\frac{H^{n-2i+1}}{\varepsilon^{d_\theta-2i-1}}-\frac{h_0^{2i-n-1}}{\varepsilon^{d_\theta-n-2}}\right)\\ &-\frac{a_{2[\frac{d_\theta}{2}]}\delta_{2[\frac{d_\theta}{2}]+1,d_\theta}}{(d_\theta-n-2)^2}\left(\frac{1+(d_\theta-n-2)\log\left(\frac{H}{\varepsilon}\right)}{H^{d_\theta-n-2}}-\frac{1-(d_\theta-n-2)\log h_0}{(\varepsilon/h_0)^{d_\theta-n-2}}\right)\\ &+\delta_{2[\frac{n}{2}]+1,n}\frac{a_{2[\frac{n}{2}]+2}}{(d_\theta-2[\frac{n}{2}]-3)}\;\frac{\log\frac{Hh_0}{\varepsilon}}{\varepsilon^{d_\theta-2[\frac{n}{2}]-3}}\,.\end{aligned} \tag{4.23}$$

Moreover from the first term in (4.20) and for $d_\theta-n\neq 2$ one gets

$$\int_{\varepsilon/h_0}^{H}\frac{d\rho}{\rho^{d_\theta-n-1}}=\frac{1}{d_\theta-n-2}\left(\frac{h_0^{d_\theta-n-2}}{\varepsilon^{d_\theta-n-2}}-\frac{1}{H^{d_\theta-n-2}}\right). \tag{4.24}$$

Altogether the divergent terms of the holographic entanglement entropy for $d_\theta\neq n+2$ are obtained

$$S=\epsilon_n\frac{\Omega_n V_{d-n-2}L^d}{4Gr_F^\theta}\left[\sum_{i=0}^{[\frac{d_\theta}{2}]-1\,\prime}\frac{a_{2i}}{(n-2i+1)(d_\theta-2i-1)}\left(\frac{H^{n-2i+1}}{\varepsilon^{d_\theta-2i-1}}-\frac{h_0^{2i-n-1}}{\varepsilon^{d_\theta-n-2}}\right)+\frac{\delta_{2[\frac{n}{2}]+1,n}a_{2[\frac{n}{2}]+2}}{(d_\theta-2[\frac{n}{2}]-3)}\;\frac{\log\frac{Hh_0}{\varepsilon}}{\varepsilon^{d_\theta-2[\frac{n}{2}]-3}}\right.$$

$$+\quad \frac{A_0}{d_\theta-n-2}\frac{h_0^{d_\theta-n-2}}{\varepsilon^{d_\theta-n-2}}-\frac{a_{2[\frac{d_\theta}{2}]}\delta_{2[\frac{d_\theta}{2}]+1,d_\theta}}{d_\theta-n-2}\left(\frac{\log\left(\frac{H}{\varepsilon}\right)}{H^{d_\theta-n-2}}-\frac{1-(d_\theta-n-2)\log h_0}{(d_\theta-n-2)(\varepsilon/h_0)^{d_\theta-n-2}}\right)\Bigg]+\text{finite terms.}\quad (4.25)$$

From this general expression we observe that the holographic entanglement entropy for a singular surface shaped as $c_n\times\mathbb{R}^{d-n-2}$ contains many divergent terms including, when d_θ is an odd number[3], a logarithmically divergent term whose coefficient is universal, in the sense that it is ε independent. This is the same behaviour for a generic entangling region where in even dimensional CFTs the entanglement entropy contains always a logarithmically divergent term.

On the other hand when $d_\theta=n+2$ the holographic entanglement entropy gets new logarithmic divergences. Indeed in this case the last two terms in (4.25) get modified, leading to

$$S=\epsilon_n\frac{\Omega_n V_{d-n-2}L^d}{4Gr_F^\theta}\Bigg[\sum_{i=0}^{\lceil\frac{d_\theta}{2}\rceil-1}{}'\frac{a_{2i}}{(n-2i+1)(d_\theta-2i-1)}\left(\frac{H^{n-2i+1}}{\varepsilon^{d_\theta-2i-1}}-\frac{h_0^{2i-n-1}}{\varepsilon^{d_\theta-n-2}}\right)+\frac{\delta_{2[\frac{n}{2}]+1,n}a_{2[\frac{n}{2}]+2}}{(d_\theta-2[\frac{n}{2}]-3)}\frac{\log\frac{Hh_0}{\varepsilon}}{\varepsilon^{d_\theta-2[\frac{n}{2}]-3}}$$
$$+A_0\log\frac{Hh_0}{\varepsilon}+\frac{a_{2[\frac{d_\theta}{2}]}}{2}\,\delta_{2[\frac{d_\theta}{2}]+1,d_\theta}\log^2\left(\frac{H}{\varepsilon}\right)\Bigg]+\text{finite terms.}\quad (4.26)$$

It is easy to see that for $\theta=0$ these results reduce to that in [120]. In particular for $\theta=0$ and odd d (even dimension in the notation of [120]) where $d=n+2$ one finds a new $\log^2 H/\varepsilon$ divergent term. Comparing with the table 1 in [120] this divergent term appears in background space-times $\mathbb{R}^4$ and $\mathbb{R}^6$ with cones c_1 and c_3 respectively. For both cases we have $d=n+2$.

It is, however, interesting to note that in the present case the condition to get squared logarithmic terms is $d_\theta=n+2$ (for $d_\theta\geq 2$) which allows us to have this divergent term in any dimension if the hyperscaling violating exponent, θ, is chosen properly.

4.2 New divergences and universal terms

In the previous section we have studied possible divergent terms which could appear in the expression for the area of minimal surfaces ending on singular boundary regions. However, we should be able to distinguish which new logarithmic divergences arise because of the singular shape of the entangling region and which arise because of the choice of a non trivial hyperscaling violating exponent θ. To this purpose and to isolate the universal terms coming from the choice of the shape and not of the background, we study, in this section, the behaviour of the divergences in the HEE for a smooth region, and compare with the results of the previous section.

To find the divergent terms for a smooth surface, following our notation, we will parametrize the metric as follows

$$ds^2=\frac{L^2}{r_F^{2\frac{\theta}{d}}}\,\frac{-r^{2(1-z)}dt^2+dr^2+d\rho^2+\rho^2(d\varphi^2+\sin^2\varphi d\Omega_n^2)+d\vec{x}_{d-n-2}^2}{r^{2(1-\frac{\theta}{d})}}.\quad (4.27)$$

We would like to compute the holographic entanglement entropy for a smooth entangling region given by

$$t=\text{fixed}\qquad \rho\leq H,\quad (4.28)$$

with this condition it is clear that the entangling region consists of the direct product between a ball and an infinite hyperplane, namely $B^n\times\mathbb{R}^{d-n-2}$. Notice that the procedure outlined here is way different than the technique adopted in Section 3.2.2 of Chapter 3, since there we kept z as a function of ρ. The final result for the divergences of the area is, of course, the same.

To compute the entanglement entropy again we should essentially minimize the area which in our case is given by

$$\mathcal{A}_{\text{smooth}}=\frac{\Omega_n V_{d-n-2}L^d}{r_F^\theta}\int_0^\pi d\varphi\sin^n\varphi\int dr\,\frac{\rho^{n+1}\sqrt{1+\rho'^2}}{r^{d_\theta}}.\quad (4.29)$$

[3]It is worth noting that although the dimension d is an integer number, the hyperscaling violating exponent, θ, does not need to be an integer number. Therefore the effective dimension, d_θ, generally, may not be an integer. For non-integer d_θ we do not get any universal terms.

Using this expression and following the procedure we have explored in the previous section one can find the divergent terms of holographic entanglement entropy for the smooth entangling surface (4.28) as follows

$$S_{\rm smooth}=\epsilon_n\frac{\sqrt{\pi}\Gamma\left(\frac{n+1}{2}\right)\Omega_n V_{d-n-2}L^d}{4Gr_F^\theta\Gamma\left(\frac{n}{2}+1\right)}\left(\sum_{i=0}^{[\frac{d_\theta}{2}]-1}\frac{b_{2i}}{d_\theta-2i-1}\frac{1}{\varepsilon^{d_\theta-2i+1}}+b_{2[\frac{d_\theta}{2}]}\delta_{2[\frac{d_\theta}{2}]+1,d_\theta}\log\frac{H}{\varepsilon}\right)+\text{finite terms}. \tag{4.30}$$

where b_{2i}'s are coefficients appearing in the expansion of the area

$$\frac{\rho^{n+1}\sqrt{1+\rho'^2}}{r^{d_\theta}}=\sum_{i=0}^{[\frac{d_\theta}{2}]-1}\frac{b_{2i}}{r^{d_\theta-2i}}+\delta_{2[\frac{d_\theta}{2}]+1,d_\theta}\frac{b_{2[\frac{d_\theta}{2}]}}{r}\,, \tag{4.31}$$

which can be found from the equation of motion deduced from (4.29). In particular the coefficient of the universal term for different (odd) d_θ is found to be

$$\begin{aligned} d_\theta=1 \quad &: \quad b_0=H^{n+1},\\ d_\theta=3 \quad &: \quad b_2=-\frac{(1+n)^2}{8}H^{n-1}. \end{aligned} \tag{4.32}$$

Setting $n=d-2$ in the above expressions we find the universal term of the holographic entanglement entropy for a sphere.

We can make another choice of a smooth entangling region, that is an infinite strip (i.e. the product between an interval and an hyperplane). Denoting the width of the strip by ℓ, the corresponding entanglement entropy for $d_\theta\neq 1$ is [78, 169]

$$S_{\rm smooth}=\frac{L^dV_{d-1}}{4(d_\theta-1)Gr_F^{d-d_\theta}}\left[\frac{2}{\varepsilon^{d_\theta-1}}-\left(\frac{2\sqrt{\pi}\Gamma\left(\frac{d_\theta+1}{2d_\theta}\right)}{\Gamma\left(\frac{1}{2d_\theta}\right)}\right)^{d_\theta}\frac{1}{\ell^{d_\theta-1}}\right], \tag{4.33}$$

while for $d_\theta=1$ one has

$$S_{\rm smooth}=\frac{L^dV_{d-1}}{2Gr_F^{d-1}}\log\frac{\ell}{\varepsilon}. \tag{4.34}$$

It is worth noting that when $d_\theta=1$ the leading divergent term is logarithmic, indicating that the dual strongly coupled field theory exhibits a Fermi surface [79, 80].

Comparing these expressions with equations (4.25) and (4.26) one observes that beside the standard divergences, there are new divergent terms due to singular structure of the entangling region. In particular there are either new log or $\log^2$ terms, whose coefficients are universal in the sense that they are independent of the UV cut-off. To proceed note that for $d_\theta\neq n+2$ the universal term should be read from equation (4.25), that is

$$S_{\rm univ}=-\delta_{2[\frac{d_\theta}{2}]+1,d_\theta}\,\epsilon_n\frac{\Omega_nV_{d-n-2}a_{2[\frac{d_\theta}{2}]}L^dH^{n+2-d_\theta}}{4(d_\theta-n-2)\,r_F^\theta\,G}\log\left(\frac{H}{\varepsilon}\right), \tag{4.35}$$

which is non-zero for odd d_θ. On the other hand for $d_\theta=n+2$ the universal term can be found from (4.26) to be

$$S_{\rm univ}=\epsilon_n\frac{\Omega_nV_{d-n-2}L^d}{4G\,r_F^\theta}\left[A_0\log\frac{Hh_0}{\varepsilon}+\frac{a_{2[\frac{d_\theta}{2}]}}{2}\,\delta_{2[\frac{d_\theta}{2}]+1,d_\theta}\log^2\left(\frac{H}{\varepsilon}\right)\right]. \tag{4.36}$$

Observe that in this case for any (integer) d_θ the first term is always present though the $\log^2$ term appears just for odd d_θ. As already noted in [120], it is important to note that when d_θ is odd the universal term is given by $\log^2$ and the term linear in $\log\varepsilon$ is not universal any more.

Using these results one may define the coefficient of the logarithmic term, normalized to the volume of the entangling region, as follows

$$C^{\rm EE}_{\rm singular}=-\epsilon_n\frac{3L^d}{4(d_\theta-n-2)G}\,a_{2[\frac{d_\theta}{2}]},\qquad \text{for } d_\theta \text{ odd, and } d_\theta\neq n+2,$$

$$C^{\rm EE}_{\rm singular} = -\epsilon_n \frac{3L^d}{4G} \frac{a_{2[\frac{d_\theta}{2}]}}{2}, \qquad \text{for } d_\theta \text{ odd, and } d_\theta = n+2,$$
$$C^{\rm EE}_{\rm singular} = -\epsilon_n \frac{3L^d}{4G} A_0, \qquad \text{for } d_\theta \text{ even, and } d_\theta = n+2, \tag{4.37}$$

where the explicit form of A_0 and $a_{2[\frac{d_\theta}{2}]}$ are given in the previous section and in the Appendix D.2. The factor of 3 in the above expressions is due to our normalization, which has been fixed by comparing with the entanglement entropy of 2D CFT written as $\frac{c}{3}\log \ell/\varepsilon$.

Although the general form of the coefficients of the universal terms are given in the equation (4.37) it is illustrative to present their explicit forms for particular values of n and d_θ.

4.2.1 $d_\theta = 1$

As we have seen the holographic entanglement entropy for a hyperscaling violating metric exhibits a log term divergence for $d_\theta = 1$ even for a smooth surface. This may be understood from the fact that the underlying dual theory may have a Fermi surface [79, 80]. For $\theta = 0$ (that is $d = 1$) we indeed recover the logarithmic term of 2D conformal field theories[18]. When $\theta \neq 0$ the physics is essentially controlled by the effective dimension $d_\theta = d - \theta$. Therefore even for higher dimensions $d \geq 2$ with a proper θ such that $d_\theta = 1$ the holographic entanglement entropy always exhibit a leading logarithmically divergent term.

In this case for an entangling region with a singularity, which clearly is meaningful only for $d \geq 2$, using the explicit expression for a_0 one gets

$$C^{\rm EE}_{\rm singular} = \epsilon_n \frac{3L^d}{4G} \frac{\sin^n \Omega}{n+1}, \tag{4.38}$$

while for a smooth surface one has

$$C^{\rm EE}_{\rm smooth} = \epsilon_n \frac{3L^d}{4G} \tag{4.39}$$

Note that for $n = 0$ both charges become the same. Note that for $n > 1$ the coefficient of universal term $C^{\rm EE}_{\rm singular}$ is smaller than the one of the strip by a factor of $\frac{\sin^n \Omega}{2(n+1)}$ and it vanishes in the limit of $\Omega \to 0$.

4.2.2 $d_\theta = 2$

For $d_\theta = 2$ being an even number, the holographic entanglement entropy has a universal logarithmic term only for $n = 0$ which is

$$C^{\rm EE}_{\rm singular} = \frac{3L^d}{2G} A_0, \tag{4.40}$$

where

$$A_0 = -\frac{1}{h_0} + \int_0^{h_0} dh \left(\frac{\sqrt{1 + (1+h^2)\varphi'^2}}{h^2} - \frac{1}{h^2} \right). \tag{4.41}$$

Actually since the expressions we have found are independent of θ one may use the results of $d = 2, \theta = 0$ to compute the above universal term. Indeed in this case one has (see for example [59, 120, 166])

$$C^{\rm EE}_{\rm singular} = \begin{cases} \frac{3L^d}{2\pi G} \frac{\Gamma(\frac{3}{4})^4}{\Omega} & \Omega \to 0, \\ \frac{3L^d}{8\pi G} (\frac{\pi}{2} - \Omega)^2 & \Omega \to \frac{\pi}{2}. \end{cases} \tag{4.42}$$

4.2.3 $d_\theta = 3$

In this case when $n \neq 1$ the holographic entanglement entropy has a log term whose coefficient may be treated as a universal factor given by

$$C^{\rm EE}_{\rm singular} = \frac{3n^2 L^d}{32G} \frac{\cos^2 \Omega}{(1-n)\sin^{2-n} \Omega}. \tag{4.43}$$

On the other hand for $n = 1$ the universal term should be read from the $\log^2$ term with the coefficient

$$C^{\rm EE}_{\rm singular} = \frac{3L^d}{32G}\frac{\cos^2\Omega}{2\sin\Omega}. \tag{4.44}$$

which in the limit of planar and zero angle behaves as

$$C^{\rm EE}_{\rm singular} = \begin{cases} \dfrac{3n^2L^d}{32G}\dfrac{1}{(1-n)\Omega^{2-n}} & \Omega \to 0, \\ \dfrac{3n^2L^d}{32G}\dfrac{(\frac{\pi}{2}-\Omega)^2}{1-n} & \Omega \to \frac{\pi}{2}. \end{cases} \tag{4.45}$$

Note that for $n = 1$ the factor of $1 - n$ in the denominator should be replaced by 2. It is worth noting that for $n = 0$ the universal charge is zero identically. Therefore for a singular surface containing a crease there is not a universal term.

4.2.4 $d_\theta = 4$

In this case we get only for $n = 2$ a universal term, which should be read from the equation (4.36), that is

$$C^{\rm EE}_{\rm singular} = \frac{3L^d}{4G}A_0, \tag{4.46}$$

where

$$A_0 = \frac{\sin^2\Omega}{3h_0^3} - \frac{4}{9}\frac{\cos^2\Omega}{h_0} + \int_0^{h_0} dh \left(\frac{\sin^2\varphi\sqrt{1+(1+h^2)\varphi'^2}}{h^4} + \frac{\sin^2\Omega}{h^4} - \frac{4}{9}\frac{\cos^2\Omega}{h^2} \right). \tag{4.47}$$

Since we have $n = 2$ this result is valid for $d \geq 4$.

The computation of A_0 cannot be performed analytically, since we are not able to find a closed expression for the profile $h(\varphi)$, however it can still be found numerically.
We solved the equation of motion for φ and found it as a function of h_0, thus founding the dependence of Ω on h_0. Then we computed the area and by shooting the solution we were able to find A_0 as a function of the opening angle Ω. The results are shown in Fig. 4.1. One observes that qualitatively

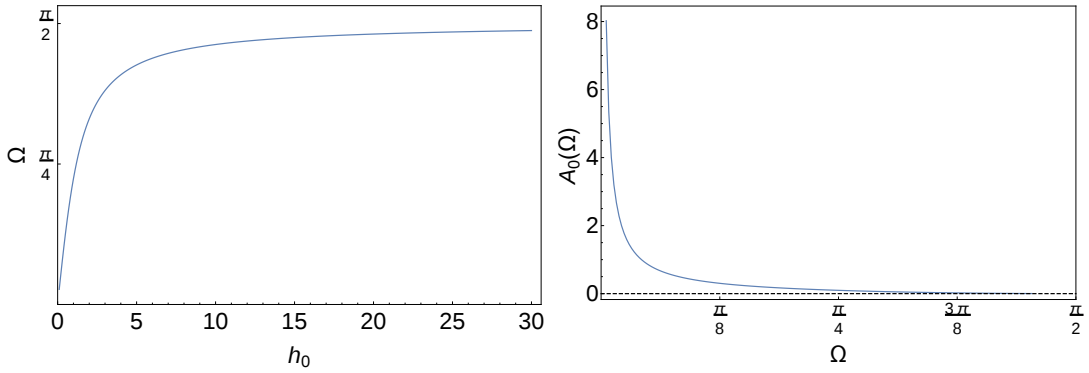

Figure 4.1: Ω as a function of h_0 (left) and A_0 as a function of Ω (right). It shows that the function A_0 diverges at $\Omega = 0$ while vanishes at $\Omega = \frac{\pi}{2}$.

A_0 diverges at $\Omega = 0$ while vanishes at $\pi/2$. To make this statement more precise we have numerically studied asymptotic behaviours of the function A_0 for $\Omega \to 0$ and $\Omega \to \frac{\pi}{2}$ limits as shown in Fig 4.2. The results may be summarized as follows

$$C^{\rm EE}_{\rm singular} = \begin{cases} \dfrac{3L^d}{4G}\dfrac{0.116}{\Omega}, & \Omega \to 0, \\ \dfrac{3L^d}{4G}\dfrac{1.683}{4\pi}\left(\dfrac{\pi}{2}-\Omega\right)^2, & \Omega \to \frac{\pi}{2}. \end{cases} \tag{4.48}$$

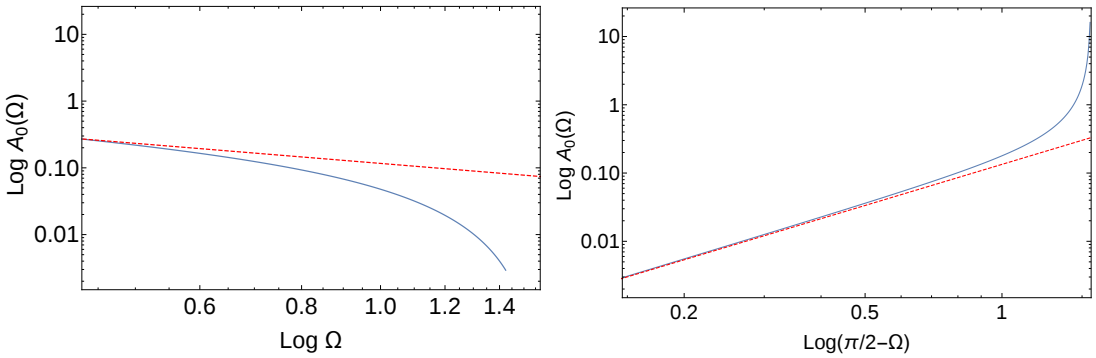

Figure 4.2: Asymptotic behaviours of A_0 at $\Omega \to 0$ (left) and $\Omega \to \frac{\pi}{2}$(right). In these plots the dashed lines correspond to test functions to probe the limiting value of A_0. The corresponding functions are given by $y = -x - 2.15$ (left) and $y = 2x - 2.01$ (right), in agreement with equation (4.48).

4.2.5 $d_\theta = 5$

In this case and when $n \neq 3$ we get

$$C^{\rm EE}_{\rm singular} = \frac{3n^2 L^d}{4G}\,\frac{\left(7n^2-64\right)\cos(2\Omega)+n(7n-32)+64}{4096(3-n)}\,\frac{\cos^2\Omega}{\sin^{4-n}\Omega} \tag{4.49}$$

while for $n = 3$

$$C^{\rm EE}_{\rm singular} = \frac{3L^d}{4G}\,\frac{9(31-\cos 2\Omega)}{4096}\,\frac{\cos^2\Omega}{\sin\Omega}. \tag{4.50}$$

Therefore the corresponding universal term has the following asymptotic behaviours

$$C^{\rm EE}_{\rm singular} = \begin{cases} \dfrac{3n^2L^d}{4G}\,\dfrac{2n(7n-16)}{4096(3-n)}\,\dfrac{1}{\Omega^{4-n}}, & \Omega \to 0, \\ \dfrac{3n^2L^d}{4G}\,\dfrac{32(4-n)}{4096(3-n)}\left(\dfrac{\pi}{2}-\Omega\right)^2, & \Omega \to \frac{\pi}{2}, \end{cases} \tag{4.51}$$

with an obvious replacement for $n = 3$.

It is also straightforward to further consider higher d_θ. The lesson we learn from these explicit examples is that for a singular surface of the form $c_n \times \mathbb{R}^{d-n-2}$ and for $d_\theta \geq 2$ the coefficient of the universal term given in the equation (4.37) has the following generic asymptotic behaviour

$$C^{\rm EE}_{\rm singular} \sim \begin{cases} \dfrac{3L^d}{4G}\,\dfrac{1}{\Omega^{d_\theta-n-1}}, & \Omega \to 0, \\ \dfrac{3L^d}{4G}\left(\dfrac{\pi}{2}-\Omega\right)^2, & \Omega \to \frac{\pi}{2}. \end{cases} \tag{4.52}$$

We see that for a generic opening angle Ω, we can infer the following expression for the coefficient of the universal term

$$C^{\rm EE}_{\rm singular} = f_{d_\theta,n}(\Omega)\,\frac{3L^d}{4G}\,\frac{\cos^2\Omega}{\sin^{d_\theta-n-1}\Omega}, \tag{4.53}$$

where $f_{d_\theta,n}(\Omega)$ is a function of Ω which is fixed for given d_θ and n by requiring it to be finite at $\Omega = 0$ and $\Omega = \frac{\pi}{2}$.

4.3 Higher derivatives corrections

In the previous section we showed that the area of minimal surfaces ending on singular entangling regions may present logarithmic divergences for specific choices of the extension of the singularity, the

dimensionality of the space time and the value of θ. The coefficients of these divergent terms depend on the opening angle of the region, and we were able to compute their value in the nearly smooth limit.

Based on these results and using the general expression given in the equation (4.37) for $d_\theta \geq 2$ one may define a new *charge* as follows

$$C_d^n = \lim_{\Omega \to \frac{\pi}{2}} \frac{C^{\rm EE}_{\rm singular}}{\cos^2 \Omega}. \tag{4.54}$$

Note that this is a well defined limit, leading to a finite quantity which is proportional to $\frac{L^d}{G}$ up to a numerical factor of order of one. Note also that as soon as we fixed d_θ the resulting charge is independent of θ, and may be defined in any dimension by setting $n = d_\theta - 2$.

As we have already mentioned there is another central charge which could be defined in any dimension: the coefficient of the $< TT >$ two-point function of the stress-energy tensor, which we denote by C_T. Following the idea of [166, 167], we can compare these two charges[4]. Unlike two-dimensional CFT where C_T is the same as the one appearing in the central extension of the Virasoro algebra, in higher dimensions it should be read from the explicit expression of the two-point function. Indeed, in the present context, the corresponding two-point function may be found from the quadratic on-shell action of the perturbation of the metric above a vacuum solution using holographic renormalization techniques[6].

We note, however, that since we do not have a well defined asymptotic behaviour of metric (D.4) in the sense of Fefferman-Graham expansion, in general it is not an easy task to compute the stress-energy tensor's two-point function for space-times with generic θ and z. Nevertheless setting $z = 1$, where one recovers the Lorentz invariance, we can still use the holographic renormalization procedure to find (see Appendix D.1)

$$C_T = \frac{L^d}{8\pi G} \frac{d+2}{d} \frac{\Gamma(d_\theta + 2)}{\pi^{\frac{d+1}{2}} \Gamma\left(\frac{1+2d_\theta - d}{2}\right)}. \tag{4.55}$$

Note that for $z = 1$, from the null energy condition one gets $\theta(d-\theta) \leq 0$ which has only a partial overlap with the parameter space of the model we are considering at $\theta = 0$. Therefore using the above expression we really should only compare it with the new central charge of the model for $\theta = 0$.
Since however the new charge defined in (4.54) for given d_θ is independent of θ, the comparison still makes sense. In particular for $d_\theta = 2, 3$ and $d_\theta = 4$, respectively, one finds[5]:

$$\frac{C_d^0}{C_T} = \frac{d\, \pi^{\frac{d+1}{2}} \Gamma\left(\frac{5-d}{2}\right)}{2(d+2)}, \qquad \frac{C_d^1}{C_T} = -\frac{d\, \pi^{\frac{d+3}{2}} \Gamma\left(\frac{7-d}{2}\right)}{64(d+2)}, \qquad \frac{C_d^2}{C_T} = 1.683 \frac{d\, \pi^{\frac{d+1}{2}} \Gamma\left(\frac{9-d}{2}\right)}{80(d+2)} \tag{4.56}$$

For $z \neq 1$, C_T depends explicitly on z and thus the above ratio will be z dependent, even though C_d^n will not.

Since both central charges considered above are proportional to $\frac{L^d}{G}$, it is evident that their ratio is a purely numerical constant. In [167] it was conjectured that for three-dimensional CFTs this ratio could be completely universal, regardless of the strength of the coupling so to hold in both known statistical models and in QFTs with gravity duals. It is thus interesting to understand whether this ratio, which could characterize whatsoever CFT of fixed dimensionality, is still universal even in the higher dimensional cases we are considering.
The easiest step we can make in this direction is to look at gravity theories with higher curvature terms in the action, and see whether the corrections alter the ratio (4.56) .

To proceed let us consider an action containing the most general curvature squared corrections as follows

$$I = -\frac{1}{16\pi G} \int d^{d+2} \sqrt{-g} \Big(R + V(\phi) + \lambda_1 R^2 + \lambda_2 R_{\mu\nu} R^{\mu\nu} + \lambda_3 R_{\mu\nu\rho\sigma} R^{\mu\nu\rho\sigma} \Big) + I_{\rm matter} \tag{4.57}$$

where $I_{\rm matter}$ is a proper matter action to make sure that the model admits hyperscaling violating geometry. It is then straightforward, although lengthy, to compute holographic entanglement entropy for

[4]Note that in even dimensions one may have another central charge, the coefficient of Euler density arising in the computations of the Weyl anomaly. It also appears as the universal term in the expression of entanglement entropy for a sphere.

[5]Due to our normalization of C_d for $d_\theta = d = 2$ there is factor $\frac{1}{3}$ mismatch with the result of [167].

this model[6]. Indeed following [53], the holographic entanglement entropy may be obtained by minimizing the following entropy functional

$$S_A=\frac{1}{4G}\int d^d\zeta\,\sqrt{\gamma}\,\left[1+2\lambda_1 R+\lambda_2\left(R_{\mu\nu}n_i^\mu n_i^\nu-\frac{1}{2}\mathcal{K}^i\mathcal{K}_i\right)+2\lambda_3\left(R_{\mu\nu\rho\sigma}n_i^\mu n_j^\nu n_i^\rho n_j^\sigma-\mathcal{K}^i_{\mu\nu}\mathcal{K}_i^{\mu\nu}\right)\right], \quad (4.58)$$

where with $i=1,2$ we denote the two transverse directions to a codimension-two hypersurface in the bulk, n_i^μ are two mutually orthogonal unit vectors to the hypersurface and $\mathcal{K}^{(i)}$ are the traces of two extrinsic curvature tensors defined by

$$\mathcal{K}^{(i)}_{\mu\nu}=\pi^\sigma{}_\mu\pi^\rho{}_\nu\nabla_\rho(n_i)_\sigma,\qquad \text{with}\quad \pi^\sigma{}_\mu=\delta^\sigma{}_\mu+\xi\sum_{i=1,2}(n_i)^\sigma(n_i)_\mu\,, \quad (4.59)$$

where $\xi=-1$ for space-like and $\xi=1$ for time-like vectors. Moreover γ is the induced metric on the hypersurface whose coordinates are denoted by ζ.

Although so far we have been considering a theory with hyperscaling violation, as we have already mentioned the holographic renormalization for generic hyperscaling exponent has not been fully worked out and thus we have restricted ourselves to to consider backgrounds with $z=1$. In this case the most interesting case allowed by the null energy condition is $\theta=0$. Therefore in what follows we just examine the relation between the two charges for $\theta=0$ in an arbitrary dimension.

To compute higher curvature corrections to the entanglement entropy we note that in our case the normal vectors are given by (note that we set $\theta=0$)

$$n_1=\frac{L}{r}\left(1,0,0,0\cdots\right),\qquad n_2=\frac{L}{r}\frac{1}{\sqrt{1+h(\varphi)^2+h'(\varphi)^2}}\left(0,1,-h(\varphi),-\rho h'(\varphi),0,\cdots\right). \quad (4.60)$$

It is then straightforward to extremize the functional (4.5) and evaluate it. In fact one only needs to expand the above entropy functional around $h=0$ to find its divergences and read the universal coefficient of the logarithmic (or $\log^2$) term to find the corrections to the central charge C_d^n. Doing so one arrives at

$$\tilde{C}_d^{\,n}=\Upsilon\,C_d^{\,n}\,, \quad (4.61)$$

where $\tilde{C}$ is the corrected central charge and

$$\Upsilon=1+\frac{4(d-2)}{L^2}\lambda_3-\frac{2(d+1)}{L^2}(\lambda_2+(d+2)\lambda_1)\,. \quad (4.62)$$

Now one needs to compute the corresponding corrections to the central charge C_T. To do so one first needs to linearize the equations of motion deduced from the action (4.57) (see for example [171])

$$\begin{aligned}&R_{\mu\nu}-\frac{1}{2}g_{\mu\nu}(R+V(\phi))+2\lambda_1\left(R_{\mu\nu}-\frac{1}{4}g_{\mu\nu}R\right)R+2\lambda_2\left(R_{\mu\sigma\nu\rho}-\frac{1}{4}g_{\mu\nu}R_{\sigma\rho}\right)R^{\sigma\rho}\\&+(2\lambda_1+\lambda_2+2\lambda_3)\left(g_{\mu\nu}\Box-\nabla_\mu\nabla_\nu\right)R+(\lambda_2+4\lambda_3)\,\Box\left(R_{\mu\nu}-\frac{1}{2}g_{\mu\nu}R\right)\\&+2\lambda_3\left(2R_{\mu\sigma\nu\rho}R^{\sigma\rho}+R_{\mu\sigma\rho\tau}R_\nu^{\sigma\rho\tau}-2R_{\mu\sigma}R^\sigma_\nu+\frac{1}{4}g_{\mu\nu}(R^2_{\alpha\beta\rho\sigma}+4R^2_{\alpha\beta})\right)=0\end{aligned} \quad (4.63)$$

Using the notation of Appendix D.1 one can linearize the above equations around the vacuum solution given by (D.4) with $\theta=0$. The result is

$$\Upsilon\,\mathcal{G}^{(1)}_{\mu\nu}+(2\lambda_1+\lambda_2+2\lambda_3)\left(\bar{g}_{\mu\nu}\bar{\Box}-\bar{\nabla}_\mu\bar{\nabla}_\nu-\frac{d+1}{L^2}\bar{g}_{\mu\nu}\right)R^{(1)}+(\lambda_2+4\lambda_3)\left((\bar{\Box}+\frac{2}{L^2})\mathcal{G}^{(1)}_{\mu\nu}+\frac{d}{L^2}\bar{g}_{\mu\nu}R^{(1)}\right)=0, \quad (4.64)$$

where Υ is exactly the one given in equation (4.62), and

$$\mathcal{G}^{(1)}_{\mu\nu}=R^{(1)}_{\mu\nu}-\frac{1}{2}\bar{g}_{\mu\nu}R^{(1)}+\frac{d+1}{L^2}h_{\mu\nu}. \quad (4.65)$$

[6]Holographic entanglement entropy for a strip entangling region in theories with hyperscaling violation in the presence of higher curvature terms has also been studied in [170].

In the transverse-traceless gauge the above equation reads

$$\left[\Upsilon + (\lambda_2 + 4\lambda_3)\left(\bar{\Box} + \frac{2}{L^2}\right)\right]\left(\bar{\Box} + \frac{2}{L^2}\right) h_{\mu\nu} = 0 \tag{4.66}$$

which has to be solved in order to find the linearized solution. Since we are interested in the correlation function of the energy momentum tensor, we should still look for a solution of $(\bar{\Box} + \frac{2}{L^2})h_{\mu\nu} = 0$. This equation is exactly the same one gets from purely Einstein gravity, and thus the linearized equation of motion reduces essentially to solving standard linearized Einstein equations. On the other hand, to evaluate the two-point function one needs to find the quadratic action which has an effective Newton constant Υ/G. Indeed going through the computations of the two-point function one finally finds that

$$\tilde{C}_T = \Upsilon\, C_T, \tag{4.67}$$

and thus we may conclude that

$$\frac{\tilde{C}_d^{\,n}}{\tilde{C}_T} = \frac{C_d^{\,n}}{C_T}. \tag{4.68}$$

for arbitrary dimensions but with $\theta = 0$.
Although we have examined the relation between the two central charges C_T and $C_d^{\,n}$ just for squared curvature modifications of Einstein gravity, based on our observations and the three-dimensional results of [167], it is tempting to conjecture that the the central charge $C_d^{\,n}$ is directly related to C_T for a generic CFT.

4.4 New charge

We have studied the holographic entanglement entropy of an entangling region $c_n \times \mathbb{R}^{d-n-2}$, i.e. an n-dimensional cone extended in $d-n-2$ transverse directions, for a $d+1$-dimensional theory in a hyperscaling violating background. We have observed that due to the presence of a corner in the entangling region the divergence structure of the entropy gets new terms.

In particular for certain values of θ, d and n the divergent terms include log or log-squared terms whose coefficients are universal, in the sense that they are independent of the UV cut-off.

Given that we have been able to extract new regularization independent quantities, it is tempting to conjecture that some information can be obtained about the underlying dual field theory. This might be compared with the case of two-dimensional conformal field theories where the central charge appears in the coefficient of the (leading) logarithmic divergence of the entanglement entropy for an interval.

Motivated by this similarity we proceed by analogy and, denoting the coefficient of the logarithmic term appearing in the expression for the entanglement entropy by C^{EE}_{singular} (see equation (4.37)), we find that for $d_\theta \geq 2$ we can define a new "central charge" as follows

$$C_d^{\,n} = \lim_{\Omega \to \frac{\pi}{2}} \frac{C^{\text{EE}}_{\text{singular}}}{\cos^2 \Omega}, \tag{4.69}$$

which is proportional to L^d/G. As soon as the effective dimension d_θ is fixed, the proportionality constant only depends on d and n, while it is independent of θ. Therefore it remains unchanged even if we set $\theta = 0$, reducing the dual theory to a $d+1$-dimensional conformal field theory. It is natural to expect that this central charge may provide a measure for the number of degrees of freedom of the theory. Note that, unlike the one obtained from Weyl anomaly, this central charge can be defined for both even and odd dimensions when $d_\theta = n + 2$.

Another central charge which could be defined in any dimension is the one entering in the expression for the stress-energy tensor' two-point function. We checked whether the ratio between these charges is a pure number and we also have computed corrections to both C_d^n and C_T for theories with quadratic correction in the curvature. We have shown that the relation between these two charges remains unchanged.

Based on this observation and the results for three-dimensional CFTs [166, 167], one may conjecture that the relation between these two central charges (C_T and C_d^n) is a somehow intrinsic property of the field theory. In fact this relation is reminiscent of the relation between Weyl anomaly of a conformal field

theory in even dimension and the logarithmic term in the entanglement entropy of the corresponding theory. If there is, indeed, such a relation one would expect to have a general proof for it independently of an explicit example.

Chapter 5

Conclusions

In this work we dealt with several aspects of the computation of holographic entanglement entropy. We developed numerical and semi-analytical techniques to find the area of minimal surfaces which gives the value of the entanglement entropy for strongly interacting field theories via the Ryu-Takayanagi prescription (1.26).

In Chapter 2 we employed *Surface Evolver* (see [83] and Appendix B.2) to compute numerically the shape dependence of holographic entanglement entropy in AdS_4 space-times. Any known result in the literature on minimal surfaces in three-dimensional hyperbolic spaces has been reproduced, including annular regions, disjoint circles and non-smooth boundaries. Moreover, we were able to find the transition curves of the mutual information between disconnected regions interpolating from two circles and two infinite strips, for which analytic results were previously known. The numerical computation is best summarized by Fig. 2.16 and Fig. 2.17. Our results were also useful to check in [172] the correctness of some perturbative computations for elliptical regions.

In Chapter 3 we studied the time-dependence of strip- and sphere-like entangling regions in asymptotically *hvLif* space-times, monitoring the transition from a theory at zero temperature to a thermal one. In gauge/gravity this can be achieved using time-dependent metrics which model the collapse of a null shell of energy up to the formation of a black-hole. Using a modification of asymptotically AdS Vaidya metrics, we found numerically the time evolution of entanglement entropy with non-trivial Lifshitz exponent ζ and hyperscaling violating factor θ. In the limit of a sharp transition (what we called the thin-shell limit) we generalized the results of [140, 141] and obtained analytic expressions for the three temporal regimes of entanglement entropy: initial, linear growth and saturation, given respectively by equations (3.84), (3.88) and (3.95).

In Chapter 4 we computed analytically how the presence of non-smooth boundaries affects the divergence structure of entanglement entropy in *hvLif* space-times, generalizing previous work of [120] which focused on generic dimensional AdS spaces. We checked when and how new logarithmically divergent terms arise. The coefficients of these new divergent terms may provide new universal quantities characterizing the UV properties of the dual field theory, since they are scheme independent. Indeed, generalizing a conjecture of [166, 167], we also checked that in the limit of nearly-smooth boundaries the coefficient of the logarithmic term is proportional to the coefficient C_T of the stress-energy two-point function $< TT >$. We worked out the results for arbitrary θ and d, which is given inequation (4.37). Finally, we also checked that for $\theta = 0$ some class of higher curvature corrections to the gravitational action do not affect the ratio between this new central charge and C_T, finding agreement with subsequent work [173, 174].

There are several directions along which this research could be continued. Regarding the use of *Surface evolver*, the most important ones concern black hole geometries, higher dimensional generalizations, domain wall geometries and time dependence for generic shapes. An interesting extension involves domains A made by three or more regions (see [175] for some results in two-dimensional conformal field theories and [176–178] for a holographic viewpoint), which become now numerically accessible: in Fig. 5.1

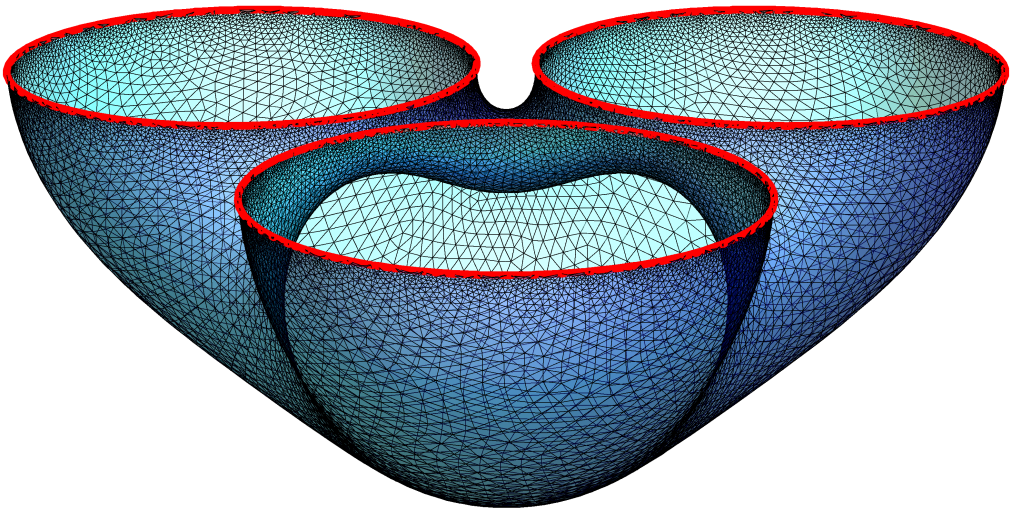

Figure 5.1: Minimal surface corresponding to three disjoint and equal red circles in the plane $z = 0$ (the z axis points downward). This surface has 13147 vertices and 26624 faces, while the number of edges is given by Euler formula with vanishing genus and 3 boundaries. This kind of surfaces occurs in the computation of the holographic tripartite information for the union of three disjoint disks.

we show a minimal surface anchored to an entangling curve made by three disjoint circles. The area of this surface provides the holographic entanglement entropy between the union of the three disjoint disks and the rest of the plane, which is the most difficult term to evaluate in the computation of the holographic tripartite information [176].

In [62, 63] it was shown how to compute a new set of analytic solutions for minimal surfaces in three-dimensional hyperbolic spaces. Since the technique proposed there involves the use of complicated algebraic functions, one has little control on the shape of the entangling curve. Our numerical tools could be used to check and further investigate the properties of these solutions.

A further direction of study would be to try to find a way to compute the shape dependence of the entanglement entropy in a CFT_{2+1} by directly employing quantum field theory techniques.

Finally, let us mention that it remains to check whether the conjecture [166, 167] can be extended to higher-dimensional CFTs, computing the entanglement entropy for singular entangling regions in non-holographic theories, like e.g. for free bosons and fermions.

Appendix A

Hypersurfaces

A.1 Minimality implies $\mathrm{Tr}K = 0$

In this section we follow slightly the notation of [179], although we keep the computation for arbitrary dimension and backgrounds. Consider a d-dimensional smooth hypersurface γ embedded in a $(d+1)-$space of arbitrary geometry. The surface can be parametrized implicitly by a position vector, let it be

$$\gamma = \{x^\mu(\sigma_i) |\ t_i \in \mathbb{I}^d\}\,, \tag{A.1}$$

where $\mathbb{I}^d$ is some direct product of intervals (eventually non-compact) which defines the parameter space. Any smooth surface can be parametrized in this way without loss of any generality. From $x^\mu(\sigma_i)$ we can define d tangent vectors $t_i^\mu \equiv \partial_i x^\mu$ and a normal vector n^μ such that $n^\mu t_{\mu i} = 0$ and $n^2 = 1$. Together, t_i^μ and n^μ form a basis for the embedding space. From the tangent vectors we can define the *induced metric* to be

$$h_{ij} = t_i^\mu t_j^\nu g_{\mu\nu}\,,\,, \tag{A.2}$$

where $g_{\mu\nu}$ is the metric of the embedding space where γ lives, and clearly $g_{\mu\nu}$ does not depend on the surface. From the condition $0 = t_i^\mu \nabla_\mu n^2 = 2 n_\nu t_i^\mu \nabla_\mu n^\nu$ we get that the tangential projection of the covariant derivative of n^μ is entirely tangent to the surface, and we define its components to be the *extrinsic curvature* of γ

$$t_i^\nu \nabla_\nu n^\mu = K_{ij} t^{\mu j}\,, \tag{A.3}$$

where we raised the j index with the inverse of the induced metric, i.e. $t^{\mu j} = h^{ji} t_i^\mu$. This equation can be rewritten as to properly define the extrinsic curvature (also known as *second fundamental form*) as

$$K_{ij} \equiv t_j^\nu t_i^\nu \nabla_\nu n_\mu\,. \tag{A.4}$$

It is easy to see that K_{ij} is a symmetric tensor. Taking the derivatives of the tangent vectors is a bit more involved. Decompose the tangential variation in the following way (since tangent and normal vectors form a basis)

$$t_i^\nu \nabla_\nu t_j^\mu = A_{ij} n^\mu + B_{ij}^k t_k^\mu\,, \tag{A.5}$$

then, from $\nabla_\mu (n^\mu t_{\mu j}) = 0$ and using (A.3) it is easy to show that $A_{ij} = -K_{ij}$. From differentiating h_{ij} one obtains instead $B_{ij}^k = \Gamma_{ij}^k$, where Γ_{ij}^k is precisely the Levi-Civita connection computed with the induced metric. We then get the final expression

$$\nabla_i t_j^\mu = -K_{ij} n^\mu\,, \tag{A.6}$$

where with ∇_i we indicated both the projection of the covariant derivative on the tangent vectors and the contribution coming from the connection constructed with the induced metric. Equations (A.3) and (A.6) are known as Weingarten-Gauss relations. We want to find the equation which minimizes the area, and therefore we need to consider fluctuations of the surface away from γ, and eventually compute the variation of the area under these fluctuations. In general, a variation of γ can be written in parametric form as

$$x^\mu \to x^\mu + \delta x^\mu = x^\mu + a n^\mu + b^i t_i^\mu\,, \tag{A.7}$$

where again we split the variation in tangent and normal components, and a, b^i are arbitrarily (small) quantities. The variation of the tangent vectors is then

$$\delta t_i^\mu = \partial_i \delta_i x^\mu = (\partial_i a) n^\mu + (\partial_i b^j) t_j^\mu + a \partial_i n^\mu + b^j \partial_i t_j^\mu \tag{A.8}$$

$$= \left(\partial_i a - b^j K_{ij}\right) n^\mu + \left(\nabla_i b^j + a K_i^j\right) t_j^\mu \,, \tag{A.9}$$

and thus, the variation of the induced metric can be computed to be

$$\delta h_{ij} = g_{\mu\nu} t^\mu_{(i} \delta t^\nu_{j)} \tag{A.10}$$

$$= \nabla_i b_j + \nabla_j b_i + 2 a K_{ij} \,, \tag{A.11}$$

where we used the fact that the extrinsic curvature is a symmetric tensor.

Now, given that the area of γ can be written as the integral over the hypersurface of the squared root of the determinant of the induced metric, i.e.

$$\mathcal{A} = \int_\gamma d^d\sigma \sqrt{\det h} \,, \tag{A.12}$$

we have that the variation of the area under the transformation (A.7) changes as[1]

$$\delta \mathcal{A} = \int_\gamma d^d\sigma \delta \sqrt{\det h} \tag{A.13}$$

$$= \int_\gamma d^d\sigma \sqrt{\det h} h^{ij} \delta h_{ij} \tag{A.14}$$

$$= 2 \int_\gamma d^d\sigma \sqrt{\det h} \left(\nabla^i b_i + a \mathrm{Tr} K\right) \,. \tag{A.15}$$

This is the expression for the general first variation of the area of a hypersurface, which as we see consists of two components: one along the tangent vectors and one along the normal. The tangent variation however does not modify the actual shape of the surface, since it corresponds more to a change of coordinates with which we parametrize the surface (namely, the change under b_i of h_{ij} is precisely the change of a metric under a general diffeomorphism). For this reason, the area will not change and we are allowed to set $b_i = 0$. The only relevant changes are the ones along the normal, and we see that a variation is zero if and only if

$$H = 0 \,, \tag{A.16}$$

where we used the common definition $H = \frac{1}{d}\mathrm{Tr}K$ for the hypersurface mean curvature. We remark that in order to derive this equation we did not assume anything about the geometry of the embedding space, i.e. it holds for arbitrary $g_{\mu\nu}$. A minimal (or rather, extremal) surface in any space is always a zero mean-curvature surface. The explicit expression for $\mathrm{Tr}K$ will however depend on the geometry, since $g_{\mu\nu}$ enters in the definition of h_{ij}.

A.2 Minimal surfaces and umbilical lines

In this section we want to understand the implications of the minimality equation (A.16) when γ is a surface with boundary, ending on the conformal boundary of (asymptotic) AdS_{d+2} space-times, as this kind of surfaces are the ones we need to study in order to compute entanglement entropy, as in (1.26). We will follow the computation of [56], who first computed the asymptotic behaviour of minimal hypersurfaces of arbitrary dimension. Here we will consider however only surfaces of codimension two, which admit only one space-like normal vector, although the generalization is straightforward.

Suppose we have a surface embedded in $\mathbb{H}^d$, let it be γ_A, such that at $z = 0$ (in Ponicaré metric) ends on $\partial\gamma_A = \partial A$. Since $\mathbb{H}^{d+1}$ is conformally flat, we can choose as representative of the conformal class of $\partial\mathbb{H}^{d+1}$ the flat Euclidean space $\mathbb{R}^d$.

We want the condition $\partial A = \partial\gamma_A$ to be implemented so that the expansion near the boundary is easily computed: to this purpose we will locally parametrize the surface as a *vertical graph* over ∂A.

[1] We assume that any variation is zero at the boundary.

We assume that the region ∂A is a submanifold of $\mathbb{R}^d$ of dimension $d-1$. As such, it can be parametrized as $X_M(\tau_a)$ where $M=1,\dots,d$ refers to components in $\mathbb{R}^d$ and $a=1,\dots,d-1$ are the world-sheet coordinates for the hypersurface. We can extend ∂A to the bulk by lifting it along the z direction, creating the *cylinder over* ∂A

$$r^\mu(\sigma_a,z)=\{\mathbf{X}(\sigma_a)\,,z\}\,. \tag{A.17}$$

Here and in the following, any bold quantity refers to vectors of $\mathbb{R}^d$. In analogy with Section A.1 we can define the tangent and normal vectors to the entangling region: the tangent space of a point in ∂A is spanned by the basis $\mathbf{T}_b(\sigma_a)=\partial_b\mathbf{X}(\sigma_a)$ and the induced metric on ∂A is $\gamma_{ab}=\mathbf{T}_a\cdot\mathbf{T}_b$. We can promote the normal vector to a vector of $\mathbb{H}^{d+1}$ with zero z component, i.e. $q^\mu(\sigma_a)=\{\mathbf{N}(\sigma_a)\,,0\}$, where the boundary normal vector is fixed by the conditions $\mathbf{N}^2=1$ and $\mathbf{N}\cdot\mathbf{T}_a=0$. We can finally parametrize the surface as a one-dimensional *vertical graph* over ∂A

$$x^\mu(\sigma_a,z)=r^\mu(\sigma_a,z)+u(\sigma_a,z)q^\mu(\sigma_a)=\{\mathbf{X}(\sigma_a)+u(\sigma_a,z)\mathbf{N}(\sigma_a),z\}\,. \tag{A.18}$$

Any surface can be expressed in this way - at least locally - so that the minimality equation can be written as just a single partial differential equation for u. The tangent space of γ_A is then

$$t_a^\mu = \partial_a x^\mu=\{\mathbf{T}_a+u_a\mathbf{N}+u\partial_a\mathbf{N},0\}=\left\{(\delta_a^b+uk_a^b)\mathbf{T}_b+u_a\mathbf{N},0\right\}\,, \tag{A.19}$$

$$\mathfrak{t}^\mu = \partial_z x^\mu=\{u_z\mathbf{N},1\}\,, \tag{A.20}$$

where we used the Weingarten-Gauss relation (A.3), i.e. $\partial_a\mathbf{N}=k_a^b\mathbf{T}_b$ with k_{ab} the extrinsic curvature of ∂A as embedded in $\mathbb{R}^d$ and $u_a\equiv\partial_a u$, $u_z\equiv\partial_z u$. The induced metric on the hypersurface can then be computed as (the index $i=1,\dots,d$ refers to comoving coordinates on γ_A)

$$h_{ij}=\begin{pmatrix} t_a^\mu t_{b\mu} & t_a^\mu\mathfrak{t}_\mu \\ \mathfrak{t}^\mu t_{b\mu} & \mathfrak{t}^\mu\mathfrak{t}_\mu\end{pmatrix}=\frac{1}{z^2}\begin{pmatrix}\gamma_{ab}+u_au_b+2uk_{ab}+u^2k_a^ck_{cb} & u_au_z\\ u_bu_z & 1+u_z^2\end{pmatrix}\,. \tag{A.21}$$

From (A.19) we can compute the normal vector n^μ to γ_A in $\mathbb{H}^{d+1}$. We can parametrize it as

$$n^\mu=\{A\mathbf{N}+B^a\mathbf{T}_a,n^z\}\,, \tag{A.22}$$

where A,B^a and n^z are coefficients to be determined from the conditions $n^\mu t_{\mu a}=n^\mu\mathfrak{t}_\mu=0$ and n^2=1. These imply (recall that $g_{\mu\nu}=z^{-2}\delta_{\mu\nu}$ for the Poincaré patch)

$$Au_a+B^b(\gamma_{ab}+uk_{ab}) = 0\,, \tag{A.23}$$

$$Au_z+n^z = 0\,, \tag{A.24}$$

$$A^2+B^aB^b\gamma_{ab}+n^{z2} = z^2\,. \tag{A.25}$$

The solution is

$$n^\mu=\frac{z}{\sqrt{1+u_z^2+u_a[(\mathbb{I}+uk)^{-2}]^{ab}u_b}}\left\{-\mathbf{N}+[(\mathbb{I}+uk)^{-1}]^{ab}u_b\mathbf{T}_a,u_z\right\}\,, \tag{A.26}$$

where $\mathbb{I}$ is our shorthand notation for the identity matrix, and we used the symmetry of k_{ab}. Computing the extrinsic curvature K_{ij} of γ_A is cumbersome using these confidantes, and therefore writing explicitly the equation $H=0$ is rather lengthy.

Since we are going to cut γ_A along a plane lying at $z=\varepsilon$ with $\varepsilon\to 0$, there is a particular vector among the tangent ones (A.19) which is of particular interest: the *tangent normal* vector. The tangent space of γ_A is d-dimensional, and there are $d-1$ linearly independent vectors which also belong to the tangent space of the $z=\varepsilon$ hyperplane: the tangent normal b^μ is defined as the only unit vector which is orthogonal to the intersection between γ_A and the hyperplane and is tangent to ${\gamma_A}^2$. Therefore, it has to satisfy $b^\mu t_{a\mu}=0$ and $b^2=1$. It is possible to write it formally but its expression for arbitrary z is not particularly illuminating.

[2] In general the tangent normal is a vector defined at intersections of hypersurfaces: it is tangent to just one of the surfaces but is orthogonal to any other vector which is tangent to both.

We want to focus however only on the near-boundary behaviour of the surfaces, and thus we will compute K_{ij} in the limit of $\varepsilon \to 0$. Firs of all we have that the surface has to satisfy the boundary condition[3]

$$z^2 h_{ij}\big|_{z=0} = \gamma_{ab} \otimes 1\,, \tag{A.27}$$

which imposes that $u(\sigma_a, z) \propto z^2$ as $z \to 0$, and thus we can expand (A.21) to first order in u,u_a and up to second order in u_z, finding

$$h_{ij} = \frac{1}{z^2}\begin{pmatrix} \gamma_{ab} + 2k_{ab}u & 0 \\ 0 & 1 + u_z^2 \end{pmatrix} + O(z)\,. \tag{A.28}$$

Now, since for any two matrices A and B we have $\det(A + \lambda B) = \det A(1 + \lambda \mathrm{Tr}(A^{-1}B) + O(\lambda^2))$, we have that the square root of the determinant of h can be expanded as

$$\sqrt{\det h} = z^{-d}\sqrt{\det \gamma}\,\left[1 + \frac{1}{2}u_z^2 + u\mathrm{Tr}k\right] + O(z^{3-d})\,. \tag{A.29}$$

It is then much easier to work out the variation of the area element, finding

$$\begin{aligned} \delta\sqrt{\det h} &= z^{-d}\sqrt{\det \gamma}\,\left[u_z \delta u_z + \mathrm{Tr}k\delta u\right] + O(z^{3-d}) && \text{(A.30)} \\ &= z^{-d}\sqrt{\det \gamma}\,\left[-u_{zz} + dz^{-1}u_z + \mathrm{Tr}k\right]\delta u + O(z^{3-d})\,, && \text{(A.31)} \end{aligned}$$

where we are allowed to integrate by parts since we set to zero variations at the boundary. We see then that u has solve the equation

$$-u_{zz} + dz^{-1}u_z + \mathrm{Tr}k = 0\,. \tag{A.32}$$

Since we can write $u = u_2(\sigma_a)z^2 + O(z^3)$, we have that the solution is given by

$$u_2(\sigma_a) = -\frac{1}{2(d-1)}\mathrm{Tr}k = -\frac{1}{2}H\,. \tag{A.33}$$

We remark that H is the mean curvature of ∂A which is a $d-1$-dimensional manifold. This relation tells us the way the surface "bends" toward the bulk direction from the boundary. γ_A will lean toward the outside of averagely concave portions of ∂A and toward the inside of averagely convex ones. We say averagely because H is the arithmetic mean of the eigenvalues of the extrinsic curvature, which can either be negative or positive.

One consequence of (A.33) is that for spherical entangling regions, the minimal surface will look precisely like a sphere. Namely in this case the full solution *is* a half sphere of one dimension higher.

Another consequence of (A.33) is that for $d = 2$ and *any* entangling curve, the minimal surface will look locally like a two-sphere, and thus the direction where the surface bends is fully determined by the geodesic curvature of the curve ∂A. In the theory of surfaces any point where the values of the two principal curvatures coincide is called *umbilical*: (A.33) tells that ∂A is an *umbilical line* for γ_A[55].

Moreover, by plugging (A.33) into (A.29) we get that the area element of γ_A can be expanded as

$$\sqrt{\det h} = z^{-d}\sqrt{\det \gamma}\,\left[1 - \frac{d-2}{2}H^2 z^2\right] + O(z^{3-d})\,. \tag{A.34}$$

We can also compute the behaviour of the normal n^μ and of the tangent-normal b^μ as $z \to 0$,

$$\begin{aligned} \frac{n^\mu}{z} &= -\frac{1}{\sqrt{1 + z^2H^2}}\{\mathbf{N}, zH\} + O(z^3)\,, && \text{(A.35)} \\ \frac{b^\mu}{z} &= \frac{1}{\sqrt{1 + z^2H^2}}\{-zH\mathbf{N}, 1\} + O(z^3)\,. && \text{(A.36)} \end{aligned}$$

[3] Actually, looking back at equation (A.18), the boundary condition $\partial A = \partial\gamma_A$ implies just $u(\sigma_a, 0) = 0$. The condition (A.27) assumes also that γ_A ends orthogonally on the $z = 0$ hyperplane, which can be proved either by keeping linear terms in the following discussion and showing they have to be zero, or by the consideration that a sufficiently small portion of ∂A always looks flat - the extrinsic curvature is a second-order quantity (for another proof see [180]).

Appendix B

Further details on shape dependence in AdS_4

B.1 Further details on minimal surfaces in $\mathbb{H}_3$

In this appendix we provide a derivation of (2.6) and describe some additional properties of minimal surfaces in AdS_4. Let us consider the area of a two dimensional surface γ_A embedded in spatial slice $t = \text{const}$

$$\mathcal{A}[\gamma_A] = \int_{\gamma_A} d\mathcal{A} = \int_{U_A} \frac{\sqrt{h}\, du^1 du^2}{z^2}\,, \tag{B.1}$$

where U_A is a coordinate patch. As mentioned in 2.1, $\mathcal{A}$ can be interpreted as the energy of a two dimensional interface immersed in $\mathbb{R}^3$ endowed with a potential energy of density $1/z^2$. To find the surface $\tilde{\gamma}_A$ minimizing $\mathcal{A}$ we consider a small displacement along the normal direction $\boldsymbol{N}$, parametrized as: $\boldsymbol{R} \to \boldsymbol{R} + w\boldsymbol{N}$, where $\boldsymbol{R}$ represents the position of a point on the surface and w is a small normal displacement. The linear area variation can be straightforwardly calculated using classic differential geometry [181]

$$\delta\mathcal{A}[\gamma_A] = \int_{U_A} \delta\big(\sqrt{h}\, du^1 du^2\big)\, \frac{1}{z^2} + \int_{U_A} \delta\left(\frac{1}{z^2}\right) \sqrt{h}\, du^1 du^2 = -\,2\int_{U_A} \frac{1}{z^2}\left(H + \frac{\hat{\boldsymbol{z}}\cdot\boldsymbol{N}}{z}\right) w\, du^1 du^2\,, \tag{B.2}$$

where H is the surface mean curvature. Setting $\delta\mathcal{A}[\gamma_A]$ to zero yields (2.6).

In a Monge patch $(u^1, u^2) = (x, y)$ and the surface can be represented as the graph of the function $z = z(x, y)$ representing the height of the surface above the (x, y) plane. In this case the mean curvature reads

$$H = \frac{z_{,xx}(1 + z_{,y}^2) + z_{,yy}(1 + z_{,x}^2) - 2z_{,xy}z_{,x}z_{,y}}{2(1 + z_{,x}^2 + z_{,y}^2)^{3/2}}\,, \tag{B.3}$$

while the outward directed normal vector is given by

$$\boldsymbol{N} = -\frac{z_{,x}\hat{\boldsymbol{x}} + z_{,y}\hat{\boldsymbol{y}} - \hat{\boldsymbol{z}}}{\sqrt{1 + z_{,x}^2 + z_{,y}^2}}\,. \tag{B.4}$$

Using Eqs. (B.3) and (B.4) in (2.6) yields the Cartesian equation (2.9).

In 2.1 we argued that a surface described by (2.6) must be orthogonal to the $z = 0$ plane. This orthogonality implies that the boundary curve $\partial\tilde{\gamma}_A$ is a geodesic of $\tilde{\gamma}_A$. To see this we can recall that the curvature κ of a curve that lies on a surface can be decomposed as

$$\kappa\,\boldsymbol{n} = \kappa_n \boldsymbol{N} + \kappa_g(\boldsymbol{N} \times \boldsymbol{t})\,, \tag{B.5}$$

with $\boldsymbol{t}$ the tangent vector of $\partial\tilde{\gamma}_A$, $\kappa\,\boldsymbol{n} = \boldsymbol{t}_{,s}$ (with s the arc lenght) and κ_n and κ_g the normal and geodesic curvature respectively. Since $\partial\tilde{\gamma}_A$ lies on the $z = 0$ plane and $\hat{\boldsymbol{z}}\cdot\boldsymbol{N} = 0$ at $z = 0$, then $\boldsymbol{N} = \pm\boldsymbol{n}$ where the choice of the sign is conventional. By virtue of (B.5) this implies that $\kappa_g = 0$. Thus $\partial\tilde{\gamma}_A$ is a geodesic over $\tilde{\gamma}_A$.

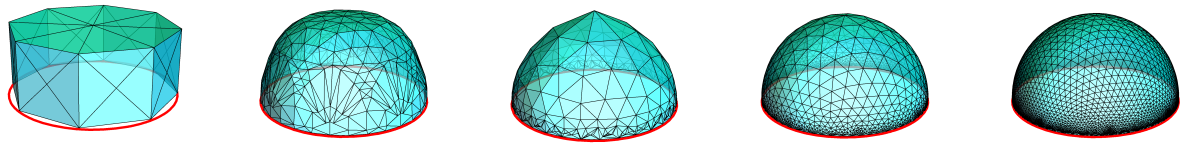

Figure B.1: Example of a typical *evolution* obtained by Surface Evolver in the case of a circular boundary. The initial configuration consists of an octagonal prism composed of 40 triangles (left). The shape is then optimized and refined as described in B.2, finding the final configuration given by the rightmost surface, which consists of 10240 triangles and yields $\widetilde{F}_A = 1.99843\pi$ whereas $F_A = 2\pi$ is the exact value from the analytic result (2.7). In this example the radius of the circle is $R = 1$ and $\varepsilon = 0.03$.

An interesting consequence of the previous statement is that the total Gaussian curvature of the surface is constant, regardless the shape of the boundary in the $z = 0$ plane. The Gauss-Bonnet theorem tells us that

$$\int_{\tilde{\gamma}_A} K_G \sqrt{h}\, du^1 du^2 + \oint_{\partial\tilde{\gamma}_A} \kappa_g\, ds \;=\; 2\pi\chi\,, \tag{B.6}$$

where K_G is the Gaussian curvature and χ is the Euler characteristic. Since $\kappa_g = 0$ in our case, we have

$$\int_{\tilde{\gamma}_A} K_G \sqrt{h}\, du^1 du^2 = 2\pi\chi\,. \tag{B.7}$$

Let us recall that the Euler characteristic is $\chi = 2 - 2g - b$, where g is the genus of the surface and b is the number of its boundaries.

B.2 Numerical Method

The numerical results presented in 2.2 and 2.3 have been obtained with Surface Evolver [83]. This is a multipurpose shape optimization program created by Brakke [83] in the context of minimal surfaces and capillarity and then expanded to address generic problems on energy minimizing surfaces. A surface is implemented as a simplicial complex, i.e. a union of triangles. Given an initial configuration of the surface, the program evolves the surface toward a local energy minimum by a gradient descent method. The energy used in our calculations is the $\mathbb{H}_3$ area function given in (2.3).

The initial configuration is preferably very simple and contains only the least number of triangles necessary to achieve a given surface topology (Fig. B.1). A typical *evolution* consists in a sequence of optimization and mesh-adjustment steps. During an optimization step, the coordinates of the vertices are updated by a local minimization algorithm (conjugate gradient in our case), resulting in a configuration of lower energy. The topology of the mesh (i.e. the number of vertices, faces and edges) is not altered during minimization. A mesh-adjustment step, on the other hand, consists of a set of operations whose purpose is to render the discretized surface smooth and uniform. These operations can be broadly divided in two class: mesh-refinements and mesh-repairs. In a mesh-refinement operation a finer grid is overlaid on the coarse one. This is obtained, for instance, by splitting a triangle in four smaller triangle obtained by joining the mid points of the original edges. In a mesh-repair operation, the triangles that are too distorted compared to the average are eliminated. This operation can change the topology of the mesh and possibly also the topology of the surface which can then breakup into two or more connected parts. This happens, for instance, in the case of the surfaces described in 2.3. As explained, the minimal surface spanning a disconnected boundary curve can be either connected or disconnected depending on the shape of the boundary. Evolving an initially connected surface in the regime of geometric parameters where the only stable solution is disconnected causes the surface to form narrow necks and eventually pinches off once the triangles around the necks become too squeezed.

Due to the divergence of the area element $d\mathcal{A} = \sqrt{h}/z^2\, du^1 du^2$ at $z = 0$, the boundary curves used in the numerical work have been defined on the plane $z = \varepsilon$. In order to maximize the accuracy of the numerical solution, it is preferable to choose value of ε that is much smaller than any other length scale in the problem and yet large enough to allow the convergence of the optimization steps. With this goal

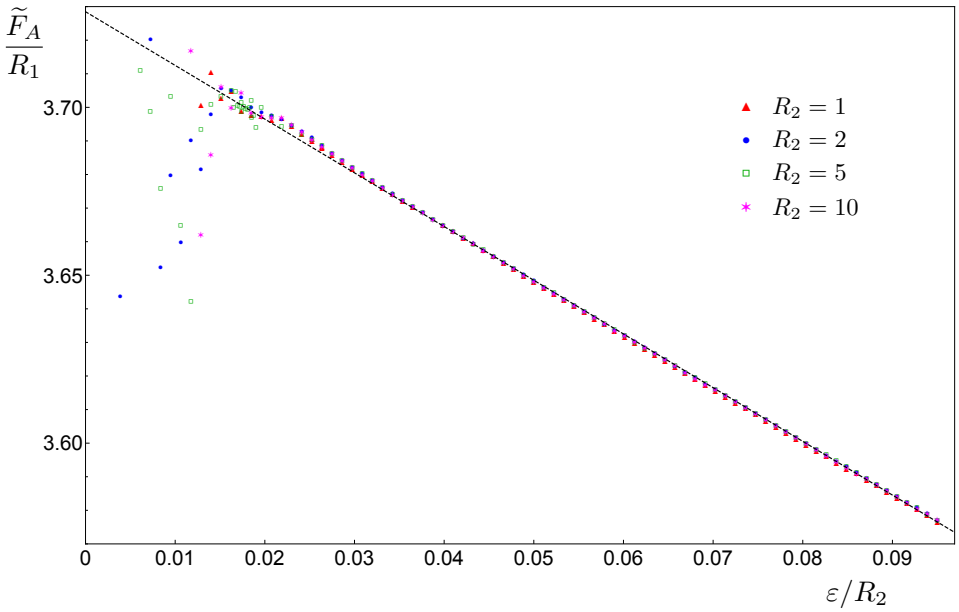

Figure B.2: The quantity $\widetilde{F}_A$ (see (2.14)) computed with Surface Evolver for ellipses having $R_1 = 2R_2$ (see the bottom panel of Fig. 2.1), for various R_2 and ε. When ε/R_2 is too small, our numerical data are not stable. The fitted value on the vertical axis is 3.728.

in mind, we have adopted an empirical selection criterion based on the following procedure. Let $\partial\tilde{\gamma}_A$ be an ellipse and let R_1 and $R_2 = R_1/2$ be the semi-major and semi-minor axes. Using Surface Evolver we have calculated the finite part of the area $\widetilde{F}_A$ for various choices of ε and R_1. In the limit of $\varepsilon \to 0$ the ratio $\widetilde{F}_A/R_1$ is expected to approach a finite value, but from the data shown in Fig. B.2 we see that for $\varepsilon/R_2 < 0.02$, the accuracy of the numerical calculation starts to drop. Based on this numerical evidence we have set in most of our numerical calculations $\varepsilon/R = 0.03$, where R is the typical length scale of the boundary. It is worth remarking that in our numerical computations it is easier (namely the evolution is more stable) to deal with smaller values of ε/R by increasing R than by decreasing ε. Smaller values of ε/R obtained by decreasing ε keeping R fixed can be achieved by setting up *ad hoc* evolutions, tailored for a specific type of boundary shape. This has been done only for the triangles in Fig. 2.4, while in the remaining figures we have increased R keeping $\varepsilon = 0.03$ fixed. Nevertheless, for ε fixed, numerical instabilities are encountered when R is too large as well. The values of ε/R adopted in our numerical calculations have been chosen to guarantee both stable evolutions and a satisfactory precision to compare the data with the analytic results, when they are available.

Other alternative methods are available to construct minimal surfaces. A popular one by [182] consists of evolving the surface level sets under the surface mean curvature flow. A variant of this method has been employed in [112] to study minimal surfaces in the Schwarzschild-AdS$_{d+2}$ background.

B.3 Superellipse: a lower bound for F_A

In this appendix we provide a lower bound for the quantity F_A (see (2.4)) associated with the entangling curves ∂A given by the superellipses (2.15), that we have discussed in 2.2.1.

If A is a simply connected domain without corners in its boundary, let us consider a surface γ_A^* anchored on ∂A, but different from $\tilde{\gamma}_A$, and such that $\mathcal{A}[\gamma_A^*] = P_A/\varepsilon - F_A^* + o(1)$ as $\varepsilon \to 0$. Being $\tilde{\gamma}_A$ the minimal area surface anchored on ∂A, it is immediate to realize that $F_A^* < F_A$. Here we consider the superellipses (2.15), whose perimeter is given by

$$P_A \;=\; 4R_1 \int_0^1 \sqrt{1 + (R_2/R_1)^2\, h_n(\tilde{x})^2}\, d\tilde{x}\,, \qquad h_n(\tilde{x}) \equiv \frac{\tilde{x}^{n-1}}{(1-\tilde{x}^n)^{1-1/n}}\,, \tag{B.8}$$

where the integration variable $\tilde{x} = x/R_1$ as been employed. Let us adapt to this case the choice of the

trial surface suggested in [91] for the ellipse, namely we consider γ_A^* such that any section along the x direction provides the profile of the infinite strip whose width is given by $y(x)$ obtained from (2.15), i.e.

$$y(\tilde{x}) = R_2 \left(1 - \tilde{x}^n\right)^{1/n} . \tag{B.9}$$

Given the symmetries of the superellipse, we are allowed to restrict ourselves to $x > 0$ and $y > 0$. From (B.19) for $d = 2$, we construct the trial surface γ_A^* by requiring that we have that any section at $x = \text{const}$ is given by

$$y(z, \tilde{x}) = z_*(\tilde{x}) \int_{z/z_*(\tilde{x})}^1 \frac{Z^2}{\sqrt{1 - Z^4}}\, dZ\,, \qquad z_*(\tilde{x}) \equiv \frac{2\, y(\tilde{x})}{\sqrt{s_\infty}}\,, \tag{B.10}$$

where the integration variable $Z \equiv z/z_*$ has been employed and $z_*(\tilde{x})$ has been introduced by taking z_* in (2.11) with s_∞ defined in (2.12) and replacing R_2 with $y(\tilde{x})$ defined in (B.9). From (B.10), it is straightforward to show that $y(0, \tilde{x}) = y(\tilde{x})$ and this guarantees that the trial surface is anchored on the superellipse (B.9).

The occurrence of the cutoff ε in the holographic direction influences the integration domain along the x direction. In particular, by employing (B.9) and (B.10), the requirement $z_*(\tilde{x}) \geqslant \varepsilon$ becomes $\tilde{x} \leqslant \tilde{x}_\varepsilon$, where

$$\tilde{x}_\varepsilon \equiv \left[1 - \left(\frac{\sqrt{s_\infty}}{2R_2}\, \varepsilon\right)^n\right]^{1/n} . \tag{B.11}$$

Plugging (B.10) inside the area functional, being y written in terms of x and z, we get

$$\mathcal{A}[\gamma_A^*] \,=\, 4 \int_0^{\tilde{x}_\varepsilon} d\tilde{x} \int_\varepsilon^{z_*(\tilde{x})} dz\, \frac{\sqrt{1 + (\partial_z y)^2 + (\partial_x y)^2}}{z^2} \,=\, \frac{2R_1\sqrt{s_\infty}}{R_2} \int_0^{\tilde{x}_\varepsilon} \frac{M_\varepsilon(\tilde{x})}{\left(1 - \tilde{x}^n\right)^{1/n}}\, d\tilde{x}\,, \tag{B.12}$$

where

$$M_\varepsilon(\tilde{x}) \equiv \int_{\varepsilon/z_*(\tilde{x})}^1 \frac{\sqrt{1 + \left(R_2/R_1\right)^2 h_n(\tilde{x})^2\, C(Z)^2}}{Z^2\sqrt{1 - Z^4}}\, dZ\,, \qquad C(Z) \equiv \frac{2}{\sqrt{s_\infty}} \left(\int_Z^1 \sqrt{\frac{1 - Z^4}{1 - u^4}}\, u^2\, du - Z^3 \right). \tag{B.13}$$

Computing (B.12) analytically is too hard, but one can check that the area law is satisfied. When $\varepsilon \to 0$, from (B.11) we have that $\tilde{x}_\varepsilon = 1 + O(\varepsilon^n)$. In this limit, the most divergent term of $M_\varepsilon(\tilde{x})$ comes from the limit of integration $\varepsilon/z_*(\tilde{x})$ and it can be found by considering an integration on the interval $[\varepsilon/z_*(\tilde{x}), a]$, where Z is infinitesimal if $a \ll 1$. The remaining integral provides $O(1)$ terms. For $Z \to 0$ we have that $C(0) = 1$ and therefore the leading term in (B.12) is given by

$$\mathcal{A}[\gamma_A^*] = \frac{2R_1\sqrt{s_\infty}}{R_2} \int_0^1 d\tilde{x}\, \frac{\sqrt{1 + \left(R_2/R_1\right)^2 h_n(\tilde{x})^2}}{\left(1 - \tilde{x}^n\right)^{1/n}} \int_{\varepsilon/z_*(\tilde{x})}^a \frac{dZ}{Z^2} + O(1) = \frac{P_A}{\varepsilon} + O(1)\,, \tag{B.14}$$

where P_A given in (B.8) can be recognized after (B.10) and (B.9) have been employed. We are not able to find F_A^* analytically but it can be obtained numerically as $F_A^* = \lim_{\varepsilon\to 0}(P_A/\varepsilon - \mathcal{A}[\gamma_A^*])$, with $\mathcal{A}[\gamma_A^*]$ given by (B.12), getting a lower bound for F_A associated with the superellipse.

It is interesting to consider F_A^* in the limit of a very elongated superellipses, namely when $R_1/R_2 \to \infty$. This means that (B.12) must be studied in the double expansion $\varepsilon \to 0$ and $R_2/R_1 \to 0$. Assuming that the order of this two limits does not matter, let us set $R_2/R_1 = 0$ in the expressions of $M_\varepsilon(\tilde{x})$ in (B.13) and expand it for small ε, finding

$$M_\varepsilon(\tilde{x})\big|_{R_2/R_1=0} = \frac{z_*(\tilde{x})}{\varepsilon} - \frac{\sqrt{s_\infty}}{2} + O(\varepsilon^2)\,, \tag{B.15}$$

where $z_*(\tilde{x})$ is given in (B.10). By plugging (B.15) into (B.12) and expanding the resulting expression for $\varepsilon \to 0$, we have that

$$\mathcal{A}[\gamma_A^*] \,=\, \frac{4R_1}{\varepsilon} - s_\infty \frac{R_1}{R_2} \int_0^{\tilde{x}_\varepsilon} \frac{d\tilde{x}}{\left(1 - \tilde{x}^n\right)^{1/n}} + o(\varepsilon) \,=\, \frac{4R_1}{\varepsilon} - \frac{\pi s_\infty}{n \sin(\pi/n)}\, \frac{R_1}{R_2} + o(\varepsilon)\,. \tag{B.16}$$

Notice that, from (B.8), one can observe that $P_A = 4R_1\big[1+o(1)\big]$ when $R_1/R_2 \to \infty$. We conclude that the leading term of F_A^* as $R_1/R_2 \to \infty$ reads

$$F_A^* \;=\; \frac{\pi s_\infty}{n\sin(\pi/n)}\,\frac{R_1}{R_2} + \dots \;. \tag{B.17}$$

When $n=2$, the result of [91] is recovered, as expected. Moreover, the expression (B.17) in the special cases of $n=2$ and $n=3$ has been checked in Fig. 2.2 against the data obtained with Surface Evolver (see respectively the red and the blue dotted horizontal lines), finding a good agreement. Notice that the expression in the r.h.s. of (B.17) is strictly larger than the value of F_A corresponding to the infinite strip (see (2.12)), which is approached as $n \to \infty$.

B.4 Some generalizations to AdS$_{d+2}$

B.4.1 Sections of the infinite strip

In this section we discuss the computation of the area of the domain identified by an orthogonal section of the minimal surfaces associated with the infinite strip.

The metric of AdS$_{d+2}$ in the Poincaré coordinates reads

$$ds^2 = \frac{-dt^2 + dz^2 + dx_1^2 + \dots + dx_d^2}{z^2}\,. \tag{B.18}$$

Considering an infinite d-dimensional strip on the spatial slice $t=$ const extended along the $x_2,\dots,x_d$ directions whose width is given by $2R_2$, i.e. $|x_1| \leqslant R_2$, the minimal area surface associated with this domain is characterized by the profile $z = z(x_1)$. Because of the symmetry of the problem, $z(x_1)$ is even and therefore we can restrict to $0 \leqslant x_1 \leqslant R_2$. The profile is obtained by solving the following differential equation [46, 47]

$$z' = -\,\frac{\sqrt{z_*^{2d} - z^{2d}}}{z^d}\,. \tag{B.19}$$

where z_* is the maximum value of z, which is reached at $x_1 = 0$.

A way to get an orthogonal section of the infinite strip is defined by $x_2 = \dots = x_d =$ const. Then, one considers the two dimensional region enclosed by the profile $z(x_1)$ and the cutoff $z=\varepsilon$ in the plane (x_1, z). The domain along the x_1 axis is $|x_1| \leqslant R_2 - a$, where a is defined by $z(R_2-a) = \varepsilon$. Its area reads

$$\hat{\mathcal{A}} \;=\; 2\int_0^{R_2-a} dx_1 \int_\varepsilon^{z(x_1)} \frac{dz}{z^2} \;=\; \frac{2(R_2-a)}{\varepsilon} - \frac{2}{d}\left[\frac{\pi}{2} - \arctan\left(\frac{\varepsilon^d}{\sqrt{z_*^{2d}-\varepsilon^{2d}}}\right)\right] \;=\; \frac{2R_2}{\varepsilon} - \frac{\pi}{d} + o(1)\,, \tag{B.20}$$

where (B.19) has been employed.

Another section of the infinite strip to study is defined by $x_i =$ const for some $2 \leqslant i \leqslant d$ and $|x_j| \leqslant R_1$ for $j \neq i$. In this case we are interested in the volume of the d dimensional region enclosed by the profile $z(x_1)$ and $z=\varepsilon$, whose projection on the $z=0$ hyperplane is included within the section of the infinite strip we are dealing with. It is given by

$$\hat{\mathcal{A}} \;=\; 2(2R_1)^{d-2}\int_0^{R_2-a} dx_1 \int_\varepsilon^{z(x_1)} \frac{dz}{z^d} \;=\; (2R_1)^{d-2}(d-1)\left[\frac{2R_2}{\varepsilon^{d-1}} - \frac{\sqrt{\pi}\,\Gamma(1+1/d)}{z_*^{d-2}\,\Gamma(1/2+1/d)} + o(1)\right]. \tag{B.21}$$

Notice that for $d=2$ the expressions (B.20) and (B.21) coincide, as expected, and the result is employed in 2.2 to study the auxiliary surface, which corresponds to the dashed curve in Fig. 2.2.

B.4.2 Annular domains

In this appendix we consider the surfaces anchored on the boundaries of annular domains which are local minima of the area functional because some analytic expressions can be found for them.

The metric of AdS_{d+2} in Poincaré coordinates (2.2) written by employing spherical coordinates for the spatial part $\mathbb{R}^d$ of the boundary $z = 0$ is

$$ds^2 = \frac{dz^2 - dt^2 + d\rho^2 + \rho^2 d\Omega_{d-1}^2}{z^2}\,, \tag{B.22}$$

where $\rho \in [0, \infty)$ and the AdS radius has been set to one.

A spherically symmetric spatial region A in the AdS boundary is completely specified by an interval in the radial direction. Because of the symmetry of A, the minimal surface anchored on ∂A is given by $z = z(\rho)$ and, for a generic profile $z = z(\rho)$, the corresponding area of the two dimensional surface γ_A reads

$$\mathcal{A}[\gamma_A] \;\; = \;\; \mathrm{Vol}(S^{d-1})\,\mathcal{R}_d\,, \qquad \mathcal{R}_d \equiv \int \frac{\rho^{d-1}}{z^d}\sqrt{1+(z')^2}\,d\rho\,, \tag{B.23}$$

where $\mathrm{Vol}(S^{d-1})$ is the volume of the $(d-1)$-dimensional unit sphere and $\mathcal{R}_d$ is the integral in the radial direction. We remark that the integration domain in $\mathcal{R}_d$ is not necessarily the interval defining A in the radial direction, as it will be clear from the case discussed in the following. In order to find the minimal surface $\tilde{\gamma}_A$, one extremizes the area functional (B.23), obtaining

$$z z'' + (1+z'^2)\left[d + (d-1)\frac{z z'}{\rho}\right] = 0\,. \tag{B.24}$$

When A is a sphere of radius R, we have that $0 \leqslant \rho \leqslant R$ and it is well known that the corresponding minimal surface is a hemisphere [46, 47].

Here we consider the region A delimited by two concentric spheres, whose radii are R_{in} and R_{out}, with $0 < R_{\text{in}} < R_{\text{out}}$. In this case $R_{\text{in}} \leqslant \rho \leqslant R_{\text{out}}$ and A is not simply connected. For $d = 2$ and $d = 3$, the corresponding minimal surface extending in the bulk and anchored on ∂A has been studied in [58, 59, 113]. In order to solve (B.24) for this configuration, we find it convenient to introduce [58, 59]

$$z(\rho) \equiv \rho\,\tilde{z}(\rho)\,, \qquad u \equiv \log\rho\,, \qquad \tilde{z}_u \equiv \partial_u \tilde{z}\,. \tag{B.25}$$

Notice that $\tilde{z} = \tan\theta$ is the angular coefficient of the line connecting the origin to a point belonging to the surface. Given (B.25), the differential equation (B.24) becomes

$$\tilde{z}\,\tilde{z}_u\big(1 + \partial_{\tilde{z}}\tilde{z}_u\big) + \big[1 + (\tilde{z}+\tilde{z}_u)^2\big]\big[d + (d-1)\tilde{z}(\tilde{z}+\tilde{z}_u)\big] = 0\,. \tag{B.26}$$

Integrating this equation, we find two solutions, namely

$$\tilde{z}_{u,\pm}(\tilde{z}) = -\frac{1+\tilde{z}^2}{\tilde{z}}\left[1 \pm \frac{\tilde{z}^{d-1}}{\sqrt{K(1+\tilde{z}^2) - \tilde{z}^{2d}}}\right]^{-1}, \qquad K \,>\, 0\,, \tag{B.27}$$

which correspond to two different parts of the profile. As for the integration constant K, it must be strictly positive because $\tilde{z} = 0$ corresponds to the boundary $z = 0$, which is included in the range of z. The domain for $\tilde{z}$ is $0 \leqslant \tilde{z} \leqslant \tilde{z}_m$, where $\tilde{z}_m$ is the first positive zero of the polynomial under the square root in (B.27). For $d = 2$ we are lead to solve a biquadratic equation, which gives $\tilde{z}_m^2 = \big(K + \sqrt{K(K+4)}\,\big)/2$. Notice that $\tilde{z}_m \to 0$ when $K \to 0$.

The differential equation (B.27) can be solved through the separation of the variables. In particular, from the r.h.s. of (B.27), we find it convenient to introduce

$$f^{(d)}_{\pm,K}(\tilde{z}) \equiv \int_0^{\tilde{z}} \frac{\lambda}{1+\lambda^2}\left[1 \pm \frac{\lambda^{d-1}}{\sqrt{K(1+\lambda^2) - \lambda^{2d}}}\right] d\lambda\,. \tag{B.28}$$

Then, the profile of the radial section is given by the following two branches

$$\begin{cases} \rho = R_{\text{in}}\, e^{-f^{(d)}_{-,K}(\tilde{z})}\,, \\ \rho = R_{\text{out}}\, e^{-f^{(d)}_{+,K}(\tilde{z})}\,. \end{cases} \tag{B.29}$$

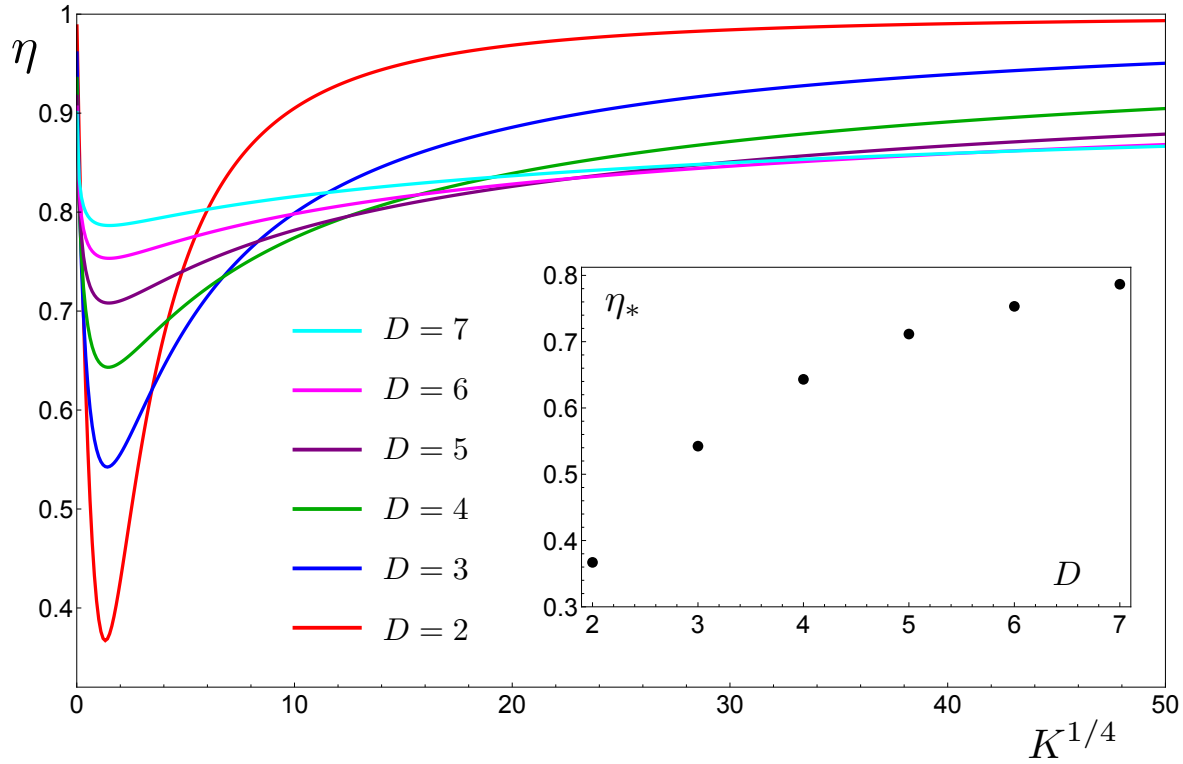

Figure B.3: Curves for η as function of K obtained from the matching condition (B.30) for various dimensions $2 \leqslant d \leqslant 7$. For any d, a minimal value $\eta_* > 1$ occurs, which is shown in the inset. Given a value $\eta \in (\eta_*, 1)$, two values of K correspond to it, providing two different radial profiles (see an example for $d = 2$ in Fig. B.4).

Imposing that these two branches match at the point P_m, whose (ρ, z) coordinates are $(\rho_m, z_m \equiv z(\rho_m))$, where z_m has been found above, we get the following relation

$$-\log(\eta) = f^{(d)}_{+,K}(\tilde{z}_m) - f^{(d)}_{-,K}(\tilde{z}_m) = \int_0^{\tilde{z}_m} \frac{2\,\lambda^d}{(1+\lambda^2)\sqrt{K(1+\lambda^2)-\lambda^{2d}}}\,d\lambda\,, \qquad \eta \equiv \frac{R_{\rm in}}{R_{\rm out}}\,. \tag{B.30}$$

Since $\tilde{z}_m$ depends on K, from (B.30) we get a relation between η and K, which is represented in Fig. B.3 for $2 \leqslant d \leqslant 7$. The first feature to point out about (B.30) is the existence of a minimal value for η that will be denoted by $\eta_* > 0$. For instance, we find $\eta_* = 0.367$, $\eta_* = 0.542$ and $\eta_* = 0.643$ for $d = 2$, $d = 3$ and $d = 4$ respectively (see the inset in Fig. B.3 for other d's). Then, for any $\eta_* < \eta < 1$, there are two values of K giving the same η, while for $0 < \eta < \eta_*$ connected solutions do not exist. The two different K's associated with the same $\eta_* < \eta < 1$ provide two different radial profiles and therefore two connected surfaces having the same ∂A. In order to find the global minimum of the area functional, we have to evaluate their area. Through a numerical analysis, one observes that z_m is an increasing function of K.

Beside P_m, another interesting point of the profile is $P_0 = (\rho_0, z_0 \equiv z(\rho_0))$, where $|z(\rho_0)'|$ diverges. From (B.27), this divergence occurs when

$$\sqrt{K(1+\tilde{z}_0^2) - \tilde{z}_0^{2d}} \pm \tilde{z}_0^{d-1} = 0 \qquad \Longrightarrow \qquad K = \tilde{z}_0^{2d-2} \equiv (\tan\theta_0)^{2d-2}\,. \tag{B.31}$$

This tells us that K has a geometric meaning because it provides $\tilde{z}_0$.

Let us also introduce the point P_*, with coordinates $(\rho_*, z_* \equiv z(\rho_*))$ as the point having the maximum value of z, which corresponds to the maximal penetration of the minimal surface into the bulk. The coordinate z_* can be found by considering the branch $z(\rho)$ characterized by $f^{(d)}_{+,K}$ in (B.29) and then computing its derivative w.r.t. ρ, which is given by

$$\frac{dz}{d\rho} = \frac{d(\tilde{z}\rho)}{d\tilde{z}}\left(\frac{d\rho}{d\tilde{z}}\right)^{-1} = \tilde{z} - \left(\frac{df^{(d)}_{+,K}(\tilde{z})}{d\tilde{z}}\right)^{-1}\,, \tag{B.32}$$

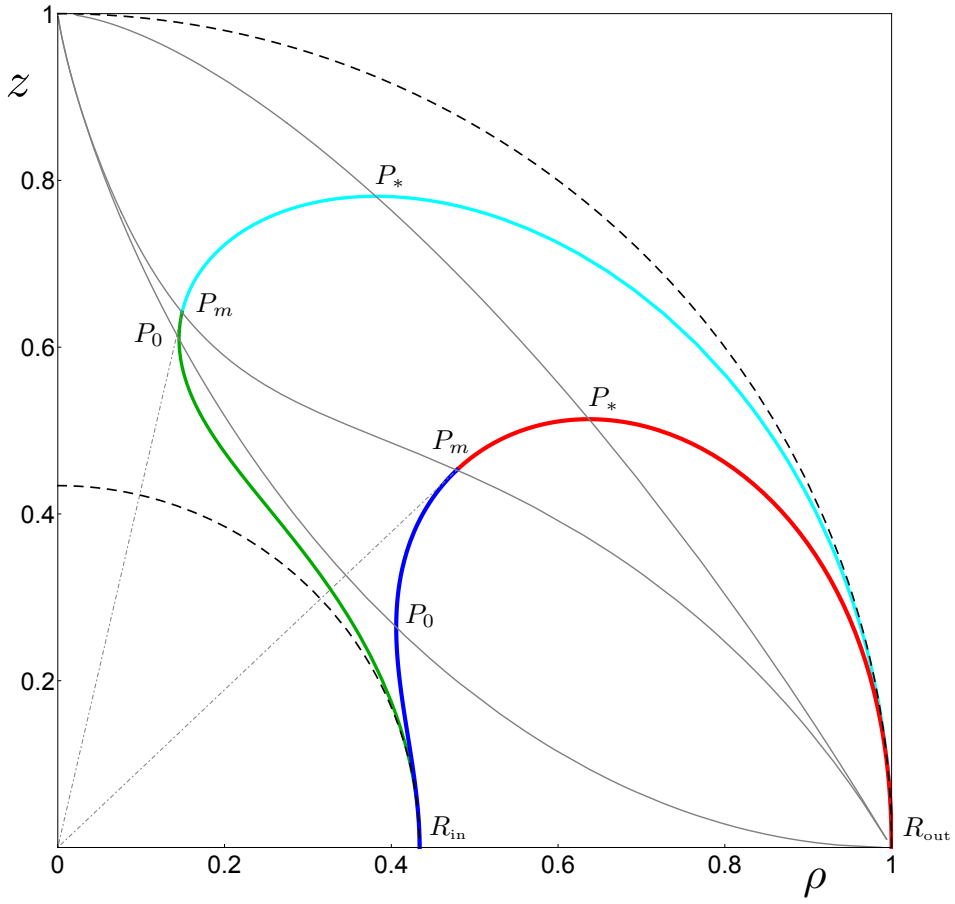

Figure B.4: Radial profiles in the (ρ, z) plane for the connected surfaces anchored on the boundary of the same annulus A having $R_{\rm in} < R_{\rm out}$. They correspond to local minima of the area functional and they are characterized by the two different values of K associated with the same η. These connected surfaces are obtained through (B.29) and (B.30), where different colours are used for the various branches. The dashed curves represent the two concentric hemispheres anchored on ∂A as well. The continuous grey curves are the paths in the (ρ, z) plane of the points P_0, P_m and P_* as $K \in (0, \infty)$. Here $d = 2$, $R_{\rm in} = 0.43$, $R_{\rm out} = 1$ and the values of K are $K = 0.81$ (global minimum) and $K = 2.05$ (local minimum). Comparing the area of the two connected surfaces, we find that the one having minimal area has P_* closer to the boundary.

where in the last step (B.29) has been used. When $d = 2$ the root of (B.32) can be found and it reads

$$\tilde{z}_* = K^{1/4} \,. \tag{B.33}$$

An explicit example in $d = 2$ is given in Fig. B.4, where we have shown the two connected radial profiles having the same $\eta > \eta_*$ but different values of K. The two different branches in (B.29) at fixed K, supported by the matching condition (B.30), have been denoted with different colours: the red and cyan curves are obtained through $f^{(2)}_{+,K}$ while the blue and the green ones through $f^{(2)}_{-,K}$. In Fig. B.4 the grey curves denote the paths described by the three points P_m, P_0 and P_* introduced above as K assumes all the positive real values.

We find it instructive to consider the limit $K \to +\infty$. From (B.28), in this limit one finds $f^{(d)}_{+,\infty} = f^{(d)}_{-,\infty}$ for any d, which reads

$$\lim_{K\to\infty} f^{(d)}_{\pm,K}(\tilde{z}) = \int_0^{\tilde{z}} \frac{\lambda}{1+\lambda^2}\, d\lambda = \frac{1}{2}\log(1+\tilde{z}^2)\,, \tag{B.34}$$

and therefore $\eta \to 1$ from (B.30), i.e. $R_{\rm in} = R_{\rm out} \equiv R$ (see also Fig. B.3). From (B.34), both the branches

in (B.29) become

$$\rho = \frac{R}{\sqrt{1+\tilde{z}^2}}\,, \tag{B.35}$$

which is the well known spherical solution $z^2 = R^2 - \rho^2$. As for the points P_m, P_0 and P_*, they tend to the same point when $\eta \to 1$, as can be seen from Fig. B.4, where the gray lines show the paths of these points in the (ρ, z) plane as K varies in $(0, \infty)$.

Given the radial profile (B.29), we can compute the area of the corresponding surface obtained by exploiting the rotational symmetry. From (B.25), the radial integral in (B.23) can be written as

$$\mathcal{R}_d^{\rm con} = \int_{\tilde{z}_m}^{\tilde{\varepsilon}_+} \frac{\sqrt{1+(\tilde{z}+\tilde{z}_{u,+})^2}}{\tilde{z}^d\,\tilde{z}_{u,+}}\,d\tilde{z} + \int_{\tilde{z}_m}^{\tilde{\varepsilon}_-} \frac{\sqrt{1+(\tilde{z}+\tilde{z}_{u,-})^2}}{\tilde{z}^d\,\tilde{z}_{u,-}}\,d\tilde{z}\,, \qquad \tilde{\varepsilon}_+ \equiv \frac{\varepsilon}{R_{\rm out}}\,, \quad \tilde{\varepsilon}_- \equiv \frac{\varepsilon}{R_{\rm in}}\,, \tag{B.36}$$

where $\tilde{z}_{u,\pm}$ have been defined in (B.27) and $0 < \varepsilon \ll 1$ is the ultraviolet cutoff of the boundary theory. Notice that the domains of integration are different for the two branches of the profile. Plugging (B.27) into (B.36), the integrands become the same and, by splitting the first integral, (B.36) becomes

$$\mathcal{R}_d^{\rm con} = \int_{\varepsilon/R_{\rm out}}^{\tilde{z}_m} \frac{\sqrt{K}\,d\tilde{z}}{\tilde{z}^d\sqrt{K(1+\tilde{z}^2)-\tilde{z}^{2d}}} + \int_{\varepsilon/R_{\rm in}}^{\tilde{z}_m} \frac{\sqrt{K}\,d\tilde{z}}{\tilde{z}^d\sqrt{K(1+\tilde{z}^2)-\tilde{z}^{2d}}} \tag{B.37}$$

$$= 2\int_{\varepsilon/R_{\rm in}}^{\tilde{z}_m} \frac{\sqrt{K}\,d\tilde{z}}{\tilde{z}^d\sqrt{K(1+\tilde{z}^2)-\tilde{z}^{2d}}} + \int_{\varepsilon/R_{\rm out}}^{\varepsilon/R_{\rm in}} \frac{\sqrt{K}\,d\tilde{z}}{\tilde{z}^d\sqrt{K(1+\tilde{z}^2)-\tilde{z}^{2d}}}\,. \tag{B.38}$$

In the second integral of (B.38), we can employ the expansion of the integrand for $\tilde{z} \sim 0$, which reads

$$\frac{1}{\tilde{z}^d\sqrt{1+\tilde{z}^2-\tilde{z}^{2d}/K}} = \frac{1}{\tilde{z}^d} + \frac{\gamma_{d,d-1}}{\tilde{z}^{d-2}} + \frac{\gamma_{d,d-3}}{\tilde{z}^{d-4}} + \cdots + \begin{cases} \dfrac{\gamma_{d,\log}}{\tilde{z}} + O(\tilde{z}) & \text{odd } d, \\ \gamma_{d,-1} + O(\tilde{z}^2) & \text{even } d, \end{cases} \tag{B.39}$$

finding that it provides a non trivial contribution $\gamma_{d,\log}\log(R_{\rm out}/R_{\rm in})$ to the finite term for odd d.

Given $R_{\rm in}$ and $R_{\rm out}$, besides the two connected surfaces having the same η but different K, we have also another surface γ_A which is a local minimum for the area functional (B.23) such that $\partial\gamma_A = \partial A$: it is made by two disjoint concentric hemispheres in the bulk with radii $R_{\rm in}$ and $R_{\rm out}$ which are anchored on the boundaries of the concentric spheres in the boundary (see the dashed curves in Fig. B.4). The area of a hemisphere of radius R in the bulk anchored on the boundary of a sphere with the same radius at $z = 0$ can be found by integrating (B.23) for $0 \leqslant \rho \leqslant R - a$, where $z(\varepsilon) \equiv a$, finding

$$\mathcal{R}_d^{\rm sph}(R) = \int_{\infty}^{\varepsilon/R} \frac{\sqrt{1+(\tilde{z}+\tilde{z}_u)^2}}{\tilde{z}^d\tilde{z}_u}\,d\tilde{z} = \int_{\varepsilon/R}^{\infty} \frac{d\tilde{z}}{\tilde{z}^d\,\sqrt{1+\tilde{z}^2}}\,, \qquad \varepsilon = \sqrt{R^2-(R-a)^2} \ll 1\,, \tag{B.40}$$

where $\tilde{z}_u$ is (B.27) in the limit $K \to +\infty$, namely $\tilde{z}_u = -(1+\tilde{z}^2)/\tilde{z}$.

Thus, the factor coming from the radial integration in (B.23) for this configuration of two disjoint hemispheres is $\mathcal{R}_d^{\rm dis} = \mathcal{R}_d^{\rm sph}(R_{\rm out}) + \mathcal{R}_d^{\rm sph}(R_{\rm in})$.

Having found three surfaces anchored on ∂A for any given $R_{\rm in} < R_{\rm out}$ such that $\eta_* < \eta < 1$ which are local minima of the area functional, the holographic entanglement entropy can be found by selecting the global minimum among them.

Considering a connected surface and the configuration made by the two disjoint hemispheres, we find it useful to introduce the following finite quantity

$$\Delta\mathcal{R}_d \equiv \lim_{\varepsilon\to 0}(\mathcal{R}_d^{\rm dis} - \mathcal{R}_d^{\rm con})\,. \tag{B.41}$$

From (B.37) and (B.40), it can be written as

$$\Delta\mathcal{R}_d = \mathcal{J}_d^{({\rm in})} + \mathcal{J}_d^{({\rm out})}\,, \tag{B.42}$$

where we have introduced

$$\mathcal{J}_d^{(j)} = \lim_{\varepsilon\to 0}\left(\int_{\varepsilon/R_j}^{\infty} \frac{d\tilde{z}}{\tilde{z}^d\,\sqrt{1+\tilde{z}^2}} - \int_{\varepsilon/R_j}^{\tilde{z}_m} \frac{d\tilde{z}}{\tilde{z}^d\sqrt{1+\tilde{z}^2-\tilde{z}^{2d}/K}}\right). \tag{B.43}$$

Splitting the second integral, we can take the limit, finding that $\mathcal{J}_d^{(\text{in})} = \mathcal{J}_d^{(\text{out})}$ and then

$$\Delta\mathcal{R}_d = 2\left[\int_{\tilde{z}_m}^{\infty} \frac{d\tilde{z}}{\tilde{z}^d\sqrt{1+\tilde{z}^2}} - \int_0^{\tilde{z}_m} \frac{1}{\tilde{z}^d\sqrt{1+\tilde{z}^2}}\left(\frac{1}{\sqrt{1-\tilde{z}^{2d}/[K(1+\tilde{z}^2)]}} - 1\right) d\tilde{z}\right]. \tag{B.44}$$

Since $z_m = z_m(K)$ and K depends on the ratio η only, also $\Delta\mathcal{R}_d$ is a function of η. Nevertheless, as discussed above, there are two values of K associated with the same η and, by computing $\Delta\mathcal{R}_d$ for both of them, we can easily find which surface has the minimal area between the two connected ones. It turns out that it is the one associated with the lowest value of K. Since z_m is an increasing function of K, the minimal area surface between the two connected ones has the lowest z_m. In the example in Fig. B.4 for $d = 2$, both the radial profiles of the two connected surfaces which are local minima of the area functional and which have the same η are shown. The one described by the red and the blue curves characterizes the minimal area surface between the two connected ones.

Once the connected surface having minimal area has been found, the sign of the corresponding $\Delta\mathcal{R}_d$ determines the configuration with minimal area, providing therefore the global minimum of the area functional, and its root (which can be found numerically) gives the value of $\eta = \eta_c$ which characterizes the transition. For $d = 2$, $d = 3$ and $d = 4$ we get respectively $\eta_c = 0.419$ [58, 107], $\eta_c = 0.562$ [59] and $\eta_c = 0.652$. Thus, for any $\eta \in (\eta_*, 1)$, we have $\eta_c > \eta_*$ and $\Delta\mathcal{R}_d > 0$ when $\eta \in (\eta_c, 1)$. This tells us that for $\eta < \eta_c$ the configuration occurring in the holographic entanglement entropy for the annular domains is the one made by two disjoint hemispheres.

B.5 Elliptic integrals

When $d = 2$, the integrals encountered in 2.2.2 and in B.4.2 can be computed analytically in terms of elliptic integrals. Here we report their definitions for completeness, following [183] (notice that Mathematica adopts the same notation).

The incomplete elliptic integrals of the first, second and third kind are defined respectively as follows

$$\mathbb{F}(x|m) \equiv \int_0^x \frac{d\theta}{\sqrt{1-m\sin^2\theta}}, \tag{B.45}$$

$$\mathbb{E}(x|m) \equiv \int_0^x \sqrt{1-m\sin^2\theta}\, d\theta, \tag{B.46}$$

$$\Pi(n,x|m) \equiv \int_0^x \frac{d\theta}{(1-n\sin^2\theta)\sqrt{1-m\sin^2\theta}}. \tag{B.47}$$

Setting $x = \pi/2$ in these expressions, we have

$$\mathbb{K}(m) \equiv \mathbb{F}(\pi/2|m), \qquad \mathbb{E}(m) \equiv \mathbb{E}(\pi/2|m), \qquad \Pi(n,m) \equiv \Pi(n,\pi/2|m), \tag{B.48}$$

which are the complete elliptic integrals of the first, second and third kind respectively.

Appendix C

Explicit computations for hvLif-Vaidya backgrounds

C.1 Spherical region for hvLif

In this appendix we construct a sequence of curves $\{x_i(s), z_i(s)\}$ for $i \in \mathbb{N}$ defined in a parametric way, whose asymptotic one $\{x_\infty(s), z_\infty(s)\}$ is the solution of (3.31).
The extremal surface ending on the sphere of radius R and extended in the $t = \text{const}$ section of the $d+2$ dimensional space-time hvLif obeys (3.31) with the boundary conditions $z'(0) = 0$ and $z(R) = 0$. We recall that for hvLif without black holes the Lifshitz exponent ζ does not enter in the equation. The equation (3.31) can be rewritten as

$$d\left(\frac{z'}{\rho}+\frac{1}{z}\right)+\left(\frac{z''}{1+z'^2}-\frac{z'}{\rho}\right)=\frac{\theta}{z}\,. \tag{C.1}$$

We find it convenient to introduce

$$\tilde{z}(x)\equiv\frac{z(\rho(x))}{R}\,,\qquad x\equiv 1-\frac{\rho}{R}\in[0,1]\qquad\Longrightarrow\qquad z'(\rho)=-\dot{\tilde{z}}(x)\,,\qquad z''(\rho)=\frac{\ddot{\tilde{z}}(x)}{R}\,. \tag{C.2}$$

By employing (C.2), (C.1) becomes (3.32), which can be written as follows

$$d\left(\frac{1}{\tilde{z}}-\frac{\dot{\tilde{z}}}{1-x}\right)+\frac{\ddot{\tilde{z}}}{1+\dot{\tilde{z}}^2}+\frac{\dot{\tilde{z}}}{1-x}=\frac{\theta}{\tilde{z}}\,,\qquad\qquad \tilde{z}(0)=0\,,\qquad \dot{\tilde{z}}(1)=0\,. \tag{C.3}$$

The well known hemispherical solution for $\theta = 0$ becomes

$$\tilde{z}(x)\big|_{\theta=0}=\sqrt{x(2-x)}=\sqrt{2x}\left(\sum_{n=0}^{+\infty}\frac{\Gamma(n-3/2)}{\Gamma(-3/2)n!}x^n\right)\,, \tag{C.4}$$

which evidences that $\tilde{z}(x) = \sqrt{2x}$ when $x \to 0$. Also for $\theta \neq 0$ we have $\tilde{z} \simeq 0$ near the boundary $x \simeq 0$ and here we are interested in the way it vanishes. First, from (C.3) one observes that, when $d - \theta \neq 0$ (the case $d - \theta = 0$ is not allowed by NEC), the solution must have a divergent $\tilde{z}'(0)$. Introducing the following ansatz for the solution close to the boundary

$$\tilde{z}(x)=c_0x^\alpha\,,\qquad 0<\alpha<1\,,\qquad x\sim 0\,, \tag{C.5}$$

and plugging it into (C.1), the first order for $x \to 0$ provides the following equation

$$\left(d-\theta+1-\frac{1}{\alpha}\right)x^{-\alpha}+c_0^2\alpha(1-d)x^{\alpha-1}=0\,. \tag{C.6}$$

We can recognize three cases:

1. $d = 1$. In this case we find
$$\tilde{z}(x) \simeq c_0 x^{\frac{1}{2-\theta}}\,, \tag{C.7}$$
where the condition $0 < \alpha < 1$ becomes $\theta < 1$. In particular, for $\theta = 0$ we recover the expected $\sqrt{x}$ behaviour, although the overall constant is not fixed. Since for $d = 1$ the calculations from the strip hold, we have that (see (3.26))
$$x(\tilde{z}) = \frac{\tilde{z}_*}{2-\theta}\left(\frac{\tilde{z}}{\tilde{z}_*}\right)^{2-\theta} {}_2F_1\left(\frac{1}{2}, \frac{1}{2} + \frac{1}{2(1-\theta)}; \frac{3}{2} + \frac{1}{2(1-\theta)}; (\tilde{z}/\tilde{z}_*)^{2(1-\theta)}\right), \tag{C.8}$$
where the constant $\tilde{z}_*$ reads
$$\tilde{z}_* = \frac{\Gamma(1/(2-2\theta))}{\sqrt{\pi}\,\Gamma(1/2 + 1/(2-2\theta))}\,. \tag{C.9}$$
Since the hypergeometric function in (C.8) goes to 1 at the boundary, from (C.7) we can write
$$c_0 = \left(\tilde{z}_*^{1-\theta}(2-\theta)\right)^{\frac{1}{2-\theta}}\,, \tag{C.10}$$
which simplifies to $c_0 = \sqrt{2}$ when $\theta = 0$ because $\tilde{z}_*|_{\theta=0} = 1$.

2. $d \neq 1$ and $d_\theta \neq 1$. In this regime one finds that
$$\tilde{z}(x) = \sqrt{\frac{d_\theta - 1}{d-1}\,2x}\left[1 - \frac{1}{4}\left(1 + \frac{d-1}{d_\theta - 1} - \frac{d-3}{d_\theta - 3}\right)x + O(x^2)\right], \tag{C.11}$$
again, notice how when $d_\theta = d$ we recover the AdS solution but now with even the correct value of the coefficient, $c_0 = \sqrt{2}$. We included also the c_1 correction to show the emergence of poles in the coefficient for any odd integer value of d_θ. It is possible to compute the expansion up to arbitrary order, but it appears the terms in the series cannot be written in any compact or recursive form.

3. $d \neq 1$ and $d_\theta = 1$. In this case (C.6) becomes
$$x^{-\alpha}\frac{2\alpha - 1}{\alpha} + x^{\alpha-1}c_0^2\alpha(1-d) = 0\,, \tag{C.12}$$
which gives $\alpha = 1/2$ and $c_0 = 0$. This tells us that the ansatz (C.5) is meaningless in this case.

C.1.1 A parametric reformulation

In order to improve this analysis and understand better the last case, following [184] (where the $d = 2$ case has been studied) we introduce
$$s \equiv \frac{1}{\tilde{z}^{d_\theta}\sqrt{1 + \dot{\tilde{z}}^2}}\,. \tag{C.13}$$
This allows to write the term containing $\ddot{\tilde{z}}$ in (C.3) as follows
$$\frac{\ddot{\tilde{z}}}{1 + \dot{\tilde{z}}^2} = -\frac{d_\theta}{\tilde{z}} - \left(s\,\frac{d\tilde{z}}{ds}\right)^{-1}\,. \tag{C.14}$$
Thus, the equation (C.3) can be written as
$$\frac{d-1}{x-1}\,\frac{\frac{d\tilde{z}}{ds}}{\frac{dx}{ds}} - \left(s\,\frac{d\tilde{z}}{ds}\right)^{-1} = 0\,. \tag{C.15}$$
From (C.13) it is straightforward to write that
$$\frac{dx}{ds} = \frac{s\tilde{z}^{d_\theta}}{\sqrt{1 - s^2\tilde{z}^{2d_\theta}}}\,\frac{d\tilde{z}}{ds}\,. \tag{C.16}$$
Then, by isolating x in (C.15) and employing (C.16), the differential equation (C.15) becomes
$$x = 1 + \frac{(d-1)\sqrt{1 - s^2\tilde{z}^{2d_\theta}}}{\tilde{z}^{d_\theta}}\,\frac{d\tilde{z}}{ds}\,. \tag{C.17}$$

We find it convenient to rewrite (C.17) and (C.16) respectively as follows

$$\begin{cases} \dfrac{d}{ds}\tilde{z}(s)^{-(d_\theta-1)} \;=\; \dfrac{(d_\theta-1)[1-x(s)]}{(d-1)\sqrt{1-s^2\tilde{z}(s)^{2d_\theta}}} & d_\theta \neq 1 \\ \dfrac{d}{ds}\log\tilde{z}(s) \;=\; -\dfrac{1-x(s)}{(d-1)\sqrt{1-s^2\tilde{z}(s)^2}} & d_\theta = 1 \end{cases} , \qquad \frac{d}{ds}x(s) \;=\; -\frac{[1-x(s)]\,s\tilde{z}(s)^{2d_\theta}}{(d-1)[1-s^2\tilde{z}(s)^{2d_\theta}]}\,. \tag{C.18}$$

Integrating these equations, one finds

$$\tilde{z}(s) \;=\; \begin{cases} \left(\dfrac{d_\theta-1}{d-1}\displaystyle\sum_{n=0}^{+\infty}\frac{\Gamma(n+1/2)}{\sqrt{\pi}n!}\int_{s_{\min}}^{s}[1-x(r)]r^{2n}\tilde{z}(r)^{2d_\theta n}dr\right)^{-\frac{1}{d_\theta}-1} & d_\theta \neq 1 \\ \exp\left(-\dfrac{1}{d-1}\displaystyle\sum_{n=0}^{+\infty}\frac{\Gamma(n+1/2)}{\sqrt{\pi}n!}\int_{s_{\min}}^{s}[1-x(r)]r^{2n}\tilde{z}(r)^{2n}dr\right) & d_\theta = 1 \end{cases} \tag{C.19}$$

and

$$x(s) \;=\; -\frac{1}{d-1}\sum_{n=0}^{+\infty}\int_{s_{\min}}^{s}[1-x(r)]r^{1+2n}\tilde{z}(r)^{2d_\theta(1+n)}dr\,, \tag{C.20}$$

where the expansion of $(1-w)^{-\alpha}$ for $w\to 0$ has been used. This can be done because (C.13) implies that $s\tilde{z}^{d_\theta}$ is infinitesimal when s is large. Moreover, $s_{\min}$ is the value of s at which the tip of the minimal surface is reached and it can be found from (C.13)

$$s_{\min} = \tilde{z}_*^{-d_\theta}\,. \tag{C.21}$$

It is evident that (C.19) and (C.20) is only a formal solution and it does not even allow to plot the solution numerically. Nevertheless, this form allows us to construct the solution $\{\tilde{z}(s),x(s)\}$ recursively through an inductive procedure.
Since large s corresponds to the boundary, we have that $x(s)=o(1)$ for large s. This allows us to observe that the leading order of the integrals in (C.19) and (C.20) can be obtained by neglecting $x(r)$ within the square brackets occurring in the integrands. We find it convenient to define the first pair of functions in the inductive process through the boundary conditions $x(s)\to 0$ and $\tilde{z}(s)\to 0$ for $s\to\infty$, namely

$$\tilde{z}_0(s) = 0\,, \qquad x_0(s) = 0\,. \tag{C.22}$$

Then for $i>0$ we define

$$\tilde{z}_{i+1}(s) \;=\; \begin{cases} \left(\dfrac{d_\theta-1}{d-1}\displaystyle\sum_{n=0}^{i}\frac{\Gamma(n+1/2)}{\sqrt{\pi}n!}\int_{s_{\min}}^{s}[\tilde{z}_{i-n+1}(r)^{2d_\theta n}-x_{i-n}(r)\tilde{z}_{i-n}(r)^{2d_\theta n}]r^{2n}dr\right)^{-\frac{1}{d_\theta-1}} & d_\theta \neq 1 \\ \exp\left(-\dfrac{1}{d-1}\displaystyle\sum_{n=0}^{i}\frac{\Gamma(n+1/2)}{\sqrt{\pi}n!}\int_{s_{\min}}^{s}[\tilde{z}_{i-n+1}(r)^{2n}-x_{i-n}(r)\tilde{z}_{i-n}(r)^{2n}]r^{2n}dr\right) & d_\theta = 1 \end{cases} \tag{C.23}$$

and

$$x_{i+1}(s) \;=\; -\frac{1}{d-1}\sum_{n=0}^{i}\int_{s_{\min}}^{s}[\tilde{z}_{i-n+1}(r)^{2d_\theta(1+n)}-x_{i-n}(r)\tilde{z}_{i-n}(r)^{2d_\theta(1+n)}]r^{1+2n}dr\,. \tag{C.24}$$

Given the pairs $\{\tilde{z}_j(s),x_j(s)\}$ for $j\leqslant i$, this equation give $\{\tilde{z}_{i+1}(s),x_{i+1}(s)\}$. Notice that x_{i+1} depends on $\tilde{z}_{i+1}$ through the $n=0$ term and this means that one has to solve (C.23) first and then (C.24). This procedure defines a sequence of pairs $\{\tilde{z}_i(s),x_i(s)\}$ for $i\in\mathbb{N}$ and the exact solution of (C.18) is the asymptotic one $\{\tilde{z}_\infty(s),x_\infty(s)\}$ for $i\to+\infty$. The pair $\{\tilde{z}_i(s),x_i(s)\}$ for some finite i gives a better approximation of the asymptotic solution the higher i is, starting from the regime of large s.
Given (C.22), for $i=1$ we find

$$\tilde{z}_1(s) \;=\; \begin{cases} \left(\dfrac{d-1}{d_\theta-1}\right)^{\frac{1}{d_\theta-1}}(s-s_{\min})^{-\frac{1}{d_\theta-1}} \\ e^{-\frac{s-s_{\min}}{d-1}} \end{cases} , \qquad x_1(s) = \begin{cases} \dfrac{1}{2}\left(\dfrac{d_\theta-1}{d-1}\right)^{\frac{d_\theta+1}{d_\theta-1}}(s-s_{\min})^{-\frac{2}{d_\theta-1}} & d_\theta\neq 1 \\ \dfrac{2s+d-1}{4}\,e^{-2\frac{s-s_{\min}}{d-1}} & d_\theta = 1 \end{cases} \tag{C.25}$$

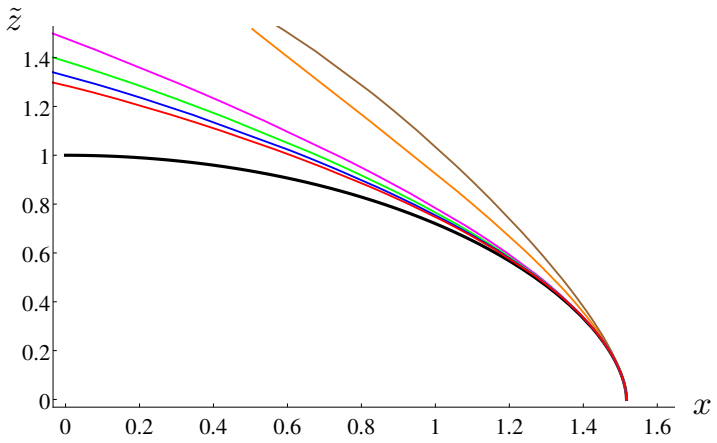

Figure C.1: The black curve is the numerical solution $\tilde{z} = \tilde{z}(x)$ of (C.3) for $d = 2$ and $d_\theta = 1$. The remaining curves are $(x_i(s), \tilde{z}_i(s))$ for $i = 1, 2, 3, 4, 5, 6$ (respectively orange, brown, magenta, green, blue and red), constructed in C.1.1.

From (C.25) for $d_\theta \neq 1$ and large s, we can write

$$s = \left(\frac{d-1}{d_\theta - 1}\right)^{\frac{1+d_\theta}{2}} (2x_1)^{-\frac{d_\theta - 1}{2}} . \tag{C.26}$$

Plugging this back into the corresponding $\tilde{z}_1$ in (C.25), we get the first term of (C.11) and the first term of (C.4) when $\theta = 0$, as expected. By employing (C.22) and (C.25), for $i = 2$ in the regime of large s we find

$$\tilde{z}_2(s) = \begin{cases} \left(\dfrac{d-1}{d_\theta - 1}\right)^{\frac{1}{d_\theta - 1}} s^{-\frac{1}{d_\theta - 1}} \left[1 - \left(\dfrac{d-1}{d_\theta - 1}\right)^{\frac{d_\theta + 1}{d_\theta - 1}} \dfrac{\theta\, s^{-\frac{2}{d_\theta - 1}}}{2(d_\theta - 3)}\right]^{-\frac{1}{d_\theta - 1}} & d_\theta \neq 1, 3 \\ e^{-\frac{1}{d-1}s} + \dfrac{(d-1)(d-3) + 2(d-2)s + 2s^2}{8} e^{-\frac{3}{d-1}s} & d_\theta = 1 \\ \left[\dfrac{2s}{d-1} + \dfrac{(d-1)(d-3)}{8} \log s\right]^{-\frac{1}{2}} & d_\theta = 3 \end{cases} \tag{C.27}$$

The expression for x_2 is quite complicated even at large s and we do not find it useful to write it here. We have neglected $s_{\min}$ because s is large, but it must be taken into account properly to obtain the plot in Fig. C.1. Higher orders are rather complicated as well and therefore we do not write them. Repeating the procedure we can find the various curves in Fig. C.1, from which it is evident that the exact solution of (3.32) is better approximated as i increases.

C.1.1.1 Area

The area functional is given by (3.29) $F(z) = 1$), namely

$$\mathcal{A} = \frac{2\pi^{d/2} R^\theta}{\Gamma(d/2)} \int_0^1 \frac{(1-x)^{d-1}}{\tilde{z}^{d_\theta}} \sqrt{1 + \dot{z}^2}\, dx = \frac{2\pi^{d/2} R^\theta}{(d-1)\Gamma(d/2)} \int_{s_{\min}}^{+\infty} \frac{(1-x)^d}{1 - s^2 \tilde{z}^{2d_\theta}}\, ds\,. \tag{C.28}$$

Since the integral is divergent, we must introduce the UV cutoff $\tilde{\epsilon} = \epsilon/R$ in the $\tilde{z}$ variable. It corresponds to a large value $s_{\max}$ such that $z(s_{\max}) = \epsilon$. By employing the expressions $\{\tilde{z}_i(s), x_i(s)\}$ discussed above in (C.28), one gets a corresponding area $\mathcal{A}_i$. Thus, we have

$$\mathcal{A} = \lim_{i \to \infty} \mathcal{A}_i\,, \qquad \mathcal{A}_i \equiv \frac{2\pi^{d/2} R^\theta}{(d-1)\Gamma(d/2)} \int_{s_{\min}}^{s_{\max}} \frac{(1 - x_{i-1})^d}{1 - s^2 \tilde{z}_{i-1}^{2d_\theta}}\, ds\,. \tag{C.29}$$

A crucial point consists in finding $s_{\rm max}(\epsilon)$, but the relation $\tilde{z}_i(s_{\rm max}) = \tilde{\epsilon}$ is typically transcendental and therefore it cannot be inverted. Introducing $s_{{\rm max},i}$ as the solution of $\tilde{z}_i(s_{{\rm max},i}) = \tilde{\epsilon}$, we have that for $i = 1$ the inversion can be performed, giving

$$s_{\rm max,1} = \begin{cases} \dfrac{d-1}{(d_\theta - 1)\tilde{\epsilon}^{d_\theta - 1}} & d_\theta \neq 1 \\ -(d-1)\log\tilde{\epsilon} & d_\theta = 1 \end{cases} \tag{C.30}$$

which gives

$$\mathcal{A}_1 = \begin{cases} \dfrac{2\pi^{d/2}}{(d_\theta - 1)\Gamma(d/2)} \dfrac{R^{d-1}}{\epsilon^{d_\theta - 1}} & d_\theta \neq 1 \\ -\dfrac{2\pi^{d/2}}{\Gamma(d/2)} R^{d-1}\log(\epsilon/R) & d_\theta = 1 \end{cases} \tag{C.31}$$

For $i = 2$, it is clear from (C.27) that $\tilde{z}_2(s_{\rm max,2}) = \tilde{\epsilon}$ cannot be inverted. Nevertheless, we can find the first terms of the expansion of $s_{\rm max}(\tilde{\epsilon})$ for $\tilde{\epsilon} \to 0$ as follows. The relation $\tilde{z}_2(s_{\rm max,2}) = \tilde{\epsilon}$ can be written as

$$\tilde{\epsilon} = f_1(s) + f_2(s)\,, \tag{C.32}$$

where both f_1 and f_2 vanish for $s \to \infty$, while $f_1/f_2 \to 0$. Assuming that f_1 is invertible, we have that

$$s = f_1^{-1}(\tilde{\epsilon} - f_2(s)) = f_1^{-1}(\tilde{\epsilon}) - [\partial_{\tilde{\epsilon}} f_1^{-1}(\tilde{\epsilon})] f_2(s) + O\big(f_2(s)^2\big) = f_1^{-1}(\tilde{\epsilon}) - [\partial_{\tilde{\epsilon}} f_1^{-1}(\tilde{\epsilon})] f_2(f_1^{-1}(\tilde{\epsilon})) + \dots \tag{C.33}$$

where in the second step we have employed that $f_2/\tilde{\epsilon} = (f_2/f_1)/(1 + f_2/f_1) \to 0$ when $s \to \infty$, while in the last one the first order of the expansion has been used. The dots denote higher orders that we are neglecting. Thus, for $i = 2$ we find

$$s_{\rm max,2} = \begin{cases} \dfrac{d-1}{(d_\theta - 1)\tilde{\epsilon}^{d_\theta - 1}} \left[1 - \dfrac{(d-1)\theta}{2(d_\theta - 1)(d_\theta - 3)}\,\tilde{\epsilon}^2 + \dots\right] & d_\theta \neq 1, 3 \\ -(d-1)\log\tilde{\epsilon}\left[1 - \dfrac{(d-1)^2}{4}\,\tilde{\epsilon}^2\log\tilde{\epsilon} + \dots\right] & d_\theta = 1 \\ \dfrac{d-1}{2\tilde{\epsilon}^2} - \dfrac{(d-1)^2(d-3)}{8}\log\tilde{\epsilon} + \dots & d_\theta = 3 \end{cases} \tag{C.34}$$

As for the integral (C.29) with $i = 2$, we find

$$\mathcal{A}_2 = \begin{cases} \dfrac{2\pi^{d/2}R^{d-1}}{\Gamma(d/2)\,\epsilon^{d_\theta - 1}} \left[\dfrac{1}{d_\theta - 1} - \dfrac{(d-1)^2(d_\theta - 2)}{2(d_\theta - 1)^2(d_\theta - 3)}\,\dfrac{\epsilon^2}{R^2} + O(\epsilon^4)\right] & d_\theta \neq 1, 3 \\ -\dfrac{2\pi^{d/2}R^{d-1}}{\Gamma(d/2)}\log(\epsilon/R)\left[1 + \dfrac{(d-1)^2}{4}\,\dfrac{\epsilon^2}{R^2}\log(\epsilon/R) + \dots\right] & d_\theta = 1 \\ \dfrac{2\pi^{d/2}R^{d-1}}{\Gamma(d/2)\,\epsilon^2}\left[\dfrac{1}{2} - \dfrac{(d-1)(d-5)}{8}\,\dfrac{\epsilon^2}{R^2}\log(\epsilon/R) + o\big(\epsilon^2\big)\right] & d_\theta = 3 \end{cases} \tag{C.35}$$

As a check of this formula, notice that the first expression for $\theta = 0$ provides the expansion at this order of the hemisphere [46]. Moreover, we have also checked that the first expression in (C.35) can be found by plugging (C.11) into (C.28), properly regulated through the introduction of $x_{\rm min} > 0$ such that $x_{\rm min} = x(s_{\rm max})$.

C.2 Computational details for the entanglement growth

C.2.1 Initial growth: generic shape

Let us consider a n dimensional region embedded into $\mathbb{R}^d$, which is the spatial part of the boundary (i.e. $z = 0$) of the Vaidya background (3.11). The boundary of such region will be denoted by Σ and it has a generic shape. The submanifold Σ is $n - 1$ dimensional and therefore it can be parameterized through

a $n-1$ dimensional vector of intrinsic coordinates ξ^α. Thus, being x_a the cartesian coordinates of $\mathbb{R}^d$, the submanifold Σ is specified by

$$x_a(\xi^\alpha)\,, \qquad a\in\{1,\dots,d\}\,, \qquad \alpha\in\{1,\dots,n-1\}\,. \tag{C.36}$$

The surface Γ_Σ we are looking for is also n dimensional and it extends into the bulk, arriving to the boundary along Σ, i.e. $\partial\Gamma_\Sigma=\Sigma$ at certain time t. It is described by the functions

$$v(\xi^\alpha,z)\,, \qquad X_a(\xi^\alpha,z)\,, \tag{C.37}$$

satisfying the following boundary conditions

$$v(\xi^\alpha,0)=t\,, \qquad X_a(\xi^\alpha,0)=x_a(\xi^\alpha)\,. \tag{C.38}$$

We remark that for the holographic entanglement entropy $n=d$, for the holographic counterpart of the Wilson loop $n=2$ and for the holographic two point function $n=1$ (Γ_Σ is a geodesic and Σ is made by two points spacelike separated).
The area A_Σ of Γ_Σ is given by

$$\mathcal{A}_{\Gamma_\Sigma}=\int_0^{z_*}dz\int d\xi^\alpha\,\frac{\sqrt{\det\gamma}}{z^{nd_\theta/d}}\,, \tag{C.39}$$

where $z^{-2d_\theta/d}\gamma_{ab}$ is the induced metric on Γ_Σ and $\det\gamma$ denotes the determinant of γ_{ab}. Differentiating (C.37) and plugging the results into (3.11), we find that

$$\gamma_{zz} \;=\; -z^{2(1-\zeta)}Fv_z^2-2z^{1-\zeta}v_z+\boldsymbol{X}_z\cdot\boldsymbol{X}_z\,, \tag{C.40}$$
$$\gamma_{\alpha z} \;=\; -z^{2(1-\zeta)}Fv_\alpha v_z-z^{1-\zeta}v_\alpha+\boldsymbol{X}_\alpha\cdot\boldsymbol{X}_z\,, \tag{C.41}$$
$$\gamma_{\alpha\beta} \;=\; -z^{2(1-\zeta)}Fv_\alpha v_\beta+\boldsymbol{X}_\alpha\cdot\boldsymbol{X}_\beta\,, \tag{C.42}$$

where $\boldsymbol{X}$ denotes the vector whose components are X_a, the dots stand for the scalar product and the subindices indicate the corresponding partial derivatives.
Here we consider the analogue of $A^{(3)}_{\rm reg}$ defined in (3.47), namely the area of Γ_Σ regularized through the area of $\widehat{\Gamma}_\Sigma$ computed in hvLif, when $F=1$. Given that the hatted quantities refer to hvLif, it reads

$$\mathcal{A}^{(3)}_{\rm reg}(t)=\int\left[\int_0^{z_*}\frac{\sqrt{\det\gamma}}{z^{nd_\theta/d}}\,dz-\int_0^{\hat{z}_*}\frac{\sqrt{\det\hat{\gamma}}}{z^{nd_\theta/d}}\,dz\right]d^{n-1}\xi\,. \tag{C.43}$$

The initial regime is characterized by $0<t\ll z_h$ and we want to compute $\mathcal{A}^{(3)}_{\rm reg}(t)$ for small t. Keeping the first order in (C.43) and repeating the same arguments discussed in [141], we find

$$\mathcal{A}^{(3)}_{\rm reg}(t)=\int\left[\int_0^{\hat{z}_*}\frac{\partial_F\big(\sqrt{\det\gamma}\,\big)\big|_{F=1}}{z^{nd_\theta/d}}\,\delta F\,dz+\frac{\sqrt{\det\hat{\gamma}}}{z_*^{nd_\theta/d}}\,\delta z_*+\sum_{A=0,a}\frac{\partial}{\partial X_{A,z}}\left(\frac{\sqrt{\det\hat{\gamma}}}{z^{nd_\theta/d}}\right)\delta X_A\Big|_0^{\hat{z}_*}\right]d^{n-1}\xi\,, \tag{C.44}$$

where $X_0\equiv v$, $X_{A,z}\equiv\partial_z X_A$ and only the first term within the square brackets provides a non-vanishing contribution. In order to find it, we employ the well known formula for the variation of the determinant

$$\partial_F\big(\sqrt{\det\gamma}\,\big)=\frac{\sqrt{\det\gamma}}{2}\,\mathrm{Tr}\big(\gamma^{-1}\partial_F\gamma\big)\,. \tag{C.45}$$

From (C.40), (C.41) and (C.42), we get respectively

$$\partial_F(\gamma_{zz})\big|_{F=1}=-\frac{v_z^2}{z^{2(\zeta-1)}}\,, \qquad \partial_F(\gamma_{\alpha z})\big|_{F=1}=-\frac{v_\alpha v_z}{z^{2(1-\zeta)}}\,, \qquad \partial_F(\gamma_{\alpha\beta})\big|_{F=1}=-\frac{v_\alpha v_\beta}{z^{2(1-\zeta)}}\,. \tag{C.46}$$

Now, from (3.9) with $F=1$ we find that $\hat{v}=t-z^\zeta/\zeta$. Since t is a constant in terms of ξ^α, in (C.46) we have that $v_\alpha=o(t)$ and $v_z=-z^{\zeta-1}+o(t)$. Plugging these behaviors into (C.46), only the first expression is non vanishing and equal to -1. Then, by using that $X_a(\xi^\alpha,z)=x_a(\xi^\alpha)+o(z)$, where $o(z)$ vanishes fast enough when $z\to 0$, we have

$$\gamma_{\alpha\beta}=h_{\alpha\beta}+o(z)\,, \qquad \gamma_{\alpha z}=o(z)\,, \qquad \gamma_{zz}=1+o(z)\,, \tag{C.47}$$

where $h_{\alpha\beta} \equiv \partial_\alpha x_a \partial_\beta x_a$ is the induced metric on Σ. Notice that (C.47) tells us that the contribution of the term $\mathrm{Tr}(\gamma^{-1}\partial_F\gamma)$ to $\partial_F(\sqrt{\det\gamma})|_{F=1}$ is equal to -1. Collecting these observations, we find

$$\partial_F\big(\sqrt{\det\gamma}\big)\big|_{F=1} = -\frac{\sqrt{\det h}}{2}\,. \tag{C.48}$$

Finally, since in our case $\delta F = F(z) - 1 = -Mz^{d_\theta+\zeta}$ is non vanishing only for $0 < z < z_c$, the first term in (C.44) becomes

$$\mathcal{A}^{(3)}_{\rm reg}(t) = \frac{MA_\Sigma}{2}\int_0^{z_c} z^{d_\theta(1-n/d)+\zeta}dz = \frac{MA_\Sigma\, z_c^{d_\theta(1-n/d)+\zeta+1}}{2[d_\theta(1-n/d)+\zeta+1]} = \frac{MA_\Sigma(\zeta t)^{[d_\theta(1-n/d)+\zeta+1]/\zeta}}{2[d_\theta(1-n/d)+\zeta+1]}\,. \tag{C.49}$$

In the last step we have used that $z_c = (\zeta t)^{1/\zeta}$ to the first order, which is obtained from $\hat{v} = t - z^\zeta/\zeta$ and the condition $v = 0$ at the shell.

C.2.2 Linear growth

In order to study this regime, we consider the strip (see 3.3.1). Following [141], let us start from (3.58) for the black hole regime. By employing (3.60) and (3.22) with $F(z) = 1$, we can write it as follows

$$z'^2 = F(z)\left[\left(\frac{z_*}{z}\right)^{2d_\theta} - 1\right] + g(z)\left[\left(\frac{z_*}{z_c}\right)^{2d_\theta} - 1\right] \equiv H(z)\,, \qquad x_c < x \leqslant \ell/2\,, \tag{C.50}$$

where

$$g(z) \equiv \frac{(F(z_c)-1)^2}{4}\left(\frac{z_c}{z}\right)^{2(1-\zeta)}\,. \tag{C.51}$$

Notice that the dependence on z of $g(z)$ disappears when $\zeta = 1$. Assuming that $H(z)$ has a minimum at $z = z_m$ with $z_m < z_*$, its defining equation $\partial_z H(z)|_{z_m} = 0$ gives

$$z_*^{2d_\theta} = \frac{z_m F'(z_m) + 2(\zeta-1)g(z_m)}{z_m F'(z_m) - 2d_\theta F(z_m) + 2(\zeta-1)(z_m/z_c)^{2d_\theta} g(z_m)}\, z_m^{2d_\theta}\,. \tag{C.52}$$

Assuming also that at $z = z_m$, it is possible to find $z_c = z_c^*$ such that $H(z_m) = 0$ (thus $z_c^* = z_c^*(z_m)$). Then, z_c^* is given by

$$\frac{2d_\theta F(z_m)\big[F(z_m) + g(z_m)|_{z_c=z_c^*}\big] + \big[(z_m/z_c^*)^{2d_\theta} - 1\big]\big[2(1-\zeta)F(z_m) + z_m F'(z_m)\big]g(z_m)|_{z_c=z_c^*}}{z_m F'(z_m) - 2d_\theta(z_m)F(z_m) + 2(\zeta-1)(z_m/z_c^*)^{2d_\theta} g(z_m)|_{z_c=z_c^*}} = 0\,. \tag{C.53}$$

When $F(z)$ is given by (3.5), (C.52) and (C.53) become respectively

$$z_*^{2d_\theta} = \frac{2(d_\theta+\zeta)(z_m/z_h)^{d_\theta+\zeta} + (1-\zeta)(z_c/z_h)^{2(d_\theta+\zeta)}(z_c/z_m)^{2(1-\zeta)}}{4d_\theta - 2(d_\theta-\zeta)(z_m/z_h)^{d_\theta+\zeta} + (1-\zeta)(z_m/z_h)^{2(d_\theta+\zeta)}(z_c/z_m)^2}\, z_m^{2d_\theta}\,, \tag{C.54}$$

and

$$\begin{aligned} &2d_\theta\big[1-(z_m/z_h)^{d_\theta+\zeta}\big]^2 = \\ &\quad = -\frac{(z_c^*/z_h)^{2(d_\theta+\zeta)}}{(z_c^*/z_m)^{2(1-\zeta)}}\left\{1 - \left(\frac{z_m}{z_h}\right)^{d_\theta+\zeta} + \left[\left(\frac{z_m}{z_c^*}\right)^{2d_\theta} - 1\right]\left[2(1-\zeta) - (d_\theta+2-\zeta)\left(\frac{z_m}{z_h}\right)^{d_\theta+\zeta}\right]\right\}. \end{aligned} \tag{C.55}$$

We note that the expression (C.54) simplifies dramatically for $\zeta = 1$ and provides a simple relation between z_* and z_m without any reference to z_c in this case.
At this point, let us consider the limit $z_* \to \infty$ with both z_m and z_c^* kept fixed. For the moment we just assume to be in a regime where this is allowed. The equations (C.52) and (C.53) become respectively

$$z_m F'(z_m) - 2d_\theta F(z_m) = 2(1-\zeta)\left(\frac{z_m}{z_c}\right)^{2d_\theta} g(z_m)\,, \qquad F(z_m) = -\left(\frac{z_m}{z_c^*}\right)^{2d_\theta} g(z_m)\big|_{z_c^*}\,. \tag{C.56}$$

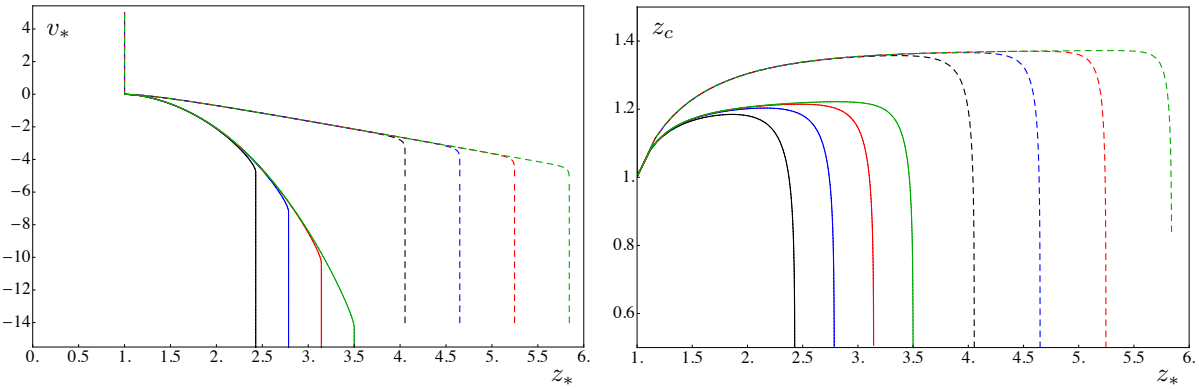

Figure C.2: Thin shell regime: v_* and z_c for the strip in terms of z_* at constant size ℓ. Here $d = 2$ and The horizon is $z_h = 1$. Dashed curves correspond to $\theta = 0$ and $\zeta = 1$, while continuous curves have $\theta = 1$ and $\zeta = 3$. Different colors denote different strips: $\ell = 4$ (black), $\ell = 5$ (blue), $\ell = 6$ (red) and $\ell = 7$ (green).

Plugging the second equation in (C.56) into the first one, one finds

$$z_m F'(z_m) + 2(1 - \zeta - d_\theta) F(z_m) = 0\,, \qquad \text{at} \quad z_c = z_c^*\,, \tag{C.57}$$

which can be written also in the following form

$$\partial_{z_m} \left(\frac{F(z_m)}{z_m^{2(d_\theta+\zeta-1)}} \right) = 0\,. \tag{C.58}$$

For $F(z)$ given by (3.5) this equation tells us that

$$\frac{z_m}{z_h} = \left(\frac{2(d_\theta + \zeta - 1)}{d_\theta + \zeta - 2} \right)^{\frac{1}{d_\theta+\zeta}} = \left(\frac{\eta}{\eta - 1} \right)^{\frac{1}{2}(2-\eta)}\,, \qquad \eta \equiv \frac{2(d_\theta + \zeta - 1)}{d_\theta + \zeta}\,. \tag{C.59}$$

Notice that in this expression, the dimensionality, the Lifshitz and the hyperscaling exponents occur only through the combination $d_\theta + \zeta$. In order to have a positive expression within the brackets of the first equation in (C.59), we need to require $\eta > 1$, i.e.

$$d_\theta + \zeta > 2\,. \tag{C.60}$$

Plugging (C.59) into the second equation of (C.56) computed for (3.5), we find that

$$\frac{z_c^*}{z_h} = \frac{2(\eta - 1)^{\frac{1}{2}(\eta-1)}}{\eta^{\frac{1}{2}\eta}}\,. \tag{C.61}$$

It is useful to plot curves C_ℓ with constant ℓ in the plane (z_*, z_c) or (v_*, z_c) as done in Fig. C.2. As t evolves, z_* decreases along each curve. After some time (which changes with ℓ), all the curves lie on a limiting one C^*. For any fixed ℓ, it will be shown that $A_{\rm reg}(t)$ is linear when the curve C_ℓ coincides with C^*. From Fig. C.2 it is clear that, as ℓ increases, also the linear regime increases. Thus, now we are considering

$$z_* \to \infty\,, \qquad \eta > 1\,, \qquad z_c = (1 - \varepsilon) z_c^*\,, \tag{C.62}$$

where $0 < \varepsilon \ll 1$. When z_* is large, for $F(z)$ given by (3.5), from (C.59) and (C.61) we have that

$$\frac{z_m}{z_c^*} = \frac{\eta}{2\sqrt{\eta - 1}} > 1\,. \tag{C.63}$$

This tells us that the solutions $z(x)$ are not injective for $0 \leqslant x \leqslant \ell/2$, which implies that we cannot employ (3.62), (3.63) and (3.64) because they have been derived assuming that $z(x)$ is invertible. In this case we have to use the following ones (see [141] for a detailed discussion)

$$\frac{\ell}{2} = \int_{z_c}^{z_*} \frac{z^{d_\theta}}{\sqrt{z_*^{2d_\theta} - z^{2d_\theta}}}\, dz + \int_{z_c}^{z_m} \frac{dz}{\sqrt{H(z)}} + \int_0^{z_m} \frac{dz}{\sqrt{H(z)}}\,, \tag{C.64}$$

$$t = \int_{z_c}^{z_m} \frac{1}{z^{1-\zeta}F(z)}\left(\frac{E_+}{z^{1-\zeta}\sqrt{H(z)}}+1\right)dz + \int_0^{z_m} \frac{dz}{z^{1-\zeta}F(z)}\left(\frac{E_+}{z^{1-\zeta}\sqrt{H(z)}}+1\right)dz\,, \quad \text{(C.65)}$$

$$\mathcal{A} = 2\ell_\perp^{d-1} z_*^{d_\theta}\left(\int_{z_c}^{z_*} \frac{dz}{z^{d_\theta}\sqrt{z_*^{2d_\theta}-z^{2d_\theta}}}\int_{z_c}^{z_m} \frac{dz}{z^{2d_\theta}\sqrt{H(z)}} + \int_0^{z_m} \frac{dz}{z^{2d_\theta}\sqrt{H(z)}}\right). \quad \text{(C.66)}$$

Comparing these equations with (3.62), (3.63) and (3.64), notice that only the part outside the shell is different.
Since the point $z = z_m$ and $z_c = z_c^*$ is a quadratic zero of $H(z)$, it provides a leading contribution to the integrals in (C.64), (C.65) and (C.66). Thus, expanding $H(z)$ around $z = z_m$, we find

$$H(z) = H_2(z-z_m)^2 + b\varepsilon\,. \quad \text{(C.67)}$$

By employing that for a smooth function $f(z)$ we have

$$\int \frac{f(z)}{\sqrt{H_2(z-z_m)^2+b\epsilon}}\,dz = \frac{f(z_m)}{\sqrt{H_2}}\operatorname{arcsinh}\big(H_2(z-z_m)/(b\varepsilon)\big) + \cdots = -\frac{f(z_m)}{\sqrt{H_2}}\log\varepsilon + \dots\,, \quad \text{(C.68)}$$

we conclude that

$$\ell/2 = \frac{\sqrt{\pi}\,\Gamma\big(1/(2d_\theta)+1/2\big)}{\Gamma\big(1/(2d_\theta)\big)}\,z_* - \frac{\log\varepsilon}{\sqrt{H_2}}\,, \quad \text{(C.69)}$$

$$t = -\frac{E_+(z_c^*)}{z_m^{2(1-\zeta)}F(z_m)\sqrt{H_2}}\log\varepsilon = -\frac{z_*^{d_\theta}}{z_m^{d_\theta+1-\zeta}\sqrt{-H_2F(z_m)}}\log\varepsilon\,, \quad \text{(C.70)}$$

$$\mathcal{A}_{\rm reg}^{(3)} = -2\ell_\perp^{d-1}\frac{z_*^{d_\theta}}{z_m^{2d_\theta}\sqrt{H_2}}\log\varepsilon\,, \quad \text{(C.71)}$$

where in the second equality of (C.70) we used the second equation of (C.56). Combining (C.70) and (C.71), we also obtain that

$$\mathcal{A}_{\rm reg}^{(3)} = 2\ell_\perp^{d-1}\frac{\sqrt{-F(z_m)}}{z_m^{d_\theta+\zeta-1}}\,t \equiv 2\ell_\perp^{d-1}\frac{v_E}{z_h^{d_\theta+\zeta-1}}\,t\,. \quad \text{(C.72)}$$

For a $F(z)$ given by (3.5), the linear growth velocity reads

$$v_E = \left(\frac{z_h}{z_m}\right)^{d_\theta+\zeta-1}\sqrt{-F(z_m)} = \frac{(\eta-1)^{\frac{\eta-1}{2}}}{\eta^{\frac{\eta}{2}}}\,, \quad \text{(C.73)}$$

where η has been defined in (C.59) and (C.60) guarantees that $\eta > 1$.

We note that the turning point in C.61 admits a nontrivial limit for $\eta \to 1$, namely $z_c^* = 2z_h$. Given this limit, we can solve (C.54) when $d_\theta > 0$, finding that

$$z_m = d_\theta^{\frac{1}{2(d_\theta+1)}} z_h \left(\frac{z_*}{z_h}\right)^{\frac{d_\theta}{d_\theta+1}}\,, \quad \text{(C.74)}$$

which tells us that z_m diverges when $z_* \to \infty$, while z_c^* remains finite. This implies that a linear regime is still possible and its velocity is $v_E = 1$, consistent with taking $\eta \to 1$ in (C.73).

Let us briefly comment on what happens when instead $\eta < 1$. Fig. C.3 shows numerical results for z_c^* obtained from (C.55) for several different η values. When $\eta < 1$ there is no turning point and z_c^* diverges as $z_* \to \infty$. This means that ε, as defined in (C.62), is not small anymore and therefore the method of [140, 141] cannot be applied.

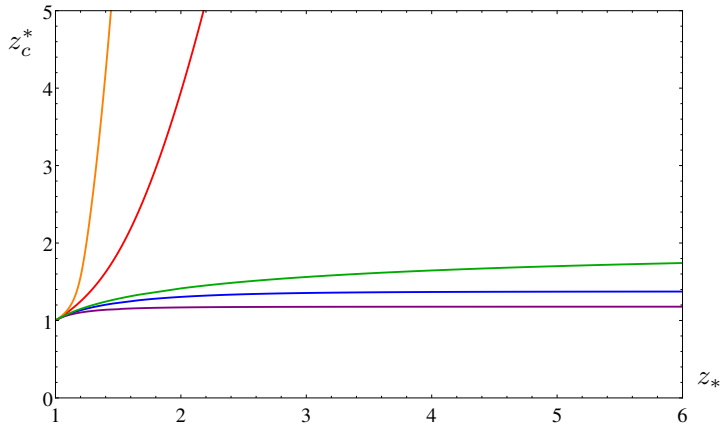

Figure C.3: Numerical solution of (C.54) and (C.55) for $d = 2$, $z_h = 1$ and some values of (ζ, θ). The curves for $\zeta = 3$, $\theta = 0$ (purple), $\zeta = 1$, $\theta = 0$ (blue) correspond to $\eta > 1$, while $\zeta = 1$, $\theta = 4$ (red) and $\zeta = 1$, $\theta = 6$ (orange) have $\eta < 1$ and violate the condition (C.60). The green curve with $\theta = \zeta = 1$ corresponds to the limiting case $\eta = 1$. In the curves for $\eta \geqslant 1$ the turning point z_c^* approaches a finite value for large z_* but this is not the case for the $\eta < 1$ curves.

C.2.3 Saturation

C.2.3.1 Large regions in static backgrounds

In order to understand the regime of saturation, when the holographic entanglement entropy approaches the thermal value, let us consider the static case when the size of the boundary region is large with respect to z_h. In this case a large part of the extremal surface is very close to the horizon.
Starting with the strip, when $\ell \gg z_h$, we have that (we recall that tilded values of z refer to the static black hole case, following the notation introduced in 3.3.1)

$$\tilde{z}_* = (1 - \varepsilon) z_h \,, \tag{C.75}$$

where ε is a positive infinitesimal parameter. Expanding (3.25), we find

$$\frac{\ell}{2} = -\frac{z_h \log \varepsilon}{\sqrt{2 d_\theta z_h F_h'}} + \dots \,, \qquad F_h' \equiv -\partial_z F(z)\big|_{z=z_h} \,. \tag{C.76}$$

In a similar way, plugging (C.75) into (3.21) and keeping the first divergent term as $\varepsilon \to 0$, we get

$$\mathcal{A} = -\frac{\sqrt{2}\, \ell_\perp^{d-1} \log \varepsilon}{z_h^{d_\theta - 1} \sqrt{d_\theta F_h'}} + \dots = \frac{\ell_\perp^{d-1} \ell}{z_h^{d_\theta}} + \dots \,. \tag{C.77}$$

For a sphere, the analysis is slightly more complicated because we have to expand the differential equation for the minimal surface [185]. Setting

$$z(\rho) = z_h - \varepsilon\, a(\rho) + O(\varepsilon^2) \,, \tag{C.78}$$

and expanding (3.30), the first order reads

$$2 z_h \big[(d-1) a' + \rho a''\big] a - z_h \rho a'^2 - 2 d_\theta F_h' a^2 = 0 \,. \tag{C.79}$$

This equation cannot be solved exactly, but, at large ρ, we can find that the solution behaves as

$$a(\rho) = C\, \frac{e^{\rho \sqrt{2 d_\theta F_h'/z_h}}}{\rho^{d-1}} + \dots \,, \tag{C.80}$$

where C is an arbitrary constant. Keeping only the first order in ε in (C.78) and imposing $z(R) = 0$, one finds $a(R) = z_h/\varepsilon$, whose logarithm gives

$$-\log \varepsilon = R \sqrt{-2 d_\theta F'(z_h)/z_h} - (d-1) \log R + \dots \,. \tag{C.81}$$

As for the area, plugging (C.78) into (3.29) and keeping the first divergent term as $\varepsilon \to 0$, (C.81) allows us to conclude that

$$\mathcal{A} = \frac{2\pi^{d/2} R^d}{d\Gamma(d/2) z_h^{d_\theta}} + \dots \,. \tag{C.82}$$

C.2.3.2 Saturation time

In the thin shell regime and whenever the saturation to the thermal value of the holographic entanglement entropy is smooth (the derivative does not jump), we can define the saturation time t_s as the time such that $\tilde{v}_* = 0$. For $t > t_s$, the extremal surface is entirely within the black hole region. Thus, the equation for t_s reads

$$0 = \tilde{v}_*(t_s) = t_s - \int_0^{\tilde{z}_*} \frac{dz}{z^{1-\zeta} F(z)} \,. \tag{C.83}$$

For $F(z)$ given by (3.5) the integral can be solved explicitly, finding

$$t_s = \frac{(\tilde{z}_*)^\zeta}{\zeta} \, {}_2F_1\Big(1, \zeta/(d_\theta+\zeta); 1+\zeta/(d_\theta+\zeta); (\tilde{z}_*/z_h)^{d_\theta+\zeta}\Big) \,. \tag{C.84}$$

For very large regions, $\tilde{z}_* = z_h(1-\varepsilon)$ and therefore (C.84) expanded to the first order in ε gives

$$t_s = -\frac{z_h^{\zeta-1} \log \varepsilon}{F_h'} = -\frac{z_h^\zeta \log \varepsilon}{d_\theta + \zeta} \,, \tag{C.85}$$

where in the second step we have employed (3.5). If the region on the boundary is a strip, we can use (C.76) to obtain

$$t_s = z_h^{\zeta-1} \sqrt{\frac{2d_\theta}{z_h F_h'}} \, \frac{\ell}{2} + \dots = z_h^{\frac{\zeta-d_\theta}{2}-1} \sqrt{\frac{d_\theta}{2(d_\theta+\zeta)}} \, \ell + \dots \,. \tag{C.86}$$

For a sphere, (C.81) gives us

$$t_s = z_h^{\zeta-1} \sqrt{\frac{2d_\theta}{z_h F_h'}} \, R - \frac{(d-1) z_h^{\zeta-1}}{F_h'} \log R + \dots \,. \tag{C.87}$$

C.2.3.3 Saturation of the holographic entanglement entropy: strip

In this section we try to estimate $A^{(2)}_{\text{reg}}(t)$ as a function of $t - t_s$, being t_s the saturation time computed above. As the holographic entanglement entropy approaches its thermal value, the extremal surface is almost entirely within the black hole region. This means that the point z_c, where the extremal surface crosses the shell, is very close to z_*.
Let us consider the strip first and introduce a positive infinitesimal parameter ε as follows

$$z_c = z_* \left(1 - \frac{\varepsilon^2}{2d_\theta}\right) \,. \tag{C.88}$$

Plugging this expansion into (3.60), at first order we get

$$E_+ = \frac{z_c^{1-\zeta}(F(z_c)-1)}{2} \sqrt{\left(\frac{z_*}{z_c}\right)^{2d_\theta} - 1} = \frac{z_*^{1-\zeta}(F(z_*)-1)}{2} \, \varepsilon + O(\varepsilon^2) \,. \tag{C.89}$$

Since we are approaching the extremal surface corresponding to the one of the static black hole, z_* is close to its thermal value $\tilde{z}_*$, namely we are allowed to introduce another positive infinitesimal parameter δ as

$$z_* = \tilde{z}_* \left(1 - \frac{\delta}{2d_\theta}\right) \,. \tag{C.90}$$

We want to estimate $t - t_s$ in terms of the infinitesimal parameters ε and δ. Using (3.63) and (C.84), we find that

$$t - t_s \;=\; \int_0^{z_c} \frac{z^{\zeta-1}}{F(z)} \left(\frac{E_+}{z^{1-\zeta}\sqrt{H(z)}} + 1\right) - \int_0^{\tilde{z}_*} \frac{z^{\zeta-1}}{F(z)} \, dz \,, \tag{C.91}$$

$$= \int_{\tilde{z}_*}^{z_c} \frac{z^{\zeta-1}}{F(z)}\,dz + \int_0^{z_*} \frac{E_+ z^{2(\zeta-1)}}{F(z)\sqrt{H(z)}}\,dz - \int_{z_c}^{z_*} \frac{E_+ z^{2(\zeta-1)}}{F(z)\sqrt{H(z)}}\,dz\,, \tag{C.92}$$

$$= -\frac{\tilde{z}_*^{\zeta}}{2d_\theta F(\tilde{z}_*)}\,\delta + \frac{\tilde{z}_*^{1-\zeta}(F(\tilde{z}_*)-1)Q_1(\tilde{z}_*)}{2}\,\varepsilon + \dots\,, \tag{C.93}$$

where $H(z)$ is defined as the r.h.s. of (3.58) (see also (C.50)), $Q_1(z_*)$ is defined as follows

$$Q_1(z_*) \equiv \int_0^{z_*} \frac{z^{2(\zeta-1)}}{F(z)\sqrt{F(z)\big[(z_*/z)^{2d_\theta}-1\big]}}\,dz\,, \tag{C.94}$$

and the dots denote higher orders in ε and δ. Following [141], one can find a relation between δ or ε from the expansion of (3.62). The presence of ζ does not modify the result, which reads

$$\delta = \frac{1-F(\tilde{z}_*)}{F(\tilde{z}_*)Q_2'(\tilde{z}_*)}\,\varepsilon + O(\varepsilon^2)\,, \tag{C.95}$$

where (see [141] for further details)

$$Q_2(z_*) \equiv \int_0^{z_*} \frac{dz}{\sqrt{F(z)\big[(z_*/z)^{2d_\theta}-1\big]}}\,. \tag{C.96}$$

Thus, plugging this result into (C.93), one finds

$$t - t_s \propto \varepsilon + O(\varepsilon^2)\,, \tag{C.97}$$

where the coefficient in front of ε depends on ζ and θ, as can be clearly seen from (C.93), but the power of ε does not. Given this result, one can repeat precisely the computation of [141] and show that in this regime

$$A^{(2)}_{\text{reg}}(t) \propto \varepsilon^2 + O(\varepsilon^3)\,, \tag{C.98}$$

i.e.

$$A^{(2)}_{\text{reg}}(t) \propto (t-t_s)^2 + O\big((t-t_s)^3\big)\,. \tag{C.99}$$

Notice that the exponent is independent of θ and ζ.

C.2.3.4 Saturation of the holographic entanglement entropy: sphere

Given a black hole in the hvLif space-time, the corresponding area functional is (3.29), whose extremization gives (3.30). Since (3.30) is invariant under the change $\rho \to -\rho$, its solution $z(\rho)$ is an even function. In particular, its Taylor series expansion contains only positive even powers of ρ. Introducing $z(0) = \tilde{z}_*$, the expansion of $z(\rho)$ for $\rho \sim 0$ gives

$$z(\rho) = \tilde{z}_* - \frac{d_\theta}{2d\tilde{z}_*} F(\tilde{z}_*)\rho^2 + O(\rho^4)\,. \tag{C.100}$$

For the Vaidya space-time in the thin shell regime, the equation for $z(\rho)$ for $0 < \rho_c < \rho < R$ is (3.79), where E_+ has been defined in (3.77). We recall that the quantities associated to the hvLif vacuum part can be obtained by sustituting E_+ with $E_- = 0$ in all the corresponding expressions for the black hole part. The relation defining v in the black hole part of the metric is (3.78). The total area is (3.81), while the boundary time t is obtained by integrating v' (see (3.78)) outside the shell, i.e. (3.80).

The assumption in the following is that we are at a boundary time such that the minimal surface lies almost entirely outside the shell and has almost reached its static configuration, that is

$$z(\rho) = z_0(\rho) + \delta z_1(\rho) + O(\delta^2)\,, \tag{C.101}$$

where δ is supposed small and z_0 is solution of (3.30) which is just (3.79) with $E_+ = 0$. The boundary conditions are such that $z_0(R) = z_1(R) = 0$. Expanding (3.79) to the first order in δ, we find the following differential equation for z_1

$$z_1'' + P(\rho)z_1' + Q(\rho)z_1 = S(\rho)\,, \qquad z_1'(0) = z_1(R) = 0\,, \tag{C.102}$$

where

$$P(\rho) = \frac{d-1}{\rho} + \left(\frac{2d_\theta}{z_0} + \frac{3(d-1)z_0' - \rho F'(z_0)}{\rho F(z_0)}\right) z_0' \,, \tag{C.103}$$

$$Q(\rho) = \frac{d_\theta}{z_0}\left(F'(z_0) - \frac{F(z_0)+z_0'^2}{z_0}\right) - \frac{1}{2F(z_0)}\left(z_0'^2 F''(z_0) - \frac{F'(z_0) z_0'^2\left[\rho F'(z_0) - 2(d-1)z_0'\right]}{\rho F(z_0)}\right) \tag{C.104}$$

$$S(\rho) = \frac{E_+^2}{\delta}\left(1 + \frac{z_0'^2}{F(z_0)}\right)\left(\frac{(d_\theta+\zeta-1)\rho}{z_0} + \frac{2(d-1)z_0' - \rho F'(z_0)}{2F(z_0)}\right)\rho^{2(1-d)} z_0^{2(d_\theta+\zeta-1)} \,. \tag{C.105}$$

Notice that $S(\rho)$ depends on E_+^2/δ. Indeed, since $E_+ \to 0$ when $\delta \to 0$, we could have $E_+^2/\delta = O(1)$ as $\delta \to 0$. In the following the correct relation between E_+ and δ will be obtained and $E_+/\delta = O(1)$ (see (C.127) and (C.133)).
It is useful to remind that, given a second order linear differential equation

$$f''(x) + A(x) f'(x) + B(x) f(x) = C(x) \,, \tag{C.106}$$

a solution can be written in terms of the solutions $f_j(x)$ $(j = 1, 2)$ of the corresponding homogenous differential equation (i.e. (C.106) with $C = 0$). It reads

$$f_{\rm inh}(x) = f_1(x)\int_{x_0}^{x} \frac{f_2(y)C(y)}{f_1(y)f_2'(y) - f_2(y)f_1'(y)}\, dy - f_2(x)\int_{x_0}^{x} \frac{f_1(y)C(y)}{f_1(y)f_2'(y) - f_2(y)f_1'(y)}\, dy \,, \tag{C.107}$$

where x_0 is arbitrary and $f_{\rm inh}(x_0) = 0$ is trivially satisfied. Then, since (C.106) is linear, its most general solution is $f_{\rm inh} + A f_1 + B f_2$.

C.2.3.4.1 Expansion for $\rho \simeq 0$. In this regime we can expand $z_0(\rho)$ as in (C.100). Then, (C.103), (C.104) and (C.105) become respectively

$$P(\rho) = \frac{d-1}{\rho} + \frac{d_\theta}{d}\,\frac{(d-3)F(\tilde z_*) + \tilde z_* F'(\tilde z_*)}{\tilde z_*^2}\,\rho + O(\rho^3) \,, \tag{C.108}$$

$$Q(\rho) = d_\theta \frac{\tilde z_* F'(\tilde z_*) - F(\tilde z_*)}{\tilde z_*^2} + O(\rho^2) \,, \tag{C.109}$$

$$S(\rho) = \frac{E_+^2}{\delta}\,\frac{\left[2(\theta - \zeta d)F(\tilde z_*) + d\tilde z_* F'(\tilde z_*)\right]\tilde z_*^{2(d_\theta+\zeta)-3}}{2d\, F(\tilde z_*)\,\rho^{2(d-1)}} + O(1/\rho^{2(d-2)}) \,. \tag{C.110}$$

The homogeneous equation is

$$z_1''(\rho) + \frac{d-1}{\rho} z_1'(\rho) + Q_0 z_1(\rho) = 0 \,, \qquad Q_0 \equiv Q(0) = d_\theta \frac{\tilde z_* F'(\tilde z_*) - F(\tilde z_*)}{\tilde z_*^2} \,. \tag{C.111}$$

The independent solutions j_1, j_2 of this equation can be expressed in terms of Bessel functions as follows

$$j_1(\rho) = \frac{\Gamma(d/2)}{(\sqrt{Q_0}\rho/2)^{\frac{d-2}{2}}} J_{\frac{d-2}{2}}(\sqrt{Q_0}\rho) \,, \qquad j_2(\rho) = \begin{cases} -\dfrac{\pi}{2} Y_0(\sqrt{Q_0}\rho) & d = 2 \\ -\dfrac{\pi}{\Gamma(\frac{d-2}{2})}\left(\dfrac{\sqrt{Q_0}}{2\rho}\right)^{\frac{d-2}{2}} Y_{\frac{d-2}{2}}(\sqrt{Q_0}\rho) & d > 2 \end{cases} \tag{C.112}$$

whose behavior for $\rho \to 0$ is given respectively by

$$j_1(\rho) = 1 - \frac{Q_0}{2d}\rho^2 + O(\rho^4) \,, \qquad j_2(\rho) = \begin{cases} \log\rho + \log(\sqrt{Q_0}/2) + \gamma_E + \dots & d = 2 \\ \rho^{2-d} + \dots & d > 2 \end{cases} \tag{C.113}$$

Considering only the first terms of the expansions (C.113) and (C.110) and plugging them into (C.107), one finds

$$z_{1,{\rm inh}}(\rho) = \begin{cases} \dfrac{E_+^2}{\delta}\,\dfrac{\tilde z_*^{2(1-\theta+\zeta)-1}(\tilde z_* F'(\tilde z_*) - (2\zeta - \theta)F(\tilde z_*))}{4F(\tilde z_*)}\,\log^2\rho & d = 2 \\ \dfrac{E_+^2}{\delta}\,\dfrac{\tilde z_*^{2(d_\theta+\zeta-1)-1}(d\tilde z_* F'(\tilde z_*) - 2(d\zeta - \theta)F(\tilde z_*))}{4d(d-2)^2 F(\tilde z_*)}\,\rho^{-2(d-2)} & d > 2 \end{cases} \tag{C.114}$$

In the following j_1, j_2 of $z_{1,{\rm inh}}$ will indicate only their ρ dependence.

C.2.3.4.2 Expansion for $\rho \simeq R$. First, let us consider the case $d_\theta \neq 1$, when (C.11) can be applied. Introducing the variable $\sigma \equiv R - \rho$, from (C.103), (C.104) and (C.105) we find

$$P(\rho) = \frac{d_\theta - 3}{2\sigma} + O(\sigma^0)\,, \tag{C.115}$$

$$Q(\rho) = -\frac{d_\theta}{4\sigma^2} + O(\sigma^{-1})\,, \tag{C.116}$$

$$S(\rho) = \frac{E_+^2}{\delta}\left(\frac{2(d_\theta-1)\sigma}{(d-1)R}\right)^{d_\theta+\zeta-5/2} \frac{\zeta(d-1)R^{2(\zeta-\theta-1/2)}}{d_\theta - 1} + \dots\,. \tag{C.117}$$

Near the boundary we find the following homogeneous equation

$$z_1''(\sigma) - \frac{d_\theta - 3}{2\sigma}\, z_1'(\sigma) - \frac{d_\theta}{4\sigma^2}\, z_1(\sigma) = 0\,, \tag{C.118}$$

whose solutions read

$$k_1(\sigma) = \sigma^{-1/2}\,, \qquad k_2(\sigma) = \sigma^{d_\theta/2}\,. \tag{C.119}$$

Since $z_1(R) = 0$ and $k_1(\sigma)$ diverges when $\sigma \to 0$, the solution of (C.118) is proportional to k_2. Adapting (C.107) to this case through (C.119) and (C.117) we obtain that

$$z_{1,\mathrm{inh}}(\sigma) = \frac{E_+^2}{\delta}\, \frac{4\zeta R^{3/2-d-\theta+\zeta}}{(d\theta+\zeta)(d\theta+2\zeta-1)} \left(\frac{2(d_\theta-1)}{d-1}\right)^{d_\theta+\zeta-7/2} \sigma^{\zeta-1/2+d_\theta} + \dots\,, \tag{C.120}$$

which vanishes for $\sigma \to 0$ because $\zeta \geqslant 1$.
Note that (C.120) in the limit $\sigma \to 0$, z_1 is well behaved and thus in the following calculation the boundary contribution will be ignored being $E_+/\delta \sim \delta \to 0$ when approaching saturation. We have checked that, by employing the parametric reformulation (C.22), this happens also when $d_\theta = 1$. This is not the case for (C.114) which will play an important role in determine the late time behaviour of the entanglement entropy.

C.2.3.4.3 Approaching saturation. Let us now try to put things together. First, notice that as the solution approaches its thermal value, we have that

$$z_c \to \tilde{z}_*\,, \qquad z_* \to \tilde{z}_*\,, \tag{C.121}$$

where $\tilde{z}_*$ is associated to the tip of the static black hole geodesic, and at the same time

$$\rho_c \to 0\,, \qquad E_+ \to 0\,, \qquad \delta \to 0\,. \tag{C.122}$$

In the following we will try to relate the above quantities in their approach to equilibrium values. To this purpose it turns out to be useful to relate the three infinitesimal quantities ρ_c, δ and E_+ among themselves.
First, one introduces a new infinitesimal parameter ε

$$\rho_c \equiv z_c \varepsilon\,. \tag{C.123}$$

From (C.100) with $F = 1$ we have that

$$z_* = z_c\left(1 + \frac{d_\theta}{2d}\varepsilon^2 + O(\varepsilon^4)\right)\,, \tag{C.124}$$

and also

$$z_-'(\rho_c) = -\frac{d_\theta}{dz_*}\rho_c + O(\rho_c^3) = -\frac{d_\theta}{d}\varepsilon + O(\varepsilon^3)\,, \tag{C.125}$$

where we recall that z_- refers to the value of the solution at $\rho = \rho_c$ coming from the hvLif part living in $[0, \rho_c]$. From (3.78) with $E_+ = 0$ and $F = 1$ we find

$$v_c' = \frac{d_\theta z_c^\zeta}{dz_*}\,\varepsilon + O(\varepsilon^3) = \frac{d_\theta}{d} z_c^{\zeta-1}\varepsilon + O(\varepsilon^3)\,, \tag{C.126}$$

and finally, plugging (C.126) and (C.123) into (3.78), we get that

$$E_+ = \frac{d_\theta}{2d}(F(z_c)-1)z_c^{\theta-\zeta}\varepsilon^d\,. \tag{C.127}$$

By employing (C.101), (C.112) and (C.113) we can write $z(\rho)$ at $\rho=\rho_c$ as follows

$$z(\rho_c) = z_0(\rho_c) + \delta\big[\alpha_1 j_1(\rho_c) + \alpha_2 j_2(\rho_c) + z_{1,\text{inh}}(\rho_c)\big]\,, \tag{C.128}$$

where the constants α_1 and α_2 are constrained by the boundary condition $z_1(R)=0$. Since $z'(\rho)$ has a jump at $\rho=\rho_c$, the matching constraint (3.72) allows to relate (C.125) and (C.128) (the latter one gives $z'_+(\rho_c)$), namely we have

$$z'_+(\rho_c) - z'_-(\rho_c) = \frac{z_c^{1-\zeta}v'_c}{2}\big(1-F(z_c)\big)\,, \tag{C.129}$$

which gives

$$z'_+(\rho_c) = z'_-(\rho_c) + \frac{z_c^{1-\zeta}v'_c}{2}\big(1-F(z_c)\big) = z'_0(\rho_c) + \delta\big[\alpha_1 j'_1(\rho_c) + \alpha_2 j'_2(\rho_c) + z_{1,\text{inh}}{}'(\rho_c)\big]\,. \tag{C.130}$$

When $d>2$, (C.128) and (C.130) become respectively

$$z_c \;=\; \tilde z_* - \frac{d_\theta}{2d}F(\tilde z_*)\frac{z_c^2}{\tilde z_*}\varepsilon^2 + \delta\left(\alpha_1 + \alpha_2 z_c^{2-d}\varepsilon^{2-d}\right) + O(\varepsilon^4)\,, \tag{C.131}$$

$$\frac{d_\theta}{d}\left(\frac{1-F(z_c)}{2}-1\right)\frac{z_c}{z_*}\varepsilon \;=\; -\frac{d_\theta}{d}F(\tilde z_*)\frac{z_c}{\tilde z_*}\varepsilon + \delta\alpha_2(2-d)z_c^{1-d}\varepsilon^{1-d} + O(\varepsilon^3)\,, \tag{C.132}$$

Since $z_c\to\tilde z_*$ when $\varepsilon\to 0$, at first order we have $z_c/\tilde z_*=1$ in (C.132), and therefore

$$\delta = \frac{d_\theta(1-F(\tilde z_*))\tilde z_*^{d-1}}{2d\alpha_2(d-2)}\,\varepsilon^d + O(\varepsilon^{d+2})\,. \tag{C.133}$$

Plugging this result into (C.131) we obtain

$$z_c = \tilde z_*\left[1 - \frac{d_\theta}{2d}\left(F(\tilde z_*) + \frac{1-F(\tilde z_*)}{2-d}\right)\varepsilon^2 + O(\varepsilon^4)\right]\,. \tag{C.134}$$

Instead, for $d=2$ (C.128) and (C.130) become respectively

$$z_c = \tilde z_* - \frac{2-\theta}{4}F(\tilde z_*)\frac{z_c^2}{\tilde z_*}\varepsilon^2 + \delta\left[\alpha_1 + \alpha_2\left(\log\varepsilon + \gamma_E + \log\frac{\sqrt{Q_0}z_c}{2}\right)\right] + O(\varepsilon^4\log^2\varepsilon)\,, \tag{C.135}$$

$$\frac{2-\theta}{2}\left(\frac{1-F(z_c)}{2}-1\right)\frac{z_c}{z_*}\varepsilon = -\frac{2-\theta}{2}F(\tilde z_*)\frac{z_c}{\tilde z_*}\varepsilon + \frac{\alpha_2\delta}{z_c\varepsilon} + \dots\,. \tag{C.136}$$

Notice that the constant factor multiplying α_2 in (C.135) can be reabsorbed by a redefinition of α_1

$$\tilde\alpha_1 \equiv \alpha_1 + \alpha_2\gamma_E + \alpha_2\log\frac{\sqrt{Q_0}}{2}\,. \tag{C.137}$$

From (C.136) we find

$$\delta = -\frac{(2-\theta)[1-F(\tilde z_*)]\tilde z_*}{4\alpha_2}\,\varepsilon^2 + O(\varepsilon^4\log\varepsilon)\,, \tag{C.138}$$

which can be plugged into (C.135), giving

$$z_c = \tilde z_*\left\{1 - \frac{(2-\theta)[1-F(\tilde z_*)]}{4}\,\varepsilon^2\log\varepsilon - \frac{2-\theta}{4}\left[F(\tilde z_*) + \frac{1-F(\tilde z_*)}{\alpha_2}(\tilde\alpha_1 + \alpha_2\log\tilde z_*)\right]\varepsilon^2\right\}\,. \tag{C.139}$$

C.2.3.4.4 Time. Now we can proceed by evaluating the boundary time at first nontrivial order in ε. By using (3.80) we get

$$t = t_s + \frac{z_c - \tilde{z}_*}{\tilde{z}_*^{1-\zeta} F(\tilde{z}_*)} + E_+ \int_{\rho_c}^{R} \frac{z_0^{d_\theta+2(\zeta-1)} \sqrt{1 + z_0'^2/F(z_0)}}{\rho^{d-1} F(z_0)} \, d\rho + O(E_+^2)\,, \tag{C.140}$$

where we have employed the definition of saturation time given in (C.83) and we have approximated z with z_0 in the integral occurring in (C.140) because $E_+ \propto \varepsilon^d$. The integrand in (C.140) can be written as $h(\rho)/\rho^{d-1}$ where $h(0)$ is finite. Thus, when $\rho_c \to 0$, the divergent part of the integral can be computed as $h(\rho_c)$ times the divergent part of integral of $1/\rho^{d-1}$ between ρ_c and R. This gives for (C.140) the following result

$$t - t_s = \frac{z_c - \tilde{z}_*}{\tilde{z}_*^{1-\zeta} F(\tilde{z}_*)} + \frac{E_+ \tilde{z}_*^{d_\theta+2(\zeta-1)}}{F(\tilde{z}_*)} \times \begin{cases} -\log\varepsilon - I_0 + \dots & d = 2 \\ \dfrac{(\tilde{z}_*\varepsilon)^{2-d}}{d-2} + \dots & d > 2 \end{cases} \tag{C.141}$$

where I_0 is a numerical constant containing the $O(\varepsilon^0)$ terms of the expansion. Now, using (C.127),(C.134) and (C.139) we obtain

$$t - t_s \;=\; \begin{cases} -\dfrac{(2-\theta)\tilde{z}_*^\zeta}{4} \left[1 + \dfrac{1 - F(\tilde{z}_*)}{F(\tilde{z}_*)} \left(\dfrac{\tilde{\alpha}_1}{\alpha_2} + I_0\right)\right] \varepsilon^2 & d = 2 \\ -\dfrac{d_\theta}{2d}\, \tilde{z}_*^\zeta \varepsilon^2 & d > 2 \end{cases} \tag{C.142}$$

C.2.3.4.5 Area. The same strategy can be followed to compute the area. From (3.81) we find

$$\mathcal{A} \;=\; \frac{2\pi^{d/2}}{\Gamma(d/2)} \left[\int_0^{\rho_c} \frac{\rho^{d-1}\sqrt{1+z'^2}}{z^{d_\theta}}\, d\rho + \int_{\rho_c}^{R} d\rho \frac{\rho^{d-1}\sqrt{1+z'^2/F(z)}}{z^{d_\theta}\sqrt{1 + A^2 E_+^2/F(z)}} \right] \tag{C.143}$$

$$\;=\; \frac{2\pi^{d/2}}{\Gamma(d/2)} \left[\mathcal{C}_0 + \mathcal{C}_1 - \frac{E_+^2}{2}\, \mathcal{C}_2 + O(E_+^4) \right], \tag{C.144}$$

where we have kept only the first non trivial order in $E_+ \propto \varepsilon^d$ and the $\mathcal{C}_i$ are defined as follows

$$\mathcal{C}_0 \equiv \int_0^{\rho_c} \frac{\rho^{d-1}\sqrt{1+z'^2}}{z^{d_\theta}}\, d\rho\,, \quad \mathcal{C}_1 \equiv \int_{\rho_c}^{R} \frac{\rho^{d-1}}{z^{d_\theta}} \sqrt{1 + \frac{z'^2}{F(z)}}\, d\rho\,, \quad \mathcal{C}_2 \equiv \int_{\rho_c}^{R} d\rho \rho^{1-d} z^{d_\theta+2(\zeta-1)} \frac{\sqrt{1+z'^2/F(z)}}{F(z)}\,. \tag{C.145}$$

From (C.123), (C.125), (C.134) and (C.139) we get

$$\mathcal{C}_0 \;\simeq\; \left.\frac{\rho^{d-1}\sqrt{1+z'^2}}{z^{d_\theta}}\right|_{\rho\to\rho_c^-} \rho_c \;=\; \frac{z_c^\theta \varepsilon^d}{d} - \frac{d_\theta^2 z_c^\theta \varepsilon^{d+2}}{2d^2(d+2)} + O(\varepsilon^{d+4})\,. \tag{C.146}$$

As for the functional $\mathcal{C}_1$, notice that its integrand is the same occurring in (3.29) (which is minimized by z_0) but the integration domain is (ρ_c, R) instead of $(0, R)$. Since $\rho_c \to 0$, we have that $\mathcal{C}_1$ is equal to the static black hole area $\mathcal{A}_{\rm bh}$ plus small corrections, which can be originated both from the fact that now the integration domain is not $(0, R)$ and also from evaluating the integral at $z = z_0 + \delta z_1$. The second kind of contribution, obtained by computing the variation of the integrand on z_0, gives only a boundary term (computed at $\rho = \rho_c$). Thus we have

$$\mathcal{C}_1 \;=\; \mathcal{A}_{\rm bh} - \int_0^{\rho_c} \frac{\rho^{d-1}}{z_0^{d_\theta}} \sqrt{1 + \frac{z_0'^2}{F(z_0)}}\, d\rho + \delta z_1 \left(\frac{\rho^{d-1}}{z^{d_\theta}}\, \partial_{z'} \sqrt{1 + z'^2/F(z)}\Big|_{z=z_0} \right) \Bigg|_{\rho=\rho_c} \tag{C.147}$$

$$\;=\; \mathcal{A}_{\rm bh} - \frac{z_c^\theta \varepsilon^d}{d} - \frac{d_\theta^2[(d+1)F(z_c) - (d+2)]}{2d^2(d+2)}\, z_c^\theta \varepsilon^{d+2} + \frac{d_\theta}{d}[z_c - z_0(\rho_c)]\, z_c^{\theta-1}\varepsilon^d + O(\varepsilon^{d+4})\,, \tag{C.148}$$

where

$$z_c - z_0(\rho_c) = \begin{cases} -\dfrac{(2-\theta)[1-F(z_c)]}{4}\, z_c \log\varepsilon & d=2 \\ \dfrac{d_\theta[1-F(z_c)]}{2d(d-2)}\, z_c\, \varepsilon^2 & d\neq 2 \end{cases} \tag{C.149}$$

As for $\mathcal{C}_2$, since it is already multiplied by E_+^2 in (C.144), it is enough to compute it at $z = z_0$ and keep only the most divergent term (at $\rho = \rho_c$). This turns out to provide the same integral occurring in (C.141) and for $\mathcal{C}_2$ we find

$$\mathcal{C}_2\big|_{z_0} = -\frac{z_c^{d_\theta+2(\zeta-1)}}{F(z_c)} \times \begin{cases} \log\varepsilon + I_0 + \dots & d=2 \\ \dfrac{(z_c\varepsilon)^{2-d}}{2-d} + \dots & d>2 \end{cases} \tag{C.150}$$

where I_0 is the same quantity as in (C.141).
Finally, putting (C.146),(C.148) and (C.150) together we find

$$\mathcal{A}^{(2)}_{\rm reg} = \frac{2\pi^{d/2}}{\Gamma(d/2)}\, \frac{d_\theta^2[1-F(\tilde z_*)]\tilde z_*^\theta}{2d^2} \times \begin{cases} \dfrac{1-F(\tilde z_*)}{4F(\tilde z_*)}\, \varepsilon^4 \log\varepsilon + \dots & d=2 \\ \left(\dfrac{d-2}{d+2} + \dfrac{1-F(\tilde z_*)}{4F(\tilde z_*)}\right) \dfrac{\varepsilon^{d+2}}{2-d} + \dots & d>2 \end{cases} \tag{C.151}$$

Finally, comparing (C.142) and (C.151), we find (3.95).

C.2.4 Initial conditions for the shooting procedure

The numerical analysis of the ordinary differential equations (3.40) and (3.41) for the strip and (3.67) and (3.68) for the sphere employs the shooting method to relate $\{z_*, v_*\}$ to $\{\ell/2, t\}$ for the strip or $\{R, t\}$ for the sphere. The numerical procedure does not allow us to impose initial conditions at $x = 0$, so we instead start from $x = \tilde\varepsilon$, where $\tilde\varepsilon$ is a small positive number.
Expanding the solution $(z(x), v(x))$ for both the strip and the sphere around $x = 0$, we have that

$$v = v_* + \frac{1}{2}\, v_*''\, x^2 + o(x^2)\,, \qquad z = z_* + \frac{1}{2}\, z_*''\, x^2 + o(x^2)\,, \tag{C.152}$$

where $z'(0) = v'(0) = 0$ for parity and we have introduced the notation $v_*'' \equiv v''(0)$ and $z_*'' \equiv z''(0)$. Plugging (C.152) into (3.40) and (3.41), for the strip we find

$$v_*'' = d_\theta z_*^{\zeta-2}\,, \qquad z_*'' = -\frac{d_\theta}{z_*} F(v_*, z_*)\,, \tag{C.153}$$

while for the sphere, from (3.67) and (3.68) we obtain

$$v_*'' = \frac{d_\theta}{d} z_*^{\zeta-2}\,, \qquad z_*'' = -\frac{d_\theta}{z_* d} F(v_*, z_*)\,. \tag{C.154}$$

From these expressions we can then read off initial conditions $(v(\tilde\varepsilon), v'(\tilde\varepsilon))$ and $(z(\tilde\varepsilon), z'(\tilde\varepsilon))$ for the shooting algorithm.
Note that for both the strip and the sphere the sign of z_*'' is opposite to that of d_θ. It follows that we must have $d_\theta > 0$ for our numerics to converge to a solution ending on the boundary at $z = 0$.

C.3 Strip in more generic backgrounds

In order to understand the terms of the metric determining the linear regime, let us consider the following static background

$$ds^2 = \frac{1}{z^{2d_\theta/d}} \left(-Q(z) dt^2 - \frac{P(z)^2}{Q(z)}\, dz^2 + d\boldsymbol{x}^2 \right)\,, \tag{C.155}$$

which reduces to the black hole (3.4) when $Q(z) = z^{2(1-\zeta)}F(z)$ and $P(z) = z^{1-\zeta}$. By introducing the time coordinate v as

$$dv = dt - \frac{P(z)}{Q(z)}\,dz\,, \tag{C.156}$$

the metric (C.155) can be written as

$$ds^2 = \frac{1}{z^{2d_\theta/d}}\big(-Q(z)dv^2 - 2P(z)dvdz + d\boldsymbol{x}^2\big)\,. \tag{C.157}$$

Here we consider the Vaidya background obtained by promoting Q to a time dependent function, i.e.

$$ds^2 = \frac{1}{z^{2d_\theta/d}}\big(-Q(v,z)dv^2 - 2P(z)dvdz + d\boldsymbol{x}^2\big)\,. \tag{C.158}$$

Considering a strip in the spatial part of the boundary $z = 0$, its holographic entanglement entropy is obtained by finding the extremal surface of the following functional area

$$\mathcal{A}[v(x), z(x)] = 2\ell_\perp^{d-1}\int_0^{\ell/2}\frac{\sqrt{\mathcal{B}}}{z^{d_\theta}}\,dx\,, \qquad \mathcal{B} \equiv 1 - Q(v,z)v'^2 - 2P(z)z'v'\,, \tag{C.159}$$

and the boundary conditions for $v(x)$ and $z(x)$ are given by (3.38). We only have to adapt the analysis performed in 3.3.1 to the background (C.158). The equations of motion of (C.159) read

$$\partial_x\big[Qv' + Pz'\big] = Q_v v'^2/2\,, \tag{C.160}$$

$$\partial_x\big[Pv'\big] = d_\theta\mathcal{B}/z + Q_z v'^2/2 + P_z v'z'\,. \tag{C.161}$$

Choosing the thin shell profile

$$Q(v,z) = P(z)^2 + \theta(v)\big[Q(z) - P(z)^2\big]\,, \tag{C.162}$$

we have that for $v < 0$ the backgrounds is

$$ds^2 = \frac{1}{z^{2d_\theta/d}}\big(-P(z)^2dt^2 + dz^2 + d\boldsymbol{x}^2\big)\,, \tag{C.163}$$

while for $v > 0$ the metric becomes (C.155). The equation (C.160) tells us that $Qv' + Pz'$ is constant for $v \neq 0$ but we recall that it takes two different values E_- (for $v < 0$) and E_+ (for $v > 0$). Since $v'(0) = z'(0) = 0$, we have that $E_- = 0$. Integrating across the shell as in 3.3.1, (C.161) implies again that

$$v'_+ = v'_- \equiv v'_c\,, \qquad \text{at} \quad x = x_c\,. \tag{C.164}$$

Then (C.160) leads to

$$z'_+ - z'_- = -\frac{1}{2P(z)}(Q(z) - P^2(z))v'_c\,. \tag{C.165}$$

From these equations, we get

$$E_+ = \frac{(Q_c - P_c^2)v'_c}{2} = -\frac{(Q_c - P_c^2)z'_-}{2P_c}\,, \tag{C.166}$$

where $P_c \equiv P(z_c)$, $Q_c \equiv Q(z_c)$ and again $z'_- = -\sqrt{(z_*/z_c)^{2d_\theta} - 1}$. Thus, in the black hole part $x_c < x \leqslant \ell/2$ we have

$$v' = \frac{E_+ - Q(z)z'}{P(z)}\,, \tag{C.167}$$

$$z'^2 = \frac{Q(z)}{P(z)^2}\left[\left(\frac{z_*}{z}\right)^{2d_\theta} - 1\right] + \frac{(Q_c - P_c^2)^2}{4P_c^2P(z)^2}\left[\left(\frac{z_*}{z_c}\right)^{2d_\theta} - 1\right] \equiv H(z)\,. \tag{C.168}$$

Repeating the steps explained to get (3.63) and (3.64), in this case we find

$$t = \int_0^{z_c}\frac{P(z)}{Q(z)}\left(\frac{E_+}{P(z)\sqrt{H(z)}} + 1\right)dz\,, \qquad \mathcal{A} = 2\ell_\perp^{d-1}z_*^{d_\theta}\int_0^{z_c}\frac{dz}{z^{2d_\theta}\sqrt{H(z)}}\,. \tag{C.169}$$

C.3.1 Linear growth

At this point we take the limit of large z_*, keeping z_m and z_c finite. In this limit, (C.168) becomes

$$z'^2 = \left(\frac{Q(z)}{z^{2d_\theta}} + \frac{(Q_c - P_c^2)^2}{4z_c^{2d_\theta} P_c^2}\right) \frac{z_*^{2d_\theta}}{P(z)^2} = H(z)\,. \tag{C.170}$$

The equation $\partial_{z_m} H(z_m) = 0$, which defines z_m, reads

$$(Q'_m P_m - 2Q_m P'_m) z_m - 2d_\theta P_m Q_m - 2P'_m \gamma_c z_m^{2d_\theta+1} = 0\,, \tag{C.171}$$

where the subindex m denotes that the corresponding quantity is computed at $z = z_m$ and we defined

$$\gamma_c \equiv \frac{(Q_c - P_c^2)^2}{4z_c^{2d_\theta} P_c^2}\,. \tag{C.172}$$

Introducing $\gamma_c^* \equiv \gamma_c|_{z_c = z_c^*}$, the equation for z_c^* reads

$$\gamma_c^* = -\frac{Q_m}{z_m^{2d_\theta}}\,, \tag{C.173}$$

which reduces to the second equation of (C.56) for the case considered in the Appendix C.2. Then, plugging (C.173) into (C.171) we find

$$Q'_m z_m - 2d_\theta Q_m = 0\,, \qquad \text{at } \; z_c = z_c^*\,, \tag{C.174}$$

which can also be written as

$$\partial_{z_m}\left(\frac{Q_m}{z_m^{2d_\theta}}\right) = 0\,. \tag{C.175}$$

Repeating the steps done to get (C.69), (C.70) and (C.71), in this case we obtain

$$\ell/2 = \frac{\sqrt{\pi}\,\Gamma(1/(2d_\theta)+1/2)}{\Gamma(1/(2d_\theta))}\, z_* - \frac{\log\varepsilon}{\sqrt{H_2}}\,, \tag{C.176}$$

$$t = -\frac{E_+}{Q_m\sqrt{H_2}}\,\log\varepsilon = -\frac{z_*^{d_\theta}}{z_m^{d_\theta}\sqrt{-H_2 Q_m}}\,\log\epsilon\,, \tag{C.177}$$

$$A^{(3)}_{\rm reg} = -2\ell_\perp^{d-1}\frac{z_*^{d_\theta}}{z_m^{2d_\theta}\sqrt{H_2}}\,\log\varepsilon\,. \tag{C.178}$$

Thus, (C.177) and (C.178) allow us to find that

$$A^{(3)}_{\rm reg} = 2\ell_\perp^{d-1}\frac{\sqrt{-Q_m}}{z_m^{d_\theta}}\,t\,. \tag{C.179}$$

We conclude that $P(z)$ does not affect the linear growth regime.

C.4 Vaidya backgrounds with time dependent exponents

In this appendix we consider the following generalization of (3.11)

$$ds^2 = z^{2\theta(v)/d-2}\left(-z^{2(1-\zeta(v))}F(v,z)\,dv^2 - 2z^{1-\zeta(v)}\,dv\,dz + d\boldsymbol{x}^2\right)\,, \tag{C.180}$$

where we have introduced a temporal dependence in the Lifshitz and hyperscaling exponents. Let us discuss the energy-momentum tensor when the metric (C.180) is on shell. For simplicity, we consider only the backgrounds (C.180) with $F(v,z) = 1$ identically.
The first case we consider is given by $\theta(v) = \text{const}$. The associated energy-momentum tensor reads

$$T_{\mu\nu} = T^{(\rm hs)}_{\mu\nu} + T^{(\zeta)}_{\mu\nu}\,, \tag{C.181}$$

where $T^{(\mathrm{hs})}_{\mu\nu}$ is the part containing the hyperscaling exponent, which occurs also when $\zeta(v)$ is constant, namely

$$T^{(\mathrm{hs})}_{\mu\nu} = \begin{pmatrix} -z^{-2\zeta}(d_\theta+1+\theta/d)d_\theta/2 & -z^{1-\zeta}(d_\theta+1+\theta/d)d_\theta/2 & 0 \\ -z^{1-\zeta}(d_\theta+1+\theta/d)d_\theta/2 & z^{-2}d_\theta(\theta/d-\zeta+1) & 0 \\ 0 & 0 & z^{-2}[d_\theta^2(d-1)/d+2\zeta(\zeta-1+d_\theta)]\,\mathbb{I}_d/2 \end{pmatrix}, \tag{C.182}$$

(we have denoted by $\mathbb{I}_d$ the d dimensional identity matrix), while $T^{(\zeta)}_{\mu\nu}$ is the term due to $\zeta' \neq 0$

$$T^{(\zeta)}_{\mu\nu} = \begin{pmatrix} 0 & 0 & 0 \\ 0 & 0 & 0 \\ 0 & 0 & z^\zeta \zeta' \,\mathbb{I}_d \end{pmatrix}. \tag{C.183}$$

Similarly, we can consider the situation where $\zeta(v) = \text{const}$. It leads to

$$T_{\mu\nu} = T^{(\mathrm{hs})}_{\mu\nu} + T^{(\theta)}_{\mu\nu}\,, \tag{C.184}$$

where $T^{(\mathrm{hs})}_{\mu\nu}$ is (C.182) and

$$T^{(\theta)}_{\mu\nu} = \frac{\theta'}{z}\begin{pmatrix} z^{\zeta-1}\big[2+\log z\big(\zeta-d_\theta-\theta/d+(\theta'/d)\log z\big)\big] & (1-d_\theta\log z) & 0 \\ (1-d_\theta\log z) & 0 & 0 \\ 0 & 0 & z^{\zeta-1}\big[2+(d-1)(d_\theta/d)\log z\big]\,\mathbb{I}_d \end{pmatrix}, \tag{C.185}$$

which vanishes when $\theta(v)$ is constant, as expected. When both $\theta'(v) \neq 0$ and $\zeta'(v) \neq 0$, we find that

$$T_{\mu\nu} = T^{(\mathrm{hs})}_{\mu\nu} + T^{(\zeta)}_{\mu\nu} + T^{(\theta)}_{\mu\nu} + T^{(\theta\zeta)}_{\mu\nu}\,, \tag{C.186}$$

where $T^{(\mathrm{hs})}_{\mu\nu}$, $T^{(\zeta)}_{\mu\nu}$ and $T^{(\theta)}_{\mu\nu}$ have been defined respectively in (C.182), (C.183) and (C.185), while $T^{(\theta\zeta)}_{\mu\nu}$ is given by

$$T^{(\theta\zeta)}_{\mu\nu} = \begin{pmatrix} -\zeta'\theta'\log^2(z) & 0 & 0 \\ 0 & 0 & 0 \\ 0 & 0 & \mathbf{0}_d \end{pmatrix}, \tag{C.187}$$

being $\mathbf{0}_d$ is the $d \times d$ matrix whose elements are zero.
It could be interesting to analyze the Null Energy Condition for these kind of backgrounds. Unfortunately, since the inequalities turn out to be lengthy and not very illuminating, we will consider here only the case of $\theta(v) = \text{const}$. First, since a null vector with respect to the metric (C.180) is null also with respect to (3.11), we can employ the vectors (3.14). Secondly, given the additive structure of $T_{\mu\nu}$ in (C.181), we can consider the results of 3.1 and add to them the contribution of $T^{(\zeta)}_{\mu\nu}N^\mu N^\nu$. The resulting inequalities read

$$d_\theta\big[\zeta(v)-1-\theta/d\big] \;\geqslant\; 0\,, \tag{C.188}$$

$$\big[\zeta(v)-1\big]\big[d_\theta+\zeta(v)\big] + z^{\zeta(v)}\zeta'(v) \;\geqslant\; 0\,, \tag{C.189}$$

which reduce respectively to (3.7) and (3.8) when $\zeta(v) = \text{const}$, as expected. When $\theta = 0$, the inequality (C.188) tells us that $\zeta(v) \geqslant 1$. As for (C.189), it allows, for instance, a profile with $\zeta'(v) \geqslant 0$. In the critical case $\theta = d-1$, (C.188) becomes $\zeta(v) \geqslant 2-1/d \geqslant 1$ while (C.188) becomes $[\zeta(v)^2-1]+z^{\zeta(v)}\zeta'(v) \geqslant 0$. Thus, for instance, profiles having $\zeta'(v) \geqslant 0$ are again allowed.

Appendix D

Non-smooth boundaries and hyperscaling

D.1 Backgrounds with hyperscaling violating factor

In this section we will review certain features of gravitational backgrounds with hyperscaling violating factor[78, 143, 145]. In what follows we will follow the notation of [158] and consider a minimal dilaton-Einstein-Maxwell action, that is

$$S = -\frac{1}{16\pi G}\int d^{d+2}x\sqrt{-g}\left[R - \frac{1}{2}(\partial\phi)^2 + V(\phi) - \frac{1}{4}e^{\lambda\phi}F_{\mu\nu}F^{\mu\nu}\right], \tag{D.1}$$

where, motivated by the typical exponential potentials of string theories, we will consider the following potential

$$V = V_0 e^{\gamma\phi}. \tag{D.2}$$

The equations of motion of the above action read

$$\begin{aligned} R_{\mu\nu} + \frac{V(\phi)}{d}g_{\mu\nu} &= \frac{1}{2}\partial_\mu\phi\partial_\nu\phi + \frac{1}{2}e^{\lambda\phi}\left(F_\mu^\rho F_{\rho\nu} - \frac{g_{\mu\nu}}{2d}F^2\right), \\ \nabla^2\phi = -\frac{dV(\phi)}{d\phi} + \frac{1}{4}\lambda e^{\lambda\phi}F^2, &\qquad \partial_\mu\left(\sqrt{-g}e^{\lambda\phi}F^{\mu\nu}\right) = 0. \end{aligned} \tag{D.3}$$

It is straightforward to find a solution to these equation, namely the black brane

$$\begin{aligned} ds^2 &= \frac{L^2}{r^2}\left(\frac{r}{r_F}\right)^{2\frac{\theta}{d}}\left(-\frac{f(r)dt^2}{r^{2(z-1)}} + \frac{dr^2}{f(r)} + d\vec{x}_d^2\right), \qquad f(r) = 1 - m\, r^{d_\theta+z}, \\ F_{tr} &= \sqrt{2(z-1)(d_\theta+z)}r^{d_\theta+z-1}, \qquad \phi = \sqrt{2d_\theta(z-1-\theta/d)}\log r. \end{aligned} \tag{D.4}$$

which solve (D.3) if we choose the parameters in the action to be

$$V = \frac{(d_\theta+z)(d_\theta+z-1)}{L^2}\left(\frac{r_F}{r}\right)^{\frac{2\theta}{d}}, \qquad \lambda = -2\frac{\theta+dd_\theta}{\sqrt{2dd_\theta(dz-d-\theta)}}, \qquad \gamma = \frac{2\theta}{d\sqrt{2d_\theta(z-1-\theta/d)}}. \tag{D.5}$$

Here L is the radius of curvature of the space-time and r_F is a scale which can be interpreted as the gravitational dual of the Fermi radius of the theory living on the boundary. A charged black brane solution would need more gauge fields to support its charge, although in what follows we restrict ourselves to the neutral background.

This geometry is a black brane background whose Hawking temperature is

$$T = \frac{d_\theta+z}{4\pi\, r_H^z}, \tag{D.6}$$

where r_H is the horizon radius defined by $f(r_H) = 0$. In terms of the Hawking temperature the thermal entropy can be computed to be

$$S_{\rm th} = \left(\frac{4\pi}{d_\theta + z}\right)^{\frac{d_\theta}{z}} \frac{L^d V_d}{4G\, r_F^{d-d_\theta}}\, T^{\frac{d_\theta}{z}}. \tag{D.7}$$

It is also interesting to evaluate the quadratic action for a small perturbation above the vacuum solution (D.4). This may be used to compute two point function of the energy momentum tensor. To proceed we will consider a perturbation over the vacuum in which we let vary only the metric

$$g_{\mu\nu} = \bar{g}_{\mu\nu} + h_{\mu\nu}, \qquad \phi = \bar{\phi}, \qquad A_\mu = \bar{A}_\mu. \tag{D.8}$$

where the "bar" quantities represent the vacuum solution (D.4). It is then straightforward to linearize the equations of motion, leading to

$$R^{(1)}_{\mu\nu} + \frac{V(\bar{\phi})}{d} h_{\mu\nu} = 0, \qquad \frac{1}{\sqrt{\bar{g}}}\partial_\mu\left(\sqrt{\bar{g}} h^{\mu\nu}\partial_\nu\bar{\phi}\right) = \frac{1}{2}\bar{g}^{\mu\nu}\partial_\mu h \partial_\nu\bar{\phi}, \qquad \bar{F}^{\mu\nu}\partial_\mu h = 0. \tag{D.9}$$

Here the linearized Ricci tensor is given by

$$\begin{aligned} R^{(1)}_{\mu\nu} &= \frac{1}{2}\left(-\bar{\nabla}^2 h_{\mu\nu} - \bar{\nabla}_\mu\bar{\nabla}_\nu h + \bar{\nabla}_\sigma\bar{\nabla}_\nu h^\sigma_\mu + \bar{\nabla}_\sigma\bar{\nabla}_\mu h^\sigma_\nu\right) \\ &= \frac{1}{2}\left(-\bar{\nabla}^2 h_{\mu\nu} - \bar{\nabla}_\mu\bar{\nabla}_\nu h + \bar{\nabla}_\nu\bar{\nabla}_\sigma h^\sigma_\mu + \bar{\nabla}_\mu\bar{\nabla}_\sigma h^\sigma_\nu + \bar{R}_{\sigma\nu} h^\sigma_\mu + \bar{R}_{\sigma\mu} h^\sigma_\nu - 2\bar{R}_{\lambda\mu\sigma\nu} h^{\lambda\sigma}\right). \end{aligned} \tag{D.10}$$

Moreover for the Ricci scalar one gets

$$R^{(1)} = \bar{g}^{\mu\nu} R^{(1)}_{\mu\nu} - \bar{R}_{\mu\nu} h^{\mu\nu} = -\bar{\nabla}^2 h + \bar{\nabla}_\mu\bar{\nabla}_\nu h^{\mu\nu} - \bar{R}_{\mu\nu} h^{\mu\nu}. \tag{D.11}$$

In order to solve the equations of motion one needs to properly fix the gauge freedom. In our case it turns out to be useful to choose a covariant gauge $\nabla^\mu h_{\mu\nu} = \frac{1}{2}\nabla_\nu h$, which however still does not fix all redundant degrees of freedom. Indeed, we fix the remaining ones by setting $h_{ri} = h = 0$ and thus $\nabla^\mu h_{\mu\nu} = 0$ so that we reduce to a transverse and traceless gauge. It is easy to see, with this constraint and gauge choice, that the equation of motion of the scalar field at first order will be identically satisfied and one only needs to solve the Einstein equations, which, generally, reduce to further equation of motion for a scalar field. Indeed taking into account that

$$\bar{R}_{\mu\sigma} h^\sigma_\nu = -\frac{1}{d}\left(V(\bar{\phi}) + \frac{1}{4} e^{\lambda\bar{\phi}}\bar{F}^2\right) h_{\mu\nu} + \frac{1}{2} h^\sigma_\nu\left(\partial_\mu\bar{\phi}\partial_\sigma\bar{\phi} + e^{\lambda\bar{\phi}}\bar{F}^\rho_\mu\bar{F}_{\rho\sigma}\right) \tag{D.12}$$

and using the transverse-traceless gauge we arrive at

$$\bar{\nabla}^2 h_{\mu\nu} + 2\bar{R}_{\alpha\mu\beta\nu} h^{\alpha\beta} + \frac{1}{2d} e^{\lambda\bar{\phi}}\bar{F}^2 h_{\mu\nu} - \frac{1}{2} e^{\lambda\bar{\phi}}\bar{F}_{\rho\sigma}\bar{F}^\rho_{(\mu} h^\sigma_{\nu)} = 0. \tag{D.13}$$

Using the parameters of the vacuum solution, one could in principle solve the above differential equations with given boundary condition. Then by making use of AdS/CFT correspondence from the quadratic action one can compute the two point function of the energy momentum tensor for a strongly coupled field theory whose gravitational dual is provided by a geometry with hyperscaling violating factor using holographic renormalization.
In general (D.13) cannot be solved analytically, and since for $z \neq 1$ we do not have a good control on the asymptotic behaviour of the metric (in ananlogy with the Fefferman-Graham expansion), it is hard to use holographic renormalization techniques (see however [186] for a related issue).

On the other hand, setting $z = 1$, and thus recovering Lorentz symmetry in the bulk metric, we can rely on the holographic renormalization to compute the stress-energy tensor two point's function, namely because the action reduces to a dilaton-Einstein model with a simpler equation of motion

$$\bar{\nabla}^2 h_{\mu\nu} + 2\bar{R}_{\alpha\mu\beta\nu} h^{\alpha\beta} = 0. \tag{D.14}$$

It is however important to note that the null energy condition for $z=1$ implies that $\theta(d-\theta)\leq 0$, that is either $\theta\leq 0$ or $\theta\geq d$. In all our computations we implicitly assumed $d_\theta\geq 1$, playing d_θ the role of the effective dimension, although a solution with $\theta>d$ may not be consistent[78].

Moreover, for $\theta=0$ it is clear that all equations reduce to that of Einstein gravity. In particular one gets [187]

$$h^l_k(r,x)=\frac{\Gamma\left(d+1\right)}{\pi^{\frac{d+1}{2}}\Gamma\left(\frac{1+d}{2}\right)}\int dy^{d+1}\left(\frac{r}{r^2+(x-y)^2}\right)^{d+1}J^i_k(x-y)J^l_j(x-y)P_{ijab}\,h_{ab}(y), \tag{D.15}$$

where h_{ab} is the boundary value of metric and (see [187])

$$J^j_i(x)=\delta^i_j-2\frac{x_jx^i}{|x|^2},\qquad P_{ijab}=\frac{1}{2}(\delta_{ia}\delta_{jb}+\delta_{ib}\delta_{ja})-\frac{1}{d+1}\delta_{ij}\delta_{ab}. \tag{D.16}$$

Since the quadratic on-shell action is a divergent quantity one needs to consider both boundary and counterterms in order to properly compute the two point function. In the present case for $z=1$ the terms of the renormalized action which could contribute to quadratic order perturbatively in the metric are[1]

$$S_{\text{total}}=S-\frac{1}{8\pi G}\int d^{d+1}x\sqrt{\gamma}K-\frac{1}{8\pi G}\int d^{d+1}x\sqrt{\gamma}\,\left(\frac{r_F}{r}\right)^{\frac{\theta}{d}}\,\frac{d_\theta}{L}, \tag{D.17}$$

where S is the original action (D.1). To evaluate the quadratic action it is also useful to note

$$\int d^{d+1}x\sqrt{\gamma}\;K=\partial_n\int d^{d+1}x\sqrt{\gamma}=\frac{r}{L}\left(\frac{r_F}{r}\right)^{\frac{\theta}{d}}\partial_r\int d^{d+1}x\sqrt{\gamma}, \tag{D.18}$$

with

$$\sqrt{\gamma}=\left(\frac{L}{r}\right)^{d+1}\left(\frac{r}{r_F}\right)^{\theta+\frac{\theta}{d}}\left(1+\frac{1}{2}h-\frac{1}{4}h^i_jh^j_i+\frac{1}{8}h^2+\cdots\right). \tag{D.19}$$

By plugging the linearized solution back into the action one finds (see [187] for more details)

$$S_{\text{total}}=\frac{1}{4}\frac{L^d}{16\pi G}\,\frac{d+2}{d}\,\frac{\Gamma(d+2)}{\pi^{\frac{d+1}{2}}\Gamma\left(\frac{1+d}{2}\right)}\int d^{d+1}x\;d^{d+1}y\;\frac{h_{ab}(x)G_{abcd}(x,y)h_{cd}(y)}{(x-y)^{2(d+1)}}, \tag{D.20}$$

where $G_{abcd}(x,y)=J^i_a(x-y)J^b_j(x-y)P_{ijcd}$. Having found the quadratic on-shell action the two point function of the energy momentum tensor can be found as follows

$$\langle T_{ab}(x)T_{cd}(y)\rangle=\frac{C_T}{(x-y)^{2(d+1)}}G_{abcd}(x,y). \tag{D.21}$$

where

$$C_T=\frac{L^d}{8\pi G}\,\frac{d+2}{d}\,\frac{\Gamma(d+2)}{\pi^{\frac{d+1}{2}}\Gamma\left(\frac{1+d}{2}\right)}, \tag{D.22}$$

For $z=1$ and $\theta\neq 0$ one can still find a solution for the equation of motion and evaluate the quadratic action. In this case going through the all steps mentioned above, one arrives at

$$C_T=\frac{L^d}{8\pi Gr_F^{d-d_\theta}}\,\frac{d+2}{d}\,\frac{\Gamma(d_\theta+2)}{\pi^{\frac{d+1}{2}}\Gamma\left(\frac{1+2d_\theta-d}{2}\right)}. \tag{D.23}$$

It is worth noting that the above expression may also be found from the fact that the equations of motion of metric perturbations in traceless-transverse gauge reduce to the equation of motion for a scalar field and therefore the corresponding two point function may be read from the one of a scalar field [78].

For $z\neq 1$, although it is not possible to find holographically the general form of the two point function of $T_{\mu\nu}$, we may still have a chance to compute the *equal time* correlator. Although we have not gone through the details of this idea, but from the analogous results of the scalar field [78] one might expect to get the following expression

$$C_T\propto\frac{L^d}{8\pi Gr_F^{d-d_\theta}}\,\frac{\Gamma(d_\theta+z+1)}{\pi^{\frac{d+1}{2}}\Gamma\left(\frac{2z-1+2d_\theta-d}{2}\right)}. \tag{D.24}$$

We see that here, differently from the holographic entanglement entropy, the coefficient does in fact depend on the Lifshiz exponent z.

[1] Note that we are using Euclidean signature for the metric (see for example [188, 189]).

D.2 Explicit expressions for φ_{2i} and a_{2i} for $i = 1, 2, 3$

In this appendix we will present the explicit form of the coefficients φ_{2i} for the first few orders. To proceed let us start with the following series Ansatz for φ

$$\varphi(h) = \Omega + \varphi_2 h^2 + \varphi_4 h^4 + \varphi_6 h^6 + \mathcal{O}(h^8). \tag{D.25}$$

Plugging this series in the equation of motion of φ one arrives at the equation (4.15) which can be solved order by order. Doing so one finds

$$\begin{aligned}
\varphi_2 &= -\frac{n\cot\Omega}{2(d_\theta-1)}, \quad \varphi_4 = -\frac{n\cot\Omega[(-2n+(d_\theta-1)^2)n\cot^2\Omega + (d_\theta-1)^2(6-2d_\theta+n)]}{8(d_\theta-3)(d_\theta-1)^3},\\
\varphi_6 &= -\frac{8(d_\theta+2)n^2 - 22(d_\theta-1)^2 n + (3d_\theta-7)(d_\theta-1)^3}{48(d_\theta-5)(d_\theta-3)(d_\theta-1)^5}\, n^3\cot^5\Omega\\
&\quad -\frac{2(d_\theta(d_\theta+3)-20)n - (3d_\theta-13)(d_\theta-1)^2 - 11n^2}{24(d_\theta-5)(d_\theta-3)(d_\theta-1)^3}\, n^2\cot^3\Omega\\
&\quad -\frac{(2d_\theta-n-6)(4d_\theta-n-20)}{48(d_\theta-5)(d_\theta-3)(d_\theta-1)}\, n\cot\Omega.
\end{aligned} \tag{D.26}$$

It is clear from these expressions that the solution breaks down for $d_\theta = 2k+1$, $k = 0, 1, \cdots$. In this case one needs to modify the Anstatz by adding a logarithmic term. For example for $d_\theta = 3$, using the Ansatz

$$\varphi(h) = \Omega + \varphi_2 h^2 + \varphi_4 h^4 \left(c + \frac{1}{2}\log h^2\right) + \mathcal{O}(h^6), \tag{D.27}$$

one finds[2]

$$\varphi_2 = -\frac{n}{4}\cot\Omega, \qquad \varphi_4 = -\frac{n^2}{64}\left(n - 4 + n\cos 2\Omega\right)\cot\Omega\csc^2\Omega, \tag{D.28}$$

where c remains unfixed. Similarly for $d_\theta = 5$ for the Ansatz

$$\varphi(h) = \Omega + \varphi_2 h^2 + \varphi_4 h^4 + \varphi_6 h^6 \left(c + \frac{1}{2}\log h^2\right) + \mathcal{O}(h^8) \tag{D.29}$$

one arrives at

$$\begin{aligned}
\varphi_2 &= -\frac{n}{8}\cot\Omega, \qquad \varphi_4 = \frac{n}{512}[(n-8)n\cot^2\Omega - 8(n-4)]\cot\Omega,\\
\varphi_6 &= \frac{(n-4)(7n-16)\, n\cot^4\Omega - 4(n(11n-40)+32)\cot^2\Omega + 32(n-4)}{12288}\, n^2\cot\Omega,
\end{aligned} \tag{D.30}$$

with unspecified c.

Having found the coefficients φ_{2i} it is straightforward to find the coefficients a_{2i} appearing in the equation (4.17). The results are

$$\begin{aligned}
a_0 &= \sin^n\Omega, \qquad a_2 = \varphi_2(2\varphi_2 + n\cot\Omega)\sin^n\Omega\\
a_4 &= \frac{1}{2}[n\left(2\varphi_2^3 + \varphi_4\right)\sin 2\Omega - \varphi_2\sin^2\Omega\left(\varphi_2\left(4\varphi_2^2 + n - 4\right) - 16\varphi_4\right) + \varphi_2^2(n-1)n\cos^2\Omega]\sin^{n-2}\Omega.
\end{aligned} \tag{D.31}$$

Note that for the particular values of $d_\theta = 1, 3$ one needs to use the proper results of φ_{2i} given in this appendix.

[2] See also [120]

Bibliography

[1] L. Susskind, "The World as a Hologram", *Journal of Mathematical Physics* **36** (1994), no. 11, 33, arXiv:9409089.

[2] J. Maldacena, "The large N Limit of superconformal field theories and supergravity", *Advances in Theoretical and Mathematical Physics* **2** (1998), no. 2, 231–252, arXiv:9711200.

[3] E. Witten, "Anti de sitter space and holography", *Advances in Theoretical and Mathematical Physics* **2** (1998), no. 2, 253–290, arXiv:9802150.

[4] L. Susskind and E. Witten, "The Holographic Bound in Anti-de Sitter Space", arXiv:9805114.

[5] M. Bianchi, D. Z. Freedman, and K. Skenderis, "Holographic renormalization", *Nuclear Physics B* **631** (2002), no. 1-2, 159–194, arXiv:0212314.

[6] K. Skenderis, "Lecture notes on holographic renormalization", *Classical and Quantum Gravity* **19** (2002), no. 22, 5849–5876, arXiv:0209067.

[7] J. M. Maldacena, "Wilson loops in large N field theories", *Physical Review Letters* **80** (1998), no. 22, 12, arXiv:9803002.

[8] M. a. Nielsen and I. L. Chuang, "Quantum Computation and Quantum Information: 10th Anniversary Edition", Cambridge University Press, 2010.

[9] M. B. Plenio and S. Virmani, "An introduction to entanglement measures", arXiv:0504163.

[10] D. Harlow, "Jerusalem Lectures on Black Holes and Quantum Information (Preliminary)", *The 31st Jerusalem Winter School in Theoretical Physics*, 2014 arXiv:1409.1231.

[11] T. Hartman, "Lecture notes on Quantum Gravity and Black Holes", 2015.

[12] E. Lieb and M. Ruskai, "Proof of the strong subadditivity of quantum-mechanical entropy", *Journal of Mathematical Physics* **14** (1973), no. 1973, 1938.

[13] M. M. Wolf, F. Verstraete, M. B. Hastings, and J. I. Cirac, "Area Laws in Quantum Systems: Mutual Information and Correlations", *Physical Review Letters* **100** (2008), no. 7, 070502, 0704.3906.

[14] M. Headrick, "Entanglement Rényi entropies in holographic theories", *Physical Review D* **82** (2010), no. 12, 126010, 1006.0047.

[15] M. Srednicki, "Entropy and area", *Physical Review Letters* **71** (1993), no. 5, 666–669, arXiv:9303048.

[16] C. Holzhey, F. Larsen, and F. Wilczek, "Geometric and renormalized entropy in conformal field theory", *Nuclear Physics B* **424** (1994), no. 3, 443–467, arXiv:9403108.

[17] C. Callan and F. Wilczek, "On geometric entropy", *Physics Letters B* **333** (1994), no. 1-2, 55–61, arXiv:9401072.

[18] P. Calabrese and J. Cardy, "Entanglement Entropy and Quantum Field Theory", *Journal of Statistical Mechanics: Theory and Experiment* **2004** (2004), no. 06, 33, arXiv:0405152.

[19] P. Calabrese, J. Cardy, and E. Tonni, "Entanglement entropy of two disjoint intervals in conformal field theory: II", *Journal of Statistical Mechanics: Theory and Experiment* **2011** (2011), no. 01, P01021, 1011.5482.

[20] A. B. Zamolodchikov, "Irreversibility of the Flux of the Renormalization Group in a 2D Field Theory", *Jetp Letters* **43** (1986), no. May, 730–732.

[21] J. Eisert, M. Cramer, and M. B. Plenio, "Colloquium : Area laws for the entanglement entropy", *Reviews of Modern Physics* **82** (2010), no. 1, 277–306, 0808.3773.

[22] I. R. Klebanov, S. S. Pufu, and B. R. Safdi, "F-theorem without supersymmetry", *Journal of High Energy Physics* **2011** (2011), no. 10, 38, 1105.4598.

[23] H. Casini and M. Huerta, "Renormalization group running of the entanglement entropy of a circle", *Physical Review D* **85** (2012), no. 12, 125016, 1202.5650.

[24] S. N. Solodukhin, "Entanglement entropy, conformal invariance and extrinsic geometry", *Physics Letters B* **665** (2008), no. 4, 305–309, 0802.3117.

[25] D. V. Fursaev, "Entanglement Rényi entropies in conformal field theories and holography", *Journal of High Energy Physics* **2012** (2012), no. 5, 80, 1201.1702.

[26] J. L. Cardy, "Is there a c-theorem in four dimensions?", *Physics Letters B* **215** (1988), no. 4, 749–752.

[27] Z. Komargodski and A. Schwimmer, "On renormalization group flows in four dimensions", *Journal of High Energy Physics* **2011** (2011), no. 12, 99, 1107.3987.

[28] Z. Komargodski, "The constraints of conformal symmetry on RG flows", *Journal of High Energy Physics* **2012** (2012), no. 7, 69, 1112.4538.

[29] H. Casini and M. Huerta, "Remarks on the entanglement entropy for disconnected regions", *Journal of High Energy Physics* **2009** (2009), no. 03, 048–048, 0812.1773.

[30] N. Shiba, "Entanglement entropy of two spheres", *Journal of High Energy Physics* **2012** (2012), no. 7, 100, 1201.4865.

[31] J. Cardy, "Some results on the mutual information of disjoint regions in higher dimensions", *Journal of Physics A: Mathematical and Theoretical* **46** (2013), no. 28, 285402, 1304.7985.

[32] C. A. Agón, I. Cohen-Abbo, and H. J. Schnitzer, "Large distance expansion of Mutual Information for disjoint disks in a free scalar theory", 1505.03757.

[33] H. J. Schnitzer, "Mutual Rényi information for two disjoint compound systems", 1406.1161.

[34] H. Casini and M. Huerta, "Universal terms for the entanglement entropy in 2 + 1 dimensions", *Nuclear Physics B* **764** (2007), no. 3, 183–201, arXiv:0606256v4.

[35] H. Casini and M. Huerta, "Entanglement entropy in free quantum field theory", *Journal of Physics A: Mathematical and Theoretical* **42** (2009), no. 50, 41, 0905.2562.

[36] V. Rosenhaus and M. Smolkin, "Entanglement entropy: a perturbative calculation", *Journal of High Energy Physics* **2014** (2014), no. 12, 179, arXiv:1403.3733.

[37] V. Rosenhaus and M. Smolkin, "Entanglement entropy, planar surfaces, and spectral functions", *Journal of High Energy Physics* **2014** (2014), no. 9, 119.

[38] A. Lewkowycz and E. Perlmutter, "Universality in the geometric dependence of Renyi entropy", *Journal of High Energy Physics* **2015** (2014), no. 1, 38, 1407.8171.

[39] H. Casini, M. Huerta, and R. C. Myers, "Towards a derivation of holographic entanglement entropy", *Journal of High Energy Physics* **2011** (2011), no. 5, 36, 1102.0440.

[40] L.-Y. Hung, R. C. Myers, M. Smolkin, and A. Yale, "Holographic calculations of Rényi entropy", *Journal of High Energy Physics* **2011** (2011), no. 12, 47, 1110.1084.

[41] L.-Y. Hung, R. C. Myers, and M. Smolkin, "Twist operators in higher dimensions", *Journal of High Energy Physics* **2014** (2014), no. 10, 178, 1407.6429.

[42] P. Calabrese and J. Cardy, "Evolution of Entanglement Entropy in One-Dimensional Systems", *Journal of Statistical Mechanics: Theory and Experiment* **04010** (2005), no. P04010, 26, arXiv:0503393.

[43] P. Calabrese and J. Cardy, "Time dependence of correlation functions following a quantum quench", *Physical Review Letters* **96** (2006), no. 13, 136801, arXiv:0601225.

[44] P. Calabrese and J. Cardy, "Quantum quenches in extended systems", *Journal of Statistical Mechanics: Theory and Experiment* **2007** (2007), no. 06, P06008–P06008, 0704.1880.

[45] J. Cardy, "Thermalization and Revivals after a Quantum Quench in Conformal Field Theory", *Physical Review Letters* **112** (2014), no. 22, 220401, 1403.3040.

[46] S. Ryu and T. Takayanagi, "Aspects of Holographic Entanglement Entropy", *Journal of High Energy Physics* **2006** (2006), no. 08, 55, arXiv:0605073.

[47] S. Ryu and T. Takayanagi, "Holographic derivation of entanglement entropy from the anti-de sitter space/conformal field theory correspondence", *Physical Review Letters* **96** (2006), no. 18, 5, arXiv:0603001.

[48] J. D. Brown and M. Henneaux, "Central charges in the canonical realization of asymptotic symmetries: An example from three dimensional gravity", *Communications in Mathematical Physics* **104** (1986), no. 2, 207–226, arXiv:0712.0155.

[49] M. Bañados, C. Teitelboim, and J. Zanelli, "Black hole in three-dimensional spacetime", *Physical Review Letters* **69** (1992), no. 13, 1849–1851, arXiv:9204099.

[50] E. Witten, "Anti-de Sitter space, thermal phase transition, and confinement in gauge theories", *Advances in Theoretical and Mathematical Physics* **2** (1998), no. 3, 505–532, arXiv:9803131.

[51] V. E. Hubeny, M. Rangamani, and T. Takayanagi, "A covariant holographic entanglement entropy proposal", *Journal of High Energy Physics* **2007** (2007), no. 07, 062–062, 0705.0016.

[52] X. Dong, "Holographic entanglement entropy for general higher derivative gravity", *Journal of High Energy Physics* **2014** (2014), no. 1, 1310.5713.

[53] D. V. Fursaev, A. Patrushev, and S. N. Solodukhin, "Distributional geometry of squashed cones", *Physical Review D - Particles, Fields, Gravitation and Cosmology* **88** (2013), no. 4, 044054, 1306.4000.

[54] A. Lewkowycz and J. Maldacena, "Generalized gravitational entropy", *Journal of High Energy Physics* **2013** (2013), no. 8, 7, 1304.4926.

[55] M. Babich and A. Bobenko, "Willmore tori with umbilic lines and minimal surfaces in hyperbolic space", *Duke Mathematical Journal* **72** (1993), no. 1, 151–185.

[56] C. R. Graham and E. Witten, "Conformal Anomaly Of Submanifold Observables In AdS/CFT Correspondence", *Nuclear Physics B* **546** (1999), no. 1-2, 52–64, arXiv:9901021.

[57] A. F. Astaneh, G. Gibbons, and S. N. Solodukhin, "What surface maximizes entanglement entropy?", *arXiv* **90** (2014), no. 8, 1–21, arXiv:1407.4719.

[58] N. Drukker and B. Fiol, "On the integrability of Wilson loops in AdS_5 x S^5: Some periodic ansatze", *Journal of High Energy Physics* **2006** (2005), no. 01, 49, arXiv:0506058.

[59] T. Hirata and T. Takayanagi, "AdS/CFT and strong subadditivity of entanglement entropy", *Journal of High Energy Physics* **2007** (2007), no. 02, 042–042, arXiv:0608213.

[60] P. Fonda, L. Franti, V. Keranen, E. Keski-Vakkuri, L. Thorlacius, and E. Tonni, "Holographic thermalization with Lifshitz scaling and hyperscaling violation", *Journal of High Energy Physics* **2014** (2014), no. 8, 32, 1401.6088.

[61] V. E. Hubeny, "Extremal surfaces as bulk probes in AdS/CFT", *Journal of High Energy Physics* **2012** (2012), no. 7, 93, 1203.1044.

[62] R. Ishizeki, M. Kruczenski, and S. Ziama, "Notes on Euclidean Wilson loops and Riemann theta functions", *Physical Review D - Particles, Fields, Gravitation and Cosmology* **85** (2012), no. 10, 106004, 1104.3567.

[63] M. Kruczenski, "Wilson loops and minimal area surfaces in hyperbolic space", *Journal of High Energy Physics* **2014** (2014), no. 11, 65, 1406.4945.

[64] P. C. Vaidya, "The gravitational field of a radiating star", *Proceedings of the Indian Academy of Sciences - Section A* **33** (1951), no. 5, 264–276.

[65] W. B. Bonnor and P. C. Vaidya, "Spherically symmetric radiation of charge in Einstein-Maxwell theory", *General Relativity and Gravitation* **1** (1970), no. 2, 127–130.

[66] J. Abajo-Arrastia, J. a. Aparício, and E. López, "Holographic evolution of entanglement entropy", *Journal of High Energy Physics* **2010** (2010), no. 11, 149, 1006.4090.

[67] V. Balasubramanian, A. Bernamonti, J. de Boer, N. Copland, B. Craps, E. Keski-Vakkuri, B. Müller, A. Schäfer, M. Shigemori, and W. Staessens, "Thermalization of Strongly Coupled Field Theories", *Physical Review Letters* **106** (2011), no. 19, 191601, 1012.4753.

[68] V. Balasubramanian, A. Bernamonti, J. de Boer, N. Copland, B. Craps, E. Keski-Vakkuri, B. Müller, A. Schäfer, M. Shigemori, and W. Staessens, "Holographic thermalization", *Physical Review D* **84** (2011), no. 2, 026010, 1103.2683.

[69] V. Balasubramanian, A. Bernamonti, N. Copland, B. Craps, and F. Galli, "Thermalization of mutual and tripartite information in strongly coupled two dimensional conformal field theories", *Physical Review D* **84** (2011), no. 10, 105017, 1110.0488.

[70] J. a. Aparício and E. López, "Evolution of two-point functions from holography", *Journal of High Energy Physics* **2011** (2011), no. 12, 82, 1109.3571.

[71] E. da Silva, E. López, J. Mas, and A. Serantes, "Collapse and Revival in Holographic Quenches", *Journal of High Energy Physics* **2015** (2014), no. 4, 38, 1412.6002.

[72] C. P. Herzog, "Lectures on holographic superfluidity and superconductivity", *Journal of Physics A: Mathematical and Theoretical* **42** (2009), no. 34, 343001, 0904.1975.

[73] S. a. Hartnoll, "Lectures on holographic methods for condensed matter physics", *Classical and Quantum Gravity* **26** (2009), no. 22, 224002, 0903.3246.

[74] N. Iqbal, H. Liu, and M. Mezei, "Lectures on holographic non-Fermi liquids and quantum phase transitions", *arXiv preprint arXiv:1110.3814*, 2011, no. July, 70, 1110.3814.

[75] D. Gioev and I. Klich, "Entanglement entropy of fermions in any dimension and the widom conjecture", *Physical Review Letters* **96** (2006), no. 10, 1–4, arXiv:0504151.

[76] M. M. Wolf, "Violation of the entropic area law for fermions", *Physical Review Letters* **96** (2006), no. 1, 010404, arXiv:0503219.

[77] B. Swingle, "Entanglement entropy and the Fermi surface", *Physical Review Letters* **105** (2010), no. 5, 1–4, 0908.1724.

[78] X. Dong, S. Harrison, S. Kachru, G. Torroba, and H. Wang, "Aspects of holography for theories with hyperscaling violation", *Journal of High Energy Physics* **2012** (2012), no. 6, 41, 1201.1905.

[79] N. Ogawa, T. Takayanagi, and T. Ugajin, "Holographic Fermi surfaces and entanglement entropy", *Journal of High Energy Physics* **2012** (2012), no. 1, 125, 1111.1023.

[80] L. Huijse, S. Sachdev, and B. Swingle, "Hidden Fermi surfaces in compressible states of gauge-gravity duality", *Physical Review B - Condensed Matter and Materials Physics* **85** (2012), no. 3, 33, 1112.0573.

[81] B. Li, N. Madras, and A. D. Sokal, "Critical exponents, hyperscaling, and universal amplitude ratios for two- and three-dimensional self-avoiding walks", *Journal of Statistical Physics* **80** (1995), no. 3-4, 661–754, arXiv:9409003.

[82] P. Fonda, L. Giomi, A. Salvio, and E. Tonni, "On shape dependence of holographic mutual information in AdS4", *Journal of High Energy Physics* **2015** (2015), no. 2, 5.

[83] K. a. Brakke, "The Surface Evolver", *Experimental Mathematics* **1** (1992), no. 2, 141–165.

[84] M. Alishahiha, A. F. Astaneh, P. Fonda, and F. Omidi, "Entanglement Entropy for Singular Surfaces in Hyperscaling violating Theories", 1507.05897.

[85] R. C. Myers and A. Sinha, "Holographic c-theorems in arbitrary dimensions", *Journal of High Energy Physics* **2011** (2011), no. 1, 125, 1011.5819.

[86] H. Casini and M. Huerta, "Renormalization group running of the entanglement entropy of a circle", *Physical Review D - Particles, Fields, Gravitation and Cosmology* **85** (2012), no. 12, 125016, 1202.5650.

[87] I. R. Klebanov, T. Nishioka, S. S. Pufu, and B. R. Safdi, "On shape dependence and RG flow of entanglement entropy", *Journal of High Energy Physics* **2012** (2012), no. 7, 1, 1204.4160.

[88] R. C. Myers, R. Pourhasan, and M. Smolkin, "On spacetime entanglement", *Journal of High Energy Physics* **2013** (2013), no. 6, 13, 1304.2030.

[89] I. Papadimitriou, "Holographic renormalization as a canonical transformation", *Journal of High Energy Physics* **2010** (2010), no. 11, 14, 1007.4592.

[90] L. Y. Hung, R. C. Myers, and M. Smolkin, "Some calculable contributions to holographic entanglement entropy", *Journal of High Energy Physics* **2011** (2011), no. 8, 39, 1105.6055.

[91] A. Allais and M. Mezei, "Some results on the shape dependence of entanglement and Rényi entropies", *Physical Review D* **91** (2015), no. 4, 046002, 1407.7249.

[92] G. Vidal and R. F. Werner, "Computable measure of entanglement", *Physical Review A* **65** (2002), no. 3, 032314, arXiv:0102117.

[93] P. Calabrese, J. Cardy, and E. Tonni, "Entanglement Negativity in Quantum Field Theory", *Physical Review Letters* **109** (2012), no. 13, 130502, 1206.3092.

[94] P. Calabrese, J. Cardy, and E. Tonni, "Entanglement negativity in extended systems: a field theoretical approach", *Journal of Statistical Mechanics: Theory and Experiment* **2013** (2013), no. 02, P02008, 1210.5359.

[95] P. Calabrese, J. Cardy, and E. Tonni, "Finite temperature entanglement negativity in conformal field theory", *Journal of Physics A: Mathematical and Theoretical* **48** (2015), no. 1, 015006.

[96] M. Caraglio and F. Gliozzi, "Entanglement entropy and twist fields", *Journal of High Energy Physics* **2008** (2008), no. 11, 076–076, 0808.4094.

[97] S. Furukawa, V. Pasquier, and J. Shiraishi, "Mutual information and boson radius in a c=1 critical system in one dimension", *Physical Review Letters* **102** (2009), no. 17, 170602, 0809.5113.

[98] P. Calabrese, J. Cardy, and E. Tonni, "Entanglement entropy of two disjoint intervals in conformal field theory: II", *Journal of Statistical Mechanics: Theory and Experiment* **2011** (2011), no. 01, P01021.

[99] V. Alba, L. Tagliacozzo, and P. Calabrese, "Entanglement entropy of two disjoint blocks in critical Ising models", *Physical Review B - Condensed Matter and Materials Physics* **81** (2010), no. 6, 0910.0706.

[100] M. Fagotti and P. Calabrese, "Entanglement entropy of two disjoint blocks in XY chains", *Journal of Statistical Mechanics: Theory and Experiment* **2010** (2010), no. 04, P04016.

[101] V. Alba, L. Tagliacozzo, and P. Calabrese, "Entanglement entropy of two disjoint intervals in c = 1 theories", *Journal of Statistical Mechanics: Theory and Experiment* **06** (2011) 012, 1103.3166.

[102] V. E. Hubeny and M. Rangamani, "Holographic entanglement entropy for disconnected regions", *Journal of High Energy Physics* **2008** (2008), no. 03, 006–006, 0711.4118.

[103] M. Headrick, "Entanglement Rényi entropies in holographic theories", *Physical Review D* **82** (2010), no. 12, 126010, 1006.0047.

[104] E. Tonni, "Holographic entanglement entropy: Near horizon geometry and disconnected regions", *Journal of High Energy Physics* **2011** (2011), no. 5, 4, 1011.0166.

[105] D. J. Gross and H. Ooguri, "Aspects of large <math display="inline"> <mi>N</mi> </math> gauge theory dynamics as seen by string theory", *Physical Review D* **58** (1998), no. 10, 106002, arXiv:9805129.

[106] K. Zarembo, "Wilson loop correlator in the AdS/CFT correspondence", *Physics Letters B* **459** (1999), no. 4, 527–534, arXiv:9904149.

[107] P. Olesen and K. Zarembo, "Phase transition in Wilson loop correlator from AdS/CFT correspondence", arXiv:0009210.

[108] H. Kim, D. Park, S. Tamaryan, and H. J. Müller-Kirsten, "Gross-Ooguri phase transition at zero and finite temperature: two circular Wilson loop case", *Journal of High Energy Physics* **2001** (2001), no. 03, 003–003, arXiv:0101235.

[109] T. Faulkner, A. Lewkowycz, and J. Maldacena, "Quantum corrections to holographic entanglement entropy", *Journal of High Energy Physics* **2013** (2013), no. 11, 74, 1307.2892.

[110] M. Headrick and T. Takayanagi, "Holographic proof of the strong subadditivity of entanglement entropy", *Physical Review D - Particles, Fields, Gravitation and Cosmology* **76** (2007), no. 10, 106013, 0704.3719.

[111] T. Azeyanagi, T. Nishioka, and T. Takayanagi, "Near extremal black hole entropy as entanglement entropy via AdS2/CFT1", *Physical Review D - Particles, Fields, Gravitation and Cosmology* **77** (2008), no. 6, 064005, 0710.2956.

[112] V. E. Hubeny, M. Rangamani, and E. Tonni, "Thermalization of causal holographic information", *Journal of High Energy Physics* **2013** (2013), no. 5, 136, 1302.0853.

[113] A. Dekel and T. Klose, "Correlation function of circular Wilson loops at strong coupling", *Journal of High Energy Physics* **2013** (2013), no. 11, 117, 1309.3203.

[114] P. Krtouš and A. Zelnikov, "Minimal surfaces and entanglement entropy in anti-de Sitter space", *Journal of High Energy Physics* **2014** (2014), no. 10, 77.

[115] O. Aharony, S. S. Gubser, J. Maldacena, H. Ooguri, and Y. Oz, "Large N field theories, string theory and gravity", *Physics Reports* **323** (2000), no. 3-4, 183–386, arXiv:9905111.

[116] S. J. Rey and J. T. Yee, "Macroscopic strings as heavy quarks: Large-N gauge theory and anti-de sitter supergravity", *European Physical Journal C* **22** (2001), no. 2, 379–394, arXiv:9803001.

[117] E. Fradkin and J. E. Moore, "Entanglement entropy of 2D conformal quantum critical points: Hearing the shape of a quantum drum", *Physical Review Letters* **97** (2006), no. 5, 23–26, arXiv:0605683.

[118] A. B. Kallin, E. M. Stoudenmire, P. Fendley, R. R. P. Singh, and R. G. Melko, "Corner contribution to the entanglement entropy of an O (3) quantum critical point in 2 + 1 dimensions", *Journal of Statistical Mechanics: Theory and Experiment* **2014** (2014), no. 6, P06009, 1401.3504.

[119] N. Drukker, D. J. Gross, and H. Ooguri, "Wilson Loops and Minimal Surfaces", *Physical Review D* **60** (1999), no. 12, 51, arXiv:9904191.

[120] R. C. Myers and A. Singh, "Entanglement entropy for singular surfaces", *Journal of High Energy Physics* **2012** (2012), no. 9, 13, 1206.5225.

[121] I. R. Klebanov, D. Kutasov, and A. Murugan, "Entanglement as a probe of confinement", *Nuclear Physics B* **796** (2008), no. 1-2, 274–293, 0709.2140.

[122] D. Berenstein, R. Corrado, W. Fischler, and J. Maldacena, "The Operator Product Expansion for Wilson Loops and Surfaces in the Large N Limit", *Physical Review D* **59** (1998), no. 10, 22, arXiv:9809188.

[123] E. H. Lieb and D. W. Robinson, "The finite group velocity of quantum spin systems", *Communications in Mathematical Physics* **28** (1972), no. 3, 251–257.

[124] M. Cheneau, P. Barmettler, D. Poletti, M. Endres, P. Schauß, T. Fukuhara, C. Gross, I. Bloch, C. Kollath, and S. Kuhr, "Light-cone-like spreading of correlations in a quantum many-body system", *Nature* **481** (2012), no. 7382, 484–487, 1111.0776.

[125] S. Bravyi, M. B. Hastings, and F. Verstraete, "Lieb-Robinson bounds and the generation of correlations and topological quantum order", *Physical Review Letters* **97** (2006), no. 5, 050401, arXiv:0603121.

[126] T. Takayanagi, "Entanglement entropy from a holographic viewpoint", *Classical and Quantum Gravity* **29** (2012), no. 15, 153001, 1204.2450.

[127] P. Basu, D. Das, S. R. Das, and K. Sengupta, "Quantum quench and double trace couplings", *Journal of High Energy Physics* **2013** (2013), no. 12, 70, 1308.4061.

[128] A. Buchel, R. C. Myers, and A. Van Niekerk, "Universality of abrupt holographic quenches", *Physical Review Letters* **111** (2013), no. 20, 6, 1307.4740.

[129] T. Hartman and J. Maldacena, "Time evolution of entanglement entropy from black hole interiors", *Journal of High Energy Physics* **2013** (2013), no. 5, 14, 1303.1080.

[130] A. Buchel, L. Lehner, R. C. Myers, and A. van Niekerk, "Quantum quenches of holographic plasmas", *Journal of High Energy Physics* **2013** (2013), no. 5, 67, 1302.2924.

[131] A. Buchel, L. Lehner, and R. C. Myersa, "Thermal quenches in N = 2* plasmas", *Journal of High Energy Physics* **2012** (2012), no. 8, 49, 1206.6785.

[132] M. Rigol, V. Dunjko, V. Yurovsky, and M. Olshanii, "Relaxation in a Completely Integrable Many-Body Quantum System: An Ab Initio Study of the Dynamics of the Highly Excited States of 1D Lattice Hard-Core Bosons", *Physical Review Letters* **98** (2007), no. 5, 050405, arXiv:0604476.

[133] C. Kollath, A. M. Läuchli, and E. Altman, "Quench Dynamics and Nonequilibrium Phase Diagram of the Bose-Hubbard Model", *Physical Review Letters* **98** (2007), no. 18, 180601, arXiv:0607235.

[134] S. R. Manmana, S. Wessel, R. M. Noack, and A. Muramatsu, "Strongly Correlated Fermions after a Quantum Quench", *Physical Review Letters* **98** (2007), no. 21, 210405, arXiv:0612030.

[135] S. Sotiriadis and J. Cardy, "Quantum quench in interacting field theory: A self-consistent approximation", *Physical Review B - Condensed Matter and Materials Physics* **81** (2010), no. 13, 134305, 1002.0167.

[136] T. Albash and C. V. Johnson, "Evolution of holographic entanglement entropy after thermal and electromagnetic quenches", *New Journal of Physics* **13** (2011), no. 4, 045017, 1008.3027.

[137] A. Allais and E. Tonni, "Holographic evolution of the mutual information", *Journal of High Energy Physics* **2012** (2012), no. 1, 102, 1110.1607.

[138] R. Callan, J. He, and M. Headrick, "Strong subadditivity and the covariant holographic entanglement entropy formula", *Journal of High Energy Physics* **2012** (2012), no. 6, 81, 1211.3494.

[139] V. E. Hubeny and H. Maxfield, "Holographic probes of collapsing black holes", *Journal of High Energy Physics* **2014** (2014), no. 3, 97, 1312.6887.

[140] H. Liu and S. J. Suh, "Entanglement Tsunami: Universal Scaling in Holographic Thermalization", *Physical Review Letters* **112** (2014), no. 1, 011601, 1305.7244.

[141] H. Liu and S. J. Suh, "Entanglement growth during thermalization in holographic systems", *Physical Review D* **89** (2014), no. 6, 066012, 1311.1200.

[142] S. Kachru, X. Liu, and M. Mulligan, "Gravity duals of Lifshitz-like fixed points", *Physical Review D* **78** (2008), no. 10, 106005, 0808.1725.

[143] B. Goutéraux and E. Kiritsis, "Generalized holographic quantum criticality at finite density", *Journal of High Energy Physics* **2011** (2011), no. 12, 36, 1107.2116.

[144] B. Swingle, "Conformal Field Theory on the Fermi Surface", *interactions*, 2010 4, 1002.4635.

[145] C. Charmousis, B. Goutéraux, B. S. Kim, E. Kiritsis, and R. Meyer, "Effective Holographic Theories for low-temperature condensed matter systems", *Journal of High Energy Physics* **2010** (2010), no. 11, 126, 1005.4690.

[146] N. Iizuka, N. Kundu, P. Narayan, and S. P. Trivedi, "Holographic Fermi and non-Fermi liquids with transitions in dilaton gravity", *Journal of High Energy Physics* **2012** (2012), no. 1, 94, 1105.1162.

[147] H. Singh, "Special limits and non-relativistic solutions", *Journal of High Energy Physics* **2010** (2010), no. 12, 10, 1009.0651.

[148] K. Narayan, "Lifshitz scaling and hyperscaling violation in string theory", *Physical Review D - Particles, Fields, Gravitation and Cosmology* **85** (2012), no. 10, 1202.5935.

[149] H. Singh, "Lifshitz/Schrödinger Dp-branes and dynamical exponents", *Journal of High Energy Physics* **2012** (2012), no. 7, 82, 1202.6533v1.

[150] P. Dey and S. Roy, "Lifshitz-like space-time from intersecting branes in string/M theory", *Journal of High Energy Physics* **2012** (2012), no. 6, 1203.5381.

[151] P. Dey and S. Roy, "Intersecting D-branes and Lifshitz-like space-time", *Physical Review D - Particles, Fields, Gravitation and Cosmology* **86** (2012), no. 6, 066009, 1204.4858.

[152] C. Charmousis, B. Goutéraux, and E. Kiritsis, "Higher-derivative scalar-vector-tensor theories: Black holes, galileons, singularity cloaking and holography", *Journal of High Energy Physics* **2012** (2012), no. 9, 1206.1499.

[153] M. Ammon, M. Kaminski, and A. Karch, "Hyperscaling-violation on probe D-branes", *Journal of High Energy Physics* **2012** (2012), no. 11, 1207.1726.

[154] J. Bhattacharya, S. Cremonini, and A. Sinkovics, "On the IR completion of geometries with hyperscaling violation", *Journal of High Energy Physics* **2013** (2013), no. 2, 1–25, 1208.1752.

[155] N. Kundu, P. Narayan, N. Sircar, and S. P. Trivedi, "Entangled dilaton dyons", *Journal of High Energy Physics* **2013** (2013), no. 3, 1208.2008.

[156] P. Dey and S. Roy, "Lifshitz metric with hyperscaling violation from NS5-Dp states in string theory", *Physics Letters, Section B: Nuclear, Elementary Particle and High-Energy Physics* **720** (2013), no. 4-5, 419–423, 1209.1049.

[157] E. Shaghoulian, "Holographic entanglement entropy and Fermi surfaces", *Journal of High Energy Physics* **2012** (2012), no. 5, 65, 1112.2702.

[158] M. Alishahiha, E. O. Colgáin, and H. Yavartanoo, "Charged black branes with hyperscaling violating factor", *Journal of High Energy Physics* **2012** (2012), no. 11, 1209.3946.

[159] P. Bueno, W. Chemissany, P. Meessen, T. Ortín, and C. S. Shahbazia, "Lifshitz-like solutions with hyperscaling violation in ungauged supergravity", *Journal of High Energy Physics* **2013** (2013), no. 1, 1209.4047.

[160] J. Gath, J. Hartong, R. Monteiro, and N. a. Obers, "Holographic models for theories with hyperscaling violation", *Journal of High Energy Physics* **2013** (2013), no. 4, 159, 1212.3263.

[161] B. Goutéraux and E. Kiritsis, "Quantum critical lines in holographic phases with (un)broken symmetry", *Journal of High Energy Physics* **2013** (2013), no. 4, 53, 1212.2625.

[162] V. Keränen, E. Keski-Vakkuri, and L. Thorlacius, "Thermalization and entanglement following a nonrelativistic holographic quench", *Physical Review D - Particles, Fields, Gravitation and Cosmology* **85** (2012), no. 2, 1–14, arXiv:1110.5035.

[163] E. Caceres, A. Kundu, J. F. Pedraza, and W. Tangarife, "Strong subadditivity, null energy condition and charged black holes", *Journal of High Energy Physics* **2014** (2014), no. 1, 26, 1304.3398.

[164] V. E. Hubeny, H. Liu, and M. Rangamani, "Bulk-cone singularities & signatures of horizon formation in AdS/CFT", *Journal of High Energy Physics* **2007** (2006), no. 01, 30, arXiv:0610041.

[165] R. C. Myers and A. Sinha, "Seeing a c-theorem with holography", *Physical Review D - Particles, Fields, Gravitation and Cosmology* **82** (2010), no. 4, 046006, 1006.1263.

[166] P. Bueno, R. C. Myers, and W. Witczak-Krempa, "Universality of Corner Entanglement in Conformal Field Theories", *Physical Review Letters* **115** (2015), no. 2, 021602.

[167] P. Bueno and R. C. Myers, "Corner contributions to holographic entanglement entropy", 1505.07842.

[168] D.-W. Pang, "Corner contributions to holographic entanglement entropy in non-conformal backgrounds", 1506.07979.

[169] M. Alishahiha and H. Yavartanoo, "On holography with hyperscaling violation", *Journal of High Energy Physics* **2012** (2012), no. 11, 34, 1208.6197.

[170] P. Bueno and P. F. Ramirez, "Higher-curvature corrections to holographic entanglement entropy in geometries with hyperscaling violation", 1408.6380.

[171] I. Güllü and B. Tekin, "Massive higher derivative gravity in D-dimensional anti-de Sitter spacetimes", *Physical Review D - Particles, Fields, Gravitation and Cosmology* **80** (2009), no. 6, 064033, 0906.0102.

[172] A. Dekel, "Wilson Loops and Minimal Surfaces Beyond the Wavy Approximation", 1501.04202.

[173] R.-X. Miao, "A holographic proof of the universality of corner entanglement for CFTs", 1507.06283.

[174] P. Bueno and R. C. Myers, "Universal entanglement for higher dimensional cones", 1508.00587.

[175] A. Coser, L. Tagliacozzo, and E. Tonni, "On Rényi entropies of disjoint intervals in conformal field theory", *Journal of Statistical Mechanics: Theory and Experiment* **2014** (2014), no. 1, P01008, arXiv:1309.2189.

[176] P. Hayden, M. Headrick, and A. Maloney, "Holographic mutual information is monogamous", *Physical Review D* **87** (2013), no. 4, 046003, 1107.2940.

[177] V. Balasubramanian, P. Hayden, A. Maloney, D. Marolf, and S. F. Ross, "Multiboundary wormholes and holographic entanglement", *Classical and Quantum Gravity* **31** (2014), no. 18, 185015, 1406.2663.

[178] M. Headrick, "General properties of holographic entanglement entropy", *Journal of High Energy Physics* **2014** (2014), no. 3, 27, 1312.6717.

[179] C. E. Harle, "Notes on differential geometry", *Boletim da Sociedade Brasileira de Matemática* **1** (1970), no. 2, 58–60.

[180] S. Alexakis and R. Mazzeo, "Renormalized area and properly embedded minimal surfaces in hyperbolic 3-manifolds", *Communications in Mathematical Physics* **297** (2010), no. 3, 621–651, 0802.2250.

[181] M. Spivak, "Differential Geometry", Dover Books on Mathematics, 1st ed., 1979.

[182] D. L. Chopp, "Computing Minimal Surfaces via Level Set Curvature Flow", *Journal of Computational Physics* **106** (1993), no. 1, 77–91.

[183] M. Abramowitz, "Handbook of Mathematical Functions with Formulas, Graphs, and Mathematical Tables", *American Journal of Physics* **56** (1988), no. 10, 958.

[184] L. Thorlacius, "Holographic geometries for condensed matter applications", arXiv:1307.2882.

[185] H. Liu and M. Mezei, "Probing renormalization group flows using entanglement entropy", *Journal of High Energy Physics* **2014** (2014), no. 1, 58, 1309.6935.

[186] M. Taylor, "Non-relativistic holography", 0812.0530.

[187] H. Liu and A. Tseytlin, "D = 4 super Yang-Mills, D = 5 gauged supergravity and D = 4 conformal supergravity", *Nuclear Physics B* **533** (1998), no. 1-3, 88–108, arXiv:9804083.

[188] E. Shaghoulian, "A Cardy formula for holographic hyperscaling-violating theories", 1504.02094.

[189] M. H. Dehghani, A. Sheykhi, and S. E. Sadati, "Thermodynamics of nonlinear charged Lifshitz black branes with hyperscaling violation", *Physical Review D* **91** (2015), no. 12, 124073, 1505.01134.